



MECHANICAL MODELLING OF THERMAL BARRIER COATINGS AT HIGH TEMPERATURES

Unai HERMOSILLA, Ing. Ind.

Thesis submitted to the University of Nottingham for the degree
of Doctor of Philosophy

February 2008

Esta tesis está dedicada a mis padres, a mi hermano y, sobre todo, a Carmen, por haberme aguantado y confiado en mí todo este tiempo.

Abstract

Thermal barrier coatings (TBCs) are usually applied on high temperature gas turbine components. They reduce the need for additional cooling of the exposed surfaces and improve the durability of the underlying materials. However, the lack of reliable life prediction methods limits their applicability in the design of turbine components and so they are usually employed as additional protection for components that already meet the design requirements.

In order to develop failure models and equations of practical interest, the mechanical behaviour and degradation of properties of coatings at elevated temperature needs to be understood. Several phenomena such as the growth of an oxide layer, degradation of bond coats, creep and thermal expansion mismatch between the different layers that compose the TBC contribute in the development of stresses at high temperature. The effect of thermal cycling has been covered in previous research, giving rise to models that explained how accumulated cyclic inelastic strains occurred in the bond coat and oxide layer due to the thermal expansion mismatch. This favoured the wrinkling of the oxide layer and the concentration of stresses, which could eventually cause crack nucleation, growth and failure of the coating.

The research contained in this thesis focuses mainly on the development of stress concentrations during high temperature exposure. A coupled microstructural-mechanical constitutive model was implemented in order to take into account the processes the coatings undergo at high temperature. High tensile stresses, perpendicular to the oxide-top coat interface, which may induce crack nucleation within the oxide layer at high temperature, were obtained.

Acknowledgements

First of all, I would like to express my sincere thanks to Dr I A Jones for giving me the opportunity to pursue a research degree at Nottingham. His valuable knowledge and guidance at each stage of the project ensured that I was able to achieve my objectives successfully. My deepest thanks also go to Prof T H Hyde, who provided very valuable input to my work and directed me towards its completion.

I am also grateful to Dr M S A Karunaratne and Prof R C Thomson from Loughborough University. Their contribution to the project was crucial and made it possible to expand the current knowledge in the field. My gratitude extends to Dr A Wisbey, Dr I Di Martino and Dr H Basoalto for completing the experimental tests at QinetiQ plc in Farnborough.

I would like to acknowledge the support of EPSRC through the Supergen 2 programme (GR/S86334/01) and the following companies: Alstom Power Ltd, Chromalloy UK, E.ON UK, Howmet Ltd, Mitsui Babcock Energy Ltd, National Physical Laboratory, Rolls Royce plc, RWEnpower, Sermatech Ltd and Siemens for their valuable contributions to the project.

Finally, none of this would have been possible if it had not been for the confidence my parents, my brother and Carmen transmitted me. Hence, this thesis is directly dedicated to them.

2.1.2.3	Cohesive models	16
2.1.2.4	Stress-based TGO growth	18
2.1.2.5	Coupled stress-oxidation (diffusion) constitutive models	19
2.1.3	Top coat sintering	23
2.1.4	Creep	24
2.1.5	Fracture mechanics applications to TBCs	27
2.1.5.1	Energy release rate approach	27
2.1.5.2	Stress intensity factors approach	27
2.1.6	Top coat buckling	28
2.1.7	Other relevant analyses	29
2.2	Life prediction modelling	31
2.2.1	Inelastic strain ranges and TGO thickness based life pre- diction	31
2.2.2	Fracture mechanics based life prediction	32
2.2.2.1	Energy release rate approach	32
2.2.2.2	Stress intensity factor approach	34
2.2.3	Damage mechanics based life prediction	35
2.3	Conclusions	37
3	Thermal analysis of thermal barrier coated super-alloy tensile specimens	43
3.1	Introduction	43
3.2	Finite element model	45
3.2.1	Geometry	45
3.2.2	Boundary conditions	45
3.3	Material properties	46
3.3.1	Top coat emissivity	46

3.3.2	Emissivity of remaining surfaces	48
3.4	Results and discussion	48
3.5	Conclusions	51
4	Creep property evaluation for TBC coated and uncoated IN-738LC and CMSX-4	70
4.1	Introduction	70
4.2	Creep constant fitting methodology	71
4.3	Specimen preparation and tests	72
4.4	Creep data	73
4.4.1	IN-738LC	73
4.4.2	CMSX-4	74
4.4.2.1	Strain softening model	74
4.4.2.2	Norton's creep model	74
4.5	Experimental results	76
4.5.1	Uncoated materials	76
4.5.1.1	IN-738LC	76
4.5.1.2	CMSX-4	76
4.5.2	Coated materials	76
4.5.2.1	IN-738LC	77
4.5.2.2	CMSX-4	78
4.6	Discussion and conclusions	78
5	Modelling oxidation induced stresses in TBCs by imposing TGO swelling strain rates	98
5.1	Introduction	98
5.2	Finite element model	99
5.3	Material properties	101
5.4	TGO growth model	102

5.5	Results and discussion	105
5.6	Conclusions	110
6	Self-consistent determination of elastic, thermal and creep be-	
	haviour of multiphase alloys	128
6.1	Introduction	128
6.2	Eshelby's inclusion technique - homogenization relations	131
6.2.1	Homogeneous inclusion	131
6.2.2	Inhomogeneous inclusion	132
6.3	Calculation of the elastic moduli of heterogeneous materials	134
6.4	Calculation of the coefficient of thermal expansion of heteroge-	
	neous materials	138
6.4.1	Application to the calculation of CTE of multiphase ma-	
	terials	141
6.5	Modelling of the creep behaviour of a multiphase material	143
6.5.1	Additional considerations in the creep of multiphase ma-	
	terials	146
6.5.2	Development of the additional term $\dot{\mathbf{A}}^m$	148
6.5.3	Interpretation of the $\dot{\mathbf{A}}^m$ term	150
6.6	Numerical implementation	151
6.6.1	Implementation within FE analyses	151
6.6.2	Constitutive model: complete set of differential equations	152
6.6.3	Integration algorithm	153
6.7	Conclusions	154
7	MCrAlY creep behaviour modelling by means of finite element	
	unit cells and self-consistent constitutive equations	158
7.1	Introduction	158
7.2	Finite element unit cell	161

7.2.1	Hexagonal close packing (HCP)	161
7.2.2	Simple cubic packing(SCP)	162
7.3	Boundary conditions and finite element meshes	163
7.4	Self-consistent constitutive model	164
7.5	Material properties	167
7.5.1	Creep properties of isolated phases	167
7.5.1.1	β -NiAl	167
7.5.1.2	γ -Ni	168
7.5.1.3	σ -Cr	169
7.5.1.4	γ' – Ni ₃ Al	169
7.5.2	Creep properties of MCrAlYs	170
7.6	Phase equilibrium calculation of MCrAlYs	171
7.7	Results	171
7.7.1	Praxair CO211	171
7.7.2	PWA 276	172
7.7.3	VPS NiCoCrAlY	173
7.8	Discussion and conclusions	173
8	Modelling of the high temperature behaviour of TBCs using sequentially coupled microstructural-mechanical FE analyses	188
8.1	Introduction	188
8.2	Constitutive model	190
8.2.1	Additional considerations	192
8.3	Material properties	193
8.4	Finite element model	194
8.4.1	Integration of FE and microstructural data	194
8.5	Results and discussion	195
8.5.1	Effect of imperfection size and initial oxide thickness	196

8.5.2	Effect of temperature	197
8.5.3	TGO growth stress	197
8.6	Conclusions	199
9	Conclusions	213
9.1	Thermal analysis of coated tensile specimens	213
9.2	Creep tests of coated and uncoated specimens	214
9.3	Modelling of oxidation stresses using swelling strain rates	215
9.4	Self-consistent constitutive model development and implementation	216
9.5	Modelling the creep properties of MCrAlY bond coats using finite element unit cells and self-consistent constitutive models	217
9.6	Modelling of the TBC high temperature response using a coupled microstructural-mechanical framework	218
9.7	General conclusions	219
10	Future work	222
10.1	Further research in material properties	222
10.2	Improvements in the material constitutive model	222
10.3	Response to thermal and mechanical cycling	224
	References	225
A	Calculation of the instantaneous coefficient of thermal expansion	239
B	Calculation of the average shear strain under pure shear stress for a spherical inhomogeneity	244
C	Calculation of the average volumetric change under hydrostatic loading for a spherical inhomogeneity	248

D Complete derivation of the numerical implementation of self-consistent constitutive models	252
D.1 Incremental form of the constitutive equations	252
D.2 Calculation of $\frac{\partial F_{ij}^m}{\partial \Delta \sigma_{kl}^m}$	257
D.3 Stress Jacobian calculation	260
D.4 Stress Jacobian with respect to temperature	262

List of symbols

A_s	material coefficient used in ceramic sintering model
A_h	material coefficient used in TGO growth equation
A_c	coefficient used in crack growth equation
A	creep coefficient
A_0	creep constant in Arrhenius-type equation
$\dot{\mathbf{A}}^m$	tensor used in multiphase model
A^m	creep coefficient of material m
C	constant used in damage model
\mathbf{C}	elastic tensor
\mathbf{C}^m	elastic tensor of material m
C_O	local oxygen concentration
$C_{O_{cr}}$	temperature-dependent critical oxygen concentration
D	top coat thickness
D_0	diffusion coefficient used in Arrhenius-type equation
E	elastic modulus
E	heat radiation (in Chapter 3)
\bar{E}	bimaterial plane strain modulus
E_{c0}, E_{css}	material parameter used in sintering model
E^\perp	out-of-plane elastic modulus
F	function used in cohesive model
\hat{F}	function used in microscopic damage model

F_0, F_1	material parameters used in microscopic damage model
$\frac{F_{TBC}}{F_{TGO}}$	area ratio of top coat and TGO in circumferential direction
G	shear modulus
G	energy release rate in fracture mechanics
G_{min}	minimum energy release rate in fracture mechanics
\hat{H}	dimensionless homogenization function used in self-consistent creep model
K	bulk modulus
K_I	mode I stress intensity factor
K_{Ic}	mode I top coat fracture toughness
K_{II}	mode II stress intensity factor
L_G	grain size
L	bond coat-TGO-top coat imperfection wavelength
N	number of cycles
N	number of elements (in Chapter 5)
N_0	constant used in fatigue calculations
N_f	number of cycles to failure
\dot{N}_p	rate of increase of oxide precipitates per unit volume
P	coefficient that depends on the shape of the oxide particles
Q	activation energy
R	imperfection radius
R	gas constant
R_c	TGO-bond coat coat interface imperfection radius, critical value
\mathbf{S}	Eshelby's tensor
\mathbf{S}	compliance in ceramic sintering model
\mathbf{S}^m	phase accommodation variable

S_x^y	sensitivity of y with respect to x
T	temperature
U_n	displacement jump in normal direction
U_t	displacement jump in tangential direction
V_p	average volume of each oxide particle
W_{ad}	admissible energy release
\mathbf{W}	material rotation tensor
Z	material parameter used in ceramic sintering model
$a_{\Gamma}, b_{\Gamma}, a_{\Omega}, b_{\Omega}$	material parameters used in strain softening creep model
a	amplitude of interface waviness
b, c	exponents used in fatigue calculations
b_1, b_2, \dots, b_5	parameters used in ceramic sintering equation
c	crack length
c	heat capacity (in Chapter 3)
c	speed of light ($299792458 \text{ m} \cdot \text{s}^{-1}$)
\hat{c}	function used in ceramic sintering model
c_x	supersaturation of the element x that forms the penetration
e_v^T	mean volumetric strain
\hat{f}	function used in ceramic sintering model
f	fraction of oxidation-prone phase currently oxidised
$f^{m,ini}$	initial volume fraction of m phase
$f^{m,f}$	final volume fraction of m phase
f^m	volume fraction of m phase
$\hat{f}_h^{ox}, \hat{f}_t^{si}, \hat{f}_T^{ox}, \hat{f}_T^{si}, \hat{f}_T^{th}$	stress functions used in lifetime calculations
g	dimensionless coefficient used in fracture mechanics

h	Planck's constant (6.626068×10^{-34} J · s) used in Chapter 3
h	TGO thickness
h_0	initial thickness of the TGO
h_c	critical TGO thickness
h^e	element (FE) thickness
h_0^e	initial element (FE) thickness
k	thermal conductivity (in Chapter 3)
k	Boltzmann's constant (1.380653×10^{-23} J · K ⁻¹) used in Chapter 3
k'_p	parabolic growth constant of the oxide scale
m_{cr}	parameter used in creep calculations
m	ratio of new TGO volume over consumed bond coat volume
\hat{m}	function used in damage mechanics
n_{ox}	TGO growth equation exponent
n	creep exponent
n_0, n_1	parameters used in temperature dependent creep exponent
p, q	material parameter used in damage mechanics
p_i	internal porosity
p_e	external porosity
r	numerical integration precision ratio
r_{ii}	swelling ratio
r_{\perp}	swelling ratio in perpendicular direction
r_{\parallel}	swelling ratio in parallel direction
s	creep time hardening parameter
\mathbf{s}	deviatoric stress tensor

t	time
t_d^*	lifetime
y	coordinate
$\dot{\Gamma}$	minimum creep strain rate in strain softening creep model
Γ_{cohe}	parameter used in cohesive model
Γ_0	fracture toughness
Γ_i	mode I fracture toughness
Γ_{tbc}	top coat fracture toughness
Δ	opening displacement of crack just above imperfection
$\Delta\epsilon$	maximum in-plane TGO tensile strain range
$\Delta\epsilon_f$	failure strain range
$\Delta\epsilon_{ff}$	constant used in fatigue calculations
$\Delta\epsilon^{corr}$	strain increment correction term
Θ, Ξ	dimensionless crack parameters
Π	dimensionless ratcheting (morphological instability) parameter
Σ_{cr}	dimensionless creep strength parameter
Σ_σ	dimensionless stress parameter
Φ	potential function for cohesive model
Ψ	dimensionless interface wrinkling parameter
Ω	creep softening coefficient used in strain softening creep model
α_c, β_c	parameters used in fracture mechanics equations
α_t	parameter that allows to distinguish normal and tangential behaviours in cohesive model
α^*	coefficient of thermal expansion from a reference temperature

α	instantaneous coefficient of thermal expansion
β_t	Eshelby's shear elastic accommodation factor
β_n	Eshelby's volumetric elastic accommodation factor
β	ratio between TGO growth in thickness and growth in lateral direction
β^*	ratio between TGO growth in thickness and growth in lateral direction for the thickening element row
δ_n	normal maximal opening parameter
δ_0^n	interface separation for the maximum traction
δ_t	tangential maximal opening parameter
δ_0^t	interface separation for maximum shearing
ϵ	emissivity (in Chapter 3)
ϵ	total strain
ϵ^*	eigenstrain
ϵ^e	elastic strain tensor
ϵ^{in}	inelastic strain tensor
ϵ^{cr}	creep strain tensor
ϵ^{tr}	transformation strain tensor
$\epsilon^{m,cr}$	creep strain tensor of m phase
$ \dot{\epsilon}^{m,cr} $	equivalent creep strain rate of m phase
ϵ_{f0}	static failure strain
ϵ_g	growth strain
ϵ^{th}	thermally induced strain tensor
ϵ^{cr}	creep strain
ϵ^{pl}	plastic strain
ϵ^{sw}	swelling strain due to increased alumina volume
$\dot{\epsilon}^{sw}$	volumetric swelling strain rate

ϵ_{\perp}	TGO growth strain, thickening component
ϵ_{\perp}^h	equivalent TGO growth thickening strain considering total layer thickness
ϵ_{\parallel}	TGO growth strain, lengthening component
κ	constant used in fracture mechanics equations
λ	damage
λ	radiation wavelength (in Chapter 3)
μ	shear modulus
ν	Poisson's ratio
ρ	density
σ	Stefan's constant ($5.67051 \times 10^{-8} \text{ W} \cdot \text{m}^{-2}\text{K}^{-4}$) used in Chapter 3
$\boldsymbol{\sigma}$	stress tensor
$\tilde{\sigma}$	norm of the stress tensor
σ^*	stress parameter
$\sigma_0^{ox}, \sigma_0^{si}, \sigma_0^{th}$	reference stresses used in lifetime prediction
$\bar{\sigma}_{22max}$	mean cycle stress
$\sigma_{22}^{ox}, \sigma_{22}^{th}, \sigma_{22}^{si}$	components of the maximum out-of-plane stress
σ_n	normal stress
σ_t	tangential stress
σ_L	material parameter that limits the growth stress
σ_0	thermal mismatch stress
σ_{co}	maximum or initial cleavage strength
σ_g	compressive growth stress
σ_m	mean pressure in ceramic sintering model
σ_s	sintering potential
$\boldsymbol{\sigma}^m$	stress tensor of m material

σ'_{vM}	von Mises equivalent stress
σ_Y	yield stress
τ	shear stress
ϕ	stress parameter used in lifetime calculation

Chapter 1

Introduction

1.1 General

The evolution of both gas turbine aeroengines and land-based gas turbines has been driven by three main factors: (i) increase of the specific output power, (ii) increase of the efficiency of the engine and (iii) cost reduction.

The first of the factors is due to the need to produce high performance lightweight turbines in the aerospace industry. It also applies to land-based gas turbines, where the need to increase the power output of turbines used in electricity generation requires better usage of the power supplying system. This is a way to satisfy the gradual increase in the electricity demand without the need for additional power production units.

The power output of a gas turbine engine depends on two main parameters: the mass flow and the specific core power (SCP), improving with both parameters. One way to increase the SCP of a particular unit is to arise its turbine entry temperature (TET) [1]. An increase in the mass flow rate also raises the turbine power output, but it requires bigger gas turbines and does not allow an increase in power output of machines currently in service.

The evolution of gas turbines has always been linked with high temperature

material developments. In fact, the limit for the TET in an engine is related to the materials used in its hottest parts [1]. Modern gas turbine blades and vanes are air cooled, as indicated in Fig. 1.1, since the surrounding gas temperatures are close to the melting point of the superalloys used. Furthermore, there is a compromise between the amount of cooling applied and the engine efficiency. Higher TETs need more component cooling, but cooling itself causes a reduction in engine efficiency, so there is a limit above which efficiency increases cannot be achieved exclusively by cooling; the component temperature allowed must be raised [1].

The lifetime of mechanical components is usually limited by their surface degradation. The durability of components exposed to high temperature can be extended by protecting their surface in order to avoid the onset of crack nucleation points due to the surface wear, corrosion and degradation [2] caused by high temperature exposure. In addition, some types of coatings, applied to high-temperature components, can significantly lower the temperature of the substrate on which they are applied, thus extending their life. Section 1.2 gives a brief explanation of the different coatings in current use.

1.2 Types of coatings

The types of coating under consideration serve two purposes: to provide a barrier for oxidation, and (where a ceramic top coat is present) to provide thermal insulation. The first of these functions involves the creation of a protective oxide layer upon oxidation. One of the preferred oxides is Al_2O_3 [3], which acts as an oxygen barrier for the underlying material. The formation of this oxide layer requires that the coating itself be rich in aluminium, which can be achieved by several mechanisms according to the coating manufacturing process, as explained in the next sections.

1.2.1 Diffusion coatings

The creation of an Al-rich layer, which will allow the development of a protective alumina layer, can be achieved by a process known as *diffusion aluminizing process*, *pack aluminizing process* or *pack cementation process*, which creates an enriched outer layer of aluminium on the component by its diffusion into the substrate from a halide (e.g. 1%NaF or NH_4Cl) in vapour phase that dissociates at the surface and penetrates the base material. Among the most popular diffusion coatings are ‘*platinum aluminide*’ coatings, or, more precisely, platinum-modified nickel aluminide coatings, (Pt,Ni)Al, where the platinum is electroplated onto the component prior to aluminizing by a pack cementation process [3].

1.2.2 Overlay coatings

Another method of coating a component is by the physical deposition of an alloy containing aluminium onto a substrate, which results in *overlay coatings*. This method produces coatings where the composition can be tailored to match the exact application requirements. The method also makes it possible to produce thicker coats that show longer durabilities, due to their increased reservoir of aluminium. From an engineering point of view the main limitation of overlay coatings is the poor reproducibility of their mechanical properties, which depend strongly on the specific manufacturing process used [4].

The typical formulation of overlay coatings can be represented as MCrAlY, where M stands for Ni, Co or a combination of them. Usual manufacturing processes are electron-beam physical vapour deposition (EB-PVD), vacuum plasma spray (VPS) or low-pressure plasma spray (LPPS), the last two being different names used for the same process, and high-velocity oxy-fuel (HVOF) [3].

1.2.3 Thermal barrier coatings (TBCs)

Ceramic materials have very good mechanical properties and low thermal conductivity at high temperatures, except for their brittle behaviour. The industrial method used to overcome the problem of brittleness is to use ceramic thermal barrier coatings (TBCs) in order to combine and exploit both the mechanical properties of the high temperature superalloy substrate and the thermal properties of the ceramic material [1]. High temperature resistant ceramic layers are applied to a Ni-based superalloy for components subjected to very high temperatures. The ceramic coat acts as a thermal barrier, lowering the temperature of the substrate and thus making it possible to raise the TET of an engine without needing additional cooling and hence achieving the objective of increasing the engine efficiency.

TBCs can also be used to extend component life. If TBCs are used on hot sections but the gas temperatures are not increased, the substrate (base material) temperature will be lowered, thus improving its creep behaviour and service life.

A typical TBC, as shown in Fig. 1.2, is composed of several layers:

1. A ceramic top coat (TC) ($\sim 100\text{-}200\ \mu\text{m}$ thickness), usually $\text{ZrO}_2 - 7\text{wt}\% \text{Y}_2\text{O}_3$, applied using either the air plasma spraying (APS) [5, 6] or the electron beam physical vapour deposition (EB-PVD) [7, 8] technique. This top coat acts as a thermal insulator and lowers the substrate temperature. APS TCs show isotropic mechanical behaviour as they are formed by randomly disposed material grains. EB-PVD TCs, on the other hand, have different mechanical properties and behaviours in the in-plane and through thickness directions. The deposition process produces a columnar grain structure that reflects in material anisotropy, resulting in better mechanical strength but poorer thermal insulation properties.

2. A thermally grown oxide (TGO) layer ($\sim 1-10 \mu\text{m}$ thickness, which increases with thermal exposure time), mainly composed of alumina. This layer grows when the component is at elevated temperature. Aluminium from the bond coat diffuses outwards and oxygen from the environment diffuses inwards and as a result of the reaction new oxide is formed. The TGO layer acts as an oxidation barrier as it is impermeable to oxygen, preventing it from reaching the substrate material and thus extending the substrate's life.
3. An MCrAlY or (Pt,Ni)Al bond coat (BC) ($\sim 100-200 \mu\text{m}$ thickness) manufactured as explained in Section 1.2.2. It is deposited on top of the substrate and it provides a better chemical bond between the top coat and the substrate. It provides aluminium for the TGO, producing an aluminium depletion zone in its outer part.

1.3 Mechanical loading and failure mechanisms

Depending on the application of the turbine in which TBCs are present, these will be subjected to loads of different nature. For instance, TBCs used in aero-engines are mainly subjected to thermo-mechanical fatigue, which is primarily caused by the coefficient of thermal expansion (CTE) mismatch between the different layers. The temperature of the TBC varies according to the regime of the engine and the stop-start cycles. A different load history would be found in power generation applications, where the time between stops is as long as possible in order to achieve the highest possible power output from the available power production units. In this case, the load history is more similar to a high temperature exposure, which implies oxidation and degradation of the materials rather than thermal cycling.

The failure of both land-based and aeroengine TBCs occurs upon the de-

lamination of the top coat [9, 10], usually referred to as *spallation*. This process causes the detachment of the protective ceramic top coat, rather than the fracture and loss of small parts of coating. Several spalling mechanisms have been explained [9, 10], which depend on the specific properties of the materials and load histories involved, composed of similar stages:

1. Initially, cracks nucleate at the BC-TGO-TC interface imperfections, which may have been originated during the coating deposition process, or caused by localised oxide deposition during thermal exposure or from foreign object damage.
2. Once cracks have nucleated, they grow and coalesce according to specific crack growth mechanisms that depend on the particular TBC being used and the load, thermal and mechanical, to which it is being subjected, driven primarily by the oxidation stresses.
3. Finally, TBCs spall typically upon cooling through a process usually referred to as large-scale buckling (LSB), which arises when a critical delamination length has occurred in the vicinity of the oxide layer [10].

1.4 Scope of the thesis

The objective of this thesis is the development and understanding of numerical models that allow analysis of the stresses and strains in TBC coated components and to investigate the effect that the different parameters and variables play in their mechanical behaviour. As stated previously, TBCs typically spall off upon cooling from operating or testing temperature. However, a certain amount of high-temperature exposure time needs to be accumulated for this failure to occur, which demonstrates that it is not a process driven by thermal shock alone. Significant material degradation, stress concentration and crack nucleation must

occur during high temperature exposure in order to create the conditions for spallation upon cooling. This suggests that the key for the understanding of the mechanical performance of TBCs is the set of aging processes at elevated temperature.

Chapter 2 contains a literature review that covers the most relevant papers on the subject of the modelling of TBCs. It is divided in two main parts, the first one covering the mechanical modelling, and the second involving the life assessment of coatings. The work of this thesis focuses on the mechanical modelling and calculation of stress and strain fields. However, the remaining parts, which use crack assessment techniques and fatigue calculations, give an appreciation of the parameters that are assumed to be of most influence in the mechanical performance and durability of coatings.

Chapter 3 deals with the thermal behaviour of coated solid tensile specimens, which helps to understand the transient and steady-state regimes during tests and to quantify the expectable temperature gradients and their influence in test conditions. Chapter 4 contains experimental creep results for coated and uncoated Ni-base superalloys, and a comparison of these results with predictions based on published models. These comparisons ensure that the set of material properties used in the analyses presented in this thesis is realistic. The thermal calculations carried out in Chapter 3 provide information on the test conditions and comparative behaviour of coated tensile specimens with respect to uncoated testpieces.

Chapter 5 describes the common modelling strategy for the calculation of oxidation stresses based on the implementation of swelling strains in order to simulate oxide growth. A parametric study, varying several geometric dimensions, was carried out in order to identify possible weaknesses in these models and to propose improvements. A pattern was identified in these models, which showed that the stresses which are believed to be responsible of spallation are

determined almost exclusively by one of the geometric parameters.

Chapter 6 presents a full review and derivation of a self-consistent constitutive model that allows the implementation of microstructural criteria in the mechanical behaviour of alloys. Bond coats undergo significant microstructural changes and property degradation upon thermal exposure, which can be taken into account in a realistic way by means of the self-consistent constitutive model. Additionally, the oxidation of the bond coat and the precipitation of new oxide is regarded within this framework as a phase transformation, from the compounds initially present at the bond coat to pure alumina, which is accompanied by a volume expansion according to the Pilling-Bedworth ratio of the reaction, reproducing in a more realistic manner the oxidation process. A discretisation of the differential equations that define the constitutive model is presented in Chapter 6, which were coded in ABAQUS via a user material subroutine, UMAT.

Chapter 7 contains a comparison between the predictions of creep properties of several MCrAlY types, at two different temperatures, using 3D unit-cell models, based on the microstructure of the multiphase alloy and the results obtained using the self-consistent constitutive model presented in Chapter 6. These show good agreement, which validates the numerical implementation of the constitutive model. Some remarks on the experimental data scatter and the poor mechanical property reproducibility of MCrAlY alloys are pointed out, and are assumed to be caused by the dependency of MCrAlY properties on the manufacturing process.

Chapter 8 extends the oxidation stress modelling work presented in Chapter 5, by incorporating the coupled constitutive model described in Chapter 6. The mechanical calculation is linked to a microstructural model, developed by other partners in the SuperGen 2 PLE project, in order to simulate the degradation and oxidation of the coatings. The mechanical response is different from that obtained in Chapter 5, but reproduces the trends suggested by other researchers

who used similar methods to simulate TGO growth. Additionally, a possible new phenomenon for predicting crack initiation is identified as the TGO undergoes a fast compression followed by a gradual accumulation of tension reaching high stress levels. Moreover, the concept of a critical imperfection size at the interface between the bond coat and the top coat can be envisaged.

Chapter 9 contains a review of the main conclusions extracted from the previous chapters and a discussion. Finally, Chapter 10 gives ideas of possible ways to extend in the research field presented in this thesis.



Figure 1.1: Internally cooled industrial gas turbine rotor blade.

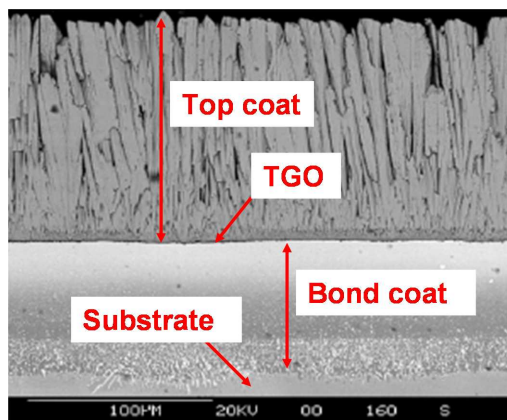


Figure 1.2: Layer distribution in an EB-PVD TBC.

Chapter 2

Literature review

This chapter contains a review of the research work published on TBC modelling. The contents have been divided in two main groups, the first one covering the mechanical behaviour modelling and the approaches that have been used in order to model the phenomena occurring in TBCs, and the second dealing with the life estimation methods.

The review is organised according to the individual phenomena and modelling criteria that have been used, in order to make it usable as a quick reference of the state of the art in each individual aspect involved in TBC modelling. The part relating to the development of life criteria could act as the basis of a possible continuation of the research reported in this thesis. It also provides insight into the critical parameters that are believed to govern TBC failure and acts as an assessment of the phenomena on which the mechanical modelling should focus.

2.1 Mechanical behaviour modelling

2.1.1 Introduction

The finite element method (FEM) has been widely used to model and study the mechanical behaviour of TBCs. The majority of authors use a two dimensional unit cell finite element (FE) model comprising the layers that compose the TBC and a wavy or sinusoidal TC-TGO-BC interface, which simulates the interface geometry that creates stress concentration points in real TBCs.

The effects of thermo-mechanical fatigue, oxidation or a combination of both on the mechanical behaviour of TBCs have been widely explored by means of the FE method. As stated in Section 1.3, the kind of loads to which TBCs are subjected depend on the application of the engine.

A summary of the main features included in the mechanical behaviour modelling is:

1. TGO growth stress: during oxidation inward oxygen diffusion and outward aluminium diffusion causes the TGO to grow and stresses are developed due to the constraint imposed by the surrounding materials.
2. TC sintering: during high temperature exposure time the TC sinters and this produces a stiffening of the material which alters the stress distribution within the TBC.
3. Creep: creep of the different layers has been considered and identified as an important factor in the determination of average stress levels.

The analyses and modelling techniques explained in this section aim towards the understanding of the mechanisms that play a major role in the lifetime of coatings and cause spallation. One of the main causes believed to be responsible of the out-of-plane stress accumulation at different points of the TC/TGO/BC

interface is the combined thermal cycling and oxidation process, which has been observed to cause morphological instabilities in TBCs [11]. It consists of the progressive wrinkling of the TC/TGO/BC interface accompanied by an increase in the amplitude of the undulations. These undulations are believed to be responsible for creating out-of-plane tensile stresses that debond the layers and finally cause spallation.

Additionally, this section contains a review of crack assessment techniques that have been applied to TBCs in order to identify the mechanisms that drive coating failure.

2.1.2 TGO modelling

2.1.2.1 TGO growth using fictitious temperature increments

Freborg *et al.* [12] simulated TGO growth by changing the material properties from bond coat to 95% dense alumina for the elements of the bond coat next to the TGO. The stresses generated by this process were modelled by assigning an artificially high CTE to the newly deposited TGO material and imposing a small change in temperature during steady state. The oxidation process increased considerably the tensile stress level achieved in the bond coat-top coat interface.

He *et al.* [13] simulated the TGO growth, upon thermal cycling, using fictitious temperature increments, ΔT_g , within the TGO during the high temperature step. Results were obtained for different initial interface undulation amplitude ratios, $\frac{a_0}{2L}$, defined using the parameters shown in Fig. 2.1. Two dimensionless parameters were used in order to post-process the results:

$$\Sigma_\sigma \equiv \frac{\sigma_0}{\sigma_Y} \quad (2.1)$$

$$\Pi \equiv \frac{\Delta a}{2L\epsilon_g} \quad (2.2)$$

where Σ_σ is a dimensionless parameter that represents the achieved stress level, σ_0 is the thermal mismatch stress in the TGO, σ_Y is the substrate yield stress, Π is a dimensionless parameter that represents morphological instabilities (interface wrinkling) caused by the ratcheting originated from the cyclic yielding of the substrate, Δa is the change in the wave amplitude per cycle, L is the wavelength as shown in Fig. 2.1 and ϵ_g is the strain increment used to represent the TGO growth, which was considered constant during each cycle of the analysis.

The instability growth rate (ratcheting rate) was found to be sensitive to the prescribed TGO growth rate, a steady-state instability growth requiring a growth strain at every cycle. A critical value of the initial $\frac{a_0}{L}$ ratio, $\frac{a_c}{L}$, which depended on the BC yield stress, was found to exist. Imperfections with amplitudes smaller than that critical value did not exhibit ratcheting under thermal cycling.

2.1.2.2 TGO growth using prescribed strain values

Rösler *et al.* [14] modelled TGO growth by changing the material properties of the adjacent elements to those of alumina. Isotropic swelling, calculated from the Pilling-Bedworth ratio of pure aluminium, was then applied to those elements in order to simulate the stress and strain created by the microstructural changes produced during oxidation. All these changes were carried out using smooth transitions in order to avoid discontinuities in the solution. Compressive stresses were developed within the TGO during that process due to the constraint of the surrounding material.

In a later analysis by Rösler *et al.* [15] the effect of TGO growth was simulated by prescribing a swelling strain rate normal to the TGO-top coat interface, based on a parabolic TGO growth equation. The value was obtained from the

growth law:

$$h^2 = k'_p t \Rightarrow \dot{h} = \frac{1}{2} \frac{k'_p}{h} \quad (2.3)$$

where k'_p is the parabolic growth constant, h is the oxide layer thickness and t is the time. The prescribed strain rate is then calculated as

$$\dot{\epsilon}_{\perp} = \frac{\dot{h}}{h} \quad (2.4)$$

The \dot{h} value was calculated at the beginning of the analysis (considering the initial TGO thickness) and assumed to be constant throughout the analysis. This constitutes a realistic simplification as for relatively long time periods the oxide growth rate is nearly constant, with only the beginning of the stress calculation being affected by the aforementioned assumption. The in-plane strain rate, which represents the lengthening of the oxide scale layer, was modelled as a ratio of the thickening strain rate to the lengthening strain rate, defined by the β parameter as

$$\beta = \frac{\dot{\epsilon}_{\perp}}{\dot{\epsilon}_{\parallel}} \quad (2.5)$$

The total anisotropic swelling was formed by combining both components (thickening and lengthening) and applying them to the elements of the TGO mesh as shown in Fig. 2.2.

Karlsson and Evans [16] performed an FE analysis in order to study the cyclic morphological instability (changes in TGO interface amplitude) caused by TGO growth combined with thermal cycling. The TGO growth was modelled prescribing a per-cycle strain normal to the TGO-top coat interface, ϵ_{\perp} , allowed to vary within experimentally obtained values, which implied that the oxide thickness after N cycles was:

$$h = h_0 + h_0^e [(N - 1)\epsilon_{\perp}] \quad (2.6)$$

where h_0 is the initial TGO thickness and h_0^e is the element thickness. The in-plane growth was simulated by applying the β ratio used by Rösler *et al.* [15].

He *et al.* [17] modified their previous TGO growth model [13], which simulated the TGO growth by imposing fictitious temperature increments, and used two different modelling strategies for oxidation stresses. The thickening of the TGO was modelled by changing the material properties of the BC elements adjacent to the TGO to those of oxide. The gradual change of properties was done according to an experimentally determined TGO growth law that specifies the increase in thickness per cycle, Δh , in terms of the thermal cycle duration, Δt :

$$\frac{\Delta h}{h - h_0} = \frac{\Delta t}{2t} \quad (2.7)$$

with t being the cumulative hot time, h_0 the initial oxide thickness and h the oxide thickness at a time t . The in-plane strain rate was calculated from $\frac{\epsilon_{\parallel}}{\frac{\Delta h}{h_0}} = 0.005$ and imposed on the elements composing the oxide layer as a stress-free strain.

In later analyses, Karlsson *et al.* [18] took into account the effect of different TC-TGO-BC interface imperfection geometries as an extension to the model in Ref. [16]. Different ratios between the prescribed normal and in-plane TGO swelling strain rates were considered. It was shown that relatively high in-plane strain rates fitted the TGO-bond coat interface shape evolution in a more accurate way. An analytical spherically symmetric model [19,20], which reproduced the main features of the used numerical model, was also formulated.

2.1.2.3 Cohesive models

Caliez *et al.* [21] modelled the TGO-top coat and TGO-bond coat interfaces using cohesive zones, as shown in Fig. 2.3, which enabled the implementation of debonding criteria that allowed the simulation of the spallation process.

The damage parameter used in the debonding constitutive law was:

$$\lambda = \sqrt{\left(\frac{\langle U_n \rangle}{\delta_n}\right)^2 + \left(\frac{U_t}{\delta_t}\right)^2}, \text{ with } \langle x \rangle = \begin{cases} x & \text{if } x > 0 \\ 0 & \text{if } x \leq 0 \end{cases} \quad (2.8)$$

where U_n and U_t are, respectively, the displacement differences in normal and tangential directions across the interface modelled as a cohesive zone and δ_n and δ_t the maximal opening parameters, which are obtained from the energy absorbed for the propagation of mode I and II cracks, respectively. The interface is assumed to fail when λ reaches a value of 1. The stress values on the interface are given by:

$$\begin{cases} \sigma_n = \frac{U_n}{\delta_n} F(\lambda) \\ \sigma_t = \alpha_t \frac{U_t}{\delta_t} F(\lambda) \end{cases}, \text{ with } F(\lambda) = \frac{27}{4} \sigma_{max} (1 - \lambda)^2 \quad (2.9)$$

with σ_{max} being the maximum allowable stress on the interface. The model showed that the BC-TGO interface fracture strength degraded with time.

Yuan and Chen [22] used cohesive models to simulate the TGO mechanical behaviour. In order to model the TC brittle behaviour, which manifests itself as strong strain-softening and failure when the ultimate stress is reached; the Rankine plasticity model was used, including a gradient plasticity criterion to overcome numerical instabilities that arise when such plastic behaviour is used. The TGO was simplified and modelled as a cohesive zone, allowing the implementation of a constitutive model to simulate the debonding of the top coat that used the stress potential:

$$\Phi(U_n, U_t) = \Gamma_{cohe} \left[1 - \left(1 + \frac{U_n}{\delta_0^n} \right) e^{\left\{ -\frac{U_n}{\delta_0^n} - \left(\frac{U_t}{\delta_0^t} \right)^2 \right\}} \right] \quad (2.10)$$

where U_n and U_t are the normal and tangential interface separation and δ_0^n and δ_0^t the separations for maximum tension and shearing respectively. The normal

and shear stresses are obtained as:

$$\sigma_n = \frac{\partial\Phi}{\partial U_n} \quad (2.11)$$

$$\sigma_t = \frac{\partial\Phi}{\partial U_t} \quad (2.12)$$

A 2D mesh with a central crack was used, and the debonding of the top coat to bond coat interface was studied. The load was applied at the crack centre, which represented the combined effects of both thermal mismatch and centrifugal loads present in gas turbine blades.

2.1.2.4 Stress-based TGO growth

Jinnestrand and Sjöström [23] developed a specific constitutive model that included alumina growth as one of its features. The bond coat elements adjacent to the TGO were considered initially to have the properties of the bond coat material. When a fully relaxed stress state was achieved in these elements, the material properties were switched to those of alumina, and then a time-dependent swelling was applied in order to simulate the volume expansion upon oxidation. Analyses were run using a fully three dimensional FE mesh. The effects of oxide growth and interface waviness on the delamination stress were investigated in their analysis.

An updated model by Jinnestrand and Brodin [24] considered that the different layers of materials composing the TBC and the substrate would show different behaviours according to their material properties and oxidation pro-

cesses. These behaviours can be summarised in the set of constitutive equations:

$$\sigma_{ij}^{SUB} = C_{ijkl}^{SUB} (\epsilon_{kl} - \epsilon_{kl}^{th} - \epsilon_{kl}^{cr} - \epsilon_{kl}^{pl}) \quad (2.13)$$

$$\sigma_{ij}^{BC} = C_{ijkl}^{BC} (\epsilon_{kl} - \epsilon_{kl}^{th} - \epsilon_{kl}^{cr} - \epsilon_{kl}^{pl}) \quad (2.14)$$

$$\sigma_{ij}^{Al_2O_3} = C_{ijkl}^{Al_2O_3} (\epsilon_{kl} - \epsilon_{kl}^{th} - \epsilon_{kl}^{cr} - \epsilon_{kl}^{sw}) \quad (2.15)$$

$$\sigma_{ij}^{TC} = C_{ijkl}^{TC} (\epsilon_{kl} - \epsilon_{kl}^{th} - \epsilon_{kl}^{cr}) \quad (2.16)$$

where ϵ_{kl}^{sw} is the swelling strain caused by the oxidizing process, defined as:

$$\Delta\epsilon_{kl}^{sw} = \delta_{kl} \frac{dV}{V_0} + \Delta\epsilon_{kl}^{corr} \quad (2.17)$$

$\Delta\epsilon_{kl}^{corr}$ is a correction strain, which introduces a deviatoric part in the swelling strain tensor, and δ_{kl} is Kronecker's delta. $\frac{dV}{V_0}$ represents the volume increase due to the formation of new oxide, which is assumed to be approximately 25%, a typical value for the alumina formation from pure aluminium, as shown by its Pilling-Bedworth ratio. The correction strain is calculated as:

$$\Delta\epsilon_{kl}^{corr} = \frac{\langle \sigma'_{vM} - \sigma_L \rangle}{2\mu\sigma'_{vM}} s_{kl}, \quad \langle x \rangle = \begin{cases} 0 & \text{if } x < 0 \\ x & \text{if } x \geq 0 \end{cases} \quad (2.18)$$

with σ'_{vM} being the von Mises equivalent stress after an isotropic volumetric increment, σ_L a material parameter that limits the growth stress, μ the shear modulus of alumina and s_{kl} the deviatoric stress tensor. Equation 2.17 specifies an anisotropic expansion when new oxide is formed, favouring the oxide formation along the directions with higher deviatoric stress levels.

2.1.2.5 Coupled stress-oxidation (diffusion) constitutive models

Busso *et al.* [25, 26] applied a coupled stress-oxidation formulation in order to model the mechanical behaviour of TBCs. The oxidising process of an originally two-phase metallic system, which simulated the bond coat, was modelled and applied to the TGO growth.

The model considered an alloy originally composed of two phases, one oxidation resistant (volume fraction $f^{(1),ini}$) and the other oxidation-prone (initial volume fraction $f^{(2),ini}$). The oxidation-prone phase reacts to produce an oxide compound, $f^{(ox)}$, and another metallic phase, $f^{(3)}$. At any instant of time during the analysis the following equation is satisfied:

$$f^{(1),ini} + f^{(2)} + f^{(3)} + f^{(ox)} = 1 \quad (2.19)$$

The volume fractions of the phases that are produced upon complete oxidation are denoted by $f^{(3),f}$ and $f^{(ox),f}$. The whole process is governed by the evolution of a single variable, f , which corresponds to the fraction of oxidation-prone phase that has currently undergone the oxidising process. This variable defines the current microstructural composition of the alloy:

$$f^{(2)} = (1 - f)f^{(2),ini} \quad (2.20)$$

$$f^{(3)} = f \cdot f^{(3),f} \quad (2.21)$$

$$f^{(ox)} = f \cdot f^{(ox),f} \quad (2.22)$$

The time evolution of f depends on the results of a mass diffusion analysis where the oxygen concentration profile within the TBC is assessed:

$$\dot{f} = (1 - f)\dot{N}_p V_p \quad \text{for } C_O \geq C_{O_{cr}}, \quad \text{else } \dot{f} = 0 \quad (2.23)$$

where \dot{N}_p is the rate of increase of oxide precipitates per unit volume, V_p the average volume of the precipitates, C_O the oxygen concentration and $C_{O_{cr}}$ the critical oxygen concentration over which the multiphase aggregate oxidises.

The considerations formulated in Equations 2.19 to 2.23 provide a way to obtain the microstructural state (i.e. the fractions of different phases) of the alloy depending on time. A hypoelastic constitutive model, expressed in terms of the Jaumann derivative of the aggregate Cauchy stress, $\boldsymbol{\sigma}$, which takes into account the multiphase character of the alloy, was then implemented and used

to model the TGO mechanical behaviour,

$$\overset{\nabla}{\boldsymbol{\sigma}} = \mathbf{C} : (\dot{\boldsymbol{\epsilon}} - \dot{\boldsymbol{\epsilon}}^{in}) - 3K\alpha\dot{T}\mathbf{1} \quad (2.24)$$

The inelastic strain tensor, $\dot{\boldsymbol{\epsilon}}^{in}$, is obtained by the addition of the creep strain tensor, $\dot{\boldsymbol{\epsilon}}^{cr}$, and a transformation strain tensor, $\dot{\boldsymbol{\epsilon}}^{tr}$, which represents oxidation-induced stresses,

$$\dot{\boldsymbol{\epsilon}}^{in} = \dot{\boldsymbol{\epsilon}}^{cr} + \dot{\boldsymbol{\epsilon}}^{tr} \quad (2.25)$$

where $\dot{\boldsymbol{\epsilon}}^{cr}$ and $\dot{\boldsymbol{\epsilon}}^{tr}$ are defined as follows,

$$\dot{\boldsymbol{\epsilon}}^{cr} = \sum_i f^{(i)} \dot{\boldsymbol{\epsilon}}^{i,cr} \quad (2.26)$$

$$\dot{\boldsymbol{\epsilon}}^{tr} = f^{(2),ini} \dot{f} \left\{ \sqrt{\frac{3}{2}} P \frac{\mathbf{s}}{\tilde{\sigma}} + e_v^T \mathbf{1} \right\} \quad (2.27)$$

P is a coefficient that depends on the oxide particles shape, and $\tilde{\sigma}$ and \mathbf{s} are the norm and deviatoric component of the aggregate stress tensor, respectively. The inclusion of the term dependent on the deviatoric stress tensor in Equation 2.27 defines the anisotropy of the oxide growth as it favours its precipitation along certain directions according to the deviatoric stresses on them.

The model uses modified Budianski and Wu [27] homogenization relations to combine the mechanical properties of the individual phases and model the behaviour of the aggregate material. The evolution of the stress tensor in each phase is described using the following equation:

$$\dot{\boldsymbol{\sigma}}^m = \dot{\boldsymbol{\sigma}} + 2\mu(1 - \beta_t) \{ \dot{\boldsymbol{\epsilon}}^{cr} - \dot{\boldsymbol{\epsilon}}^{m,cr} - \dot{\mathbf{A}}^m \} \quad (2.28)$$

where β_t is Eshelby's elastic accommodation factor, which reduces down to a scalar value from a fourth order tensor when the aggregate is assumed to be composed of a continuum matrix with spherical inclusions. \mathbf{A}^m are the phase accommodation functions for each phase, defined by the evolutionary equation:

$$\dot{\mathbf{A}}^m = \hat{H}(f, T) \left\{ \sum_k f^{(k)} \mathbf{S}^k |\dot{\boldsymbol{\epsilon}}^{k,cr}| - \mathbf{S}^m |\dot{\boldsymbol{\epsilon}}^{m,cr}| \right\} \quad (2.29)$$

with

$$\dot{\mathbf{S}}^m = \dot{\boldsymbol{\epsilon}}^{m,cr} - \hat{H}(f, T) \mathbf{S}^m |\dot{\boldsymbol{\epsilon}}^{m,cr}| \quad (2.30)$$

where the dimensionless $\hat{H}(f, T)$ functions are calibrated from test data.

Analyses were run assuming that the system was stress free at 950°C at the beginning of the oxidation process. The important results were considered to be the stresses normal to the TGO-top coat interface, as they are thought to be the cause of mesocrack nucleation. During oxidation the highest values of these stresses were developed in the TGO outer layer. These stresses were tensile with their magnitude increasing as TGO thickness increased up to levels of ~ 85 MPa. The highest stresses obtained upon cooling (~ 340 MPa) were found in the top coat and in the unoxidised bond coat. The TGO was subjected to compression and the tensile stress locations agreed with the crack nucleation points.

Caliez *et al.* [28] used a weakly coupled diffusion-mechanical behaviour model in order to simulate the growth of the TGO by changing the properties of BC elements to those of oxide. The bond coat material was assigned elasto-viscoplastic properties and the TGO-bond coat interface was modelled as a wavy surface. Oxygen and aluminium diffusion analyses were run using Fick's law, and when critical values of the activities of these elements were achieved in any BC element, its properties were changed and volumetric dilatations were imposed in order to simulate the progressive oxidation process and the growth stress. Morphological instabilities were found to propagate upon thermal cycling using this model. High values of TGO stress were calculated (between ~ 3 GPa and ~ 5 GPa).

Nusier *et al.* [29] used Fick's law to calculate the oxygen concentration profile in the TBC and to model analytically the TGO growth in early cycles. This approach did not show good correlation with later thermal cycles.

2.1.3 Top coat sintering

The sintering process of a plasma sprayed ceramic top coat was addressed by Busso *et al.* [26] using a phenomenological relation in which the elastic modulus was related to the temperature and exposure time, i.e.

$$E_c = \hat{f}(T) \left\{ E_{c0} + E_{css} \left[1 - e^{-te^{\left[\left(\frac{T_{max}-b_1}{b_2}\right)+b_3\right]}} \right] \right\} \quad (2.31)$$

where T_{max} is the sintering temperature in K, t is the sintering time in hours, $\hat{f}(T) = 1 - b_4 \exp\left(\frac{-b_5}{T}\right)$, and E_{c0} , E_{css} , b_1 , b_2 , b_3 , b_4 and b_5 are numerical parameters fitted from experimental data.

Busso and Qian [30] developed a sintering model for EB-PVD YSZ top coats. Potentially, the sintering of a ceramic can be driven by two mechanisms: the fusing of the columnar grains, known as external sintering, and the collapse of the porosity in the grains, usually referred to as internal sintering. In the case of EB-PVD top coats, the external sintering effect was assumed to have a negligible effect when compared with the internal sintering process. The model defines the relative internal and external densities, ρ_i and ρ_e respectively, as opposed to the correspondent porosities, p_i and p_e respectively, as

$$\rho_i = 1 - p_i \quad (2.32)$$

$$\rho_e = 1 - p_e \quad (2.33)$$

The total relative density, ρ , is defined as

$$\rho = -(p_e - p_i) \quad (2.34)$$

Considering that the initial total relative density is ρ_0 , the in-plane elastic modulus, $E_{1'}$, is obtained as

$$E_{1'} = \left(\frac{\rho - \rho_0}{1 - \rho_0} \right) E_{2'} \quad (2.35)$$

where $E_{2'}$ is the out of plane elastic modulus, which can be obtained from the elastic modulus of fully dense isotropic zirconia, E_{2R} , as

$$E_{2'} = \left[1 + \frac{1.5(1 - \rho_i)(1 - \nu_{2'1'})(9 + 5\nu_{2'1'})}{7 - 5\nu_{2'1'}} \right] E_{2R} \quad (2.36)$$

Since the TC is assumed to show elastic and creep behaviour, the total strain rates, $\dot{\boldsymbol{\epsilon}}$, will be composed of those two components,

$$\dot{\boldsymbol{\epsilon}} = \dot{\boldsymbol{\epsilon}}^e + \dot{\boldsymbol{\epsilon}}^{cr} \quad (2.37)$$

where the elastic component of the total strain rate tensor, $\dot{\epsilon}_{ij}^e$, is defined as

$$\dot{\epsilon}_{ij}^e = S_{ijkl} \dot{\sigma}_{kl} \quad (2.38)$$

and the creep component, $\dot{\boldsymbol{\epsilon}}^{cr}$, is

$$\dot{\boldsymbol{\epsilon}}^{cr} = \frac{A_s}{T} e^{-\frac{Q}{RT}} \left(\frac{L_{G_0}}{L_G} \right)^Z \left[\frac{3}{2} \hat{c}(\rho_i) \mathbf{s} + 3\hat{f}(\rho_i)(\sigma_m - \sigma_s) \mathbf{1} \right] \quad (2.39)$$

where A_s , Z and Q are material parameters, \hat{c} and \hat{f} dimensionless functions, L_{G_0} the initial grain size, \mathbf{s} the deviatoric stress tensor, σ_m the mean pressure and σ_s the sintering potential, which is a function of the internal density and grain size.

The external porosity, ρ_e , is assumed to be constant in EB-PVD YSZ, which implies that $\dot{\rho}_e = 0$, while the internal porosity changes according to its evolutionary equation:

$$\dot{\rho}_i = -\rho_i \dot{\epsilon}_{kk}^{cr} \quad (2.40)$$

An additional set of equations of the form $\dot{L}_G = \dot{L}_G(L_G, \rho_i)$ defines the evolution of the grain size.

2.1.4 Creep

Ferguson *et al.* [31] studied the effect that bond coat creep produced in the ceramic top coat stress and strain state. The FE model which they used took

into account three layers composing the TBC, i.e. the substrate material, the bond coat and the ceramic top coat. Different geometries based on sine waves, as shown in Fig. 2.4, were used for the bond coat/top coat interface in order to study their effect in stresses. The existence of the TGO and the bond coat oxidation process were neglected.

Rösler *et al.* [14] used FE modelling to investigate how stresses and failure mechanisms were affected by TGO creep. The geometry they used was also based on the existence of a wavy interface between the TGO and the top coat. No heat transfer calculation was performed, as the heating up and cooling down processes were considered to be isothermal, without any thermal gradients.

All the materials considered in their analysis were assigned temperature-dependent elastic-viscoplastic properties. The TGO was assumed to be composed entirely of Al_2O_3 . Alumina creep properties were used to model the TGO.

The variation of stress with time due to thermal cycling was studied using the FE model; it was concluded that TGO creep was an important factor in producing a reduction of the maximum stress achieved in TBCs.

In a later analysis, Rösler *et al.* [15] used a dimensionless creep strength parameter, Σ_{cr} , to study the sensitivity of the stress resultant from TGO oxidation when using the prescribed swelling strain rates approach to model that phenomenon,

$$\Sigma_{cr} = \frac{\dot{\epsilon}_{\parallel}}{A_{TBC}} \frac{1}{1 + m_{cr} \frac{F_{TBC} A_{TGO}}{F_{TGO} A_{TBC}}} \quad (2.41)$$

where A_{TBC} and A_{TGO} are the top coat and TGO creep coefficients used in Norton's creep law, $\frac{F_{TBC}}{F_{TGO}}$ is a microstructural-geometrical factor and m_{cr} is a fitted parameter.

Average stress levels were shown to be dependent on the creep strength parameter, Σ_{cr} , rather than on isolated creep properties or current or initial oxide thickness.

Bäker *et al.* [32] neglected growth stress when studying stresses which occur upon cooling, due to short, high temperature exposures. The stresses obtained with this type of loading were found to be very sensitive to fast creep parameters.

Karlsson and Evans [16] did not use creep properties, but stress relaxation of the oxide layer was related to a temperature dependent yield stress that enabled TGO plasticity at high temperature. The bond coat was assumed to have a temperature-independent yield strength.

The FE model used did not take into account the presence of the top coat. Its effect was neglected due to the low stiffness of that layer when compared to the rest of materials. The TGO-bond coat interface was modelled using a wavy interface.

The described model behaviour was studied under thermal cycling conditions. Extremely high compressive stresses (~ 4 GPa) were obtained for the TGO layer upon cooling and the imperfection amplitude was found to grow under certain conditions. This last finding provides a mechanism capable of explaining the cyclic morphological instabilities that occur.

A further development by Karlsson *et al.* [33] studied the effect of the top coat as an inhibitor of instability displacements. The model assumed linear elastic properties for the ceramic top coat and included internal traction free planes within the ceramic in order to simulate internal cracks near the imperfections, similar to those found experimentally. High tensile stresses were developed in these points that may cause top coat cracking.

Ali *et al.* [34] assigned creep properties to all the material layers and studied their effect on residual thermal mismatch stresses using an FE model. The top coat-TGO-bond coat interface was simulated by a sine function as shown in Fig. 2.5.

The growth stress was an input in the analysis to study the response of the system to changes in it. Growth stress was prescribed as a pressure across

the interface inside the crack. Cracks were shown to be likely to propagate for relatively low values (realistically achievable values) of growth stress. Very high compressive stresses (~ 6.4 GPa, with ~ 3.86 GPa compressive strength) were calculated for the alumina layer. It was concluded that microcracking within the TGO could occur in the first few cycles.

2.1.5 Fracture mechanics applications to TBCs

2.1.5.1 Energy release rate approach

Nusier and Newaz [35] investigated the effect of circumferential cracks between the TGO and bond coat and within the oxide layer, as shown in Fig. 2.6. The analysis was carried out combining the FE method and the virtual crack extension method (VCEM) to estimate the energy release rate, G . The J -integral approach was used to compare its results to those obtained from the G approach. The stress state was obtained from the consideration of a cool down cycle applied to the FE model. Growth stresses were simulated by applying internal surface pressure. The analysis showed that small internal pressures (oxidation stresses) may cause crack propagation upon thermal cycling. The internal pressure can be originated by volume changes due to oxidation or by the stress concentrations created by a wavy bond coat-substrate interface.

2.1.5.2 Stress intensity factors approach

Evans *et al.* [36] provided a number of correlations of the form:

$$\frac{K_i}{\sigma^* \sqrt{R}} = f\left(\frac{R}{c}\right) \quad (2.42)$$

with K_i being the stress intensity factor, R and c representing different radii and crack lengths depending on the type and disposition of the studied crack

and σ^* a stress parameter defined as

$$\sigma^* = \frac{E(m-1)}{3(1-\nu)m} \left(\frac{h}{R} \right) \quad (2.43)$$

where m is the ratio of the new TGO volume to the consumed bond coat volume and h is the TGO thickness. The stress intensity factors calculated this way consider that cracking is caused by growth stresses and not by thermal mismatch stresses, as Eq. 2.42 depends on a single stress parameter, σ^* , which is determined exclusively by the TGO growth parameters.

Chen *et al.* [37] completed the definition made of stress intensity factors in the ceramic top coat, expressing them as:

$$\frac{K_I L(1-\nu^2)}{E a_1 \sqrt{\pi c}} = f_I \left(\frac{c}{L}, \frac{y}{L}, \Psi \right) \quad (2.44)$$

$$\frac{K_{II} L(1-\nu^2)}{E a_1 \sqrt{\pi c}} = f_{II} \left(\frac{c}{L}, \frac{y}{L}, \Psi \right) \quad (2.45)$$

with L being a parameter related to the TGO-bond coat undulation wavelength, a_1 is the initial undulation amplitude, c is the crack length and $\Psi = \frac{a_2}{a_1}$ is a gradually increasing parameter that takes into account the progressive wrinkling of the oxide layer.

The corresponding energy release rate can be obtained as:

$$G = \frac{(1-\nu^2)(K_I^2 + K_{II}^2)}{E} \quad (2.46)$$

2.1.6 Top coat buckling

Evans *et al.* [38] studied the effect that interface undulations have on stresses and on the eventual buckling of the TGO due to the compressive stresses caused by the thermal expansion mismatch and identified the combinations of material properties and temperature changes that produce elastic strain shakedown and cyclic plastic straining. Thermal stress levels were approximated by:

$$\sigma_0 = - \frac{E_1 \Delta \alpha (T_4 - T_0)}{(1-\nu_1)} \quad (2.47)$$

Analyses were carried out assigning the oxide layer linear elastic properties and for different behaviours of the substrate (Ni based superalloy) material (elastic, elastic-perfectly plastic and elastic-temperature dependent plastic). The top coat-TGO-bond coat interface was modelled using a wavy interface with a_0 initial amplitude and $2L$ wavelength as shown in Fig. 2.7. Analytic and FE models were used to model the behaviour of an oxide layer over an infinite substrate. TGO growth stresses were neglected and only thermal expansion mismatch stresses were considered in their analysis.

He *et al.* [39] studied the decohesion of compressed thin oxide films over metallic substrates using the energy release rate approach for various interface imperfection geometries. They proposed an expression for the buckling of these films deduced from the energy release rates that allowed the combination of critical oxide thickness and imperfection size that lead to spallation to be calculated, i.e.,

$$\frac{R_c}{h} = 0.9 \left(\frac{E_1}{\sigma_0} \right)^{\frac{5}{6}} \left(\frac{\Gamma_i}{\sigma_0 h} \right)^{\frac{1}{3}} \quad (2.48)$$

where R is the TGO-bond coat interface imperfection radius and R_c is the critical value of R at which decohesion occurs, h the TGO thickness, E_1 the Young's modulus of the film, σ_0 is the compressive mismatch stress in the film and Γ_i the mode I fracture toughness of the interface.

2.1.7 Other relevant analyses

Cheng *et al.* [40] performed FE analyses using a two dimensional mesh generated from a microphotograph showing the TBC structure. Elastic and elastic-plastic (bond coat plasticity) analyses were run, the later showing improved experimental agreement. The TBC-top coat interface radius of curvature played a very important role in the achieved stress level. The highest stress levels were calculated for the TGO in plane compression (~ 3.46 GPa). Growth stresses

were neglected.

Hsueh and Fuller [41] investigated the effect on thermal stress of top coat-TGO-bond coat interface morphology for different oxide thicknesses, using the object oriented finite element analysis (OOF) method. The interface was modelled as a flat surface with a convex or concave circular imperfection (see Fig. 2.8) of different curvature and height. TGO growth stresses were not taken into account in this analysis. The different materials were assigned linear elastic behaviour.

Karlsson [42] modelled martensitic phase transformation stresses that occur in platinum-modified nickel-aluminide bond coats as thermally-induced stress free strains. These stresses were found to contribute to the morphological instabilities upon cooling.

Darzens and Karlsson [43] introduced a modification in the modelling of bond coats. They studied the TGO geometric instability by considering that the underlying alloy was not homogeneous, but composed of two distinct phases, β and γ' , with different high-temperature yield strengths. γ' was found to inhibit the distortion of the TGO next to it, due to its superior high-temperature strength.

Shi *et al.* [44] introduced martensitic phase transformations in the model used previously by Darzens and Karlsson [43]. Both models simulated the bond coat as a two-phase ($\beta + \gamma'$) material.

2.2 Life prediction modelling

2.2.1 Inelastic strain ranges and TGO thickness based life prediction

DeMasi *et al.* [45] developed a life prediction model based on inelastic strain ranges and on the ratio between the accumulated oxide thickness and a critical oxide thickness:

$$N_f = \left(\frac{\Delta\epsilon^{in}}{\Delta\epsilon_f} \right)^b \quad (2.49)$$

$$\Delta\epsilon_f = \epsilon_{f0} \left(1 - \frac{h}{h_c} \right) + \Delta\epsilon^{in} \left(\frac{h}{h_c} \right) \quad (2.50)$$

where ϵ^{in} is the total inelastic strain of the ceramic, ϵ_f is the static failure strain, h is the oxide thickness and h_c is the critical oxide thickness. The accumulated oxide thickness was calculated using the experimentally determined equation:

$$h = A_h \left(C e^{\frac{-Q}{RT}} t \right)^{n_{ox}} \quad (2.51)$$

The inelastic strain range was obtained using a coarse FE model with time dependent plasticity (Walker model).

Meier *et al.* [46] applied a life prediction model based on inelastic strain ranges and oxide layer growth (updated from the one above) to EB-PVD TBCs. The oxide thickness model used was:

$$h = \left\{ e^{[Q(\frac{1}{T_0} - \frac{1}{T})]} t \right\}^{n_{ox}} \quad (2.52)$$

The fatigue life was calculated using the modified power law,

$$N_f = \left[\left(\frac{\Delta\epsilon_{ff}}{\Delta\epsilon} \right) \left(1 - \frac{h}{h_c} \right)^c + \left(\frac{h}{h_c} \right)^c \right]^b \quad (2.53)$$

with $\Delta\epsilon_{ff}$ being a constant.

2.2.2 Fracture mechanics based life prediction

2.2.2.1 Energy release rate approach

Evans *et al.* [47] applied the energy release rate approach to a micromechanics model to show that the coalescence of interface cracks within imperfections in residually compressed brittle films occurs when imperfections in the interface have a radius exceeding that obtained using the equation:

$$\frac{R_c}{L} = \left(\frac{1.89}{g} \right) \sqrt{\frac{\Gamma_0}{\bar{E}(\Delta\alpha\Delta T)^2 L}} \quad (2.54)$$

where $2L$ is the distance between imperfections, g is a dimensionless coefficient of order unity, Γ_0 is the fracture toughness along the weak plane and \bar{E} the bimaterial plane strain modulus.

Their analyses used a simplified geometry and general purpose expressions of the stress intensity factors. By reformulating the crack growth problem in terms of energy release rates, they were able to propose a spalling mechanism and some critical values of the levels of stresses required for the failure of TBCs.

He *et al.* [48] made attempts at crack and fracture assessment by means of the energy release rate approach using the results obtained from an FE analysis. Dimensional analysis showed that there could be a relation between the minimum energy release rate, G_{min} , after which the crack becomes unstable, and the number of applied thermal cycles, N , of the form:

$$\frac{G_{min}}{E_{tbc}L(\Delta\alpha\Delta T)^2} = \kappa(N - N_0) \quad (2.55)$$

where E_{tbc} is the top coat stiffness modulus, L is the imperfection half-wavelength, $\Delta\alpha$ is the thermal expansion mismatch between substrate and bond coat, ΔT the temperature change and κ and N_0 fitting constants.

When the energy release rate minimum, G_{min} , reaches the TBC fracture toughness, Γ_{tbc} , crack propagation becomes unstable and failure occurs. The

failure parameter obtained using this technique is:

$$N_f = N_0 + \frac{\Gamma_{tbc}}{E_{tbc}L(\Delta\alpha\Delta T)^2\kappa} \quad (2.56)$$

Another phenomenon that leads to spallation is that related to the TGO growth stresses that build up during oxidation, as assumed by He *et al.* [39]. Their model assumed that a chemical compound, x , was diffusing through the TGO and forming inclusions in the TGO/bond coat interface. The oxidation (dwell) time needed for spallation by that mechanism was given by:

$$t_d^* = 2 \left[\frac{\phi^2(1-\nu)\Gamma_i}{\sigma_g} \right]^{\frac{4}{3}} \left[\frac{e^{\frac{Q}{RT}} \left(\frac{W_{ad}}{E_1} \right)^{\frac{2}{3}}}{D_0 c_x (\Delta\alpha\Delta T + \epsilon_*)^{\frac{11}{3}}} \right] \quad (2.57)$$

with ϕ being a dimensionless fitting parameter, ν the Poisson's ratio, σ_g the compressive growth stresses in the oxide, W_{ad} is equated to G , D_0 is the reference diffusivity for the chemical element x in the TGO as used in an Arrhenius-type equation, c_x is the supersaturation of the element x in the TGO and ϵ_* the strain in the oxide inclusions.

Xu *et al.* [49] used an FE model to study the crack propagation dependency upon the interface imperfection geometry and upon thermal cycling, and proposed a life assessment method based on the energy release rate approach. Dimensionless parameters were used in order to study the evolution of the cracks and their relation with the top coat/TGO/bond coat interface morphology:

$$\Theta = \frac{GL}{E_{tbc}^\perp \Delta^2} = f_1 \left(\frac{a}{L} \right) \quad (2.58)$$

$$\Xi = \frac{G}{E_{tbc}^\perp L} = f_2(N) \quad (2.59)$$

where Δ is the opening displacement of the crack above the top coat-TGO interface imperfection. f_1 and f_2 are functions fitted to the numerical results obtained from FE models.

A simple spallation failure criterion was also proposed, by equating the minimum energy release rate to the TC toughness:

$$N_f \approx 17 \ln \left(\frac{\Gamma_{tbc}}{LE_{tbc}^\perp} \right) \quad (2.60)$$

A sensitivity study, which identified the TC/TGO/BC interface imperfection size and the TGO growth stresses as the most important features regarding TBC failure upon thermal cycling, was carried out.

2.2.2.2 Stress intensity factor approach

Evans *et al.* [36] provided a crack coalescence criterion, which considered that crack coalescence arose when the TGO thickness exceeded a critical value, h_c , given by:

$$h_c = \frac{2\sqrt{\pi}(1 - \nu^2)mL^{\frac{3}{2}}K_{Ic}^{tbc}}{(m - 1)RE_{tbc}} \quad (2.61)$$

where R is the imperfection radius, $2L$ is the separation between adjacent imperfections and m is the ratio of new TGO volume to consumed bond coat volume. This criterion, which assumes that the spallation of the top coat was caused by its brittle fracture and driven by TGO growth, can be rewritten as a time criterion considering that the TGO thickness depends on the high temperature exposure time ($h = \sqrt{D_{ox}t}$).

Vaßen *et al.* [50] developed a life prediction model that took into account the top coat/TGO/bond coat interface waviness, oxide growth and substrate curvature. The interfacial crack growth rate was obtained as:

$$\frac{dc}{dN} = A_c \left(\frac{\Delta K_I}{\Delta K_{Ic}} \right)^n \quad (2.62)$$

The stress intensity factor was obtained as:

$$\Delta K_I = \Delta\sigma \sqrt{\frac{\pi c}{2}} \quad (2.63)$$

Empirical equations for the achieved stress levels, which fitted both the experimental and FEA results, were obtained and used as the input for the crack initiation and growth model:

$$\Delta\sigma \propto \left(\frac{a}{L}\right)^{\alpha_c}, \text{ with } \alpha_c \approx 1 \quad (2.64)$$

$$\Delta\sigma \propto E_{TBC}\Delta\alpha_{TBC-BC}\Delta T \quad (2.65)$$

where a is the sine wave amplitude and L the wavelength. The stress level was also related to the TGO thickness h by means of the following correlation:

$$\Delta\sigma \propto \left(1 - 2\left(\frac{h}{a}\right)\right)^{\beta_c}, \beta_c \approx 1 \quad (2.66)$$

Spallation was assumed to occur when a crack reached a critical length defined by:

$$c \cong 2.21D \left[\frac{E_{TBC}}{(1 - \nu^2)\Delta\sigma_t} \right]^{\frac{1}{2}} \quad (2.67)$$

where D is the top coat thickness. $\Delta\sigma_t$ is the tangential compressive stress given by:

$$\Delta\sigma_t \approx \frac{E_{TBC}}{1 - \nu^2} \Delta\alpha_{TBC-substrate} \Delta T \quad (2.68)$$

2.2.3 Damage mechanics based life prediction

Busso *et al.* [51] used a damage mechanics based life prediction model that assumed that failure of TBCs was driven by a cleavage-type mechanism within the top coat. The maximum out-of-plane stress within the top coat, σ_{22max} , was the primary variable taken into account for the life assessment model, which included the contributions due to thermal misfit, TGO oxidation and top coat

sintering stresses:

$$\sigma_{22max} = \sigma_{22}^{th} + \sigma_{22}^{ox} + \sigma_{22}^{si} \quad (2.69)$$

$$\sigma_{22}^{th} = \sigma_0^{th} \hat{f}_T^{th}(T, T_{max}) \quad (2.70)$$

$$\sigma_{22}^{ox} = \sigma_0^{ox} \hat{f}_T^{ox}(T, T_{max}) \hat{f}_h^{ox}(t_{acc}, T, T_{max}) \quad (2.71)$$

$$\sigma_{22}^{si} = \sigma_0^{si} \hat{f}_T^{si}(T, T_{max}) \hat{f}_h^{si}(t_{acc}, T_{max}) \quad (2.72)$$

σ_0^{th} , σ_0^{ox} and σ_0^{si} are reference stresses for a set of known conditions. The stress functions used were calibrated by means of the FE model developed by the same authors [25, 26].

The continuous evolution of microscopic damage with thermal cycles was proposed to have the generic form:

$$d\lambda = \hat{\lambda}\{\sigma_{22max}, \bar{\sigma}_{22max}, \lambda\}dN \quad (2.73)$$

where $\bar{\sigma}_{22max}$ is the mean cycle stress. The specific form adopted for TBC life assessment was:

$$d\lambda = \lambda^{\hat{m}(\sigma_{22max})} \left[\frac{\sigma_{22max}}{\hat{F}(\sigma_{22max})} \right]^p dN \quad (2.74)$$

$$\hat{m} = 1 - C \left[\frac{\sigma_{22max}}{\sigma_{co}} \right]^{q-p} \quad (2.75)$$

$$\hat{F} = F_0(1 - F_1\sigma_{22max}) \quad (2.76)$$

where σ_{co} is the maximum or initial cleavage strength and p , q , C , F_1 and F_0 are material parameters. A totally integrated framework, which made use of the techniques described in Refs. [25, 26, 51], to assess the mechanical performance of TBCs was described in Ref. [52].

2.3 Conclusions

A number of papers have been reviewed, covering the work carried out over recent years in order to model and understand the mechanical behaviour and failure of TBCs. The modelling efforts have been mainly concentrated on applying different constitutive models and material behaviours to the layers that compose the TBCs. Many attempts have been made to model accurately the oxidation process and the stresses generated using various approaches, with the most common methods being the assignment of swelling strains that simulate the growth of the oxide layer and the change in material properties of the elements of the bond coat adjacent to the oxide, when a certain criteria was met.

Fracture mechanics has been used in order to understand the mechanisms that drive crack nucleation and growth, which finally cause interfacial separation and spallation of coatings. However, the correct application of fracture mechanics to TBCs requires that the stress and strain levels caused by the complex loading to which coated components are subjected be accurately calculated and understood. In particular, coated components typically fail upon cooling after a certain thermal exposure time has been achieved, which suggests that oxidation and microstructural degradation and the stresses derived from them play a major role in crack nucleation and damage initiation.

In order to simulate realistically the stress development in TBCs, the most reliable set of material data possible should be gathered. A full review of the available material properties should be carried out, in order to reduce the uncertainty level of the calculations. Some particularly relevant analyses in terms of stress and strain calculation are presented in Section 2.1.2.5, which model the bond coat as a multiphase material and drive its oxidation based on a physical effect, the concentration of oxygen, rather than by imposing a growth law. It should be noted that the microstructural calculation, which only considers the

oxidation of oxidation-prone phases, does not represent some of the characteristic features in bond coat degradation such as aluminium depletion, particle precipitation and overall bond coat softening in terms of creep deduced from its evolution towards γ -Ni upon thermal exposure. The oxidation stresses are primarily caused by the volume expansion that the precipitation of the new oxide produces, which is estimated by means of its Pilling-Bedworth ratio and depends on the bond coat composition and microstructure.

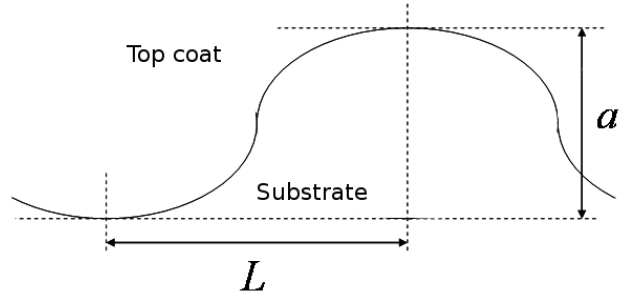


Figure 2.1: Geometric parameters used by He *et al.* [13] to define TBCs.

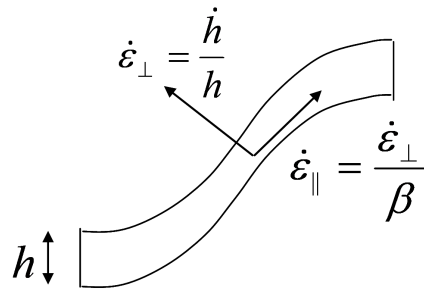


Figure 2.2: Diagram showing the TGO growth anisotropy used by Rösler *et al.* [15].

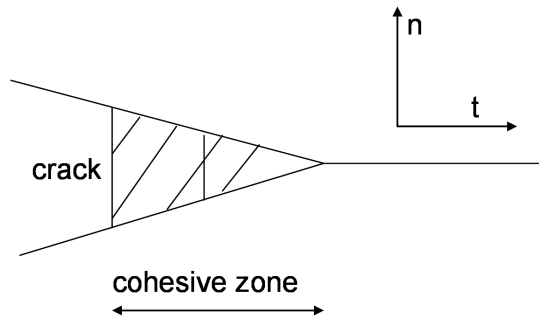


Figure 2.3: Modelling of an interface using cohesive elements, by Caliez *et al.* [21].

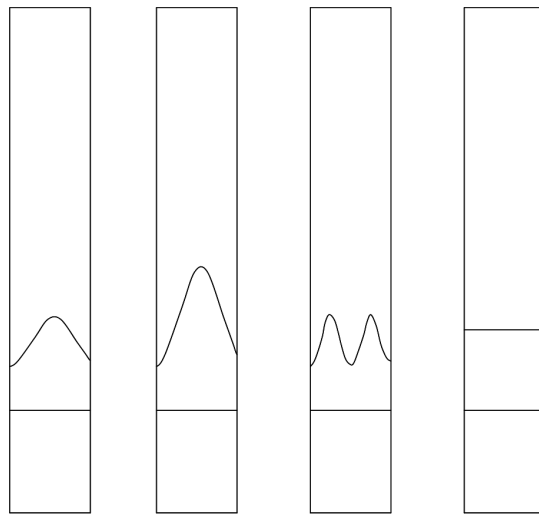


Figure 2.4: TBC geometries used by Ferguson *et al.* [31].

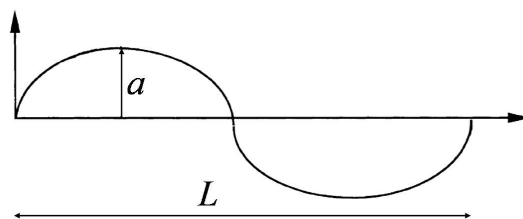


Figure 2.5: Interface geometry used by Ali *et al.* [34].

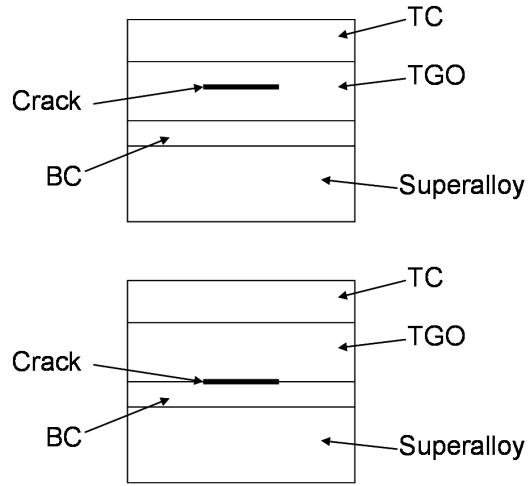


Figure 2.6: Location of the cracks studied by Nusier and Newaz [35].

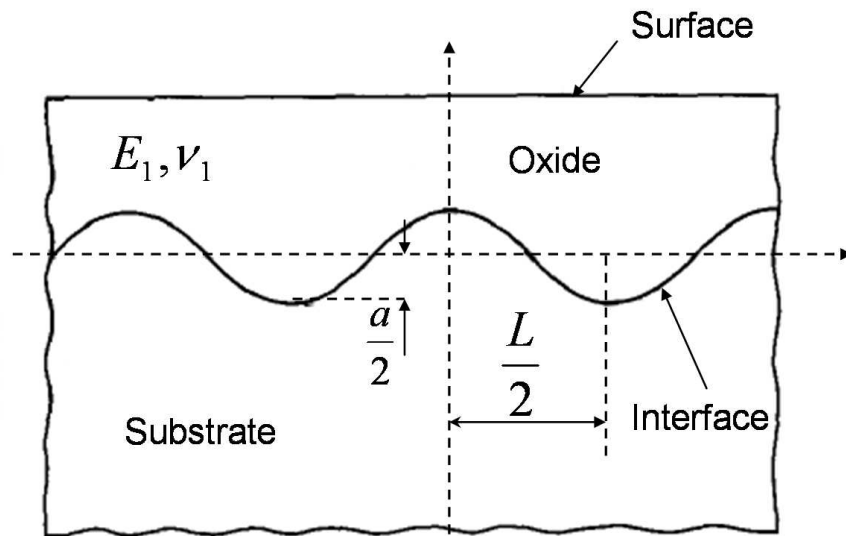


Figure 2.7: Geometry modelled by Evans *et al.* [38].

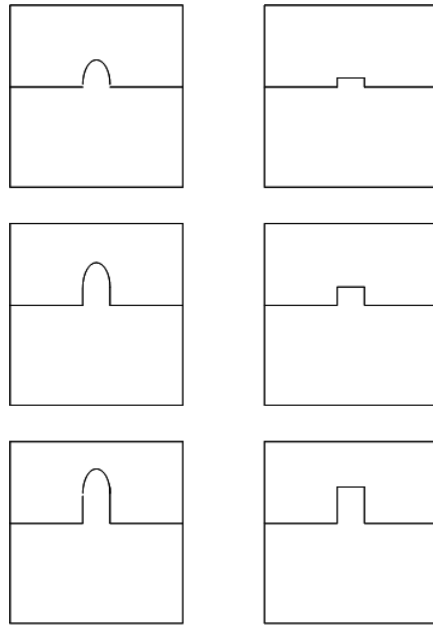


Figure 2.8: Interfaces modelled by Hsueh and Fuller [41].

Chapter 3

Thermal analysis of thermal barrier coated super-alloy tensile specimens

3.1 Introduction

Important aspects to take into account when modelling the mechanical response and stress-strain states of coatings at high temperature are the mechanical properties of the layers that compose them. More specifically, the stress relaxation due to creep plays a major role in the determination of the achieved stress levels. Chapter 4 contains experimental data on coated and uncoated tensile specimens that were used in order to validate the properties reported in published research.

The thermal properties of TBC coated tensile specimens, such as that shown in Fig. 3.1, are different from those of uncoated specimens. The furnace temperature conditions and the presence of the coating influence the temperature distribution in the specimen and it is necessary to gain an understanding of the temperature distributions in such specimens.

High temperature tests should be conducted making sure that specimens

are subjected to a uniform temperature in the region between the ridges. This implies that both the radial and axial distributions of temperature between the ridges be as small as possible. From an integrity point of view, high temperature gradients across the TC may create excessive stresses that could induce cracking prior to loading. The presence of the insulating coating will affect the thermal stabilisation time of the specimens, introducing uncertainty about the temperature of the substrate material when a certain surface temperature is measured.

The intention of the analysis presented in this chapter is to quantify the aforementioned effects caused by TBCs, during both transient and steady state thermal conditions, which occur during the test heating up and dwell times. During tests only the coating surface temperature is measured, on the specimen gauge length, using thermocouples. It is necessary to understand the magnitude of the thermal gradients across the TBC, and the extent to which they affect the underlying substrate temperature (and thus the test conditions). In order to gain the understanding required, a finite element (FE) model of the specimen, grips and furnace wall was created. Thermal analyses, taking into account heat conduction within solids and radiation from the furnace wall to the interior of the cavity containing the test specimen, were performed. The work presented in this chapter forms the basis of a paper [53].

A more detailed analytical model of the heat radiation process including transmittance across the TC was developed by Wang *et al.* [54] considering that heat was transferred only in one direction. A further embellishment of the analysis presented in this paper could be the incorporation of the model developed in Ref. [54] into an FE model.

3.2 Finite element model

3.2.1 Geometry

The geometry of the specimen is shown in Fig. 3.2. The specimens have a 20 mm gauge length, with a substrate diameter of 4 mm on the gauge length. An axisymmetric model consisting of full integration, axisymmetric, 4-node elements was used. Models have been generated for both coated and uncoated specimens. The coating dimensions are given in Fig. 3.3.

3.2.2 Boundary conditions

A heat transfer analysis, including radiation, was performed using ABAQUS. The temperature of the radiative surfaces was used as the boundary condition during the analysis. Symmetric thermal boundary conditions were applied to the horizontal plane of symmetry of the problem passing through the centre of the gauge length (see Fig. 3.4). The remainder of the components were assumed to be at 15°C at the beginning of the analysis. Fig. 3.4 summarises the boundary conditions that have been assumed for the analysis. The properties of the remaining surfaces, shown in Fig. 3.5, are assigned as explained in Section 3.3.2.

Heat is radiated from the external furnace surfaces into the cavity, causing the rest of the components to heat up until thermal equilibrium is achieved. The temperature profiles and distributions obtained at this equilibrium state are of primary interest in this analysis, in order to understand the conditions under which the specimens are being tested.

3.3 Material properties

The thermal properties used to define the behaviour of the substrate material and the TGO layer (assumed to be sintered $\alpha - \text{Al}_2\text{O}_3$) are given in Tables 3.1 and 3.2 respectively. The bond coat has been assumed to have the same thermal properties and density as the substrate material.

The heat capacity values relative to the top coat, shown in Table 3.3, are for pure zirconia. However, Hayashi *et al.* [55] showed that PSZ with yttria contents ranging from 3 mol % to 10 mol % (5.36 wt % - 16 wt %) had the same heat capacity values, justifying the use of the properties of pure zirconia in the present analysis.

Jang and Matsubara [56] estimated the porosity of 4 mol % (7.09 wt %) PSZ EB-PVD coatings to be 25.6 %. Ingel and Lewis [57] give two density values for 4 mol % PSZ: 6.042 and 6.060 $\text{g} \cdot \text{cm}^{-3}$. Combining the values for porosity and the density provided for YSZ, the value of density shown in Table 3.3 is assumed for PSZ EB-PVD TBCs.

Although this chapter mainly refers to EB-PVD TBCs due to the availability of material data, the analysis method presented here can be used to model plasma sprayed TBCs, by using their specific properties. Recent studies by An and Han [58] suggest that the thermal conductivity of plasma sprayed TBCs may be overestimated in the literature [6,8,59] by an order of magnitude. This issue is investigated in the present work by means of a sensitivity study that considers the effect of reducing the thermal conductivity of the coating to 0.15 $\text{W} \cdot \text{m}^{-1}\text{K}^{-1}$.

3.3.1 Top coat emissivity

Nicholls *et al.* [59] obtained the emissivity of zirconia as a function of wavelength as shown in Table 3.4. These values have to be transformed to temperature

dependent values, in order to be used as an input for ABAQUS. The method used for that calculation is explained through Equations 3.1 - 3.5:

$$E(\lambda, T) = \frac{2\pi hc^2}{\lambda^5(e^{\frac{hc}{\lambda kT}} - 1)} \quad (3.1)$$

$E = (\lambda, T)$ is the blackbody energy radiation per unit surface per unit wavelength at a temperature T [60]. If the total energy radiation is considered, adding the contribution of every wavelength in the spectrum, the value obtained from the Stefan-Boltzmann law [60] is:

$$E(T) = \int_0^\infty E(\lambda, T)d\lambda = \sigma T^4 \quad (3.2)$$

The radiation for a grey body is obtained by applying the concept of emissivity and using the blackbody radiation [60]; i.e.

$$E_{grey}(\lambda, T) = \epsilon(\lambda)E(\lambda, T) \quad (3.3)$$

The total radiation, in this case, is usually written as

$$E_{grey}(T) = \epsilon\sigma T^4 \quad (3.4)$$

Using Equations 3.1 - 3.4 it is possible to refer the emissivity to the surface temperature instead of to the wavelength. Hence,

$$\epsilon(T) = \frac{\int_0^\infty \epsilon(\lambda) \frac{2\pi hc^2}{\lambda^5(e^{\frac{hc}{\lambda kT}} - 1)} d\lambda}{\int_0^\infty \frac{2\pi hc^2}{\lambda^5(e^{\frac{hc}{\lambda kT}} - 1)} d\lambda} \quad (3.5)$$

The integrals in Eq. 3.5 are calculated numerically. In order to evaluate the accuracy of the numerical integration, a ratio, r , based on the relation between the numerically obtained value and the blackbody energy radiation (Eq. 3.2) is used, i.e.

$$r = \frac{\int_0^\infty \frac{2\pi hc^2}{\lambda^5(e^{\frac{hc}{\lambda kT}} - 1)} d\lambda}{\sigma T^4} \quad (3.6)$$

This ratio should be 1 (or very close to it) to ensure that the numerical integration is close to the value of the exact integral calculation. The values shown in Table 3.5 were obtained using Equations 3.5 - 3.6.

3.3.2 Emissivity of remaining surfaces

The emissivity values of Ni-based superalloys [61], and in general of any metallic surface, are very sensitive to the surface finish and oxidation level. They can vary within a range of 0.1 - 0.9, a value of 0.1 being representative of polished surfaces and 0.9 representing oxidised surfaces. An intermediate value of 0.5 was assumed for all the surfaces in the analysis, except for the top coat, which was assigned the values given in Table 3.5.

The gap radiation has been modelled assuming that the emissivity of both surfaces is 0.5 and that the geometric view-factor is 1, i.e. all of the radiation from one surface reaches the opposite surface.

3.4 Results and discussion

A transient thermal analysis was run with the specimen, initially at 15°C, exposed to thermal radiation from the furnace wall; calculations were continued until a steady state temperature distribution was achieved. Results for two different load cases are presented. Firstly, the radiative surface S2 was kept at a constant uniform temperature and the thermal histories of the other components were calculated. A temperature distribution pattern, in stationary conditions, is shown in Fig. 3.6. Secondly, a more realistic configuration was assumed, having different temperatures on the outboard and inboard furnace wall rings which creates equal temperatures at the outside surface at the centre of the specimen and just outside the knife ridges. The condition required to produce this situation was arrived at iteratively. This condition represents that which

would be produced if thermocouples were situated at the centre of the specimen and just outside the knife ridges and these were used to control the three zone furnace heating.

Fig. 3.7 gives a more detailed temperature distribution within the specimen for a uniform furnace wall temperature of 1050°C. In the radial direction, the temperature varies by less than 2°C from the surface to the centreline at the mid-length position. Significant temperature differences of up to ~30°C occur in the axial direction, due to the heat conduction towards the grips.

Fig. 3.8 shows the temperature of the centreline at mid-length position of coated and uncoated specimens for a uniform 1050°C furnace wall temperature and for outboard 1400°C and inboard 700°C ring temperatures. The temperatures of the surface, base of TGO and top of substrate are not plotted separately as they lie very close to the centreline temperature and do not provide extra information regarding thermal stabilization times. Fig. 3.8 demonstrates that the effect of the coating on the time needed to achieve stationary thermal condition is negligible.

For uniform furnace wall temperature conditions, the temperature difference across the ceramic top coat (TC) (Fig. 3.9) is ~13°C at the beginning of the heating process but it rapidly reduces to around 1°C when transient thermal effects disappear. For the situation where the outboard and inboard rings are assigned different temperatures, the temperature difference across the TC reduces from ~9°C to ~0°C during the tests.

Fig. 3.10 shows the temperature of the mid-point of the centreline vs. time for various uniform furnace wall temperatures. The general trends show that the presence of the coating produces a centreline temperature drop of ~10°C, as shown in Table 3.6. If non-uniform furnace wall temperatures are imposed (Fig. 3.11), the presence of the coating does not reduce significantly the temperature of the specimen. The temperature drop across the top coat during the heating up

of the specimens increases with the furnace temperature, as shown in Fig. 3.12, but the stationary values are not significantly affected by the test temperature. The temperature drops, for similar test conditions, are lower (Fig. 3.13) when non-uniform furnace wall temperatures are used.

Uniform furnace wall temperatures produce a non-negligible axial heat conduction along the axis of the specimen (Fig. 3.14) towards the grips, which manifests itself as temperature differences of up to $\sim 30^\circ\text{C}$ between the centre of the specimen and the knife ridges. TBCs decrease the values of the equilibrium axial temperature distribution without significantly affecting its profile. In order to achieve a uniform temperature along the axis of the specimen, different temperatures need to be used in the outboard and inboard furnace rings as shown in Fig. 3.15, which shows that the effect of the TBC on the equilibrium temperature distribution is negligible.

It has already been explained that there was considerable uncertainty regarding the appropriate value of emissivity to use for the furnace, grips, superalloy and gap surfaces. Additionally, the conductivity values used for the TC may be overestimated by one order of magnitude according to recent measurements [58]. In order to overcome these problems, parametric studies have been carried out varying the emissivities of the different surfaces, the gap radiation parameters and the TC conductivity and comparing the results with the results obtained for a 1050°C furnace wall and 1400°C outboard / 700°C inboard furnace wall temperatures. Additional analyses have been run; with all the surface emissivities (except the top coat) set to 0.1, with the emissivities set to 0.9 and with the TC conductivity set to $0.15 \text{ W} \cdot \text{m}^{-1}\text{K}^{-1}$.

The results obtained for these cases are presented in the same form as those for the main study (where an emissivity of 0.5 and the TC conductivity from Table 3.3 are assumed). Regarding the thermal stabilisation, Fig. 3.16 shows that the equilibrium centreline temperature is affected by the values of the var-

ious emissivities involved in the problem. The stabilization time, when the emissivity is set to 0.9, is about 1/2 hour, and around 3 hours when the emissivity is assumed to be 0.1. The TC conductivity change has, by contrast, a negligible effect on the thermal stabilization. Fig. 3.17 depicts the temperature values along the gauge length with uniform furnace wall temperature. For lower emissivity values, less heat is dissipated to the external medium through the grips and less heat is conducted axially along the specimen, causing a flatter axial temperature distribution. The effect of a decrease in the TC conductivity is to lower the equilibrium temperature without affecting significantly its profile. The temperature reduction caused by the TBC (Table 3.7) varies between 1.2°C and 0.8°C for uniform furnace wall temperature and between 0.3°C and -0.5°C for non-uniform temperatures if the conductivity used in the main study is considered. A different situation is presented when a $0.15 \text{ W} \cdot \text{m}^{-1}\text{K}^{-1}$ TC conductivity is assumed, which widens the temperature ranges to 7.5°C - 11.0°C for uniform furnace wall temperature and -4.0°C - 3.2°C for non-uniform temperatures, with maximum transient temperature differences across the coating of up to $\sim 134^\circ\text{C}$ and $\sim 89^\circ\text{C}$ respectively, which are lower than the calculated insulating capability of the TC (150°C) [5]. Fig. 3.18 shows that the temperature distribution along the axis is affected by the thermal characteristics of the specimen; the results for one of the extreme cases (emissivity of 0.9) indicate that heat is conducted from the ridges to the centre of the specimen and then radiated towards the furnace walls. In this case, the effect of a decrease by one order of magnitude in the TC conductivity is negligible.

3.5 Conclusions

A transient thermal radiation analysis has been run in order to gain an understanding of the thermal behaviour and to calculate the temperature profiles and

distributions which occur in tensile coated and uncoated specimens tested at elevated temperature.

The cavity radiation facility provided by ABAQUS has been used to solve this problem. The results obtained lead to the following conclusions:

- The minimum time needed by the specimen to reach thermal equilibrium is around 1/2 hour. If the lowest reasonable value of emissivity is assumed for the radiative heat transfer surfaces, the time to equilibrium rises to about 3 hours.
- The thermal profile for both coated and uncoated specimens in the region between the ridges is uniform across the thickness. The equilibrium temperature for coated specimens is $\sim 10^{\circ}\text{C}$ lower than for uncoated specimens when uniform furnace wall temperatures are specified. Under the more realistic conditions of uniform temperature distribution in the region between the ridges of the specimen, no significant variations in the temperature profile occur.
- Small transient temperature differences across the TBC of up to 16°C during heating are predicted, which are insignificant compared with in-service temperature differences, and are therefore unlikely to cause coating failure prior to loading. The temperature differences decay to a steady value of a few $^{\circ}\text{C}$. Results have been generated for a wide range of surface emissivities in order to avoid uncertainty in this conclusion.
- Under test conditions, the radial temperature gradient within the substrate is negligible. This situation contrasts sharply with the in-service situation where the applied backside cooling creates steep temperature gradients across the TBC thickness.
- If the furnace wall radiates heat with a uniform temperature distribution,

the thermal gradient along the gauge length (axial direction) is significant and will affect the creep behaviour of the specimen. This confirms the need for different temperatures for the outboard and inboard furnace in order to obtain a uniform temperature distribution along the specimen.

- The non-uniform temperatures on the furnace walls, as would be produced by a three zone heater with feedback control based on thermocouples situated at the centre of the specimen and just outside the ridges, reduce the heat transferred along the specimen, minimising all the temperature gradients to negligible values between the ridges of the specimen.
- The reduction by one order of magnitude in the top coat conductivity does not have a significant effect in the equilibrium conditions of the specimen when realistic conditions (i.e. different outboard / inboard ring temperatures) are used as this configuration seeks the minimisation of heat conduction, and thus of temperature gradients, within the specimen.

T ($^{\circ}\text{C}$)	k ($\text{W} \cdot \text{m}^{-1}\text{K}^{-1}$)	c ($\text{J} \cdot \text{kg}^{-1}\text{K}^{-1}$)	ρ ($\text{g} \cdot \text{cm}^{-3}$)
21.1	-	418.68	8.11
93.3	-	460.548	-
204.4	11.8244	502.416	-
315.6	13.699	523.35	-
426.7	15.5736	544.284	-
537.8	17.7366	565.218	-
648.9	19.7554	586.152	-
760	21.4858	628.021	-
871.1	23.3604	669.889	-
982.2	25.3792	711.757	-
1093	27.2538	711.757	-

Table 3.1: Substrate thermal properties, IN-738LC [62].

T ($^{\circ}\text{C}$)	k ($\text{W} \cdot \text{m}^{-1}\text{K}^{-1}$)	c ($\text{J} \cdot \text{kg}^{-1}\text{K}^{-1}$)	ρ ($\text{g} \cdot \text{cm}^{-3}$)
20	33	755	3.984
500	11.4	1165	3.943
1000	7.22	1255	3.891
1200	6.67	1285	3.868

Table 3.2: TGO thermal properties, sintered $\alpha - \text{Al}_2\text{O}_3$ [63].

T (°C)	k ($\text{W} \cdot \text{m}^{-1}\text{K}^{-1}$) [64]	c ($\text{J} \cdot \text{kg}^{-1}\text{K}^{-1}$) [65]	ρ ($\text{g} \cdot \text{cm}^{-3}$)
25	1.49981	455.6	4.82
26.85	-	457.224	-
126.85	-	516.142	-
226.85	-	546.98	-
326.85	-	568.08	-
426.85	-	582.688	-
526.85	-	595.673	-
626.85	-	607.034	-
726.85	-	616.773	-
826.85	-	626.512	-
926.85	-	635.438	-
1026.85	-	643.554	-
1126.85	-	652.481	-
1146.85	-	654.104	-
1156.85	-	655.727	-
1166.85	-	662.219	-
1176.85	-	719.839	-

Table 3.3: Top coat (EB-PVD PYSZ) thermal properties. Conductivity and density have been considered temperature independent due to the lack of experimental data.

λ (μm)	$\epsilon(\lambda)$
< 2.51	0.1
2.99	0.145
3.98	0.229
4.47	0.251
5.01	0.398
6.31	0.575
7.08	0.832
8.41	0.832
9.44	0.912
13.34	0.912
15.85	0.832
21.13	0.692
> 53.09	0.631

Table 3.4: Emissivity of zirconia as a function of wavelength.

T ($^{\circ}\text{C}$)	ϵ	r
0	0.791	0.959
100	0.768	0.982
200	0.705	0.99
300	0.629	0.994
400	0.555	0.996
500	0.489	0.998
600	0.432	0.999
700	0.385	0.999
800	0.345	0.997
900	0.312	0.994
1000	0.284	0.991

Table 3.5: Emissivity of zirconia as a function of surface temperature obtained from data in Table 3.4 using Eqs. 3.5 - 3.6.

T_{S2} ($^{\circ}\text{C}$)	Coated		Uncoated	T ($^{\circ}\text{C}$) reduction caused by TBC	
	$\Delta T_{top\ coat}$ ($^{\circ}\text{C}$)	ΔT_{subs} ($^{\circ}\text{C}$)	ΔT_{subs} ($^{\circ}\text{C}$)	Surface	Centre-line
950	1	0.3	0.4	5.6	6.6
1000	1.1	0.3	0.4	6.9	8
1050	1.2	0.3	0.4	8.2	9.4
1100	1.3	0.3	0.4	9.6	10.8
1250 out. 600 in.	0.1	0	0	0.5	0.5
1400 out. 700 in.	0.1	0	0	0.8	0.9

Table 3.6: Calculated radial temperature differences and reductions.

	$\Delta T_{top\ coat}$ ($^{\circ}\text{C}$), 1050 $^{\circ}\text{C}$		$\Delta T_{top\ coat}$ ($^{\circ}\text{C}$), 1400/700 $^{\circ}\text{C}$	
Analysis	1.5 $\text{W} \cdot \text{m}^{-1}\text{K}^{-1}$	0.15 $\text{W} \cdot \text{m}^{-1}\text{K}^{-1}$	1.5 $\text{W} \cdot \text{m}^{-1}\text{K}^{-1}$	0.15 $\text{W} \cdot \text{m}^{-1}\text{K}^{-1}$
$\epsilon = 0.5$ (main study)	1.2	10.9	0.1	0.6
$\epsilon = 0.1$	0.8	7.5	0.3	3.2
$\epsilon = 0.9$	1.2	11.0	-0.5	-4.0

Table 3.7: Temperature drops across ceramic top coat for different values of emissivities and TC conductivities and 1050 $^{\circ}\text{C}$ and 1400/700 $^{\circ}\text{C}$ furnace wall temperatures.



Figure 3.1: Coated creep specimen.

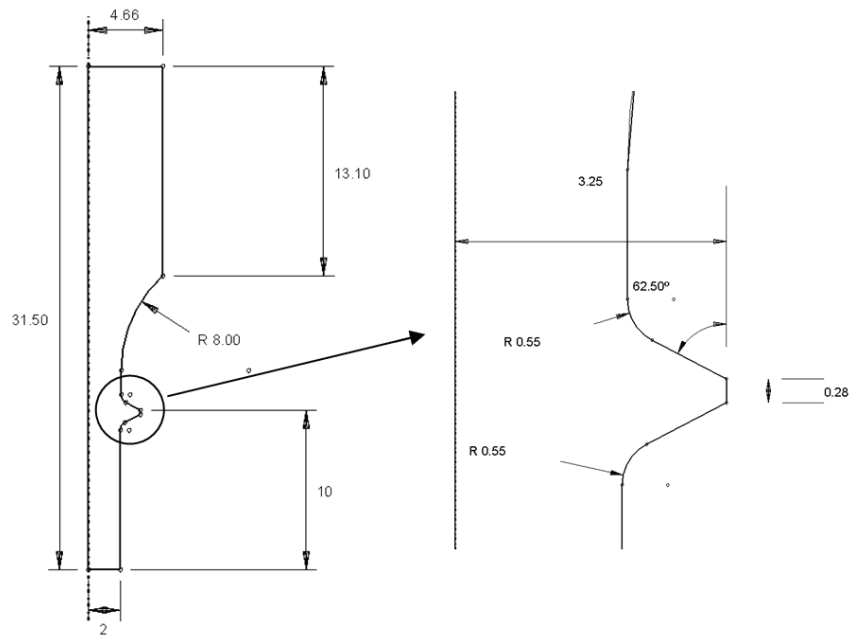


Figure 3.2: Geometry and dimensions of the axisymmetric specimen model.

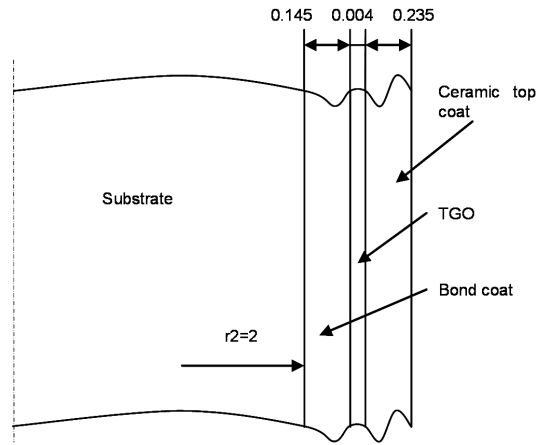


Figure 3.3: Geometry and dimensions (mm) of the TBC.

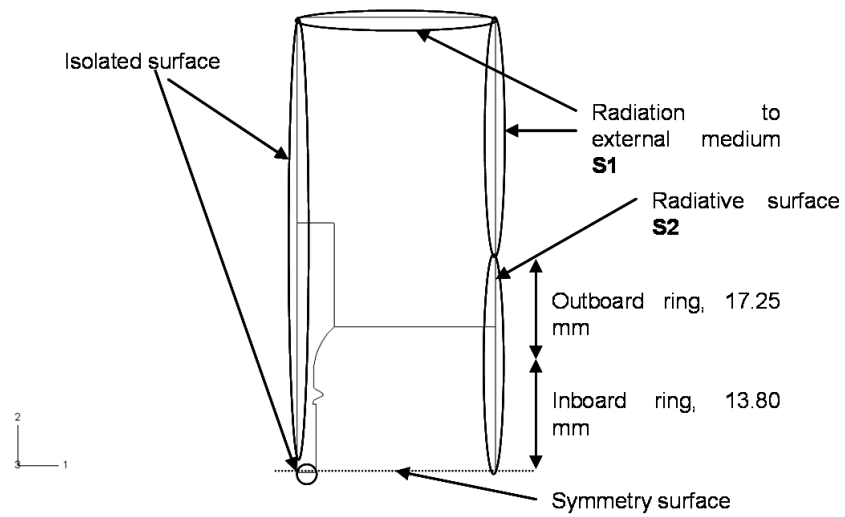


Figure 3.4: Boundary conditions applied to the model.

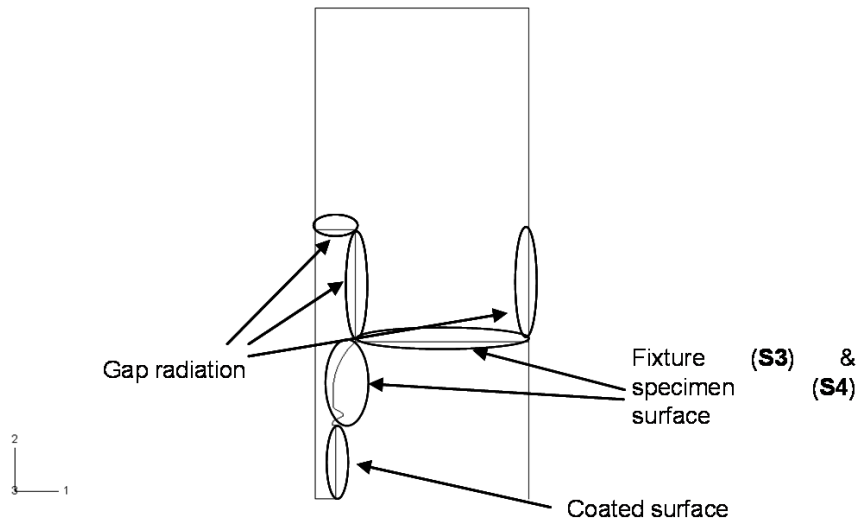


Figure 3.5: Surfaces where thermal properties are assigned.

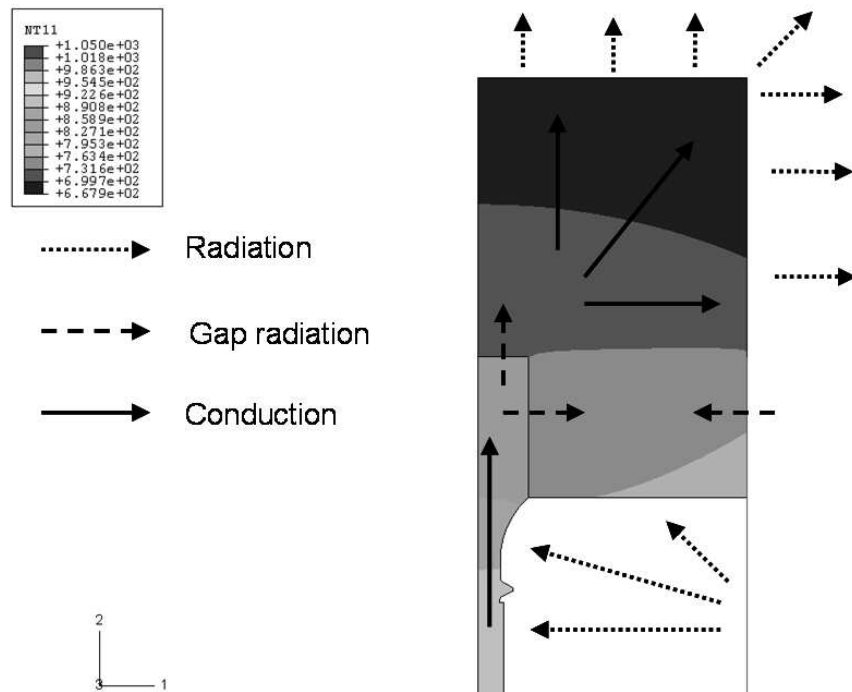


Figure 3.6: Heat fluxes in the equilibrium state.

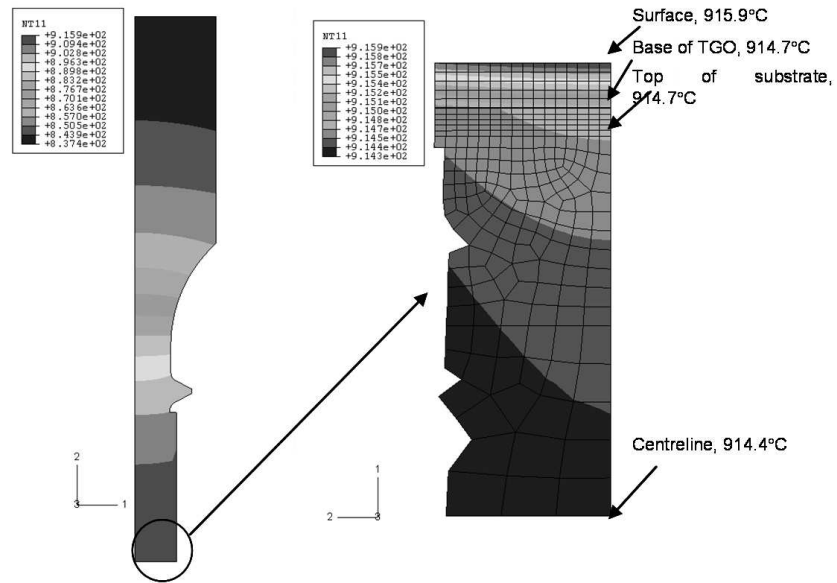


Figure 3.7: Temperature profile across the specimen radius and TBC thickness.

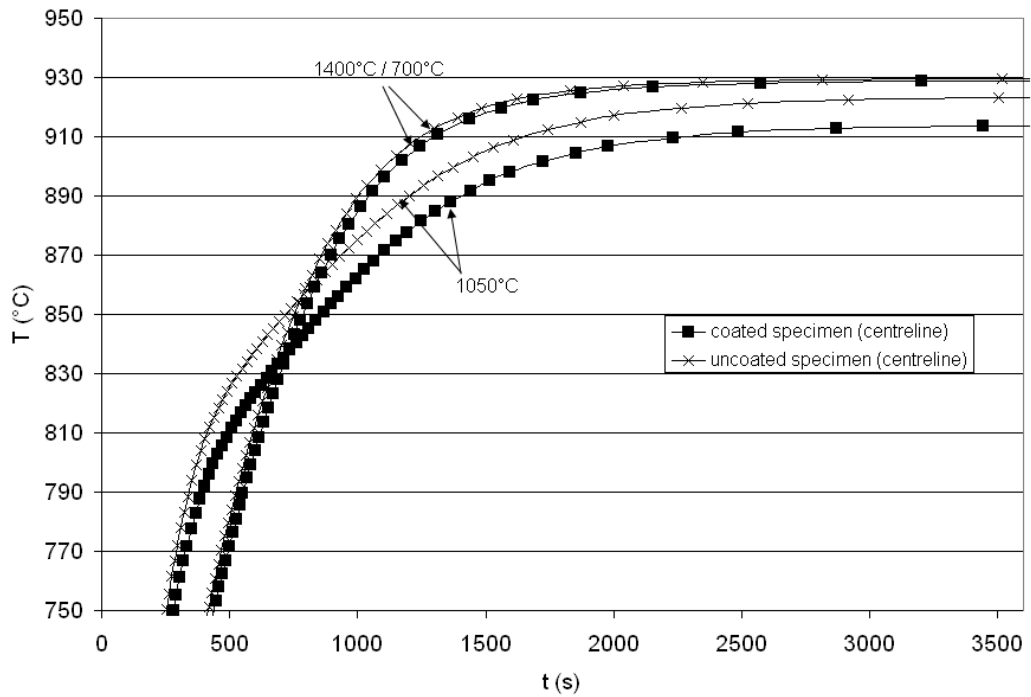


Figure 3.8: Mid-point of centreline temperature vs. time comparison for coated and uncoated specimens.

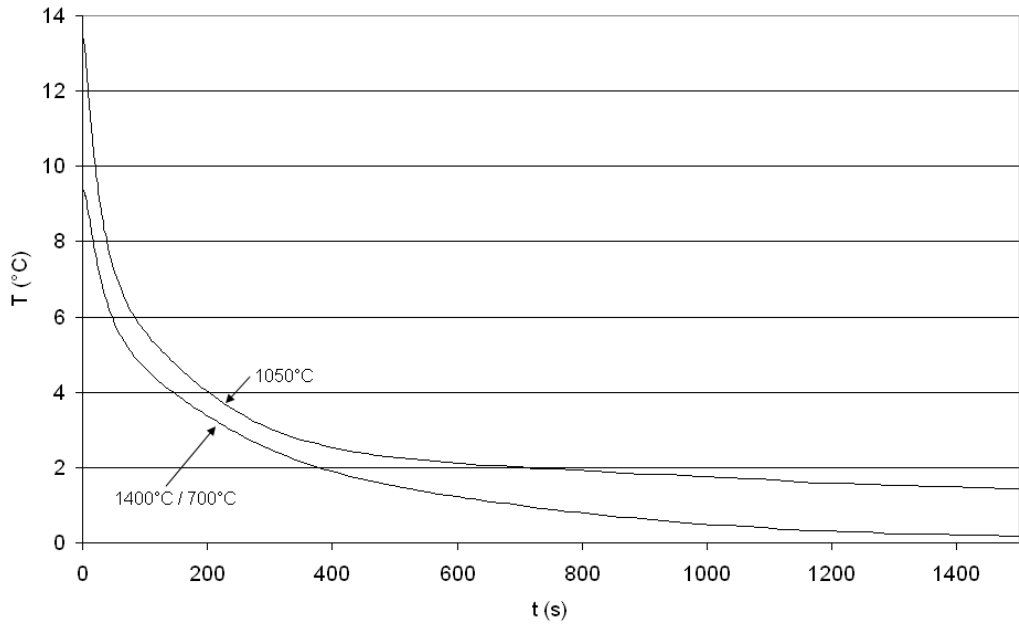


Figure 3.9: Thermal difference across top coat at 1050°C furnace temperature.

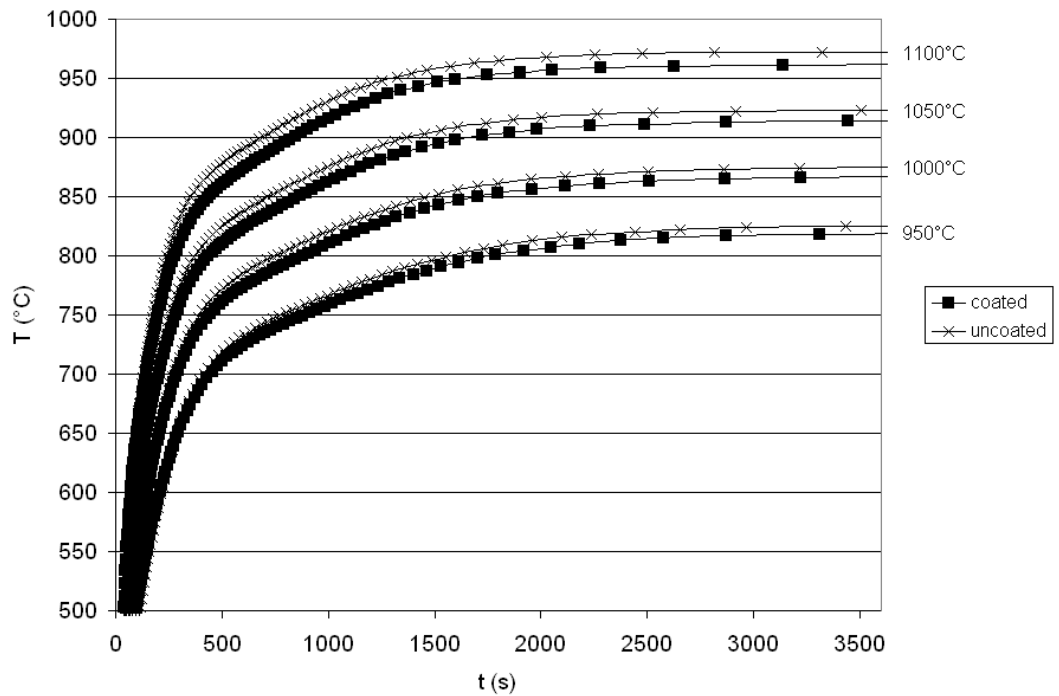


Figure 3.10: Mid-point of centreline temperature vs. time comparison for coated and uncoated specimens for various uniform furnace wall temperatures.

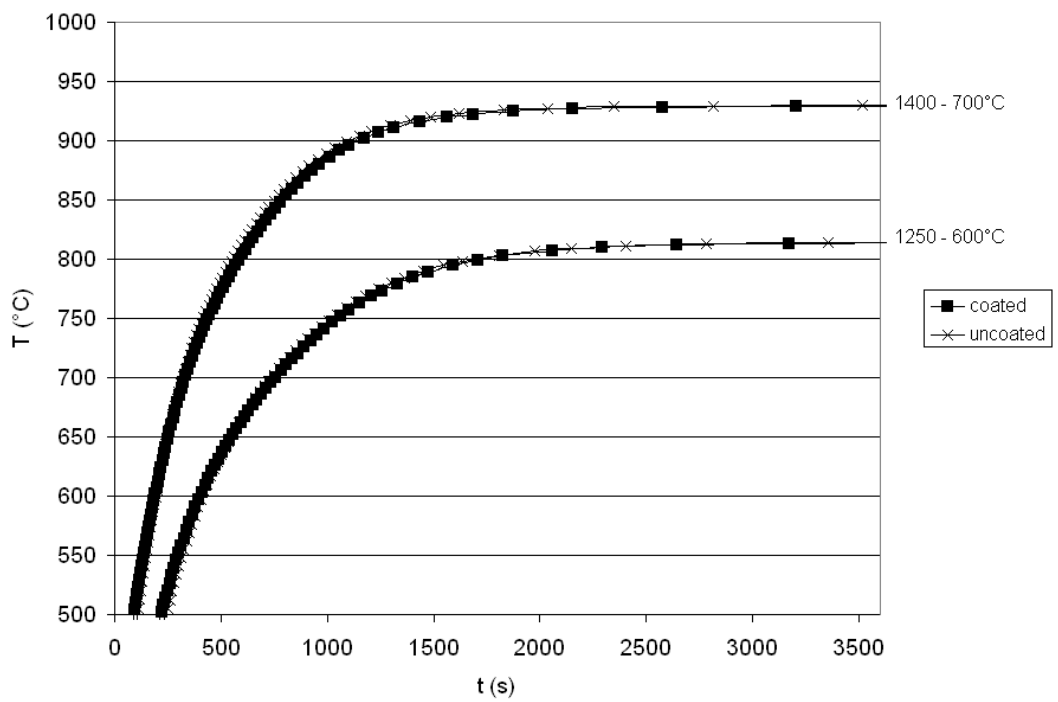


Figure 3.11: Mid-point of centreline temperature vs. time comparison for coated and uncoated specimens for various non-uniform furnace wall temperatures.

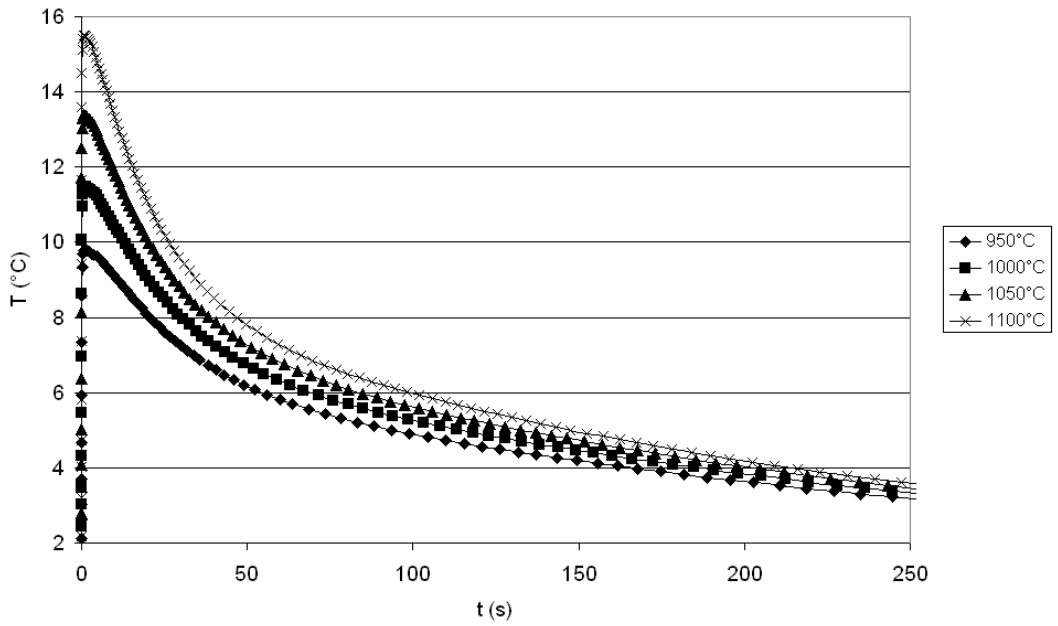


Figure 3.12: Thermal difference across top coat vs. time for different uniform furnace temperatures.

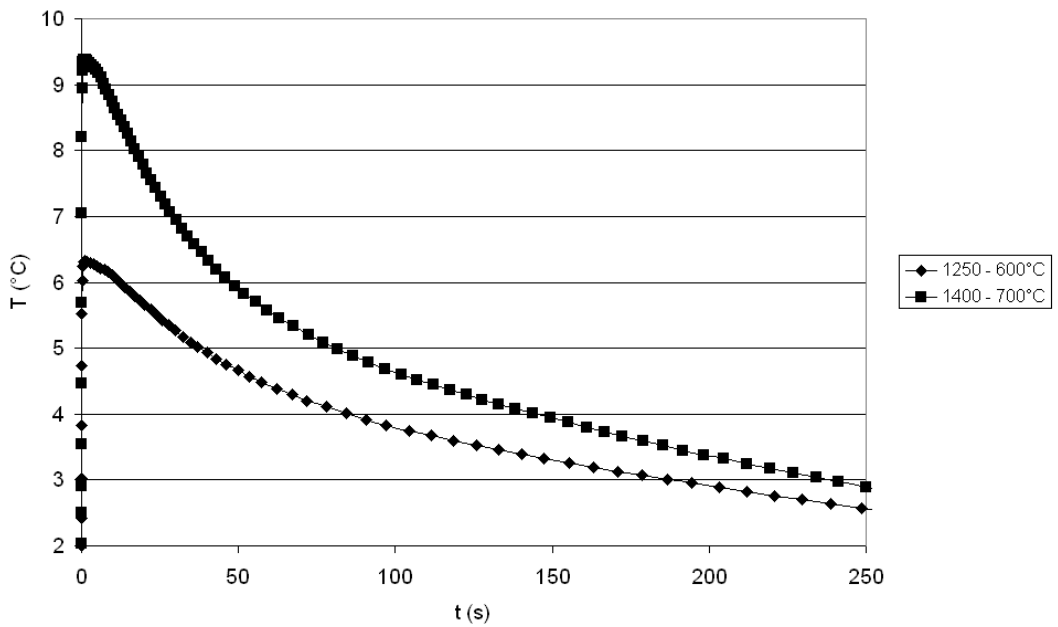


Figure 3.13: Thermal difference across top coat vs. time for different non-uniform furnace temperatures.

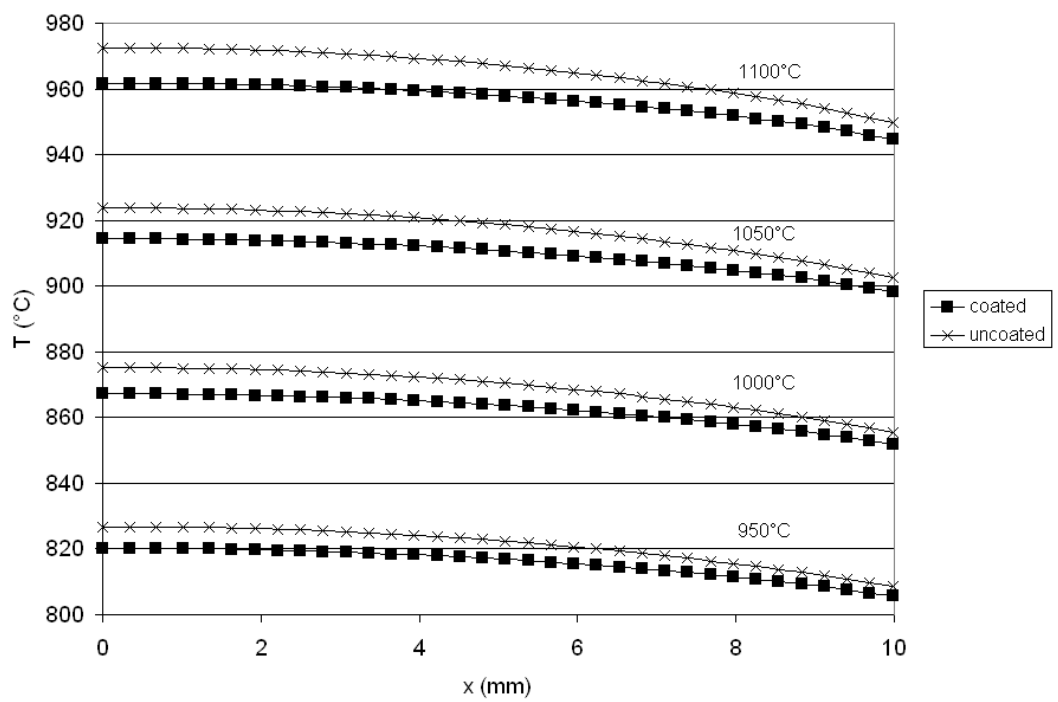


Figure 3.14: Temperature variation from the centre of the specimen ($x=0$) to the ridges ($x=10$ mm) on the axis of the specimen, with uniform furnace wall temperatures.

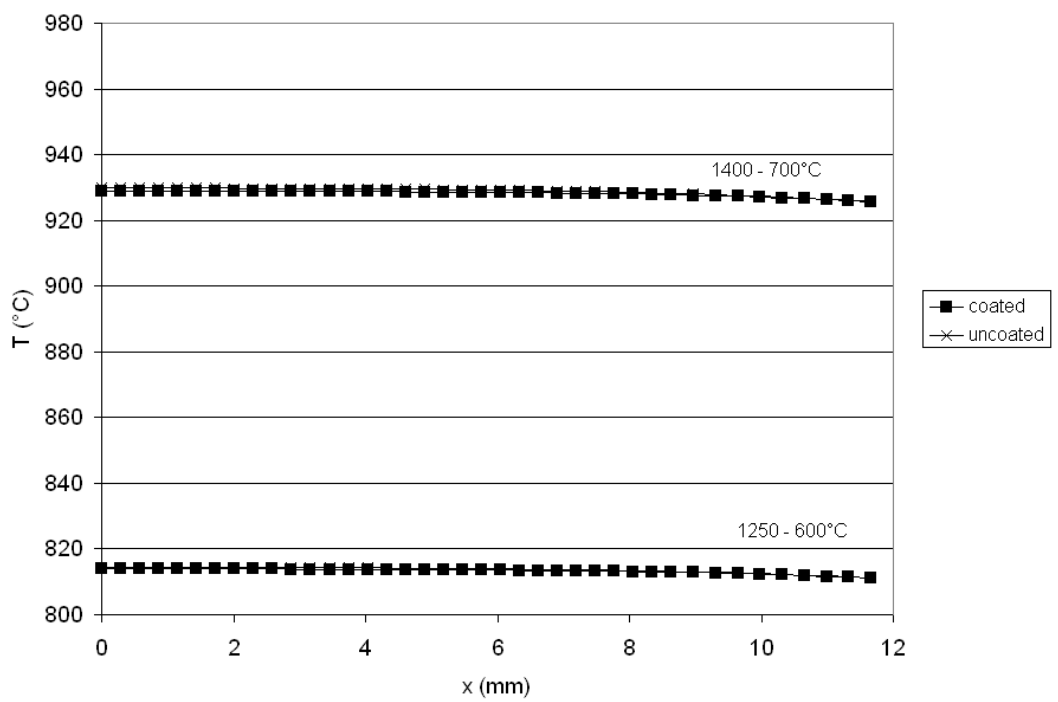


Figure 3.15: Temperature variation from the centre of the specimen ($x=0$) to the ridges ($x=10$ mm) on the axis of the specimen, with non-uniform furnace wall temperatures.

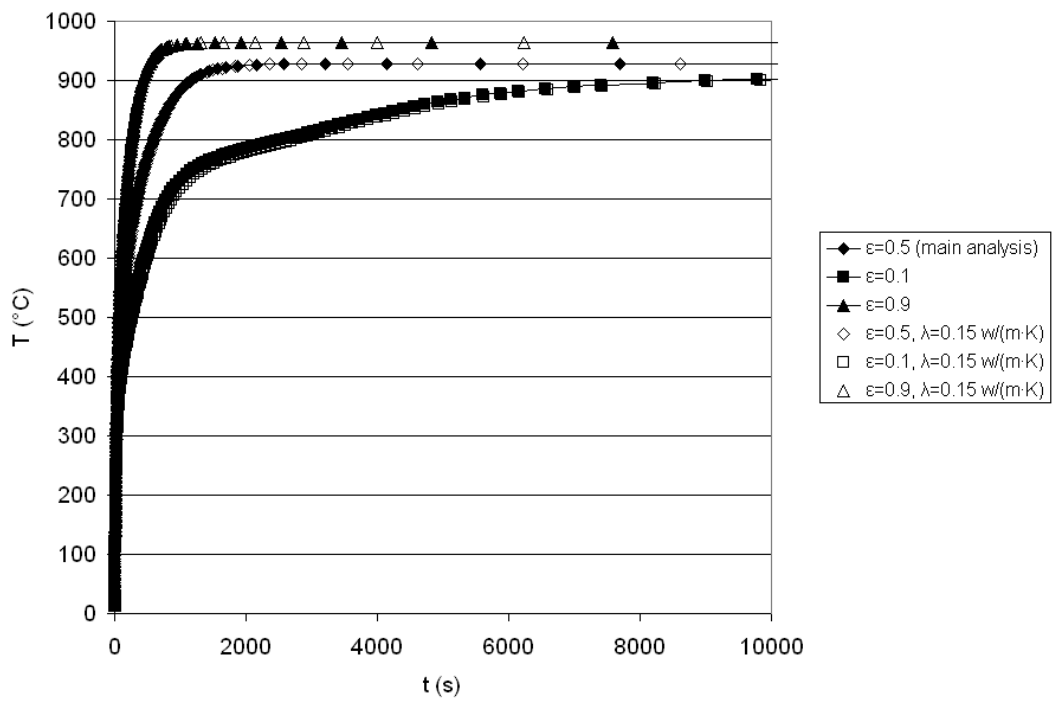


Figure 3.16: Effect of the variation of radiation parameters and TC conductivity for coated specimens on thermal stabilisation time and equilibrium temperature, imposing 1400°C and 700°C as outboard and inboard furnace ring temperatures, respectively.

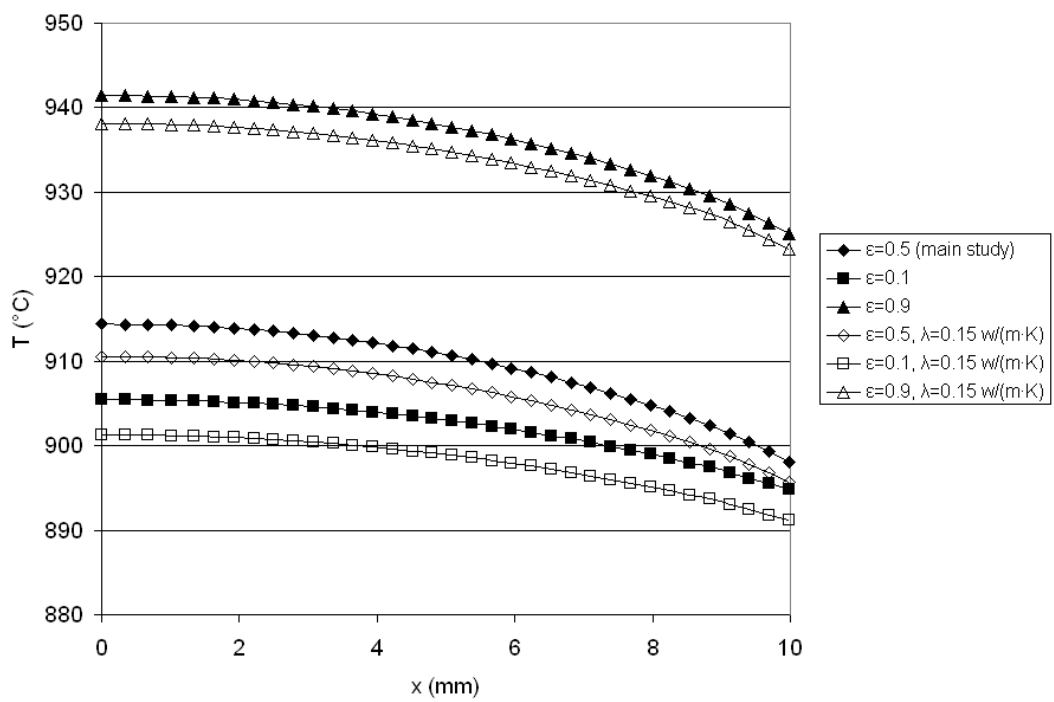


Figure 3.17: Effect of the variation of radiation parameters and TC conductivity for coated specimens on axial temperature profile, with uniform furnace wall temperature.

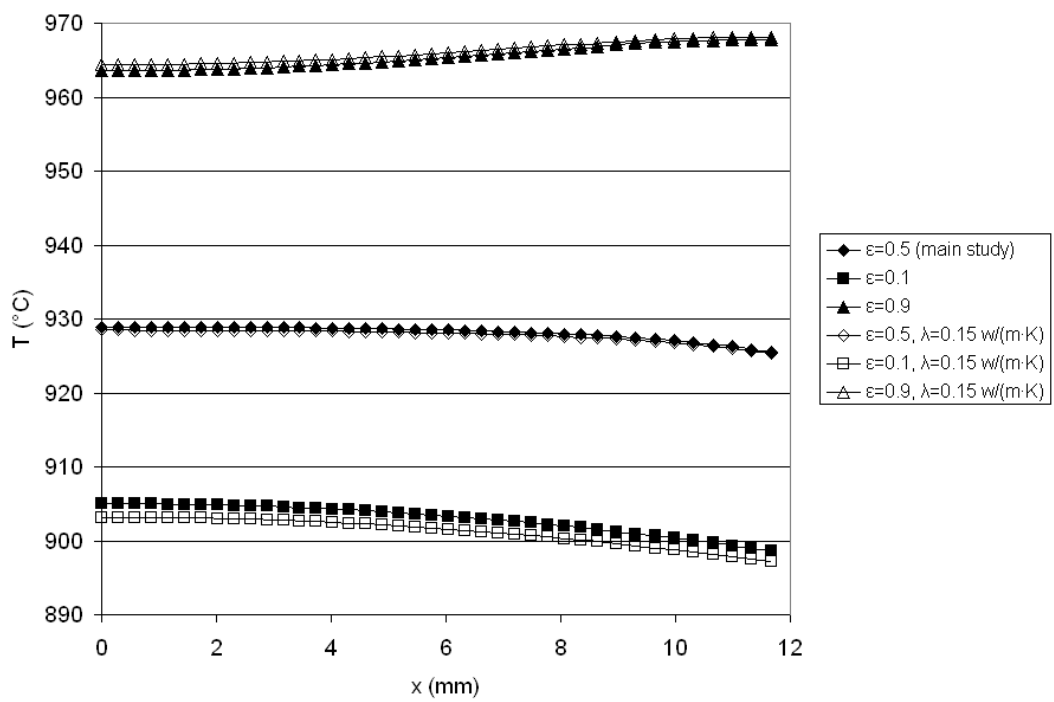


Figure 3.18: Effect of the variation of radiation parameters and TC conductivity for coated specimens on axial temperature profile, with non-uniform furnace wall temperature.

Chapter 4

Creep property evaluation for TBC coated and uncoated IN-738LC and CMSX-4

4.1 Introduction

High temperature requirements in gas turbines imply that the materials used in the hottest parts possess a combination of high-temperature elevated structural, microstructural and oxidation behaviour. Ni-based superalloys provide the combination of material properties required for those high-temperature applications. Two of the most used superalloys are IN-738LC, which is a vacuum melted, vacuum cast, low-carbon, precipitation hardenable nickel-base alloy [62], and the single crystal CMSX-4 [66] alloy. Traditionally, the development of superalloys has involved a trade-off in properties that has increased high temperature strength and creep resistance at the expense of oxidation and corrosion resistance [4, 67].

Cast materials show appropriate mechanical and oxidation properties up to $\sim 950^{\circ}\text{C}$ [67]. Single crystal superalloys extend that boundary up to $\sim 1100^{\circ}\text{C}$,

thanks to the increase in the microstructural stability [67]. Surface temperatures in excess of that limiting value require the application of a coating to protect the underlying superalloy. Thermal barrier coatings (TBCs) provide a means of thermal insulation that can be applied to Ni-base superalloys and hence increase the high temperature resistance of components made from them.

Experimental data for both alloys have been gathered from Refs. [62, 66, 68] and fitted to a Norton-type equation. Tensile specimens made of both alloys were tested in order to make sure that the material being considered in this work showed the same creep properties as have been reported in published research. Additionally, coated specimens were manufactured and tested in order to evaluate the effect that electron-beam physical vapour deposited (EB-PVD) and air plasma sprayed (APS) coatings had on their creep behaviour.

4.2 Creep constant fitting methodology

Creep data are available in the literature as secondary or minimum creep strain rates, $\dot{\epsilon}^{cr}$, for various combinations of temperature, T , and stress, σ . One of the most popular creep equations is Norton's equation [69], which can be formulated with temperature-dependent constants as

$$\dot{\epsilon}^{cr}(T, \sigma) = A(T)\sigma^{n(T)} \quad (4.1)$$

where $A(T)$ is the thermally activated creep constant and $n(T)$ is a temperature dependent creep exponent, which takes into account possible changes in the creep mechanisms at different temperatures. Taking logarithms in Equation 4.1,

$$\ln \dot{\epsilon}^{cr}(T, \sigma) = \ln A(T) + n(T) \ln \sigma \quad (4.2)$$

where $\ln \dot{\epsilon}^{cr}(T, \sigma)$ is a linear function of the variable $\ln \sigma$, for a fixed temperature, that can be fitted using the least squares method. By fitting Equation 4.2

at different temperatures, combinations of A and n at those temperatures are obtained. The temperature dependency of the creep factor can be modelled by means of an Arrhenius-type equation such as

$$A = A_0 e^{-\frac{Q}{RT}} \quad (4.3)$$

which can be written in an alternative form by applying logarithms,

$$\ln A = \ln A_0 - \frac{Q}{RT} \quad (4.4)$$

which states that $\ln A$ is a linear function of $\frac{1}{T}$. A_0 and $\frac{Q}{R}$ can be estimated by fitting Equation 4.4 using the least squares method to the values obtained from fitting Equation 4.2.

A temperature dependent stress exponent, $n(T)$, can be defined by the linear equation

$$n(T) = n_0 + n_1 T \quad (4.5)$$

which reproduces the creep mechanism dependence on temperature and proves to be more flexible when fitting experimental data to Norton's creep equation.

4.3 Specimen preparation and tests

Tensile creep specimens of 20 mm gauge length and 4 mm diameter were manufactured from IN-738LC and CMSX-4 alloys. IN-738LC specimens were then vacuum heat treated for 2 h at 1120°C (solution treatment) followed by 16 h at 870°C (ageing treatment). CMSX-4 specimens were vacuum heat treated for 2 h at 1120°C (solution) and 24 h at 840°C (ageing).

The coated specimens were not heat treated as the coating process involved additional thermal cycles that would replace the initial treatment. LCO22 bond coats were deposited between the ridges using the HVOF process, followed by APS top coats on the IN-738LC specimens and EB-PVD coatings on the CMSX-4 samples.

Creep specimens were tested, monitoring the temperature at three points using thermocouples in order to ensure that the temperature between the ridges was uniform.

4.4 Creep data

4.4.1 IN-738LC

The method described in Section 4.2 was used to fit the experimental data reported in Ref. [62], which are shown in Table 4.1. The secondary creep data were fitted to Norton-type equations, listed in Equations 4.6 - 4.8 and plotted in Fig. 4.1

$$\dot{\epsilon}^{cr} = 4.1626512 \times 10^{-41} \sigma^{11.871574}, \text{ with } R^2 = 0.96, \text{ for } 732^\circ\text{C} \quad (4.6)$$

$$\dot{\epsilon}^{cr} = 5.5464417 \times 10^{-35} \sigma^{10.658945}, \text{ with } R^2 = 0.94, \text{ for } 815^\circ\text{C} \quad (4.7)$$

$$\dot{\epsilon}^{cr} = 1.1640389 \times 10^{-26} \sigma^{8.633098}, \text{ with } R^2 = 0.94, \text{ for } 926^\circ\text{C} \quad (4.8)$$

The A and n values for various temperatures, extracted from Equations 4.6 - 4.8, are listed in Table 4.2. The creep factor, A , is plotted against the inverse of temperature, $\frac{1}{T}$, in Fig. 4.2, in order to obtain the numerical parameters in Equation 4.4 for IN-738LC. The equation that fits the data points is:

$$A = 6.6803810 \times 10^{48} e^{-\frac{2.0698940 \times 10^5}{T}}, \text{ with } R^2 = 0.997 \quad (4.9)$$

The creep exponent dependency with temperature is shown in Fig. 4.3, which can be estimated as

$$n(T) = -0.016778341T + 28.799305, \text{ with } R^2 = 0.996 \quad (4.10)$$

which gives as representative values of n 11.6 and 9.1 for 750°C and 900°C , respectively.

Hence, the creep model that best fits the experimental results for this material is:

$$\dot{\epsilon}^{cr} = 6.68038139 \times 10^{48} e^{-\frac{2.0698940 \times 10^5}{T}} \sigma^{-0.016778341T+28.799305} \text{ (K, MPa, s)} \quad (4.11)$$

which implies that the activation energy for creep, Q , is $1721 \text{ kJ} \cdot \text{mol}^{-1} \cdot \text{K}^{-1}$. Creep strain rates calculated using Equation 4.11 and provided in Ref. [62] are compared in Fig. 4.4, which shows that Norton's creep model fits reasonably well the experimental behaviour of IN-738LC.

4.4.2 CMSX-4

4.4.2.1 Strain softening model

Refs. [66, 68] provide a constitutive model for secondary and tertiary creep of CMSX-4 up to 1000°C in the $\langle 001 \rangle$ direction. This model assumes strain softening according to

$$\dot{\epsilon} = \dot{\Gamma} + \Omega \epsilon \quad (4.12)$$

where $\dot{\Gamma}$ and Ω are defined as

$$\dot{\Gamma} = a_{\dot{\Gamma}} e^{\left\{ b_{\dot{\Gamma}} \sigma - \frac{Q_{\dot{\Gamma}}}{RT} \right\}} \quad (4.13)$$

$$\Omega = a_{\Omega} e^{\left\{ b_{\Omega} \sigma - \frac{Q_{\Omega}}{RT} \right\}} \quad (4.14)$$

$\dot{\Gamma}$ represents the minimum creep strain rate, which is the value of the strain rate in the beginning of tertiary creep, and Ω is a softening coefficient related to the rate of dislocation multiplication. The numerical parameters used in Equations 4.13 and 4.14 are listed in Table 4.3.

4.4.2.2 Norton's creep model

Minimum creep strain rates, listed in Table 4.4, have been fitted to a Norton-type equation using the experimental data provided in Ref. [68], which correspond to the $\dot{\Gamma}$ parameter in Equation 4.12, for four different temperatures.

Initially all the data points available in Ref. [68] were used, as shown in Fig. 4.5, which shows that the data points for the two lower stress values at 900°C distort the overall behaviour trends. In order to avoid that distortion being transmitted into the creep model, and as the fitted $\dot{\Gamma}$ values by Reed *et al.* [68] showed the same disagreement, those two values were not taken into account when fitting the following Norton-type equations, plotted in Fig. 4.6:

$$\dot{\epsilon}^{cr} = 4.1030448 \times 10^{-44} \sigma^{12.840421}, \text{ with } R^2 = 0.89, \text{ for } 850^\circ\text{C} \quad (4.15)$$

$$\dot{\epsilon}^{cr} = 9.6176871 \times 10^{-40} \sigma^{11.743270}, \text{ with } R^2 = 0.87, \text{ for } 900^\circ\text{C} \quad (4.16)$$

$$\dot{\epsilon}^{cr} = 5.4211099 \times 10^{-30} \sigma^{8.3766264}, \text{ with } R^2 = 0.97, \text{ for } 950^\circ\text{C} \quad (4.17)$$

$$\dot{\epsilon}^{cr} = 2.6012316 \times 10^{-24} \sigma^{6.4390502}, \text{ with } R^2 = 0.82, \text{ for } 1000^\circ\text{C} \quad (4.18)$$

The creep factor, A , fitted for the different temperatures as shown in Table 4.5 and Fig. 4.7, can be estimated by means of the Arrhenius-type equation,

$$A = 1.3800081 \times 10^{131} e^{-\frac{4.5403163 \times 10^5}{T}}, \text{ with } R^2 = 0.98 \quad (4.19)$$

And, as explained in Section 4.2, the temperature-dependent stress exponent is (see Fig. 4.8):

$$n(T) = -0.045141512T + 63.929373, \text{ with } R^2 = 0.97 \quad (4.20)$$

which allows the minimum creep strain rate to be estimated as a function of stress, σ , and temperature, T , as

$$\dot{\epsilon}^{cr} = 1.3800081 \times 10^{131} e^{-\frac{4.5403163 \times 10^5}{T}} \sigma^{-0.045141512T + 63.929373} \text{ (K, MPa, s)} \quad (4.21)$$

which gives an activation energy for creep, Q , of $3775 \text{ kJ} \cdot \text{mol}^{-1} \cdot \text{K}^{-1}$. A comparison between the minimum creep strain rate data, the strain softening model and the Norton-type equation for CMSX-4 is shown in Fig. 4.9.

4.5 Experimental results

4.5.1 Uncoated materials

4.5.1.1 IN-738LC

Three creep tests, which ran until a 1% accumulated creep strain was achieved, were performed on IN-738LC, according to the conditions shown in Table 4.6; the corresponding creep curves are plotted in Fig. 4.10. The secondary creep strain rates are compared with the predictions from Equation 4.11 in Fig. 4.11, which shows good agreement, thus validating the material properties fitted in Section 4.4.1.

4.5.1.2 CMSX-4

Experimental results for creep of CMSX-4 at the three different temperature and stress combinations listed in Table 4.7 were carried out. Fig. 4.12 shows the corresponding creep curves, where the experimental results for 900°C and 950°C have been fitted to strain softening creep equations, such as Equation 4.12 with the displayed parameters. No curve was fitted for 850°C as the experimental curve did not show a relevant tertiary creep stage. Creep strain rates obtained using Equation 4.21 are compared with experimental results in Fig. 4.13, along with the $\dot{\Gamma}$ parameter fitted in Ref. [68].

The Ω parameters given in Table 4.7, which define the tertiary creep behaviour of the alloy, are in reasonable agreement with the data reported in Ref. [68].

4.5.2 Coated materials

Coated specimens have been tested in order to evaluate the effect that the coatings have on the creep response and the extent to which they carry loads.

High velocity oxygen fuel (HVOF) was used to apply the LCO22 bond coats on both the IN-738LC and the CMSX-4 tensile specimens. The process was then completed by applying APS PSZ coatings on the IN-738LC specimens and EB-PVD coatings on the CMSX-4 specimens.

The test conditions are defined as a combination of temperature and stress, which was calculated using the nominal section of the substrate material. In spite of the fact that the total section of the coated specimens is bigger than that of the uncoated ones as new material layers have been added, the stress displayed in the creep curves was calculated as the applied load divided over the section of the substrate material, which allows an easy comparison of the behaviour of the coated and uncoated specimens.

4.5.2.1 IN-738LC

Two creep tests were carried out on coated IN-738LC. The first test that was run was at 800°C and 300 MPa, as shown in Fig. 4.14, which shows that the added coating reduced the creep strain rate of the specimen. An additional test at the same temperature and 400 MPa was performed, shown in Fig. 4.14. The corresponding minimum creep strain rates are given in Table 4.8.

In order to evaluate the validity of the properties of the additional layers, i.e. bond coat, oxide layer and top coat, FE analyses were run. A full description of the models is contained in Chapter 5, where a discussion on the properties available for bond coats [70–72] and APS coatings [73] is made. Two creep curves were calculated based on the FE predictions; one using the fastest creeping bond coat [71] and the other for the slowest creeping alloy [70], which define the boundaries of the region where the experimentally obtained data points are located, as shown in Fig. 4.15, thus validating the material properties available in published research [70–73].

4.5.2.2 CMSX-4

An EB-PVD coated CMSX-4 specimen was tested at 900°C and 360 MPa, shown in Fig. 4.16. In this case, the minimum creep strain rate is higher than that corresponding to the equivalent test carried out on an uncoated specimen, although within the expected scatter according to Ref. [68], suggesting that EB-PVD coatings do not contribute significantly to the ability to carry tensile loads. The estimated strain softening parameter, Ω , is in accordance with the previously obtained data from the uncoated CMSX-4 tests and with the data reported in Ref. [68].

4.6 Discussion and conclusions

Coated and uncoated IN-738LC and CMSX-4 tensile specimens were tested in this work. The objective of the tests explained in this chapter was not to generate a full set of material data for these superalloys, but to validate the properties given in published research.

The uncoated specimens showed very good agreement with data extracted from Refs. [62, 66, 68]. Regarding coated specimens, two different conclusions were drawn. Firstly, the APS coated IN-738LC showed a lower creep strain rate compared with the uncoated specimens, suggesting that plasma-sprayed coatings contribute to their ability to carry tensile loads. FE calculations were run using properties for the bond coat [70, 71] and top coat [73] available in published research. The theoretical predictions, although they had a high uncertainty level regarding bond coat properties, matched reasonably well the experimentally obtained minimum creep strain rates. Secondly, the EB-PVD coated CMSX-4 specimens did not show significantly different behaviour from the uncoated samples, which implied that the coatings were not taking any tensile load. The columnar grain structure of EB-PVD coatings makes them

“strain tolerant”, implying that they do not develop stresses when their substrate is subjected to tensile strain. This phenomenon reflects in practice as an improved service life of these type of coatings compared with the APS layers, as they are less likely to crack.

The set of creep properties used in the forthcoming chapters has hereby been validated by means of the tests presented in this chapter and the comparison with published research. A more detailed series of material tests would identify and characterize more precisely the mechanical behaviour of the different materials involved in TBCs. The first step in the evaluation and validation of material properties has been carried out by means of tensile creep tests, which are relatively simple to postprocess and draw conclusions from.

T ($^{\circ}\text{C}$)	σ (MPa)	$\dot{\epsilon}_{min}^{cr}$ (s^{-1})
732	517	8.33×10^{-9}
732	517	5.56×10^{-9}
732	448	1.39×10^{-9}
732	448	1.11×10^{-9}
815	275	5.56×10^{-9}
815	241	1.11×10^{-9}
815	241	1.67×10^{-9}
926	117	8.33×10^{-9}
926	89	5.56×10^{-10}
926	89	1.11×10^{-9}
982	69	3.33×10^{-9}

Table 4.1: Secondary creep data IN-738LC [62].

T ($^{\circ}\text{C}$)	A , ($\text{MPa}^n \text{s}^{-1}$)	n
732	$4.1626512 \times 10^{-41}$	11.871574
815	$5.5464417 \times 10^{-35}$	10.658945
926	$1.1640389 \times 10^{-26}$	8.633098

Table 4.2: Fitted temperature-dependent creep parameters for IN-738LC.

	a (s^{-1})	b (MPa^{-1})	Q ($\text{kJ} \cdot \text{mol}^{-1}$)
$\dot{\Gamma}$	2.63×10^{14}	2.72×10^{-2}	627
Ω	1.11×10^{12}	1.29×10^{-2}	435

Table 4.3: Parameters of the strain softening creep model of CMSX-4 [68].

T ($^{\circ}\text{C}$)	σ (MPa)	$\dot{\epsilon}_{min}^{cr}$ (s^{-1})
850	370	2.50×10^{-11}
850	390	4.00×10^{-10}
850	425	1.00×10^{-10}
850	490	4.00×10^{-10}
850	560	2.00×10^{-8}
850	610	1.80×10^{-8}
850	650	7.00×10^{-8}
900	360	3.50×10^{-11}
900	400	2.50×10^{-10}
900	445	1.80×10^{-8}
900	455	1.00×10^{-8}
900	530	1.00×10^{-7}
950	180	7.00×10^{-11}
950	250	4.00×10^{-10}
950	320	4.00×10^{-9}
950	350	8.00×10^{-9}
950	445	1.50×10^{-7}
1000	175	1.50×10^{-9}
1000	200	7.00×10^{-10}
1000	275	9.00×10^{-9}
1000	300	4.00×10^{-8}

Table 4.4: CMSX-4 minimum creep strain rates from Ref. [68].

T ($^{\circ}\text{C}$)	A , ($\text{MPa}^{-n}\text{s}^{-1}$)	n
850	4.10×10^{-44}	12.8
900	9.62×10^{-40}	11.7
950	5.42×10^{-30}	8.38
1000	2.60×10^{-24}	6.44

Table 4.5: Fitted temperature-dependent creep parameters of CMSX-4.

T ($^{\circ}\text{C}$)	σ , (MPa)	$\dot{\epsilon}_{min}^{cr}$, (s^{-1})
750	418	5.57×10^{-9}
800	300	6.08×10^{-9}
900	150	5.08×10^{-9}

Table 4.6: Experimentally obtained secondary creep strain rate for IN-738LC.

T ($^{\circ}\text{C}$)	σ , (MPa)	$\dot{\epsilon}_{min}^{cr} \equiv \dot{\Gamma}$, (s^{-1})	Ω
850	510	7.81×10^{-9}	-
900	360	8.80×10^{-10}	2×10^{-6}
950	310	6.67×10^{-9}	6×10^{-6}

Table 4.7: Experimentally estimated creep parameters for CMSX-4.

T ($^{\circ}\text{C}$)	σ , (MPa)	$\dot{\epsilon}_{min}^{cr}$, (s^{-1})
800	300	1.83×10^{-9}
800	400	1.39×10^{-8}

Table 4.8: Experimentally obtained secondary creep strain rates for APS coated IN-738LC.

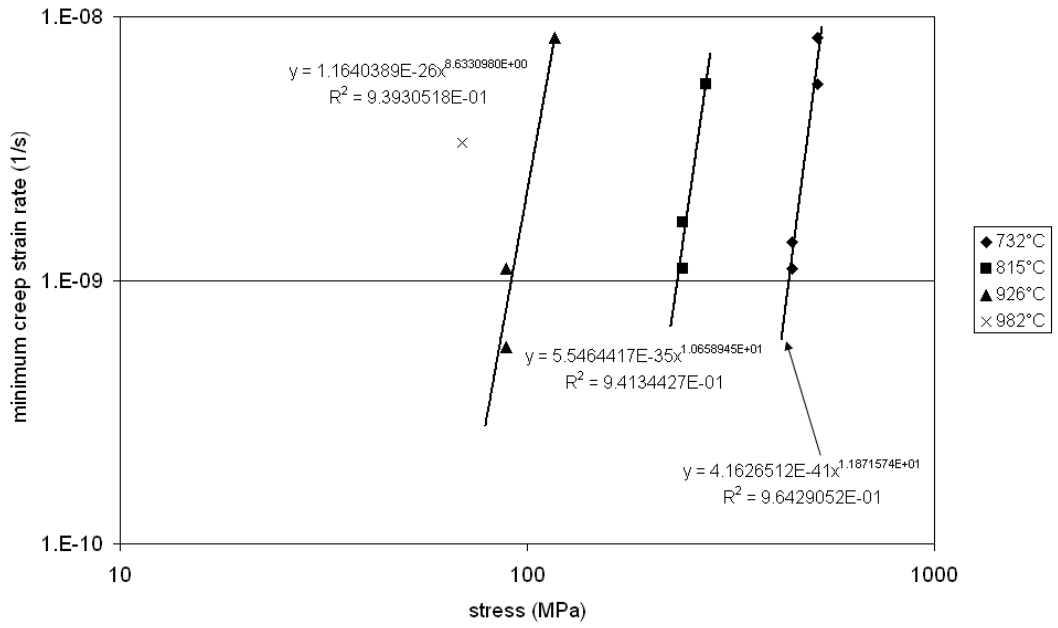


Figure 4.1: IN-738LC creep data fitting. Solid points represent data points from Ref. [62] and lines the least squares approximation to the data.

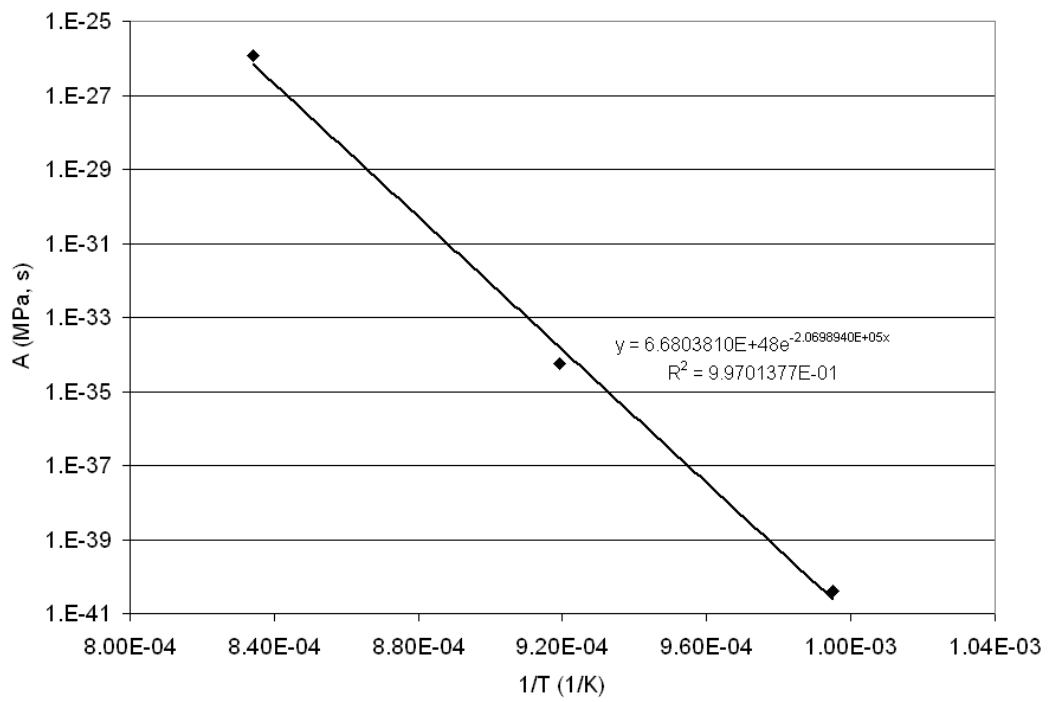


Figure 4.2: IN-738LC creep factor dependence with temperature. Solid points were extracted by fitting creep data from Ref. [62]. The line represents the least squares approximation of the behaviour of the creep constant, A , with temperature.

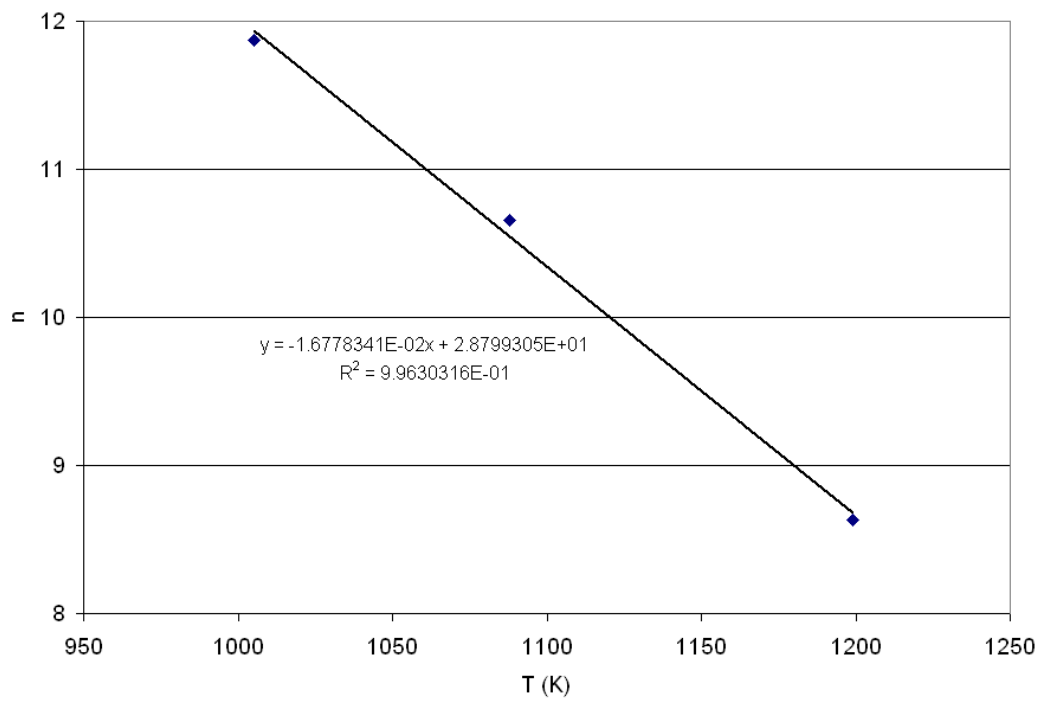


Figure 4.3: IN-738LC creep exponent dependence with temperature. The points were extracted by fitting creep data from Ref. [62]. The line represents the least squares approximation of the behaviour of the creep exponent, n , with temperature.

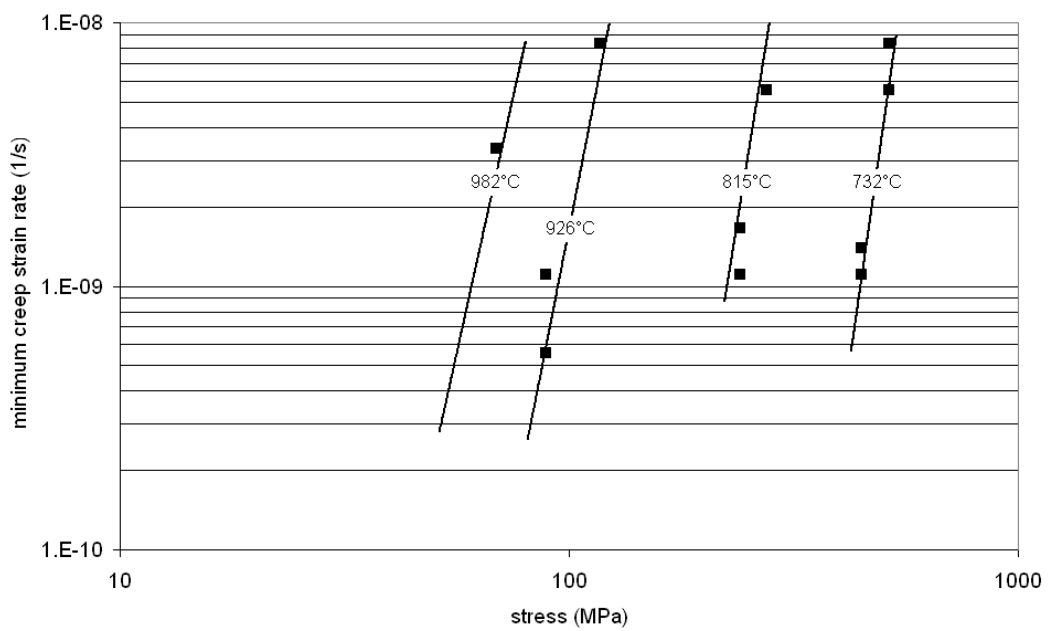


Figure 4.4: Calculated and experimental creep strain rates of IN-738LC. The points correspond to the secondary creep data from Ref. [62] used to obtain the numerical values in Equation 4.11, represented as lines in the graph.

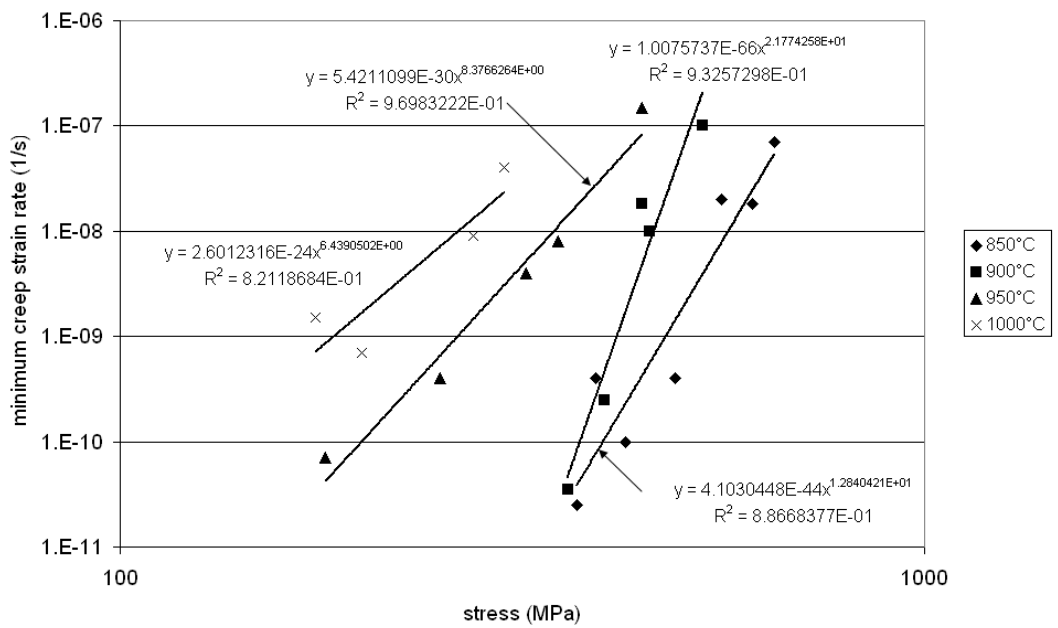


Figure 4.5: CMSX-4 creep data fitting. The points represent experimental data extracted from Ref. [68]. Data points for the two lower stresses at 900°C distort the trends shown by the rest of the points. Lines represent the least squares approximation to the creep strain rates for each temperature.

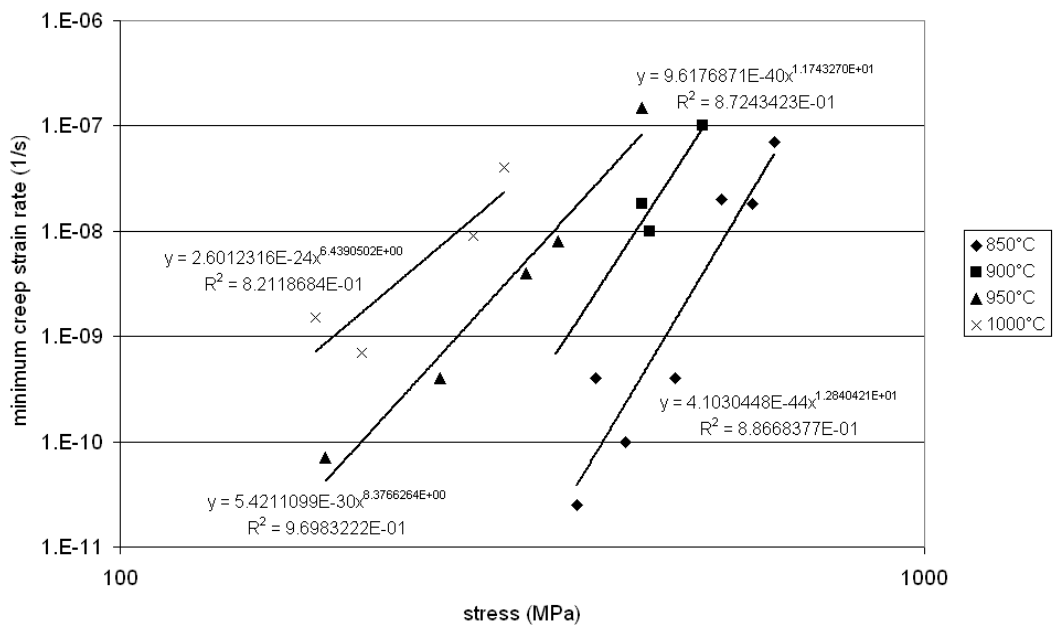


Figure 4.6: CMSX-4 creep data fitting, where data points that were distorting the trends in the creep behaviour have been omitted. The points represent experimental data extracted from Ref. [68]. Lines represent the least squares approximation to the creep strain rates for each temperature.

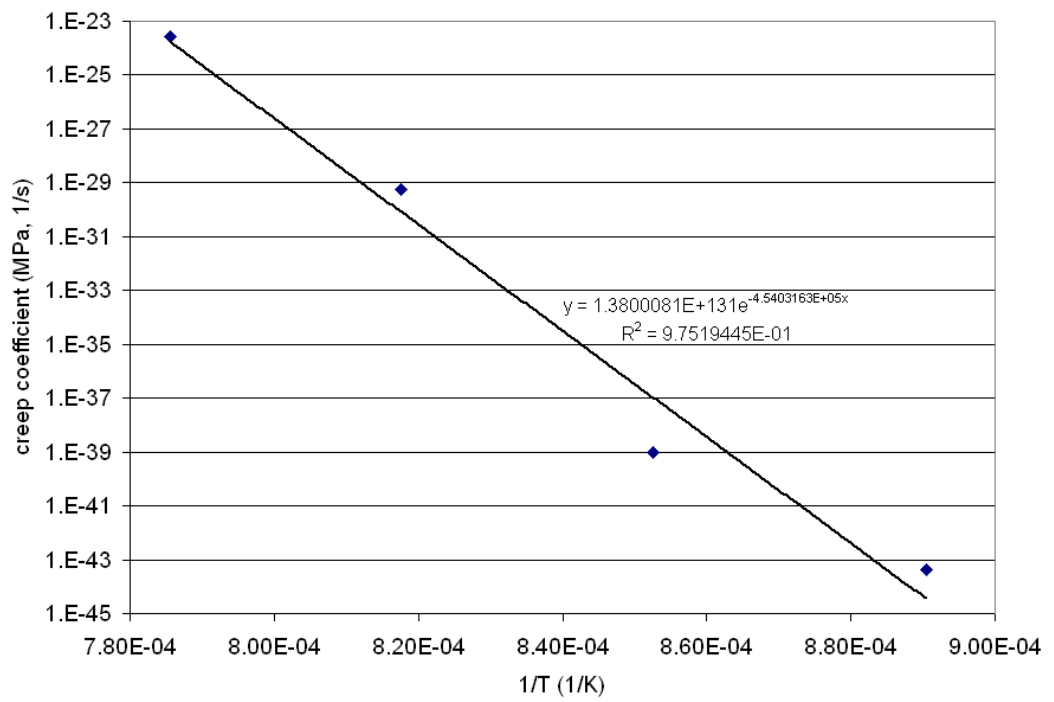


Figure 4.7: CMSX-4 creep coefficient dependence with temperature. The points were extracted by fitting creep data from Ref. [68]. The line represents the least squares approximation of the behaviour of the creep constant, A , with temperature.

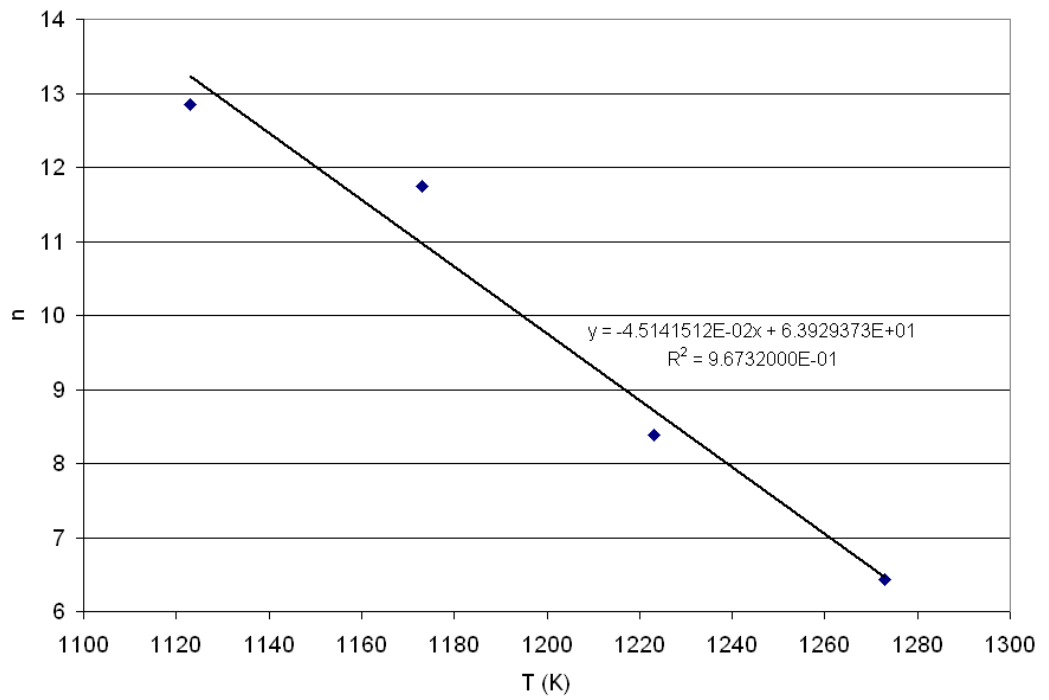


Figure 4.8: CMSX-4 creep exponent dependence with temperature. The points were extracted by fitting creep data from Ref. [68]. The line represents the least squares approximation of the behaviour of the creep exponent, n , with temperature.

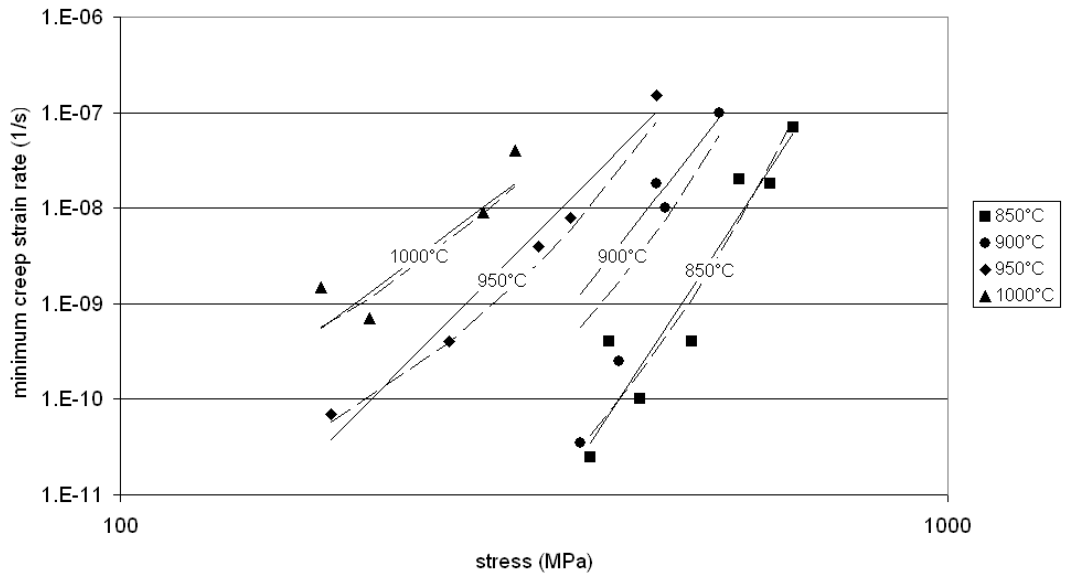


Figure 4.9: Calculated and experimental creep strain rates for CMSX-4. The points correspond to the minimum creep strain rate data, $\dot{\epsilon}_{\min}$, from Ref. [68] used to obtain the numerical values in Equation 4.21, represented as lines in the graph. The strain softening model defined in Equation 4.12 is plotted as discontinuous lines.

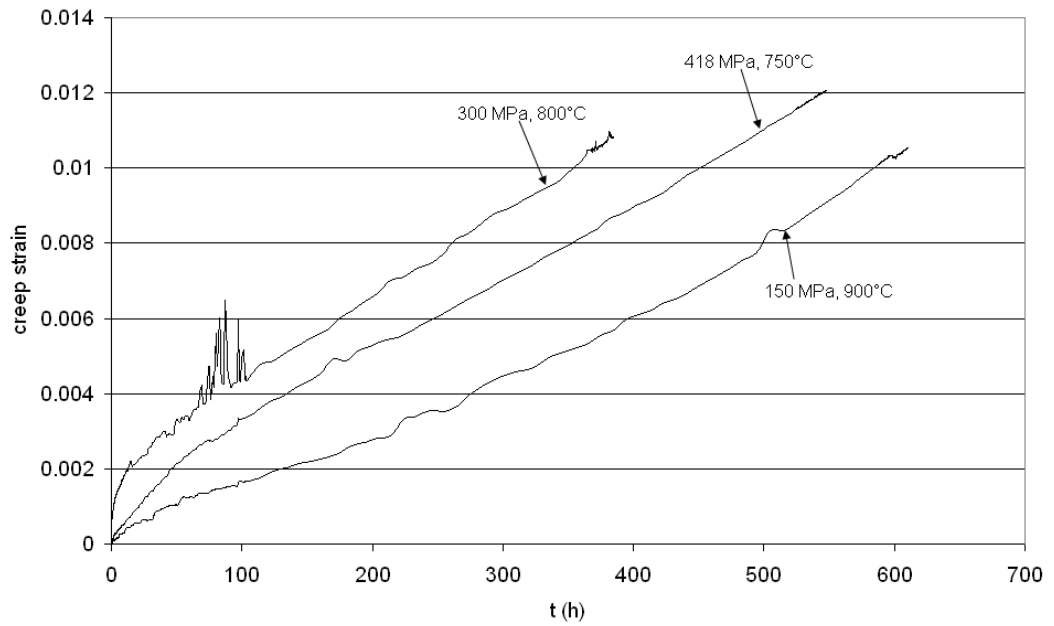


Figure 4.10: Experimental IN-738LC creep curves at several stresses and temperatures.

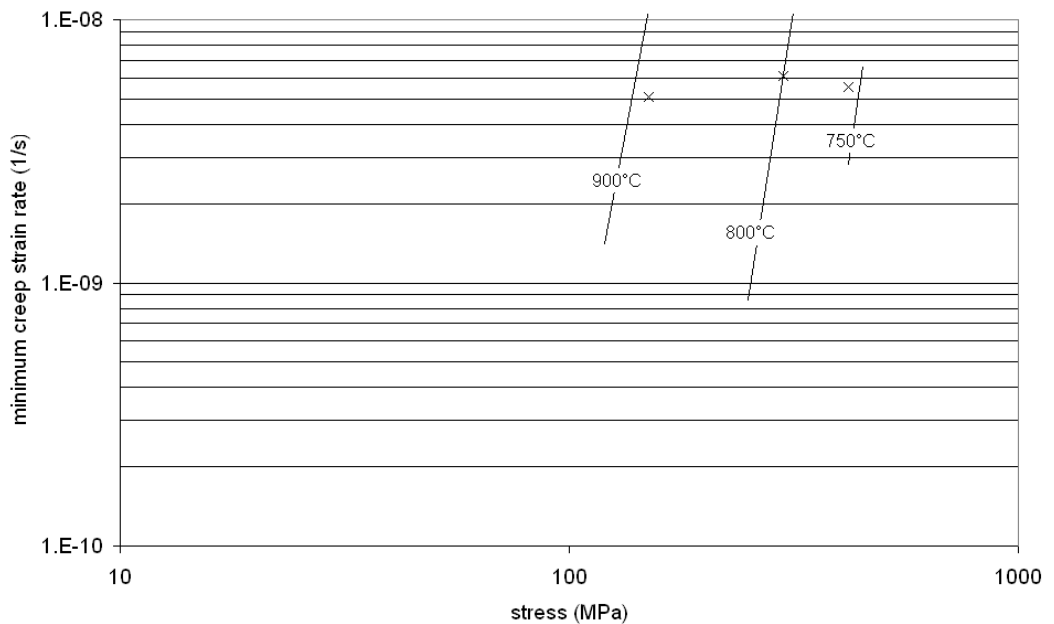


Figure 4.11: IN-738LC experimental results (represented as \times) and theoretical predictions (plotted as lines). Theoretical predictions have been obtained using Equation 4.11 and are plotted as continuous lines.

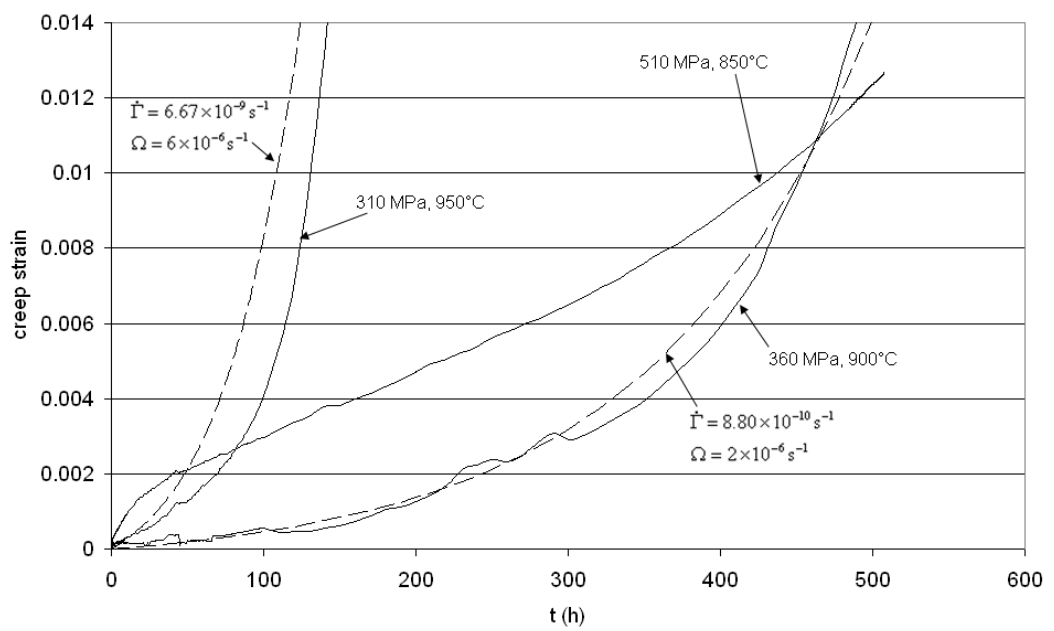


Figure 4.12: Experimental CMSX-4 creep curves (continuous lines) at several stresses and temperatures. Discontinuous lines represent the creep curves calculated with the parameters displayed for each one of them and using Equation 4.12. No line was fitted for 850°C as the experimental curve did not show a relevant tertiary creep stage.

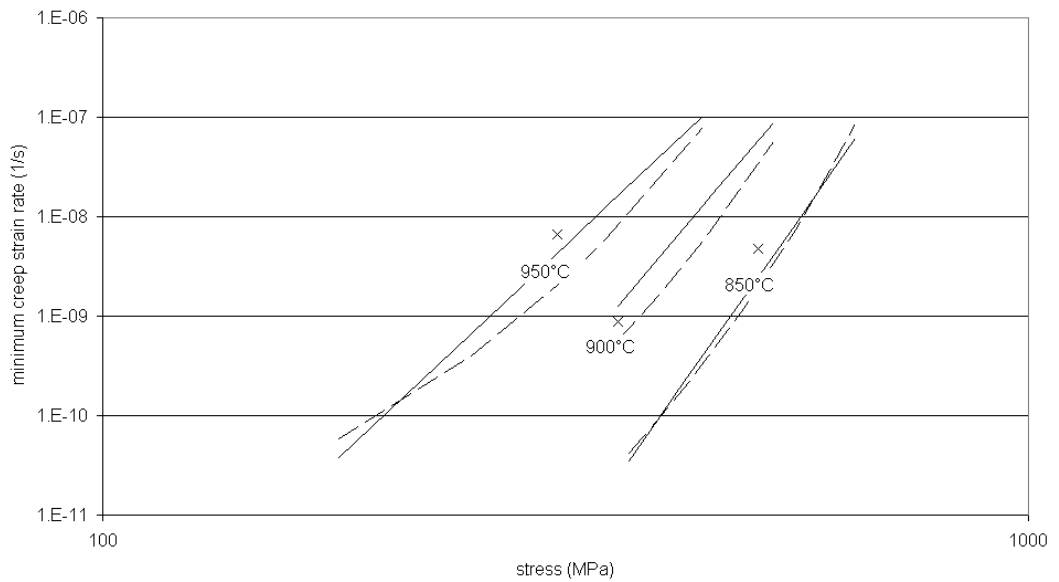


Figure 4.13: CMSX-4 experimental results (represented as \times) and theoretical predictions. Continuous lines represent show the behaviour predicted by Equation 4.21 and discontinuous lines show the $\dot{\Gamma}$ parameter according to Equation 4.13 with the numerical data from Table 4.3.

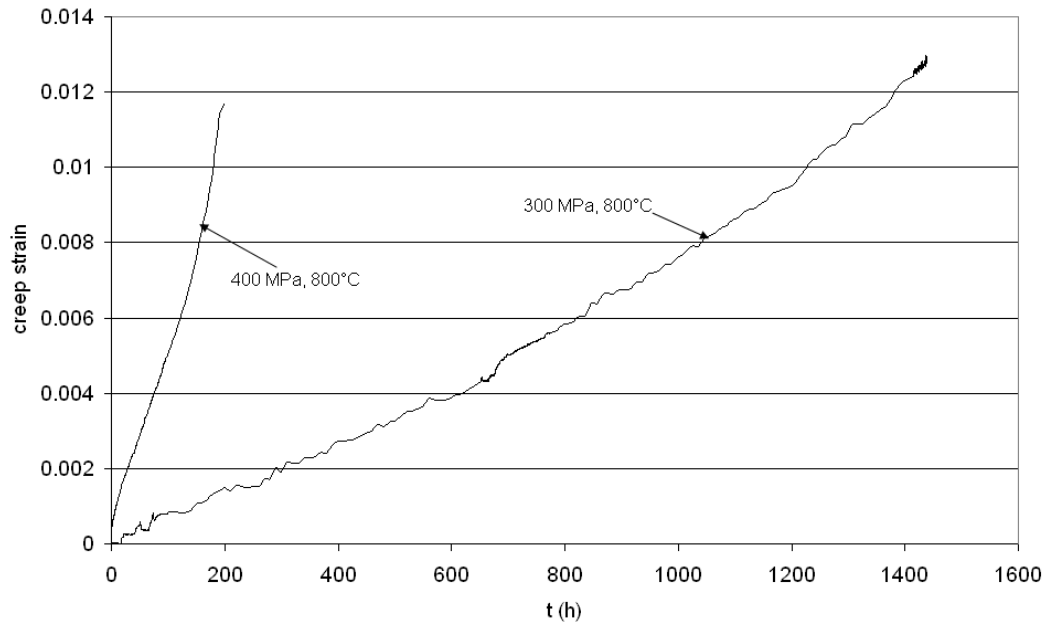


Figure 4.14: APS coated IN-738LC experimental creep curves at two stresses and temperatures.

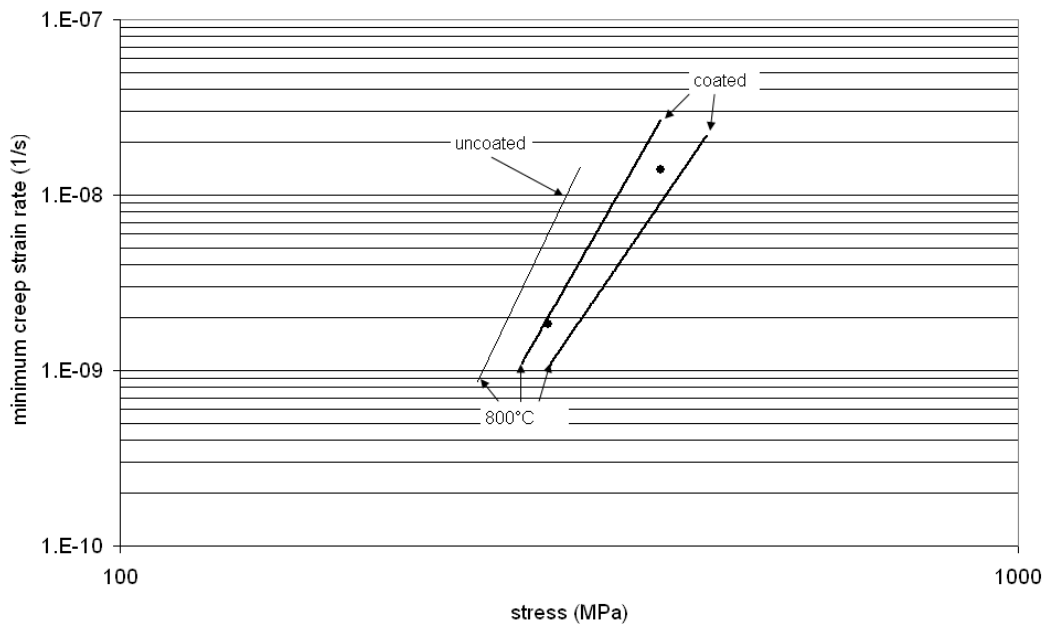


Figure 4.15: Calculated and experimental creep strain rates for APS coated IN-738LC. Solid circular points correspond to the experimentally obtained minimum creep strain rates. The thin line represents the theoretical prediction from Equation 4.11 for uncoated IN-738LC and thick lines bounding predictions from FE calculations as explained in Section 4.5.2.1, which correspond to APS coated IN-738LC.

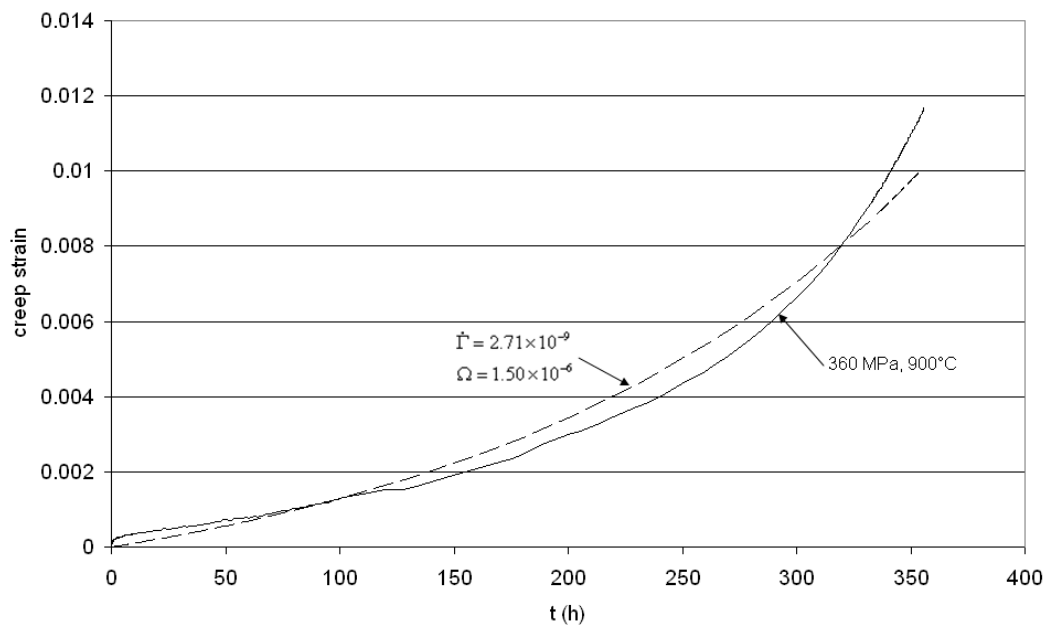


Figure 4.16: EB-PVD coated CMSX-4 experimental creep curve at 900°C and 360 MPa. The discontinuous line represents the calculated strain softening curve according to Equation 4.12, which corresponds to the predicted behaviour of uncoated CMSX-4, and the numerical parameters used in the calculation.

Chapter 5

Modelling oxidation induced stresses in TBCs by imposing TGO swelling strain rates

5.1 Introduction

The structural failure of TBCs is believed to be caused by elevated out of plane stresses developed at the TGO/TC interface and within the TGO that cause crack nucleation at particular locations within that interface [6, 9, 10]. Once cracks have nucleated, they coalesce and finally debond the TC - a process that is usually referred to as *spallation*.

The objective of this chapter is to study the stresses developed in TBCs under different thermal conditions, by simulating the oxidation process as done in previous research [15, 16, 18, 33] in order to assess the capabilities of the current oxidation models, and to try to identify any possible weaknesses or limitations present in the models. The bond coat/TGO/top coat interface is modelled as a wavy surface [12–15, 17, 34] defined by a sine function in order to simulate its geometric imperfections and account for the stress concentration points that

cause crack nucleation. TGO growth is modelled by applying swelling strain rates to the material that composes the initial oxide layer [15,16].

5.2 Finite element model

The geometry considered in the structural calculations presented here corresponds to a coated solid cylinder, as shown in Fig. 5.1, as it reproduces the situation present when testing coated tensile specimens. The FE model used to study the mechanical behaviour of the TBC consists of an axisymmetric slice of the coated solid cylinder (see Fig. 5.1), which is modelled assuming the dimensions given in Table 5.1.

The bond coat-TGO-top coat interface is modelled as a sine wave [12–15, 17,34] in order to account for the interface roughness and stress concentration points. Three geometric parameters, a , L and h , which represent the imperfection amplitude, wavelength and TGO thickness respectively, as defined in Fig. 5.2, are used to define the interface geometry.

Amplitude, a , and wavelength, L , data have been extracted from micrographs of four APS TBCs manufactured using different processes [74] and plotted along with their average values in Fig. 5.3. This graph shows some degree of correlation between amplitude and wavelengths of the interface imperfections; the average values for these four TBCs (given in Table 5.2) are seen to follow a trend which is largely independent of their method of manufacture.

In order to analyse the interdependency of the amplitude and wavelength of the surface imperfections plotted in Fig. 5.3, the aspect ratio, $\frac{a}{L}$, which characterises the intensity of the surface flaw, is plotted against the wavelength, L , as shown in Fig. 5.4, for the TBCs considered here. Wavelength values appear to be dependent upon the manufacturing process, as shown by the average values plotted in Fig. 5.3, but the dependency of the aspect ratio on the manufacturing

process seems to be weaker.

A probability distribution chart can be generated from the data in Fig. 5.4. This distribution, shown in Fig. 5.5, is obtained by projecting the data points in Fig. 5.4 onto the ordinates axis and grouping these values into discrete intervals. Realistic geometric parameters, that define the typical interface waviness found in TBCs, can be extracted from Fig. 5.5.

In this work, a series of parametric studies has been run. Several combinations of geometric parameters have been used, as shown in Table 5.3, considering three alternative interface geometries extracted from the data depicted in Figs. 5.3 - 5.5, with 48 μm wavelength and 6 μm amplitude, 24 μm and 8 μm , and 48 μm wavelength and 12 μm amplitude, respectively. For each combination of parameters, calculations with initial TGO thicknesses of 1, 3 and 5 μm have been carried out.

Axisymmetric 4-node reduced integration elements have been used in the analysis, as they produce reliable results in creep-related problems [75]. Fig. 5.6 shows a detail view of the mesh in the TGO proximity. Different mesh densities have been used, with the highest mesh density being near the position of most interest, i.e. the TGO, and the coarser mesh being in the areas far from that position of most interest.

Fig. 5.7 shows the boundary conditions applied to the model. The axial displacements are restrained for the left-hand surface, which keeps that surface flat thus representing the deformation under uniaxial loads. All the nodes on the right-hand surface have the same axial displacement, i.e. the surface remains always parallel to its initial position to ensure that the global stress state is that which corresponds to uniaxial loading, which should not introduce any distortion in planes perpendicular to the axis of the specimen. The radial displacements of the nodes on the axis of rotational symmetry are set to zero in order to simulate the conditions which represent the stress and deformation state developed in a

solid cylinder.

5.3 Material properties

Calculations have been run assuming a typical configuration of a coated component, i.e. an IN-738LC base material with an MCrAlY bond coat and a plasma sprayed PSZ top coat.

The properties of the IN-738LC alloy have been extracted from Ref. [62]. Its nominal composition is given in Table 5.4. Temperature dependent elastic constants (see Table 5.5) and coefficient of thermal expansion, shown in Table 5.6, were assumed [62]. Secondary creep data provided in Ref. [62] were fitted using the least squares method to a Norton-type equation [69] as shown in Equation 5.1,

$$\dot{\epsilon}^{cr} = A_0 e^{-\frac{Q}{RT}} \sigma^n \quad (5.1)$$

where the creep exponent, n , was linearly interpolated between the two temperatures for which it is given in Table 5.7 in order to use the numerical values that provide the best approximation to the available experimental data. Chapter 4 contains a full description and discussion regarding the creep properties of IN-738LC.

Since there is a high uncertainty regarding the creep properties of bond coats, the fastest and slowest creeping bond coat alloys available in literature [70, 71] have been considered, which correspond respectively to a PWA 276 alloy and a Praxair CO211 material, which has exactly the same nominal composition as the LCO22 alloy, as shown in Table 5.4. As some of the material properties for PWA 276 are not available, such as the elastic constants and coefficient of thermal expansion, the required set of data was completed by using the properties of PWA 286 (elastic constants shown in Table 5.5, and CTE corresponding to PWA 286 (VPS) in Table 5.6), which has a similar nominal composition, as

shown in Table 5.4. The coefficient of thermal expansion of Praxair CO211 was assumed to be the same as for LCO22, listed in Table 5.6.

The TGO was modelled as pure α -Al₂O₃. Munro [63] reviewed experimental data available in published research and generated a complete set of consistent properties for 98% dense sintered, 99.5% purity α -alumina, with a nominal grain size of 5 μ m. Temperature-dependent elastic constants are listed in Table 5.5 and CTEs in Table 5.6. These were calculated as instantaneous values from the overall expansion values from 0°C given in Ref. [63] following the method described in Appendix A. Creep constants are given in Table 5.7, fitted from data extracted from Ref. [63] for the 100-200 MPa and 1200-1800°C interval to a Norton-type equation using the least squares method, following the method described in Chapter 4 for the substrate material.

APS PSZ is known to undergo a sintering process when it is exposed to high temperature. However, based on experimental data obtained by Thompson and Clyne [76], a Young's modulus of 20 GPa was assumed for the temperature range considered in this study. A value of 0.18 for its Poisson's ratio was assumed, following the approach of Busso *et al.* [26]. Zhu and Miller [73] obtained the creep properties of a plasma sprayed zirconia 8 wt% yttria ceramic coating using experimental data produced under laser imposed temperature and stress gradients. The primary creep stage was found to be representative in the overall behaviour of the coating, which reflects in the time hardening behaviour presented in Equation 5.2 through the exponent, s , given in Table 5.7,

$$\dot{\epsilon}^{cr} = A_0 e^{-\frac{Q}{RT}} \sigma^n t^{-s} \quad (5.2)$$

5.4 TGO growth model

The TGO grows during thermal exposure, mainly driven by the oxidation of the aluminium present in the bond coat. This forms α -alumina, which subsequently

precipitates in the vicinity of the previously present TGO [10]. This oxidation process is accompanied by an increase in volume of the oxide when compared to the depleted metallic elements according to their Pilling-Bedworth ratio, which stresses the zones adjacent to the TGO and the TGO itself by creating what is usually referred to as *growth stress*.

Typical growth equations provide the oxide layer thickness, h , based on the accumulated high temperature exposure time, t . A generic growth equation, as shown in Equation 5.3 [15], characterises this phenomenon by means of two parameters, a constant, k'_p , which depends basically on temperature, and an exponent, n_{ox} , which depends on the nature of the oxide layer being formed. Theoretical models predict an n_{ox} value of 1 for non-protective coatings and $\frac{1}{2}$ for protective coatings that impede the penetration of anions into the underlying substrate [77]. The oxide growth rate, \dot{h} , is

$$h = (k'_p t)^{n_{ox}} \Rightarrow \dot{h} = n_{ox} (k'_p t)^{n_{ox}-1} k'_p = n_{ox} (k'_p)^{n_{ox}} t^{n_{ox}-1} \quad (5.3)$$

If an initial oxide thickness, h_0 , is assumed, the equation can then be modified to

$$h = (k'_p t)^{n_{ox}} + h_0 \quad (5.4)$$

The TGO layer was modelled using N elements across its thickness. The thickening strain rate, $\dot{\epsilon}_\perp$, is only applied to the element row adjacent to the bond coat, as done in previous research [15, 16] in order to simulate the precipitation of new oxide in a realistic manner. Fig. 5.8 shows the through-thickness configuration of the TGO layer at a time instant t , where the total TGO thickness, $h(t)$, can be expressed in terms of the thicknesses of each of the element layers through it, which are denoted $h^e(t)$ for the element row next to the bond coat and h_0^e for the remaining element rows:

$$h(t) = (N - 1)h_0^e + h^e(t) \quad (5.5)$$

The growth rate of the element row next to the bond coat, \dot{h}^e , is

$$\frac{dh}{dt} = \dot{h} = \frac{d}{dt} ((N-1)h_0^e + h^e(t)) = \frac{dh^e}{dt} = \dot{h}^e \quad (5.6)$$

which means that the thickness of the element row adjacent to the bond coat as a function of time, $h^e(t)$, is:

$$h^e(t) = h(t) - (N-1)h_0^e = h(t) - \frac{N-1}{N}h_0 \quad (5.7)$$

The thickening growth strain rate, $\dot{\epsilon}_\perp$, is applied to the element row adjacent to the bond coat by prescribing a swelling strain rate, calculated using Equation 5.8:

$$\dot{\epsilon}_\perp = \frac{\dot{h}^e}{h^e} = \frac{n_{ox} (k'_p)^{n_{ox}} t^{n_{ox}-1}}{(k'_p t)^{n_{ox}} + h_0 - \frac{N-1}{N}h_0} = \frac{n_{ox} (k'_p)^{n_{ox}} t^{n_{ox}-1}}{(k'_p t)^{n_{ox}} + \frac{h_0}{N}} \quad (5.8)$$

The TGO also grows in lateral direction, with a lateral growth rate, $\dot{\epsilon}_\parallel$, defined through the parameter β [15, 16]:

$$\beta = \frac{\dot{\epsilon}_\perp^h}{\dot{\epsilon}_\parallel} \quad (5.9)$$

where $\dot{\epsilon}_\perp^h$ is the equivalent thickening swelling strain rate that should be applied on the total thickness of oxide in order to achieve the same growth as with $\dot{\epsilon}_\perp$ applied to the element row closest to the bond coat, obtained as:

$$\dot{\epsilon}_\perp^h = \frac{\dot{h}}{h(t)} = \frac{n_{ox} (k'_p)^{n_{ox}} t^{n_{ox}-1}}{(k'_p t)^{n_{ox}} + h_0} \quad (5.10)$$

The β parameter relates the lengthening component of the oxidation strain rate and $\dot{\epsilon}_\perp^h$. By contrast, in this work the thickening component is applied to the element row close to the bond coat by means of the $\dot{\epsilon}_\perp$ swelling strain rate defined in Equation 5.8. Since $\dot{\epsilon}_\perp$ is different from $\dot{\epsilon}_\perp^h$, in order to apply a uniform lengthening swelling component, $\dot{\epsilon}_\parallel$, across the TGO thickness, a time dependent ratio, β^* , which decreases with time, needs to be used in the element row adjacent to the bond coat,

$$\beta^* = \frac{\dot{\epsilon}_\perp}{\dot{\epsilon}_\parallel} = \frac{\dot{\epsilon}_\perp}{\dot{\epsilon}_\perp^h} \beta = \frac{\frac{\dot{h}^e}{h^e}}{\frac{\dot{h}}{h}} \beta = \frac{\frac{\dot{h}}{h^e}}{\frac{\dot{h}}{h}} \beta = \frac{h}{h^e} \beta \quad (5.11)$$

The temperature-dependent growth constant used in the calculations is [46]:

$$k'_p = e^{Q\left(\frac{1}{T_0} - \frac{1}{T}\right)} [\mu\text{m}, \text{K}, \text{s}] \quad (5.12)$$

which uses the parameters listed in Table 5.8.

The implementation of the swelling strain rates in ABAQUS is done by imposing a volumetric swelling strain rate, $\dot{\epsilon}^{sw}$, and a ratio, r_{ii} , to the elements that compose the TGO, which induce swelling strain rates according to [75]:

$$\dot{\epsilon}_{ii}^{sw} = r_{ii} \frac{1}{3} \dot{\epsilon}^{sw}, \text{ no sum on } i \quad (5.13)$$

where $\dot{\epsilon}^{sw} = 3\dot{\epsilon}_{\perp}^h$, $r_{\perp} = 0$ and $r_{\parallel} = \frac{1}{\beta}$ for the elements that did not include thickening and $\dot{\epsilon}^{sw} = 3\dot{\epsilon}_{\perp}$, $r_{\perp} = 1$ and $r_{\parallel} = \frac{1}{\beta^*}$ was specified for the row of elements adjacent to the TGO.

5.5 Results and discussion

Radial stress values, which correspond to the out of plane stresses on the TGO vicinity, at the peak and valley positions shown in Fig. 5.9 have been calculated at different temperatures and considering different initial oxide thicknesses. The analysis assumed that the coating was stress free at room temperature [12]. In practice, the coating will exhibit residual stresses produced during its manufacturing process. However, the estimation of these stresses depends on manufacturing parameters such as temperatures and times of processing and the technology used for the deposition of each layer that composes the TBC, which make their realistic estimation unclear. A temperature rise, up to 750, 800 or 900°C, was applied over 1800 s and then the temperature was kept constant for 1000 h in order to calculate the stresses caused by oxidation, which correspond to a combination of thermal and growth stresses with creep acting as a relaxation mechanism.

As stated earlier, two alternative bond coats have been considered: the slowest creeping one for which data are available in the literature, which corresponds to hot isostatic pressed Praxair CO211 powder [70], and the fastest creeping one, a low pressure plasma sprayed PWA 276 alloy [71]. Radial stress values at different locations in the TC are plotted in Fig. 5.10, for different temperatures, bond coat materials and initial oxide thicknesses.

However, the stress dependency on the initial oxide thickness shown in Fig. 5.10 may not be a physical effect and may be just a consequence of the modelling methodology and the implementation of TGO growth by imposing swelling strain rates to the elements that compose it. This dependency suggests that the main mechanism driving creep, and hence stress development, in the TC may be the lengthening component of the oxidation strain rate, as shown in Fig. 5.11.

A relationship between the two strain rates that are susceptible of determining the TC stress state, i.e. TC creep and TGO growth, is explored. This can be formulated in terms of the proportionality relationship:

$$\dot{\epsilon}^{cr} \propto \dot{\epsilon}_{\parallel} \quad (5.14)$$

or, equivalently,

$$A\sigma^n t^{-s} \propto \frac{\dot{h}}{h\beta} \quad (5.15)$$

If a fixed time, t , and β parameter are considered, then the stress results shown in Fig. 5.10 can be plotted as σ^n vs. $\frac{\dot{h}}{hA}$ in order to identify that probable correlation, as plotted in Fig. 5.12, which shows the TC peak and valley radial stresses raised to the TC creep exponent as a function of $\frac{\dot{h}}{hA}$ for a fixed $\frac{a}{L}$ ratio and for three different temperatures. The graph suggests that the assumption made on Equation 5.15, which implies the proportionality of the TC creep strain rates and the growth strain rates is plausible.

Temperature affects both the creep properties of the TC and TGO, but the representation used in Fig. 5.12 only takes into account the variation in the

creep properties of the TC and in the swelling strain rate, ignoring the fact that temperature affects the creep behaviour of the oxide layer as well. An alternative simplified graphical representation plots σ^n vs. $\frac{\dot{h}}{h}$, i.e. the stress at different locations of the TC as a function of the imposed strain rate that represents the oxide growth, shown in Fig. 5.13.

Fig. 5.13 confirms that there is a proportionality relationship between the radial out of plane TC stress near the TGO/TC interface and the imposed swelling strain rate, which depends on the initial oxide thickness when TGO growth is implemented in FE analyses using element swelling.

Additional calculations have been run using models with $L=46 \mu\text{m}$ and $a=12 \mu\text{m}$ and $L=24 \mu\text{m}$ and $a=8 \mu\text{m}$, which showed the same qualitative behaviour. In order to assess the influence of the geometric parameters on the TC radial stresses, results have been grouped in single charts (see Figs. 5.14 and 5.15). Results for each location and for each $\frac{a}{L}$ parameter have been fitted to linear functions that depend on $\frac{\dot{h}}{h}$ using the least squares method:

$$\sigma_{peak}^n = 4.51 \times 10^8 \frac{\dot{h}}{h} + 5.07, \text{ with } R^2 = 0.97 \text{ for } L = 46, a = 6 \quad (5.16)$$

$$\sigma_{peak}^n = 5.69 \times 10^8 \frac{\dot{h}}{h} - 8.25, \text{ with } R^2 = 0.984 \text{ for } L = 46, a = 12 \quad (5.17)$$

$$\sigma_{peak}^n = 5.91 \times 10^8 \frac{\dot{h}}{h} - 19.8, \text{ with } R^2 = 0.972 \text{ for } L = 24, a = 8 \quad (5.18)$$

$$\sigma_{valley}^n = 2.92 \times 10^8 \frac{\dot{h}}{h} + 13.0, \text{ with } R^2 = 0.967 \text{ for } L = 46, a = 6 \quad (5.19)$$

$$\sigma_{valley}^n = 3.18 \times 10^8 \frac{\dot{h}}{h} + 8.51, \text{ with } R^2 = 0.953 \text{ for } L = 46, a = 12 \quad (5.20)$$

$$\sigma_{valley}^n = 2.25 \times 10^8 \frac{\dot{h}}{h} + 13.3, \text{ with } R^2 = 0.95 \text{ for } L = 24, a = 8 \quad (5.21)$$

The reasonably good agreement between the numerical results obtained from extensive FE calculations and the fitted linear Equations 5.16 - 5.21 suggest that a relationship of the type

$$\sigma^n = f_1 \left(\frac{a}{L} \right) \frac{\dot{h}}{h} + f_2 \left(\frac{a}{L} \right) \quad (5.22)$$

may exist for the radial stresses for the TC peak and valley locations considered in the present study, where the f_1 and f_2 functions were determined for peak and valley locations as

$$f_1^{peak} = -2.9624 \times 10^9 \left(\frac{a}{L}\right)^2 + 2.0639 \times 10^9 \frac{a}{L} + 2.3220 \times 10^8 \quad (5.23)$$

$$f_1^{valley} = -7.3078 \times 10^9 \left(\frac{a}{L}\right)^2 + 3.0589 \times 10^9 \frac{a}{L} + 1.7343 \times 10^7 \quad (5.24)$$

$$f_2^{peak} = -282.26 \left(\frac{a}{L}\right)^2 + 8.3293 \frac{a}{L} + 8.7857 \quad (5.25)$$

$$f_2^{valley} = 495.45 \left(\frac{a}{L}\right)^2 - 228.29 \frac{a}{L} + 34.348 \quad (5.26)$$

Once the existence of the relation stated in Equation 5.22 is accepted, which seems a realistic assumption in view of Figs. 5.14 and 5.15 and of the R^2 values in Equations 5.16- 5.21, a sensitivity study of Equation 5.22 can be carried out, both for the peak and valley locations.

The sensitivity of a function, y , with respect to a variable, x , can be represented in a dimensionless manner as

$$S_x^y = \frac{\partial y}{\partial x} \frac{x}{y} \quad (5.27)$$

The interpretation of the S_x^y values is the proportion on which perturbations in the x variable are transferred to the y function, i.e. if x changes by 100%, the percentage that affects y would be 100 multiplied by S_x^y .

Figs. 5.16 and 5.17 show the sensitivity of the radial TC stresses with respect to the TGO growth strain rate, $\frac{\dot{h}}{h}$, for the peak and valley locations respectively. The peak radial stress is more sensitive to changes in $\frac{\dot{h}}{h}$ than the valley stress, with opposite behaviour regarding the intensity of the imperfection modelled, i.e. while higher $\frac{a}{L}$ parameters increase the sensitivity of peak stress with $\frac{\dot{h}}{h}$, the valley stress responds with a lower sensitivity. In any case, the sensitivities

tend to converge to 1 with increasing $\frac{\dot{h}}{h}$ values, which is consistent with the fitted numerical data in Equation 5.22.

The study of the sensitivity of the radial stress with respect to $\frac{a}{L}$ reveals that peak stress values (Fig. 5.18) are less affected by $\frac{a}{L}$ for high $\frac{\dot{h}}{h}$ than valley stresses (Fig. 5.19).

The swelling strain rate, $\frac{\dot{h}}{h}$, is a function of two variables, as can be seen in Equation 5.10, temperature (through the oxide growth constant, as k'_p is a function of temperature) and initial oxide thickness, h_0 . In order to separate the isolated effects of each one of the variables, the sensitivity of $\frac{\dot{h}}{h}$ with respect to its variables is studied, as shown in Figs. 5.20 and 5.21. Since σ^n is an implicit function of the initial oxide thickness through the swelling strain rate, the dependency of σ^n upon the initial oxide thickness can be estimated by multiplying the sensitivities plotted in Figs. 5.16, or 5.17 for the valley location, and Fig 5.20. This sensitivity is of order unity, i.e. the initial oxide thickness plays a major role in the stress levels achieved. However, this conclusion does not seem very realistic and may be a consequence of the technique used to model TGO growth. The volume expansion as a consequence of oxidation depends on the amount of new oxide being formed through its Pilling-Bedworth ratio. The consequence of this is that a more realistic representation of this phenomenon should imply that the growth stresses should be determined by the oxidation rate alone, the initial oxide thickness having a secondary effect on the stress levels achieved in the ceramic top coat. Moreover, the initial oxide thickness depends on manufacturing parameters and on the exact technique being used and presents high scatter. Fig. 5.21 shows a manifestation of a physical effect, i.e. the oxide grows faster with higher temperature.

5.6 Conclusions

FE models, which represent the deformation state of tensile specimens, have been used to calculate the out of plane stresses, considered to be responsible for crack nucleation and growth, developed in different locations of the ceramic coat. The BC/TGO/TC interface was modelled as a wavy surface defined by a sinusoidal function, defined by two geometric parameters, amplitude, a , and wavelength, L . An additional variable taken into account when creating the FE models was the initial oxide thickness, h_0 .

Analyses were run for a range of geometric parameters in order to assess their influence on the stress state of the ceramic top coat. Similarly, the effect of changes in the parameters on the TC stresses was estimated and quantified by means of a sensitivity study carried out on stress functions fitted to the numerical results obtained from extensive FE calculations, leading to the following conclusions:

- The TGO lengthening swelling strain rate, which simulates the precipitation of new oxide between the grains of alumina already present in the layer, produces tensile radial stresses in the TC valley location and compressive radial stresses in the peak points.
- The compressive stresses predicted in the peak locations are greater in magnitude than the tensile stresses in the valleys.
- Thinner initial TGO thicknesses require higher swelling strain rates in order to achieve the same thickening for a fixed time and temperature, producing greater TC out-of-plane stresses.
- A relationship was identified between the specified swelling strain rates used to model TGO growth and the stresses obtained in the TC. Swelling of the elements that compose the TGO does not seem to be a realistic

method to implement TGO oxidation and further developments in this area are needed.

- The final stress level is determined by the equilibrium of the stresses that arise from different sources, i.e. thermal mismatch, growth stress and creep. Since higher temperatures induce higher stresses, the stress relieving through creep appears to be less intense when compared to the former two stress increasing mechanisms.

Layer	Thickness
Substrate	2 mm
Bond coat	225 μm
TGO	h_0 (parameter)
Top coat	178 μm

Table 5.1: Model dimensions.

TBC number	\bar{L} , μm	\bar{a} , μm	$\frac{\bar{a}}{\bar{L}}$
1	64.8	9.7	0.157
2	27.7	3.3	0.154
3	37.5	7.1	0.226
4	51.8	8.2	0.171

Table 5.2: Wavelength, amplitude and aspect ratio averages for the imperfections in the TBCs from Ref. [74]

Parameter	Value
a	6-8-12 μm
h_0	1-3-5 μm
L	24-48 μm

Table 5.3: TBC geometric parameters.

Element wt%	IN- 738LC, [62]	LCO22 [72]	Praxair CO211 [70]	PWA 276 [71]	PWA 286 [72]
Ni	61	32	32	48.29	49.4
C	0.11	-	-	0.01	-
Co	8.5	38.5	38.5	20.3	21
Cr	16	21	21	17.3	17
Mo	1.75	-	-	-	-
W	2.6	-	-	-	-
Ta	1.75	-	-	-	-
Nb	0.9	-	-	-	-
Al	3.4	8	8	13.6	12
Ti	3.4	-	-	-	-
Al+Ti	6.8	-	-	-	-
B	0.01	-	-	-	-
Zr	0.05	-	-	-	-
Fe, Mn, Si, S	low as pos- sible	-	-	-	-
Y	-	0.5	0.5	0.5	0.6

Table 5.4: Nominal compositions of materials.

T (°C)	IN-738LC, [62]	LCO22, [72]	Praxair CO211, [70]	PWA 286, [72]	$\alpha - \text{Al}_2\text{O}_3$, [63]
20	-	-	200	141.2	416 / 0.231
23.9	200.6 / 0.28	-	-	-	-
93.3	195.1 / 0.27	-	-	-	-
100	-	-	-	-	-
200	-	-	-	122.5	-
204.4	190.3 / 0.27	-	-	-	-
232	-	-	186.2	-	-
300	-	175	-	-	-
315.6	184.8 / 0.28	-	-	-	-
400	-	167.5	-	110	-
426.7	179.3 / 0.28	-	-	-	-
452	-	-	162	-	-
500	-	162.5	-	102.5	390 / 0.237
537.8	175.1 / 0.30	-	-	-	-
600	-	160	-	95	-
648.9	167.6 / 0.30	-	-	-	-
677	-	-	110.3	-	-
700	-	148.8	-	85	-
732	-	-	82.7	-	-
750	-	-	-	82.5	-
760	157 / 0.3	-	-	-	-
788	-	-	82.7	-	-
800	-	142.5	-	75	-
843	-	-	113.8	-	-
850	-	-	-	67.5	-
871.1	151 / 0.29	-	-	-	-
899	-	-	96.5	-	-
900	-	137.5	-	61.25	-
962.2	-	-	-	-	-
982.2	140 / 0.30	-	-	-	-
1000	-	-	-	-	364 / 0.244
1050	-	125	-	-	-
1200	-	-	-	-	354 / 0.247
1400	-	-	-	-	343 / 0.25
1500	-	-	-	-	338 / 0.252

Table 5.5: Elastic properties of materials, E (GPa) / ν , where available

T (°C)	IN-738LC, [62]	LCO22, [72]	PWA 286 (VPS), [72]	PWA 286 (EB-PVD), [72]	Al ₂ O ₃ , [63]	APS PSZ, [45]
20	-	-	-	8.6×10^{-6}	5.2×10^{-6}	-
23.9	11.23×10^{-6}	-	-	-	-	-
93.3	11.97×10^{-6}	-	-	-	-	-
100	-	-	-	9.4×10^{-6}	-	8.82×10^{-6}
200	-	13.5×10^{-6}	13.2×10^{-6}	10.2×10^{-6}	-	9.4×10^{-6}
204.4	13.23×10^{-6}	-	-	-	-	-
300	-	-	13.4×10^{-6}	-	-	9.75×10^{-6}
315.6	14.4×10^{-6}	-	-	-	-	-
400	-	14.5×10^{-6}	13.8×10^{-6}	11.8×10^{-6}	-	10×10^{-6}
426.7	15.46×10^{-6}	-	-	-	-	-
500	-	14.9×10^{-6}	14.3×10^{-6}	-	8.3×10^{-6}	10.2×10^{-6}
537.8	16.2×10^{-6}	-	-	-	-	-
600	-	15.5×10^{-6}	14.6×10^{-6}	-	-	10.4×10^{-6}
648.9	16.63×10^{-6}	-	-	-	-	-
700	-	16.3×10^{-6}	15.2×10^{-6}	-	-	10.5×10^{-6}
750	-	17×10^{-6}	15.9×10^{-6}	-	-	-
760	18.38×10^{-6}	-	-	-	-	-
800	-	17.5×10^{-6}	16.4×10^{-6}	15×10^{-6}	-	10.6×10^{-6}
850	-	18.5×10^{-6}	16.7×10^{-6}	-	-	-
871.1	19.42×10^{-6}	-	-	-	-	-
900	-	18.9×10^{-6}	17×10^{-6}	-	-	10.7×10^{-6}
950	-	-	17.2×10^{-6}	-	-	-
962.2	20.7×10^{-6}	-	-	-	-	-
1000	-	-	17.5×10^{-6}	16.6×10^{-6}	9.1×10^{-6}	10.8×10^{-6}
1050	-	-	17.9×10^{-6}	-	-	-
1100	-	-	18×10^{-6}	-	-	10.9×10^{-6}
1175	-	-	-	-	-	11×10^{-6}
1200	-	-	-	-	9.4×10^{-6}	-
1400	-	-	-	-	9.6×10^{-6}	-
1500	-	-	-	-	9.7×10^{-6}	-

Table 5.6: CTE of materials ($^{\circ}C^{-1}$).

Material	A_0 (MPa ⁻ⁿ s ⁻¹)	Q kJ · mol ⁻¹	n at 850°C	n at 1050°C	s
IN-738LC, [62]	6.68×10^{48}	1721	9.96	6.6	-
Praxair CO211, [70]	6.31×10^{-6}	165	2.2	2.2	-
LPPS PWA 276, [71]	1.01×10^{-4}	120	3.47	3.47	-
α - Al ₂ O ₃ , [63]	415.12	325	1.08	1.08	-
YSZ, [73]	0.026	104.5	0.56	0.56	0.67

Table 5.7: Creep properties of materials.

Parameter	Value
Q	27777.4 K
T_0	2423.7 K
n_{ox}	0.332
β	10

Table 5.8: Parameters used in TGO growth calculation. Q , T_0 and n_{ox} were extracted from Ref [46] and β from Refs. [15, 16].

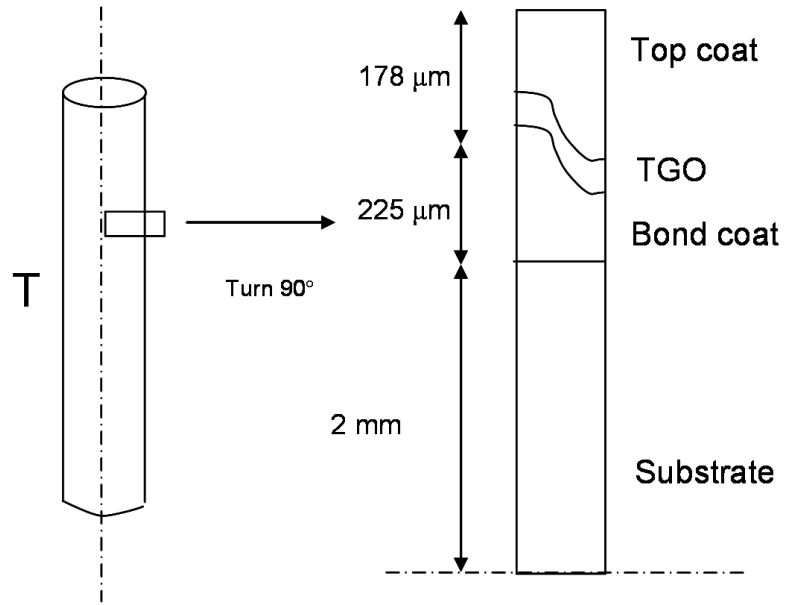


Figure 5.1: Model geometry.

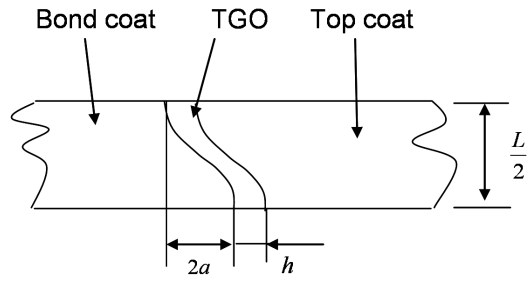


Figure 5.2: Geometric parameters that define the TBC.

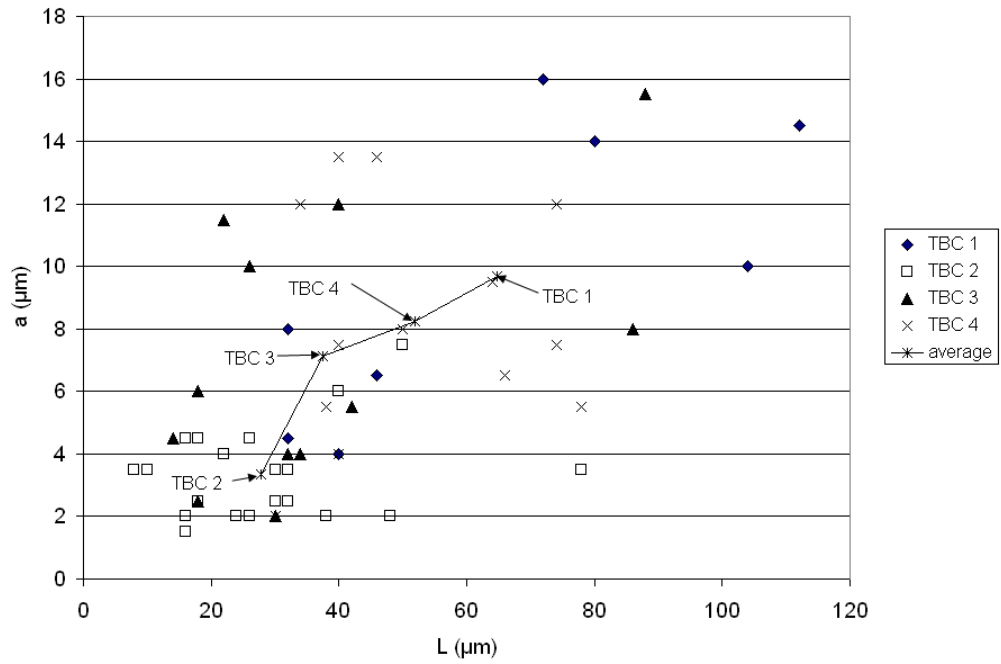


Figure 5.3: Amplitude, a , and wavelength, L , parameters obtained with different manufacturing processes.

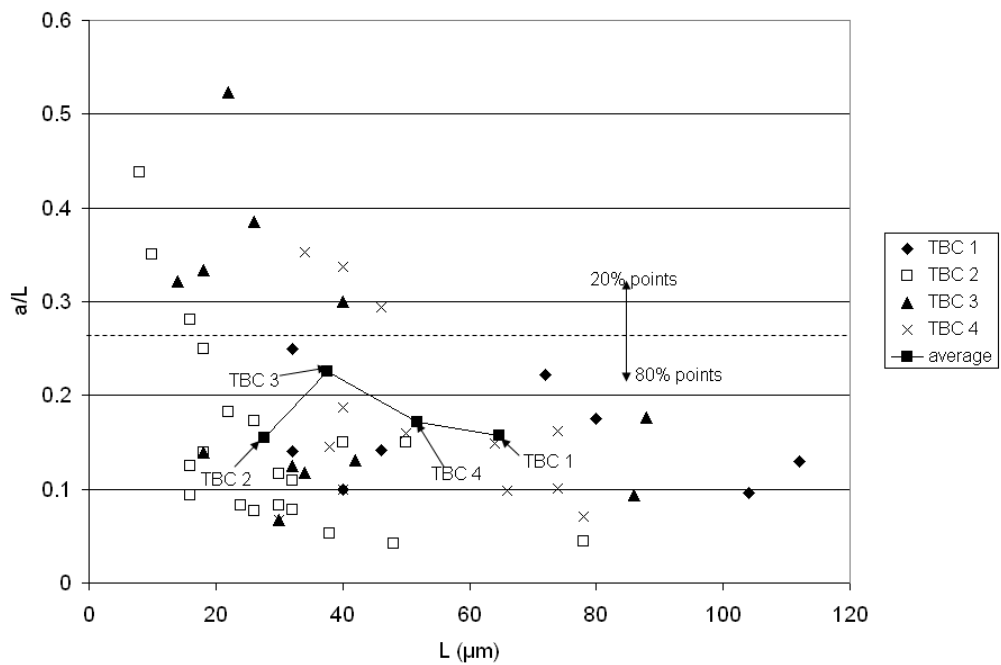


Figure 5.4: $\frac{a}{L}$ vs. L for different manufacturing processes.

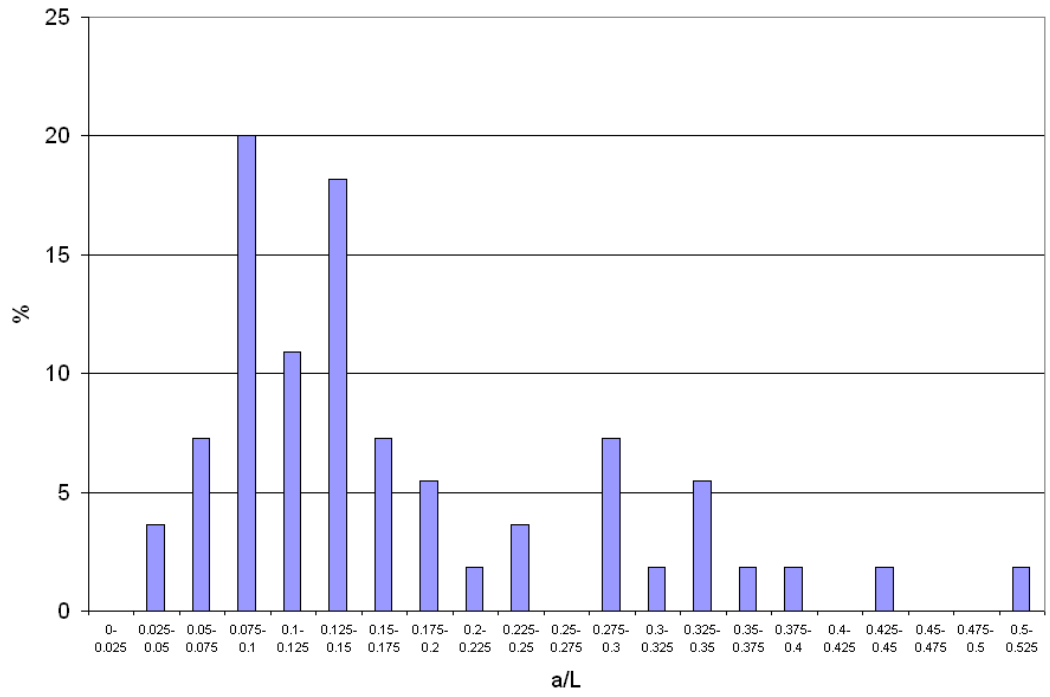


Figure 5.5: $\frac{a}{L}$ distribution.

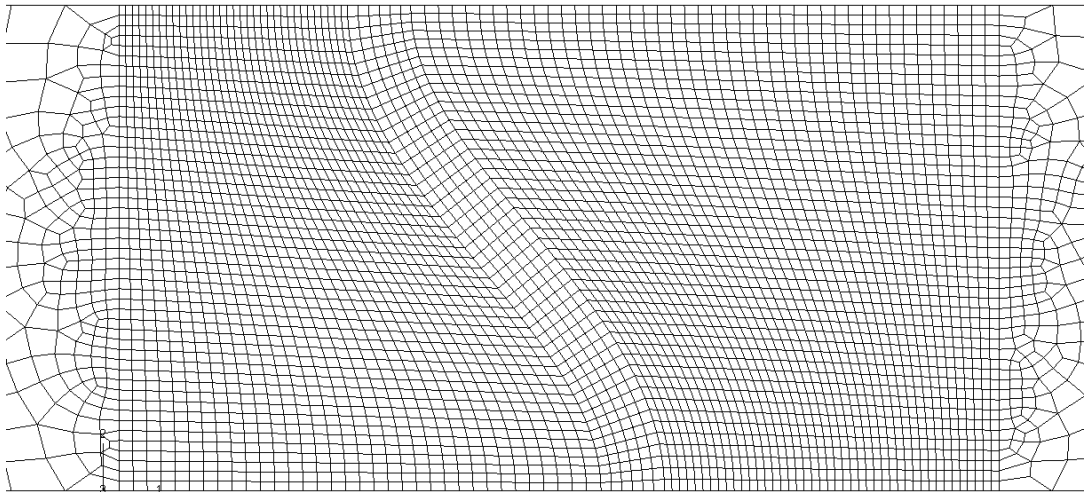


Figure 5.6: Detail of FE mesh.

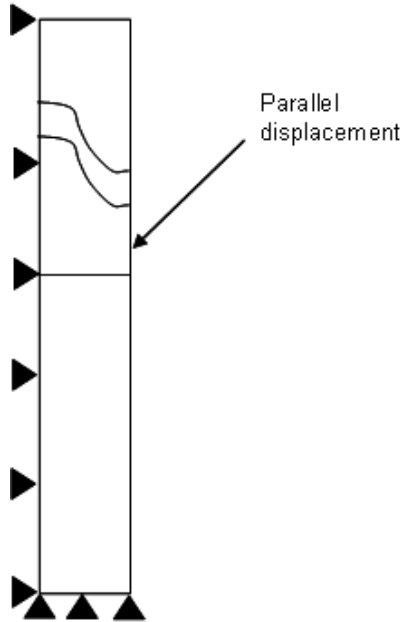


Figure 5.7: Boundary conditions.

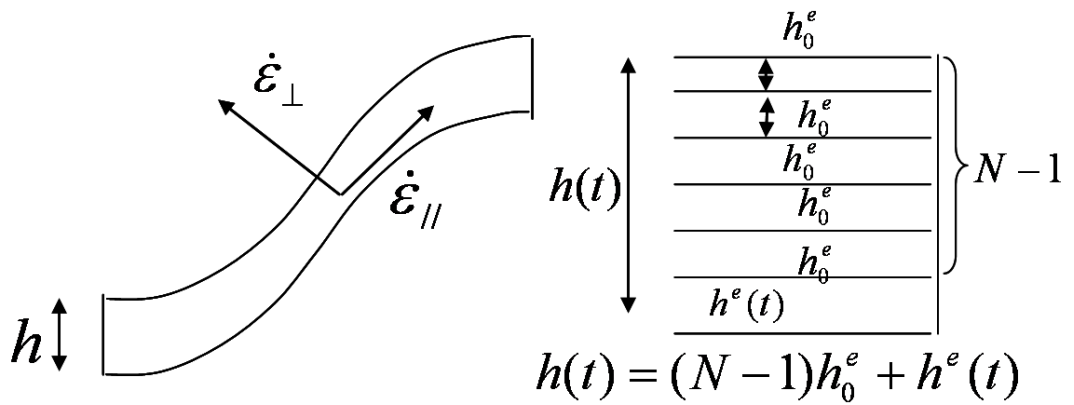


Figure 5.8: Prescribed strains to simulate TGO growth.

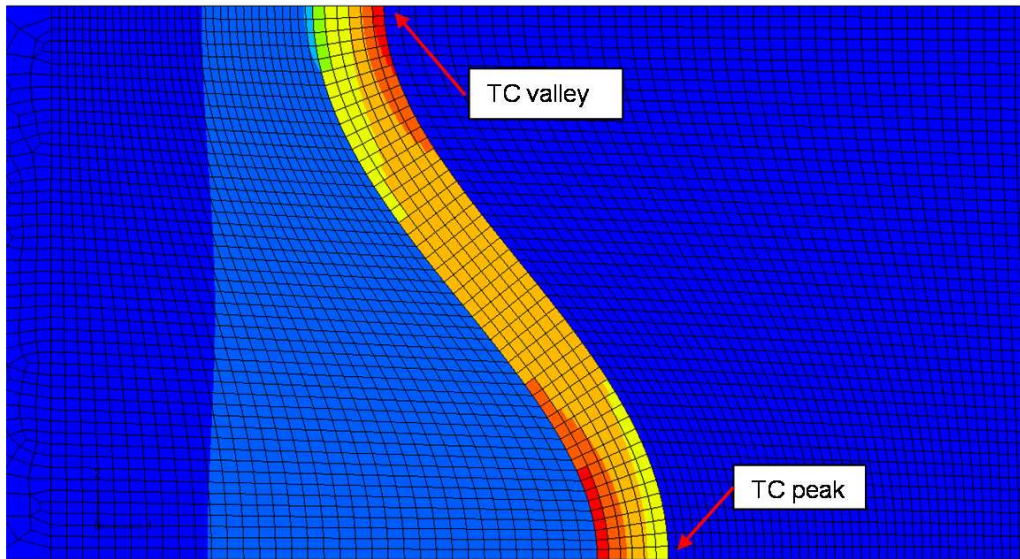


Figure 5.9: TC and BC peak and valley locations.

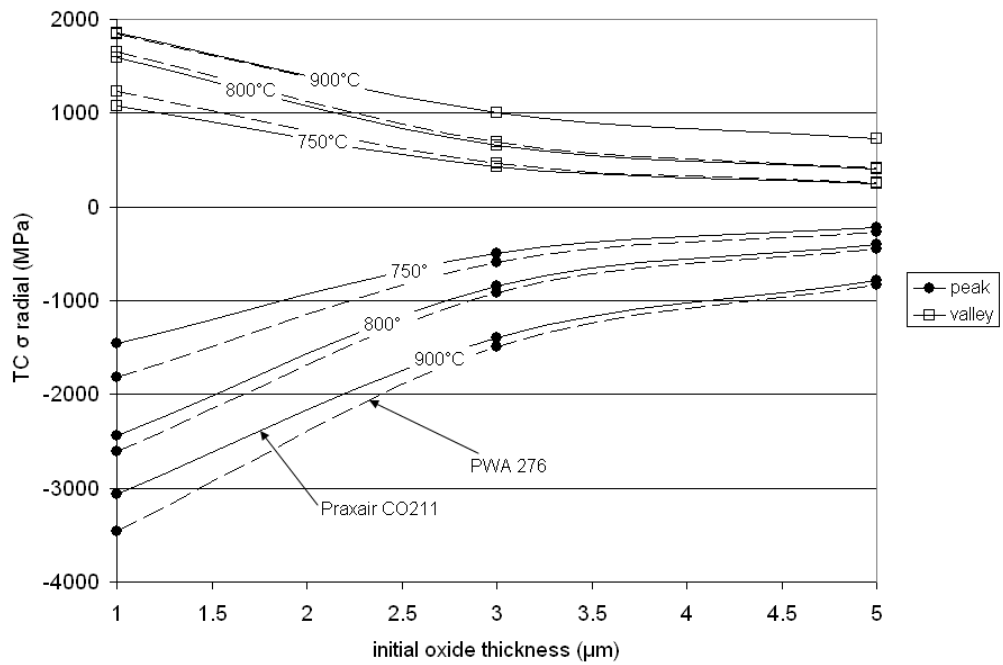


Figure 5.10: TC radial stress at peak and valley locations vs. initial oxide thickness after 1000 h exposure time using a model with $L=46 \mu\text{m}$ and $a=6 \mu\text{m}$.

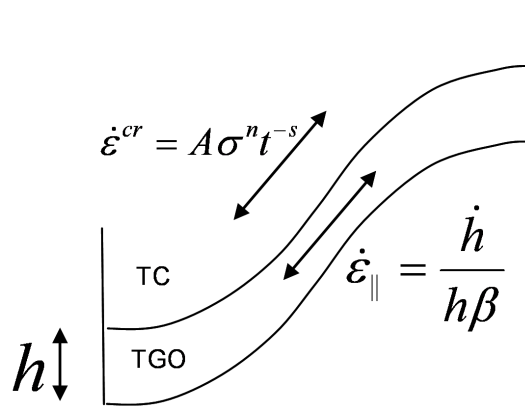


Figure 5.11: Lengthening component of the oxidation strain rate and TC creep strain rate.

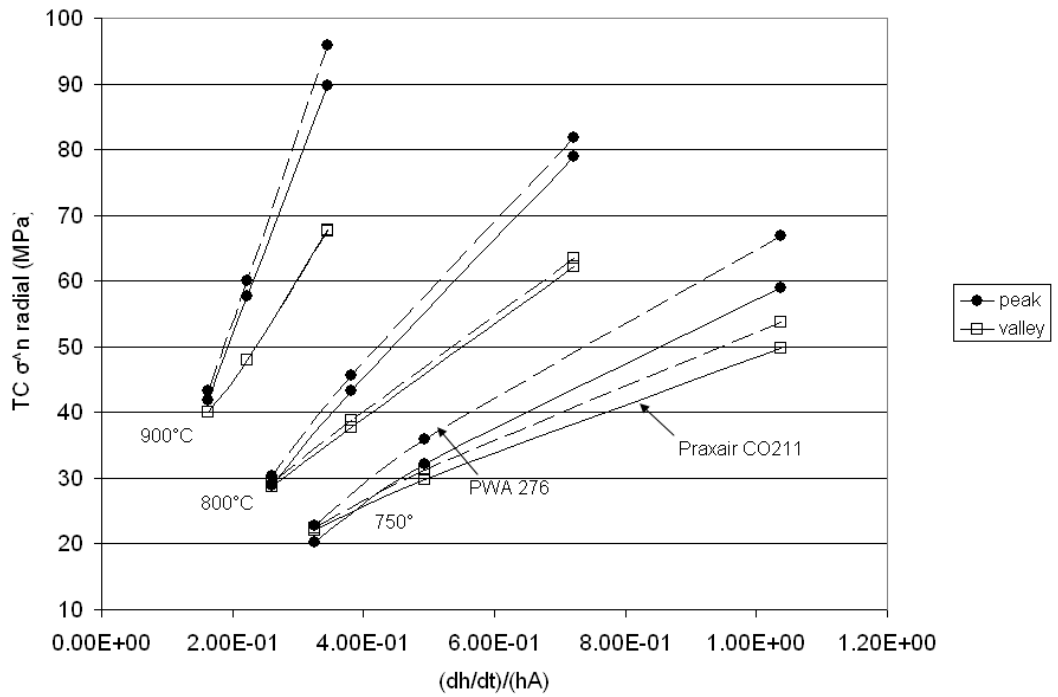


Figure 5.12: σ^n vs. $\frac{\dot{h}}{hA}$ plot of TC stress values after 1000 h exposure time using a model with $L=46 \mu\text{m}$ and $a=6 \mu\text{m}$.

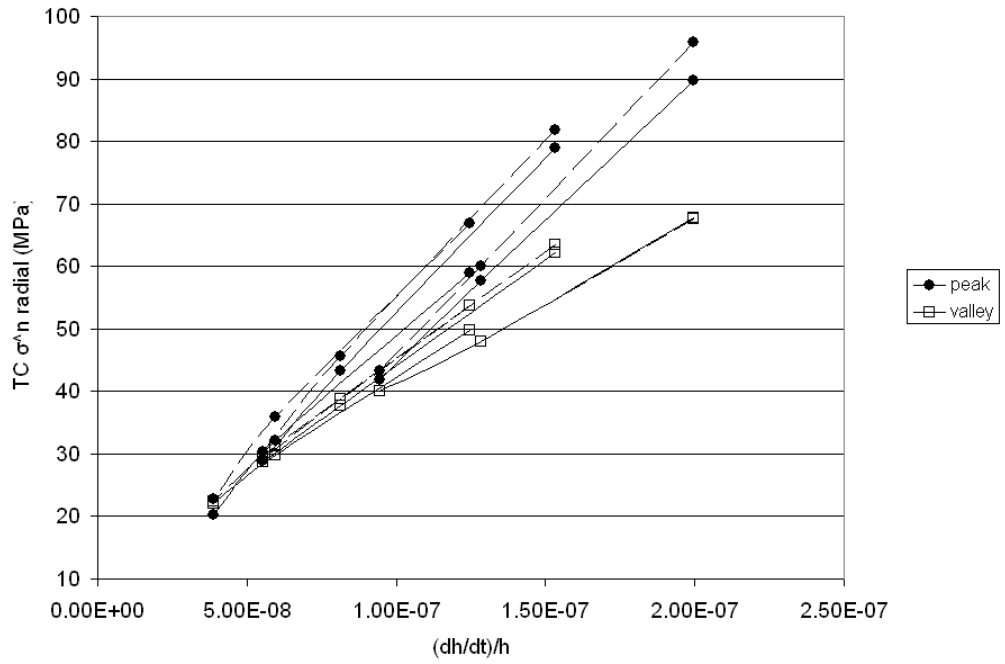


Figure 5.13: σ^n vs. $\frac{\dot{h}}{h}$ plot of TC stress values after 1000 h exposure time using a model with $L=46 \mu\text{m}$ and $a=6 \mu\text{m}$.

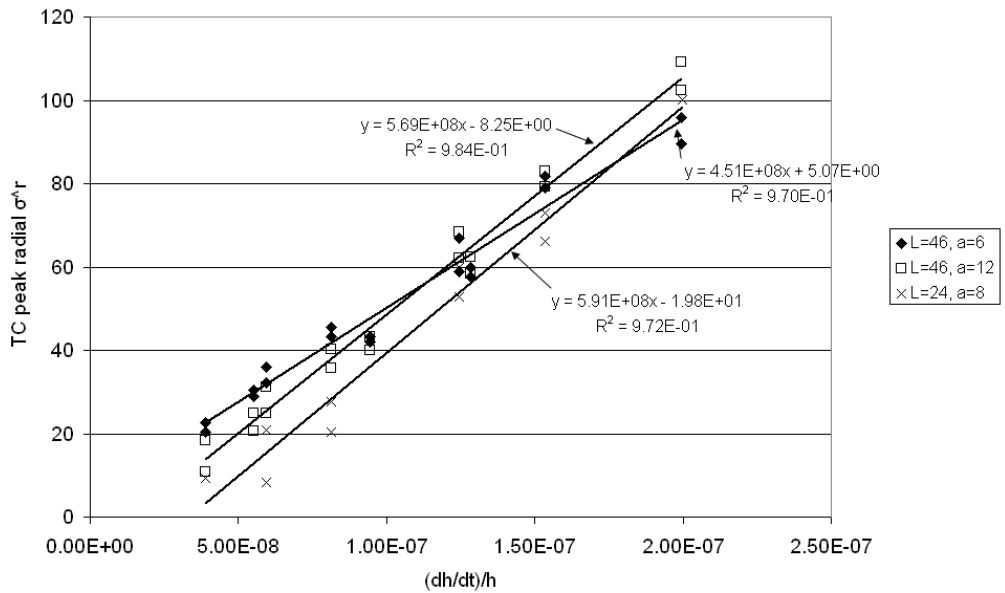


Figure 5.14: σ^n vs. $\frac{\dot{h}}{h}$ plot of TC peak radial stress values after 1000 h exposure time.

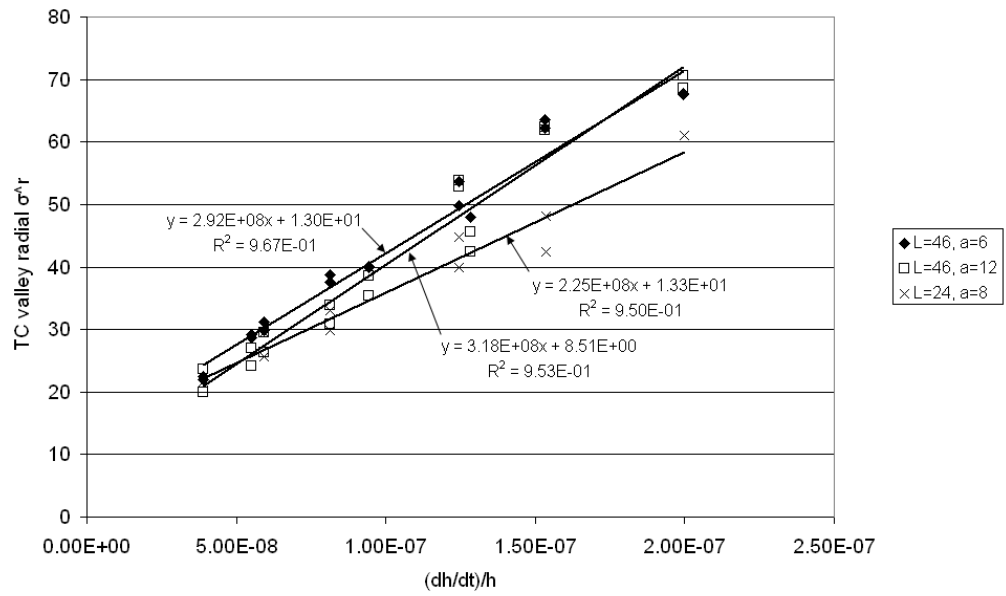


Figure 5.15: σ^n vs. $\frac{\dot{h}}{h}$ plot of TC valley radial stress values after 1000 h exposure time.

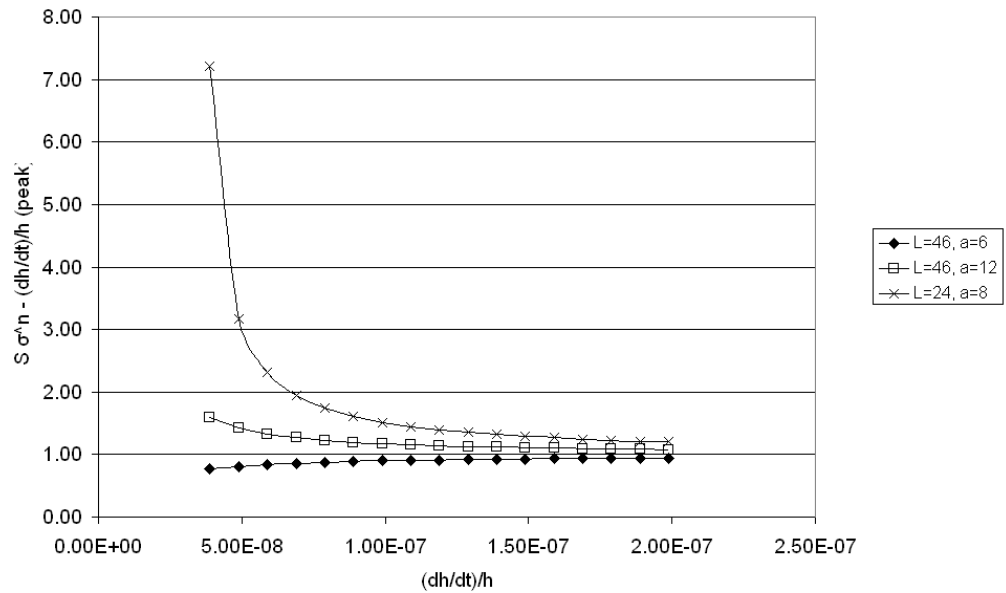


Figure 5.16: σ^n sensitivity with respect to $\frac{\dot{h}}{h}$ for peak location.

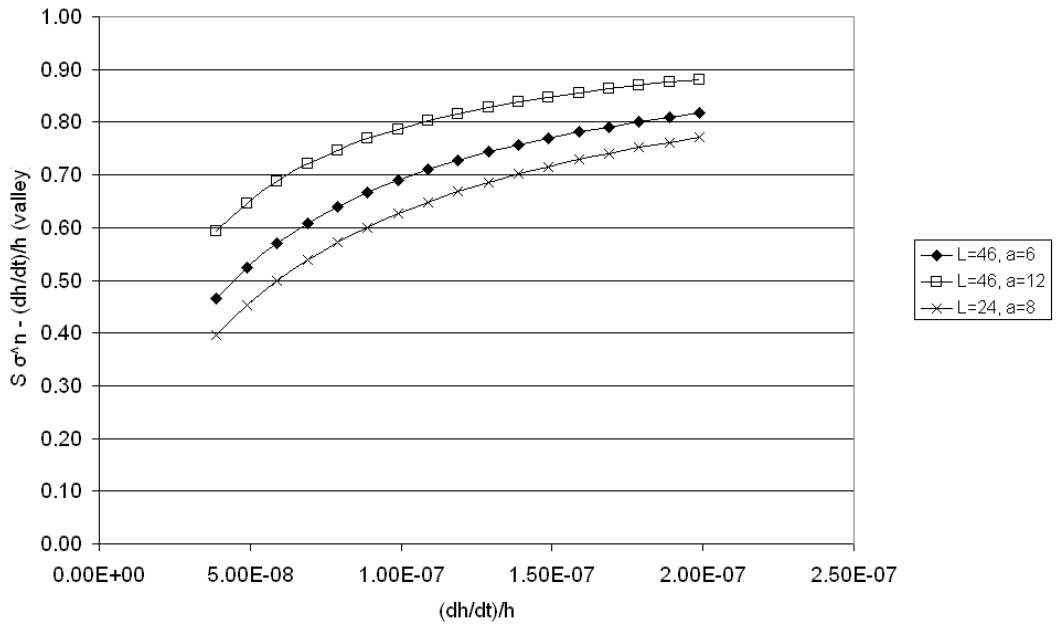


Figure 5.17: σ^n sensitivity with respect to $\frac{\dot{h}}{h}$ for valley location.

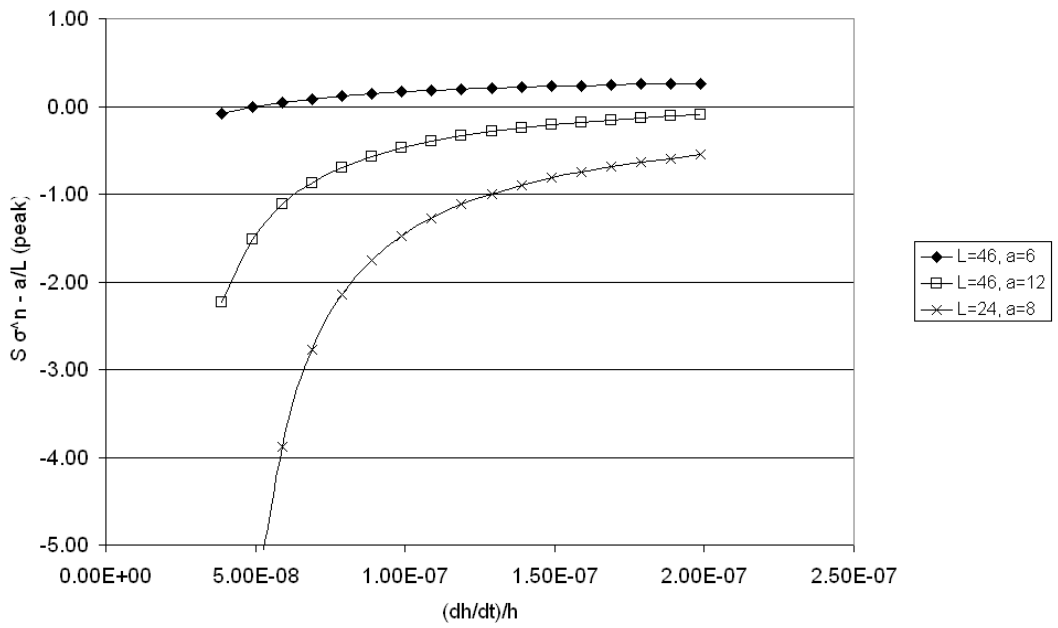


Figure 5.18: σ^n sensitivity with respect to $\frac{a}{L}$ for peak location.

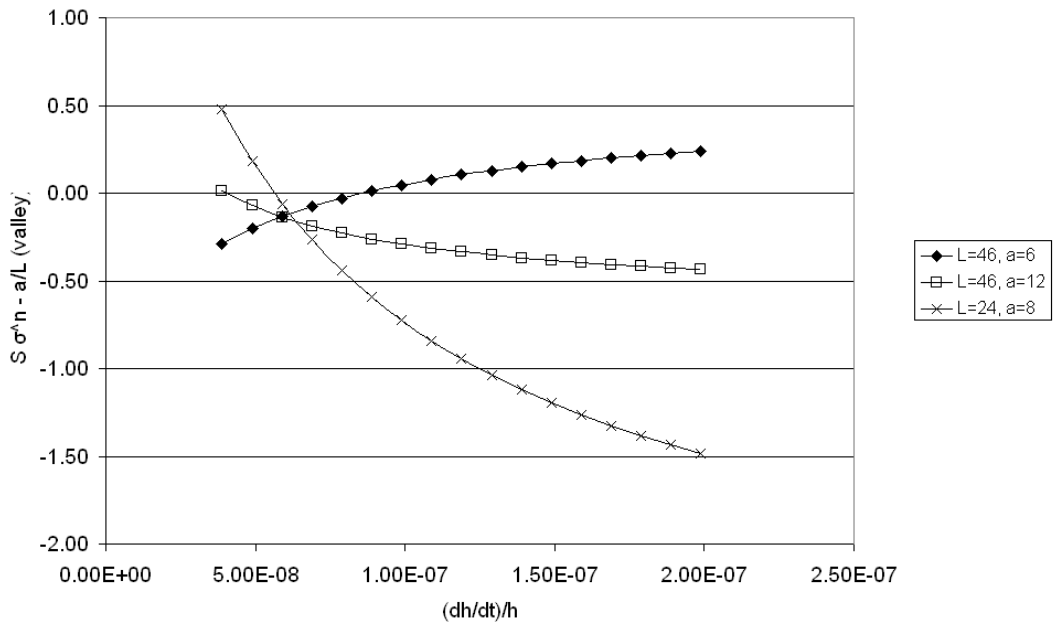


Figure 5.19: σ^n sensitivity with respect to $\frac{a}{L}$ for valley location.

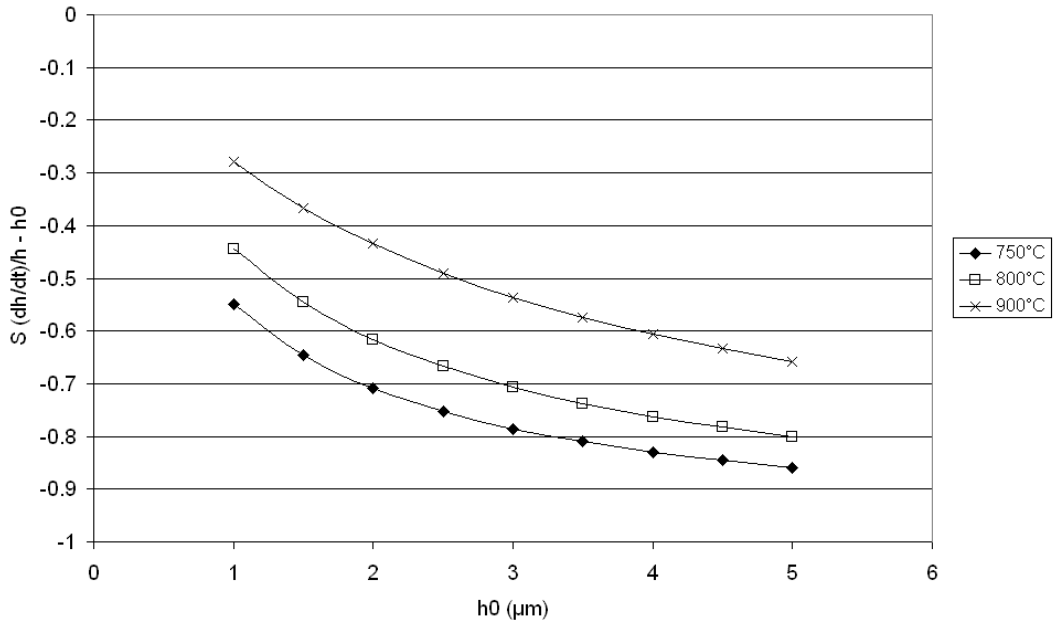


Figure 5.20: $\frac{\dot{h}}{h}$ sensitivity with respect to h_0 .

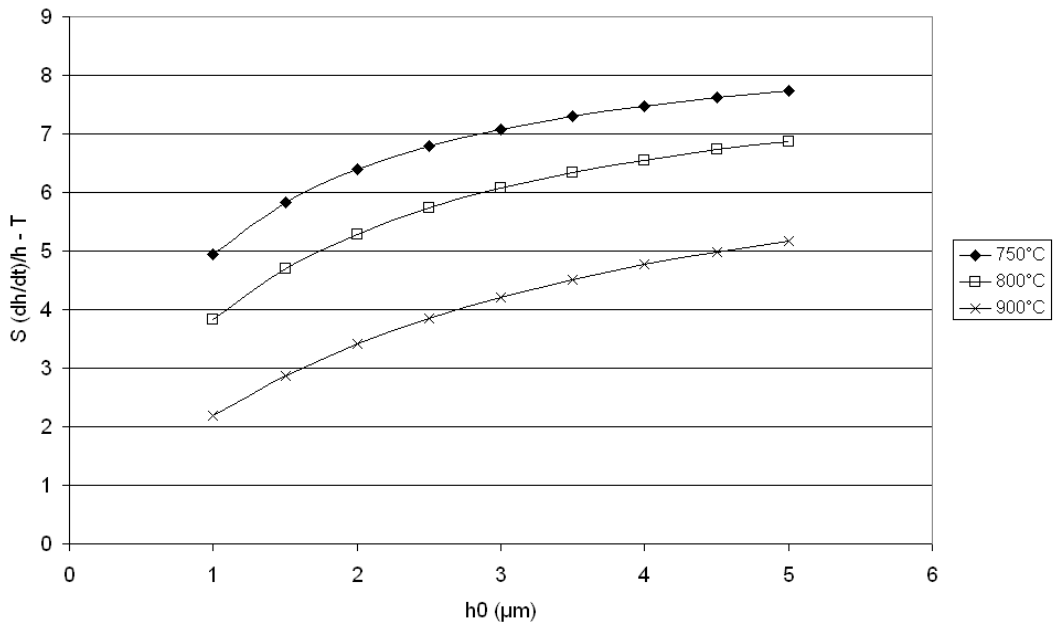


Figure 5.21: $\frac{\dot{h}}{h}$ sensitivity with respect to temperature.

Chapter 6

Self-consistent determination of elastic, thermal and creep behaviour of multiphase alloys

6.1 Introduction

A relevant part of the work done in TBC life assessment techniques has been carried out through the usage of microstructural criteria [36,45,46]. Examples of microstructure-based failure mechanisms are those which assume that coatings fail when a critical value of TGO thickness is achieved.

The TGO growth is caused by two parallel phenomena: the inward oxygen diffusion from the external hot gas stream and the outward diffusion of oxidation-prone elements, mainly aluminium. The interdiffusion of elements through the different layers creates particular zones where some elements or phases may not be present at a certain time instant and different precipitates may have formed instead, hence changing the mechanical properties and behaviour of the material.

The stress analysis of TBCs has been typically carried out by dividing the

TBC system into its constituent layers and considering the material properties within those layers to be homogeneous and dependent on their original microstructure, without taking into account the diffusion interactions and microstructural changes that arise when they are exposed to high temperature. TGO growth has usually been implemented by prescribing an inelastic swelling strain obtained from semi-empirical equations in order to simulate its thickening and lengthening.

This FE modelling technique does not account for the gradual changes in material properties that occur in real situations, i.e. the appearance of depletion zones and the formation of new precipitates that alter the mechanical properties of the materials being considered and induce stresses derived from phase changes.

In this chapter, a method of taking into account results obtained from microstructural analyses of TBC systems in their mechanical behaviour modelling is presented. The self-consistent constitutive model explained in the following sections can be used to model the bond coat and TGO as a material composed of several phases. Results of microstructural calculations are obtained using a computer program that employs the thermodynamic phase calculation technique [78, 79]; these results are then fed to FE analyses that take into account their effect on the material behaviour in Chapters 7 and 8. The applicability of self-consistent models to reproduce the creep behaviour of multiphase alloys is explored in Chapter 7 by means of the comparison of predictions from unit cells and from the constitutive model presented here. The unit cells reproduce the phase proportions of bond coats of different compositions at two different temperatures, which were obtained using thermodynamic phase calculations [78]. Chapter 8 contains full TBCs models in which thermodynamics-based diffusion calculations have been sequentially coupled to FE calculations. The time-dependent microstructure of the bond coat, which represents its degradation

and oxide growth, defines its mechanical behaviour and oxide growth according to the theory explained in this chapter.

Due to the ranges of stress and temperatures to which TBCs are exposed, the main material properties to take into account are the elastic and creep properties of the composing layers and individual phases.

A very simple method to estimate the elastic properties of a multiphase material or alloy is the rule of mixtures, but it is not very precise when the precipitate structure of an alloy is considered. The use of a modified version of the rule of mixtures for the creep properties does not seem very realistic either. The self-consistent models explained in this chapter make use of Eshelby's [80] inclusion technique to obtain homogenization relations applicable for both the calculation of elastic constants and for the modelling of inelastic behaviours such as creep. A mean-field method used to model the thermal expansion of a continuum material containing a uniform dispersion of particles [81] will be presented as well. However, the model proposed in this chapter for thermal expansion is based on the self-consistency hypothesis [27, 82–84], although it makes use of some of the techniques used in Ref. [81].

The theory contained in this paper sets the background of the calculations carried out in Chapters 7 and 8; the first of these focuses on the validity of the models to represent creep and the second on developing a comprehensive framework that integrates microstructural effects into the mechanical modelling of TBCs exposed to elevated temperatures.

6.2 Eshelby's inclusion technique - homogenization relations

Eshelby [80, 85] postulated a model that allowed calculation of the stress and strain fields caused by a solid inclusion in a solid matrix. The strain field within the inclusion is constrained to be uniform across the inclusion. Figure 6.1 shows the geometry considered for the derivation of Eshelby's technique, which consists of an infinite matrix with a single inclusion within it.

The domain containing the aggregate material is denoted by D and is assumed to be infinite in extent. The Ω domain corresponds to the inclusion and $D - \Omega$ to the matrix material. The inclusion can be considered to be composed of the same material as the matrix, defining what is known as the *homogeneous inclusion* problem, or of a different material, defining the problem usually referred to as the *inhomogeneous inclusion* or *inhomogeneity* problem.

6.2.1 Homogeneous inclusion

The first case to be studied is the homogeneous inclusion problem. In order to understand the stresses and strains involved, Figure 6.2 is used [86] to define the magnitudes used in the solution of the problem. First, the material contained in Ω is extracted from the domain D . Then, it is subjected to a stress-free strain, e.g. a thermal strain, also called an *eigenstrain*, denoted by e_{ij}^* . Next, the part of material extracted from the domain is subjected to surface stresses to return it to its original shape and finally re-inserted into the original continuum. The surface stresses are then released and the inclusion will deform and accommodate within the continuum medium, inducing both stresses and strains within it and in the surrounding material. Once this process has been carried out, the stress

within the inclusion is:

$$\sigma_{ij} = C_{ijkl} (\epsilon_{kl} - \epsilon_{kl}^*) \quad (6.1)$$

where C_{ijkl} is the elastic stiffness tensor of the material, which is defined using Lamé's elastic constants, and ϵ_{kl} the total strain. The $(\epsilon_{kl} - \epsilon_{kl}^*)$ term represents the elastic strain tensor as it is the result of deducting the eigenstrain from the total strain. The total strain and eigenstrain can be related through Eshelby's tensor S_{klmn} , which depends on the shape of the considered inclusion and the material Poisson's ratio, through the expression:

$$\epsilon_{kl} = S_{klmn} \epsilon_{mn}^* \quad (6.2)$$

Various values of the S_{klmn} tensors are available in the literature [80, 85, 86] for a variety of inclusion shapes. Equations 6.1 and 6.2 allow calculation of the stress within a homogeneous inclusion after the application of a stress-free strain ϵ_{ij}^* .

6.2.2 Inhomogeneous inclusion

The method applied for the calculation of the stresses and strains within homogeneous inclusions can be extended to consider an inclusion of a different material, usually referred to as an *inhomogeneous inclusion* or *inhomogeneity*. When a matrix containing an inhomogeneity is subjected to a uniform stress, the presence of the inclusion disturbs the stress and strain fields in its vicinity. The external stress manifests itself as a uniform strain field within the matrix, ϵ_{ij}^0 . The first step towards the solution of this problem is the consideration of the *equivalent homogeneous inclusion*, which is defined as a homogeneous inclusion subjected to the same strain derived from the externally applied load, ϵ_{ij}^0 , with the same stresses and strains within it, so they are statically equivalent, but with the elastic properties of the matrix. The stress within the equivalent

homogeneous inclusion, when a stress-free strain ϵ_{ij}^* is applied, is:

$$\sigma_{ij} = C_{ijkl} (\epsilon_{kl} + \epsilon_{kl}^0 - \epsilon_{kl}^*) \quad (6.3)$$

The inhomogeneous inclusion is stress free before the application of the external load. After the loading process, it will be subjected to the strain derived from it, ϵ_{ij}^0 , which will be distorted by the inhomogeneous elastic behaviour of the inclusion. The strain tensor due to the distortion of the inhomogeneity must be equal to the strain tensor in the equivalent homogeneous inclusion, since they have to be interchangeable and fit perfectly one in the other. Hence, the strain in the inhomogeneity is $\epsilon_{ij} + \epsilon_{ij}^0$. If the elastic constants of the inhomogeneity are denoted C_{ijkl}^m , the stress developed under these conditions is:

$$\sigma_{ij}^m = C_{ijkl}^m (\epsilon_{kl} + \epsilon_{kl}^0) \quad (6.4)$$

Combining the equivalent inclusion stress from Equation 6.3 and the inhomogeneity stress from Equation 6.4, the following expression is obtained:

$$C_{ijkl}^m (\epsilon_{kl} + \epsilon_{kl}^0) = C_{ijkl} (\epsilon_{kl} + \epsilon_{kl}^0 - \epsilon_{kl}^*) \quad (6.5)$$

Equation 6.5 states the equivalence criterion between a homogeneous and an inhomogeneous inclusion when an external load is applied. The strain in both inclusions has to be equal to make sure that they occupy the same volume and have the same shape within the continuum matrix. Equation 6.5 is obtained by directly equating the stress tensor for both inclusion types, in order to satisfy the equilibrium condition, i.e. the inhomogeneous inclusion and the equivalent homogeneous inclusion are totally interchangeable.

Using the results obtained for the homogeneous inclusion problem stated in Equation 6.2, Equation 6.5 can be rewritten as:

$$C_{ijkl}^m (S_{klmn} \epsilon_{mn}^* + \epsilon_{kl}^0) = C_{ijkl} (S_{klmn} \epsilon_{mn}^* + \epsilon_{kl}^0 - \epsilon_{kl}^*) \quad (6.6)$$

The only unknown term in Equation 6.6 is ϵ_{ij}^* . ϵ_{ij}^0 can be obtained from the externally applied load using

$$\sigma_{ij}^0 = C_{ijkl}\epsilon_{kl}^0 \quad (6.7)$$

where σ_{ij}^0 represents the externally applied load. Equation 6.6 provides a method of calculating the stress-strain state of an inhomogeneous inclusion, which can be used to model multiphase alloys, as explained in the following sections.

6.3 Calculation of the elastic moduli of heterogeneous materials

The elastic properties of a composite formed by N phases were studied by Budiansky [82] using Eshelby's inclusion technique [80] to predict the strains in the precipitates. The material considered to develop this method is a solid containing a uniform spatial distribution of nearly-spherical precipitates of different phases of similar shape. The volume of each individual phase is denoted V_i and its volume fraction $f^i = \frac{V_i}{V}$. The matrix is the N -th phase and the remaining phases represent precipitates or reinforcements added to the matrix to increase its mechanical properties.

In order to obtain the elastic properties of the multiphase material, a cube of the heterogeneous aggregate is considered. An external shear load consisting of a $\sigma_{12} = \tau^0$ stress is applied on its surface. The shear strain γ_{12} is not uniform throughout the cube, but the following definition of the shear modulus is used:

$$G = \frac{\tau^0}{\bar{\gamma}} \quad (6.8)$$

where $\bar{\gamma}$ is the average value of γ_{12} , defined as

$$\bar{\gamma} = \frac{1}{V} \int_V \gamma_{12} dV \quad (6.9)$$

The average value of σ_{12} is τ^0 and the elastic strain energy is exactly [82]:

$$E = \frac{1}{2} \int_V \tau^0 \gamma_{12} dV = \frac{1}{2} V \tau^0 \bar{\gamma} = \frac{V (\tau^0)^2}{2G} \quad (6.10)$$

And, as a function of individual phases,

$$\begin{aligned} E &= \frac{1}{2} \int_V \frac{\tau^0 \sigma_{12}}{G^N} dV + \frac{1}{2} \int_V \tau^0 \left(\gamma_{12} - \frac{\sigma_{12}}{G^N} \right) dV \\ &= \frac{V (\tau^0)^2}{2G^N} + \frac{\tau^0}{2} \sum_{i=1}^N \int_{V_i} \left(\gamma_{12} - \frac{\sigma_{12}}{G^N} \right) dV \\ &= \frac{V (\tau^0)^2}{2G^N} + \frac{\tau^0}{2} \sum_{i=1}^N \int_{V_i} \left(\gamma_{12} - \frac{\gamma_{12} G^i}{G^N} \right) dV \\ &= \frac{V (\tau^0)^2}{2G^N} + \frac{\tau^0}{2} \sum_{i=1}^N \left(1 - \frac{G^i}{G^N} \right) \int_{V_i} \gamma_{12} dV \\ &= \frac{V (\tau^0)^2}{2G^N} + \frac{\tau^0}{2} \sum_{i=1}^N \left(1 - \frac{G^i}{G^N} \right) V_i \bar{\gamma}_i \\ &= \frac{V (\tau^0)^2}{2} \left[\frac{1}{G^N} + \sum_{i=1}^N f^i \left(1 - \frac{G^i}{G^N} \right) \left(\frac{\bar{\gamma}_i}{\tau^0} \right) \right] \end{aligned} \quad (6.11)$$

with $\bar{\gamma}_i$ being the average value of γ_{12} in the i th phase:

$$\bar{\gamma}_i = \frac{1}{V_i} \int_{V_i} \gamma_{12} dV \quad (6.12)$$

Equating Equations 6.10 and 6.11 for the elastic strain energy:

$$\frac{V (\tau^0)^2}{2G} = \frac{V (\tau^0)^2}{2} \left[\frac{1}{G^N} + \sum_{i=1}^{N-1} f^i \left(1 - \frac{G^i}{G^N} \right) \left(\frac{\bar{\gamma}_i}{\tau^0} \right) \right] \quad (6.13)$$

The expression for the shear modulus of the composite material is obtained from simplification of Equation 6.13:

$$\frac{1}{G} = \frac{1}{G^N} + \sum_{i=1}^{N-1} f^i \left(1 - \frac{G^i}{G^N} \right) \left(\frac{\bar{\gamma}_i}{\tau^0} \right) \quad (6.14)$$

The only unknown value in Equation 6.14 is the average shear strain for each individual phase, $\bar{\gamma}_i$, which can be obtained using Eshelby's technique [80] to calculate the average strain in an inhomogeneity. $\bar{\gamma}_i$ corresponds to the shear stress in an inhomogeneous inclusion in an infinite matrix subjected to an

external load $\sigma_{12} = \tau^0$. The matrix stiffness is equated to that of the composite material, which is unknown yet, in order to simulate a continuum dispersion of inclusions, as usually assumed in self-consistent models. The solution for the strain within the inclusion under these conditions is:

$$\bar{\gamma}_i = \frac{\tau^0}{G + \beta_t (G^i - G)} \quad (6.15)$$

with

$$\beta_t = \frac{2(4 - 5\nu)}{15(1 - \nu)} \quad (6.16)$$

The complete derivation of Equations 6.15 and 6.16 is explained in Appendix B. Substituting Equation 6.15 back into Equation 6.14, the expression for the shear modulus of the multiphase aggregate is

$$\frac{1}{G} = \frac{1}{G^N} + \sum_{i=1}^{N-1} f^i \left(1 - \frac{G^i}{G^N}\right) \left(\frac{f^i}{G + \beta_t (G^i - G)}\right) \quad (6.17)$$

Equation 6.17 makes it possible to calculate the shear modulus of a multiphase material from the shear moduli of the phases present in it and from their volume proportions. It is an implicit equation that requires the use of numerical methods such as that of Newton and Raphson for its solution. Although one of the phases has been identified as a “matrix”, the self-consistent approach is used, which implies that the unknown aggregate properties are used in Equations 6.15 and 6.16, leading eventually to implicit equations.

If the process followed through Equations 6.8 - 6.12 is applied to the bulk modulus, $K = \frac{p^0}{\theta}$, with θ being the average volumetric contraction and p^0 the applied hydrostatic pressure on the surface, the following equation is obtained:

$$\frac{1}{K} = \frac{1}{K^N} + \sum_{i=1}^{N-1} f^i \left(1 - \frac{K^i}{K^N}\right) \left(\frac{\bar{\theta}_i}{p^0}\right) \quad (6.18)$$

where $\bar{\theta}_i$ is the average volume contraction in an inhomogeneous inclusion, which can be estimated using Eshelby’s technique as

$$\bar{\theta}_i = \frac{p^0}{K + \beta_n (K^i - K)} \quad (6.19)$$

and substituted back into Equation 6.18 yielding

$$\frac{1}{K} = \frac{1}{K^N} + \sum_{i=1}^{N-1} f^i \left(1 - \frac{K^i}{K^N} \right) \left(\frac{f^i}{K + \beta_n (K^i - K)} \right) \quad (6.20)$$

where β_n corresponds to

$$\beta_n = \frac{1 + \nu}{3(1 - \nu)} \quad (6.21)$$

For further information on the calculation of $\bar{\theta}_i$ and β_n refer to Appendix C. The elastic constants of an isotropic multiphase material can be calculated using Equations 6.16, 6.17, 6.20 - 6.22, provided the stiffnesses of the phases that compose it and their volume proportions are known. Since isotropic elasticity is defined by two constants, the Poisson's ratio of the aggregate material can be expressed as

$$\nu = \frac{3K - 2G}{6K + 2G} \quad (6.22)$$

Once again, Equations 6.20 and 6.17 are implicit equations that need to be solved using numerical methods such as that of Newton and Raphson.

In the derivation of Equations 6.17 and 6.20, a phase was assumed to be the "matrix", even if no further hypotheses were made regarding its phase proportion, which implies that any of the phases may arbitrarily be chosen as the matrix. This fact suggests that an alternative form of both equations might be found. More specifically, Equations 6.17 and 6.20 can be simplified through algebraic manipulation as [82]:

$$\sum_{i=1}^N \frac{f^i}{1 + \beta_t \left(\frac{G^i}{G} - 1 \right)} = 1 \quad (6.23)$$

$$\sum_{i=1}^N \frac{f^i}{1 + \beta_n \left(\frac{K^i}{K} - 1 \right)} = 1 \quad (6.24)$$

These forms of the equations show that they are symmetrical in any phase and that the choice of which phase is assumed to be the matrix does not alter the

result of the calculation when a certain phase proportion is fixed, as expected since no further assumption regarding the “matrix” was made in the development of Equations 6.17 and 6.20. They suggest the existence of an alternative derivation of the equations, without the need to assume a “matrix” phase, using directly the inhomogeneity strain tensors specified in Equations 6.15 and 6.19, which were obtained using Eshelby’s technique [80]. From Equation 6.15, the average shear strain in an inclusion can be expressed as:

$$\bar{\gamma}_i = \frac{\tau^0}{G} \left[\frac{1}{1 + \beta_t \left(\frac{G^i}{G} - 1 \right)} \right] \quad (6.25)$$

and the average strain in the multiphase material is:

$$\bar{\gamma} = \frac{\tau^0}{G} = \sum_{i=1}^N f^i \bar{\gamma}_i \quad (6.26)$$

The combination of Equations 6.8 and 6.25 provides a straightforward method of deriving Equation 6.23. Similarly, the volume expansion in an inhomogeneous inclusion is:

$$\bar{\theta}_i = \frac{p^0}{K} \left[\frac{1}{1 + \beta_n \left(\frac{K^i}{K} - 1 \right)} \right] \quad (6.27)$$

Equation 6.24 can be directly obtained from

$$\bar{\theta} = \frac{p^0}{K} = \sum_{i=1}^N f^i \bar{\theta}_i \quad (6.28)$$

6.4 Calculation of the coefficient of thermal expansion of heterogeneous materials

Wakashima *et al.* [81] presented a method of calculating the thermal expansion coefficient of heterogeneous solids with embedded inclusions of various shapes. The method uses the concept of *mean-field stress* developed by Mori and Tanaka

[87] when calculating the strain within an inclusion in a matrix containing a dispersion of particles.

According to Mori and Tanaka [87], the average constrained stress, ϵ_{ij}^m , in any inclusion of the phase m is,

$$\epsilon_{ij}^m = \epsilon_{ij}^{m'} + \bar{\epsilon}_{ij}^{m''} \quad (6.29)$$

where $\epsilon_{ij}^{m'}$ is the constrained strain for a single inclusion as obtained by Eshelby [80] and the m superscript refers to an inclusion made of a material denoted m . Mori and Tanaka [87] extended Eshelby's work to consider not just a single inclusion but a spatially uniform dispersion of particles within a continuum matrix, originating the methods known as *mean-field methods*. Since a dispersion of particles instead of a single inclusion was modelled, their effect on the matrix average stress and strain was no longer negligible. They considered that an additional strain term, $\bar{\epsilon}_{ij}^{m''}$, which represents the average strain due to the presence of the remaining inclusions and the free boundary, had to be superposed onto the single inclusion strain, as stated in Equation 6.29. This term is entirely elastic and assumed to be constant in and around the inclusion. The constrained strain, according to Eshelby, is

$$\epsilon_{ij}^{m'} = S_{ijkl} \epsilon_{kl}^* \quad (6.30)$$

The average strain in the matrix is $\bar{\epsilon}_{ij}^{m''}$, which implies that the average stress developed in it is

$$\sigma_{ij} = C_{ijkl} \bar{\epsilon}_{ij}^{m''} \quad (6.31)$$

The stress in the inclusion is obtained taking into account that ϵ_{ij}^* is a stress-free strain applied to a homogeneous inclusion

$$\sigma_{ij}^m = C_{ijkl} (\epsilon_{kl}^m - \epsilon_{kl}^*) \quad (6.32)$$

If there is no external load and the inclusion is assumed to be homogeneous,

the integration of the stress in the volume of the aggregate yields

$$(1 - f^m) \bar{\epsilon}_{ij}^{m''} + f^m (\epsilon_{ij}^m - \epsilon_{ij}^*) = 0 \quad (6.33)$$

Combining Equations 6.33, 6.30 and 6.29, the total strain in an inclusion when a finite dispersion of particles within a continuum matrix is considered is

$$\epsilon_{ij}^m = (1 - f^m) S_{ijkl} \epsilon_{kl}^* + f^m \epsilon_{ij}^* \quad (6.34)$$

Equation 6.34 contains additional terms that differentiate the single inclusion approach, as used in Section 6.3 and developed originally by Eshelby [80], and the mean-field method. In this case the strain within an inclusion is defined by Equation 6.34, as opposed to Equation 6.2, the differences arising from the consideration of the average strain produced by the remaining inclusions and the presence of the aggregate free boundary.

In the case of an inhomogeneous inclusion, i.e. an inclusion with properties different from those of the matrix, the equivalent inclusion technique provides the equation

$$C_{ijkl} (\epsilon_{kl}^m - \epsilon_{kl}^*) = C_{ijkl}^m (\epsilon_{kl}^m - e_{kl}^{*m}) \quad (6.35)$$

which is obtained by equating the stress in the inhomogeneity and in the equivalent homogeneous inclusion and considering that the total strains to which both inclusions are subjected are equal, i.e. ϵ_{ij}^m , even though they originate from different eigenstrains. Equation 6.35 is slightly different from Equation 6.5, as it does not consider the presence of a strain caused by an externally applied load, and the right hand side, which corresponds to the stress calculation of the inhomogeneous inclusion, contains an eigenstrain that can be directly formulated in terms of the CTEs of matrix and inclusion and the temperature increment.

It can be shown that the overall strain experienced by the aggregate is [81,87]:

$$\bar{\epsilon}_{ij} = f^m \epsilon_{ij}^* \quad (6.36)$$

which allows the formulation of the equations developed by Wakashima *et al.* [81] for the calculation of CTEs of various materials.

6.4.1 Application to the calculation of CTE of multiphase materials

Section 6.4 contains an explanation of the application of mean-field models to the calculation of the strains in inclusions when these form a non-dilute dispersion within a continuum matrix. Wakashima *et al.* [81] used mean-field models [87] to calculate the CTE of heterogeneous materials with inclusions of various shapes. One limitation in their model is the consideration of two phases, the matrix and one type of inclusions.

Since the definition of the background average stress, $\bar{\epsilon}_{ij}^{m''}$, is not totally clear when more than two phases are considered, another approach to include the effect of non-dilute dispersions is to use self-consistent models, i.e. to replace the properties of the “matrix” as defined in Eshelby’s technique with the properties of the unknown aggregate material, generally obtaining implicit equations that require numerical solution.

The method described here is based on the self-consistence hypothesis, but making use of some general equations used by Wakashima *et al.* [81]. It is initially considered that a multiphase material similar to the aggregate described in Section 6.3 is subjected to a uniform temperature increase ΔT . Under those conditions, the eigenstrain applied to an inhomogeneous inclusion made of material m is

$$\epsilon_{ij}^{*m} = (\alpha^m - \alpha) \Delta T \delta_{ij} \quad (6.37)$$

where α^m is the coefficient of thermal expansion of the m phase, α is the CTE of the aggregate material and δ_{ij} is the Kronecker delta. Since $(\alpha^m - \alpha)$ is being used, ϵ_{ij}^{*m} represents a stress-free strain applied to the inhomogeneous inclusion,

as opposed to the eigenstrain used in Eshelby's technique, which is applied to the equivalent homogeneous inclusion, represented by ϵ_{ij}^* in Equation 6.35.

The total strain in an inclusion is obtained superposing the thermal expansion of the aggregate and its particular differential strain with respect to the aggregate,

$$\epsilon_{ij}^{m,total} = \alpha \Delta T \delta_{ij} + \epsilon_{ij}^m \quad (6.38)$$

If the total strain is integrated in the volume the aggregate occupies,

$$\epsilon_{ij}^{total} = \alpha \Delta T \delta_{ij} + \sum_g f^g \epsilon_{ij}^g \quad (6.39)$$

The definition of coefficient of thermal expansion states that

$$\epsilon_{ij}^{total} = \alpha \Delta T \delta_{ij} \quad (6.40)$$

which, combined with Equation 6.39, provides the equation for the calculation of α ,

$$\sum_g f^g \epsilon_{ij}^g = 0 \quad (6.41)$$

Since thermal expansion only produces volume changes that manifest themselves as direct strains, one component of the tensor in Equation 6.41 is considered:

$$\sum_g f^g \epsilon_{11}^g = 0 \quad (6.42)$$

The calculation of the ϵ_{11}^m strain in Equation 6.42 is carried out using the equivalent homogeneous inclusion as in Equation 6.35. If a derivation similar to that in Appendix C is undertaken, the resulting equation is

$$K \left[\frac{1 + \nu}{3(1 - \nu)} \epsilon_{11}^* - \epsilon_{11}^* \right] = K^m \left[\frac{1 + \nu}{3(1 - \nu)} \epsilon_{11}^* - \epsilon_{11}^{*m} \right] \quad (6.43)$$

Rearranging Equation 6.43 and using Equation 6.37,

$$\epsilon_{11}^* = \frac{\frac{1 + \nu}{3(1 - \nu)} K^m}{\frac{1 + \nu}{3(1 - \nu)} K^m - \left[\frac{1 + \nu}{3(1 - \nu)} - 1 \right] K} (\alpha^m - \alpha) \Delta T \quad (6.44)$$

Making use of Equation 6.2,

$$\epsilon_{11}^m = \frac{1 + \nu}{3(1 - \nu)} \epsilon_{11}^* \quad (6.45)$$

Through algebraic manipulation of Equations 6.45 and 6.44

$$\epsilon_{11}^m = \frac{\frac{1 + \nu}{3(1 - \nu)} K^m}{K^m + \frac{2 - 4\nu}{1 + \nu} K} (\alpha^m - \alpha) \Delta T \quad (6.46)$$

Finally, the expression for the coefficient of thermal expansion of the aggregate is obtained from the combination of Equations 6.46 and 6.42:

$$\alpha = \frac{\sum_g f^g \frac{K^g}{K^g + \frac{2 - 4\nu}{1 + \nu} K} \alpha^g}{\sum_g f^g \frac{K^g}{K^g + \frac{2 - 4\nu}{1 + \nu} K}} \quad (6.47)$$

In this particular case, the CTE of the aggregate, α , can be explicitly expressed in terms of the CTEs of the composing phases, α^g , as seen in Equation 6.47.

6.5 Modelling of the creep behaviour of a multiphase material

Budiansky and Wu [27] studied the plastic behaviour of polycrystals in terms of the plastic behaviour of the grains that compose them. Their analysis was applied to elasto-plastic materials in a self-consistent manner and made use of Eshelby's inclusion technique [80]. Their work extended the work by Kröner [83], which reached the same mathematical solution based upon different reasoning.

Weng [84] considered that creep deformation was a stress-free strain in the sense of Eshelby, as it depends on the stress value but not on the stress rate value. In order to model the creep behaviour of a multiphase material, a spatially

uniform dispersion of spherical inclusions or *grains* within a continuum matrix is considered. Both the inclusions and the matrix are creeping over a time period dt . Under the hypotheses used in self-consistent models, the stress and creep strain for a single inclusion are respectively σ_{ij}^m and $\epsilon_{ij}^{m,cr}$, while the matrix is assumed to behave as the aggregate material in order to account for the non-dilute dispersion of precipitates. The stress and strain values of the aggregate are σ_{ij} and ϵ_{ij}^{cr} , respectively. Small material rotation is assumed.

At the end of the incremental time period, the inclusion and the matrix have undergone creep strains of $d\epsilon_{ij}^{m,cr}$ and $d\epsilon_{ij}^{cr}$, respectively. If the inclusion creep strain is referred to the matrix creep, i.e. the inclusion is assumed to undergo a stress-free strain $d\epsilon_{ij}^*$ and the matrix does not deform, the situation is analogous to Eshelby's problem with an eigenstrain:

$$d\epsilon_{ij}^* = d\epsilon_{ij}^{m,cr} - d\epsilon_{ij}^{cr} \quad (6.48)$$

Equation 6.48 is in agreement with the self-consistent models as the matrix incremental strain tensor is replaced with the aggregate incremental strain tensor, $d\epsilon_{ij}^{cr}$, which includes the effects of the dispersion of particles. The strain within the inclusion is

$$d\epsilon_{ij}^m = S_{ijkl} d\epsilon_{kl}^* \quad (6.49)$$

Equation 6.49 is obtained from the application of Eshelby's tensor to calculation of the strain within the inclusion. The inclusion stress increment is, according to Hooke's law,

$$\begin{aligned} d\sigma_{ij}^m &= C_{ijkl} (d\epsilon_{kl}^m - d\epsilon_{kl}^*) \\ &= C_{ijkl} [S_{klmn} (d\epsilon_{mn}^{m,cr} - d\epsilon_{mn}^{cr}) - (d\epsilon_{mn}^{m,cr} - d\epsilon_{mn}^{cr})] \\ &= C_{ijkl} (S_{klmn} - I_{klmn}) (d\epsilon_{mn}^{m,cr} - d\epsilon_{mn}^{cr}) \end{aligned} \quad (6.50)$$

where I_{klmn} is the fourth order identity tensor.

If an elastic isotropic behaviour is assumed, Hooke's law can be expressed in

terms of Lamé's constants as:

$$d\sigma_{ij}^m = \lambda d\epsilon_{kk}^m \delta_{ij} + 2\mu d\epsilon_{ij}^m \quad (6.51)$$

Taking into account that the strain increment under consideration is a creep strain increment and, since it is proportional to the deviatoric stress tensor, it implies no volume change, i.e. $d\epsilon_{kk}^m = 0$, Equation 6.51 reduces to

$$d\sigma_{ij}^m = 2\mu d\epsilon_{ij}^m \quad (6.52)$$

The same conclusion can be applied to Equation 6.50, simplifying the dilatational terms as:

$$d\sigma_{ij}^m = 2\mu (S_{ijkl} - I_{ijkl}) (d\epsilon_{kl}^{m,cr} - d\epsilon_{kl}^{cr}) \quad (6.53)$$

If the considered inclusion is spherical and the deformation is at constant volume, the following identity is obtained:

$$S_{ijkl}\epsilon_{kl} \equiv \beta_t \epsilon_{ij}, \quad \text{with} \quad \beta_t = \frac{2(4 - 5\nu)}{15(1 - \nu)} \quad (6.54)$$

For further explanation regarding the calculation of β_t refer to Appendix B. Equations 6.53 and 6.54 can be combined and finally written as:

$$d\sigma_{ij}^m = -2\mu (1 - \beta_t) (d\epsilon_{ij}^{m,cr} - d\epsilon_{ij}^{cr}) \quad (6.55)$$

Additionally, if during the incremental deformation the matrix load is externally increased by $d\sigma_{ij}$, Equation 6.55 can be modified as

$$d\sigma_{ij}^m - d\sigma_{ij} = -2\mu (1 - \beta_t) (d\epsilon_{ij}^{m,cr} - d\epsilon_{ij}^{cr}) \quad (6.56)$$

Equation 6.56 is the same equation obtained by Weng [84] using Eshelby's inclusion technique. Budiansky and Wu [27] obtained a similar expression, but referred to plastic strains rather than to creep strains. However, as long as the hypothesis relevant to the consideration of the stress-free strain stated in

Equation 6.48 remains valid, the equation obtained is similar to Equation 6.56, regardless of the nature of the inelastic strains taken into account.

The use of the creep strain of the aggregate, $d\epsilon^{cr}$, which takes into account the effect of the dispersion of particles in the matrix, is a consequence of the self-consistency hypotheses under which the model has been formulated. Equation 6.56 is an implicit equation that requires numerical methods for its solution, following a numerical scheme that is explained in Section 6.6.

6.5.1 Additional considerations in the creep of multiphase materials

The most general form of Hooke's law, considering material rotation, inelastic stresses and thermal stresses was used by Busso [25] and can be written in rate form as

$$\overset{\nabla}{\boldsymbol{\sigma}} = \mathbf{C} : (\dot{\boldsymbol{\epsilon}} - \dot{\boldsymbol{\epsilon}}^{in}) - 3K\alpha\dot{T}\mathbf{1} \quad (6.57)$$

where $\overset{\nabla}{\boldsymbol{\sigma}}$ is the Jaumann derivative of the total stress $\overset{\nabla}{\boldsymbol{\sigma}} = \dot{\boldsymbol{\sigma}} - \mathbf{W}\boldsymbol{\sigma} + \boldsymbol{\sigma}\mathbf{W}$, $\dot{\boldsymbol{\epsilon}}$ is the total strain rate tensor, $\dot{\boldsymbol{\epsilon}}^{in}$ is the inelastic strain rate tensor, \mathbf{C} represents the elastic constants tensor, K is the aggregate bulk modulus, α is the aggregate coefficient of thermal expansion and \dot{T} is the temperature change rate. \mathbf{W} is the total material rotation, which can be neglected when material rotations are small.

The inelastic strain rate tensor, $\dot{\boldsymbol{\epsilon}}^{in}$, is composed of two parts, the creep strain rate tensor, $\dot{\boldsymbol{\epsilon}}^{cr}$, and the transformation strain rate tensor, $\dot{\boldsymbol{\epsilon}}^{tr}$, due to microstructural changes:

$$\dot{\boldsymbol{\epsilon}}^{in} = \dot{\boldsymbol{\epsilon}}^{cr} + \dot{\boldsymbol{\epsilon}}^{tr} \quad (6.58)$$

The aggregate creep strain tensor is obtained averaging the phase strain rate

tensor, $\dot{\epsilon}^{m,cr}$, over the volume as:

$$\dot{\epsilon}^{cr} = \sum_g f^g \dot{\epsilon}^{g,cr} \quad (6.59)$$

In order to account for the creep strain rate of each of the phases, $\dot{\epsilon}^{m,cr}$, it is necessary to know the stress in each of the inclusions that model the various phases present in the alloy. Instead of using Equation 6.56, Busso [25] used a modified equation that included a phase accommodation term, $\dot{\mathbf{A}}^m$, derived according to the models proposed by Cailletaud and Pilvin [88], and expressed the result in rate form as:

$$\dot{\sigma}^m = \dot{\sigma} + 2\mu(1 - \beta_t) \left(\dot{\epsilon}^{cr} - \dot{\epsilon}^{m,cr} - \dot{\mathbf{A}}^m \right) \quad (6.60)$$

Equation 6.56 obtained by Weng [84], written in rate form is

$$\dot{\sigma}^m = \dot{\sigma} + 2\mu(1 - \beta_t) (\dot{\epsilon}^{cr} - \dot{\epsilon}^{m,cr}) \quad (6.61)$$

It can be seen that Equation 6.60, used by Busso [25], contains an additional term, $\dot{\mathbf{A}}^m$, compared with Equation 6.61, which accounts for the accommodation of phases that behave in very different ways. More specifically, the purpose of Equation 6.60 is the modelling of materials with phases that show creep behaviour and phases that remain elastic at high temperature. The tensorial variable $\dot{\mathbf{A}}^m$ is defined as [25]

$$\dot{\mathbf{A}}^m = \hat{H}(f, T) \left\{ \sum_g f^g \mathbf{S}^g |\dot{\epsilon}^{g,cr}| - \mathbf{S}^m |\dot{\epsilon}^{m,cr}| \right\} \quad (6.62)$$

with

$$\dot{\mathbf{S}}^m = \dot{\epsilon}^{m,cr} - \hat{H}(f, T) \mathbf{S}^m |\dot{\epsilon}^{m,cr}| \quad (6.63)$$

where $\hat{H}(f, T)$ is a homogenisation function that is calibrated using finite element unit cells that simulate different proportions of an elastic oxide within a creeping matrix. An explanation and investigation of the $\dot{\mathbf{A}}^m$ term is presented in 6.5.2, with references to the work where the theory was originally developed.

6.5.2 Development of the additional term $\dot{\mathbf{A}}^m$

Cailletaud and Pilvin [88] propose a model that considers the individual viscoplastic behaviour of a set of 1000-10000 single crystals to obtain the viscoplastic response of a polycrystal. In contrast to the models derived using Eshelby's inclusion technique, their model uses an alternative internal stress inelastic accommodation factor based on a tensor, denoted $\boldsymbol{\beta}^m$, instead of using the creep strain tensors. The model proposed in Ref. [88] is

$$\boldsymbol{\sigma}^m = \boldsymbol{\sigma} + a\mu(\boldsymbol{\beta} - \boldsymbol{\beta}^m) \quad (6.64)$$

where a is a factor that can take different values according to the hypothesis assumed for the stress redistribution between grains. A value of $a = 0$ implies that the stress is not redistributed and every grain has an identical stress. The Lin-Taylor model assumes $a = 2$ and self-consistent models [83] consider $a = 1$, which is in agreement with the model derived using Eshelby's inclusion technique. $\boldsymbol{\beta}$ is defined as the sum of $\boldsymbol{\beta}^m$ over all the grains that compose the polycrystal,

$$\boldsymbol{\beta} = \sum_g f^g \boldsymbol{\beta}^g \quad (6.65)$$

The rate equation that defines the evolution of $\boldsymbol{\beta}^m$ for each grain is

$$\dot{\boldsymbol{\beta}}^m = \dot{\boldsymbol{\epsilon}}^{m,p} - D(\boldsymbol{\beta}^m - \delta \boldsymbol{\epsilon}^{m,p}) |\dot{\boldsymbol{\epsilon}}^{m,p}| \quad (6.66)$$

where $\dot{\boldsymbol{\epsilon}}^{m,p}$ is the inelastic strain rate of the m th grain, D and δ are constants that need to be fitted and $|\dot{\boldsymbol{\epsilon}}^{m,p}|$ is the equivalent inelastic strain rate, which is defined as

$$|\dot{\boldsymbol{\epsilon}}^{m,p}| = \sqrt{\frac{2}{3} \dot{\boldsymbol{\epsilon}}^{m,p} : \dot{\boldsymbol{\epsilon}}^{m,p}} \quad (6.67)$$

In order to evaluate the differences between the model defined in Equations 6.64 - 6.67 and the currently used model that considers Equation 6.61, Equation 6.64 needs to be rewritten in rate form,

$$\dot{\boldsymbol{\sigma}}^m = \dot{\boldsymbol{\sigma}} + a\mu(\dot{\boldsymbol{\beta}} - \dot{\boldsymbol{\beta}}^m) \quad (6.68)$$

$\dot{\beta}$ is expressed in terms of its individual components as:

$$\begin{aligned}\dot{\beta} &= \sum_g f^g \dot{\beta}^g = \sum_g f^g \dot{\epsilon}^{g,p} - D \sum_g f^g (\beta^g - \delta \epsilon^{g,p}) |\dot{\epsilon}^{g,p}| \\ &= \dot{\epsilon}^p - D \sum_g f^g (\beta^g - \delta \epsilon^{g,p}) |\dot{\epsilon}^{g,p}|\end{aligned}\quad (6.69)$$

$\dot{\beta} - \dot{\beta}^m$ is expressed as

$$\begin{aligned}\dot{\beta} - \dot{\beta}^m &= \dot{\epsilon}^p - D \sum_g f^g (\beta^g - \delta \epsilon^{g,p}) |\dot{\epsilon}^{g,p}| - \dot{\epsilon}^{m,p} - D \sum_g f^g (\beta^m - \delta \epsilon^{m,p}) |\dot{\epsilon}^{m,p}| \\ &= \dot{\epsilon}^p - \dot{\epsilon}^{m,p} - \dot{\mathbf{A}}^m\end{aligned}\quad (6.70)$$

where an additional function $\dot{\mathbf{A}}^m$ has been introduced, which is defined as

$$\begin{aligned}\dot{\mathbf{A}}^m &= D \left[\sum_g f^g (\beta^g - \delta \epsilon^{g,p}) |\dot{\epsilon}^{g,p}| - (\beta^m - \delta \epsilon^{m,p}) |\dot{\epsilon}^{m,p}| \right] \\ &= D \left[\sum_g f^g \mathbf{S}^g |\dot{\epsilon}^{g,p}| - \mathbf{S}^m |\dot{\epsilon}^{m,p}| \right]\end{aligned}\quad (6.71)$$

with \mathbf{S}^m being

$$\begin{aligned}\dot{\mathbf{S}}^m &= \dot{\beta}^m - \delta \dot{\epsilon}^{m,p} = (1 - \delta) \dot{\epsilon}^{m,p} - D (\beta^m - \delta \epsilon^{m,p}) |\dot{\epsilon}^{m,p}| \\ &= (1 - \delta) \dot{\epsilon}^{m,p} - D \mathbf{S}^m |\dot{\epsilon}^{m,p}|\end{aligned}\quad (6.72)$$

Substituting Equations 6.69 - 6.72 back into Equation 6.64 the model can finally be formulated as

$$\dot{\sigma}^m = \dot{\sigma} + a\mu(\dot{\epsilon}^p - \dot{\epsilon}^{m,p} - \dot{\mathbf{A}}^m) \quad (6.73)$$

$$\dot{\mathbf{A}}^m = D \left[\sum_g f^g \mathbf{S}^g |\dot{\epsilon}^{g,p}| - \mathbf{S}^m |\dot{\epsilon}^{m,p}| \right] \quad (6.74)$$

$$\dot{\mathbf{S}}^m = (1 - \delta) \dot{\epsilon}^{m,p} - D \mathbf{S}^m |\dot{\epsilon}^{m,p}| \quad (6.75)$$

Equations 6.73 - 6.75 are equivalent to Equations 6.60, 6.62 and 6.63, with the only difference being the use of the factor a in Equation 6.73. However, since β values for realistic materials are ~ 0.5 , Equation 6.60 reduces to Equation 6.73 with $a = 1$.

6.5.3 Interpretation of the \dot{A}^m term

The equation directly obtained from the application of Eshelby's technique to calculate the stress tensor in the phases that form a multiphase aggregate is [84]:

$$\dot{\sigma}_{ij}^m = \dot{\sigma}_{ij} + 2\mu(1 - \beta_t) (\dot{\epsilon}_{ij}^{cr} - \dot{\epsilon}_{ij}^{m,cr}) \quad (6.76)$$

Under certain conditions, i.e. extreme differences in creep resistance of the constituents of a multiphase material, Equation 6.76 may overestimate the stress transmission among phases, predicting stress levels which are too low for the fast creeping phases and too high for the more resistant inclusions, when compared to the results obtained using other modelling techniques such as unit cell calculations.

In order to overcome this problem, a stress accommodation tensor, \dot{A}_{ij}^m , as explained in Sections 6.5.1 and 6.5.2, can be introduced. Then, the terms in the parenthesis in Equation 6.60, which control the load transfer between phases, can be expressed as:

$$\begin{aligned} \dot{\epsilon}_{ij}^{cr} - \dot{\epsilon}_{ij}^{m,cr} - \dot{A}_{ij}^m &= \left[\sum_g f^g (\dot{\epsilon}_{ij}^{g,cr} - DS_{ij}^g |\dot{\epsilon}^{g,cr}|) - (\dot{\epsilon}_{ij}^{m,cr} - DS_{ij}^m |\dot{\epsilon}^{m,cr}|) \right] \\ &\equiv \sum_g \dot{S}_{ij}^g - \dot{S}_{ij}^m \end{aligned} \quad (6.77)$$

In this case, the stress transmission is not proportional to the creep strain rate difference but to the difference between the $\dot{\mathbf{S}}$ tensor of the aggregate and the $\dot{\mathbf{S}}^m$ tensor of each individual phase, where \dot{S}_{ij}^m is

$$\dot{S}_{ij}^m = \dot{\epsilon}_{ij}^{m,cr} - DS_{ij}^m |\dot{\epsilon}^{m,cr}| \quad (6.78)$$

Let us consider a one dimensional case of tensile creep and obtain the creep strain rate and accumulated creep strain values. Under those conditions,

$$|\dot{\epsilon}^{m,cr}| = \sqrt{\frac{2}{3}} \dot{\epsilon}_{11}^{m,cr} \quad (6.79)$$

Equation 6.79 is now substituted in Equation 6.78 to yield

$$\dot{S}_{11}^m = \dot{\epsilon}_{11}^{m,cr} - DS_{11}^m \dot{\epsilon}_{11}^{m,cr} \quad (6.80)$$

Integrating Equation 6.80,

$$S_{11}^m = \frac{1 - e^{-\sqrt{\frac{2}{3}} D \epsilon_{11}^{m,cr}}}{\sqrt{\frac{2}{3}} D} \quad (6.81)$$

And, by derivation of Equation 6.81, \dot{S}_{11}^m can be expressed in a simpler form as

$$\dot{S}_{11}^m = e^{-\sqrt{\frac{2}{3}} D \epsilon_{11}^{m,cr}} \dot{\epsilon}_{11}^{m,cr} \quad (6.82)$$

For fast creeping phases, the exponential term in Equation 6.82 will decrease and the S_{11}^m values will be reduced compared with the terms corresponding to slow creeping phases. The stress redistribution factor, i.e. the term derived in Equation 6.77, is then reduced compared to the theoretically obtained Equation 6.76 and the stresses are “locked” within the fast creeping phases, avoiding excessive load redistribution from fast creeping phases to slow creeping phases.

6.6 Numerical implementation

6.6.1 Implementation within FE analyses

The diagram in Fig. 6.3 shows how the microstructural, stress analysis and constitutive model are combined in a coupled calculation.

An interface between the thermodynamic phase calculation and ABAQUS has been created and used in Chapter 8. For each increment and integration point, ABAQUS passes the phase proportions obtained from the microstructural calculation, the current stress and strain values and the correspondent aggregate total strain increments to the subroutine that contains the constitutive model.

Once the results of aggregate stress in the end of the time increment and aggregate stress Jacobian have been obtained, these values are passed back to ABAQUS that will check the equilibrium of the model. If the residuals are too big, a new estimation of the strain increments will be produced and passed to the subroutine until equilibrium is achieved.

The constitutive model uses the coefficient of thermal expansion, elastic properties and creep properties, according to a Norton-type behaviour, of the individual phases to define the aggregate material. A linear dependency with temperature is used for all the constants except for the creep factor, which is interpolated for different temperatures using an Arrhenius-type equation and the corresponding activation energy of each phase.

6.6.2 Constitutive model: complete set of differential equations

Hooke's law, when inelastic strain rates and thermal stresses are considered, is expressed in rate form as:

$$\dot{\sigma}_{ij} = \lambda \dot{\epsilon}_{kk} \delta_{ij} + 2\mu(\dot{\epsilon}_{ij} - \dot{\epsilon}_{ij}^{in}) - 3K\alpha\dot{T}\delta_{ij} \quad (6.83)$$

The inelastic strain rate tensor is composed of two terms, the creep strain rate tensor, $\dot{\epsilon}_{ij}^{cr}$, and the transformation strain rate tensor, $\dot{\epsilon}_{ij}^{tr}$, which accounts in this case for volume changes originated from microstructural changes in the aggregate material:

$$\dot{\epsilon}_{ij}^{in} = \dot{\epsilon}_{ij}^{cr} + \dot{\epsilon}_{ij}^{tr} \quad (6.84)$$

The creep strain rate tensor of the aggregate is obtained averaging the corresponding tensors over volume for the phases present in the material:

$$\dot{\epsilon}_{ij}^{cr} = \sum_g f^g \dot{\epsilon}_{ij}^{g,cr} \quad (6.85)$$

where $\dot{\epsilon}_{ij}^{m,cr}$, which represents the creep strain rate of each individual phase, is calculated from Norton's equation:

$$\dot{\epsilon}_{ij}^{m,cr} = \frac{3}{2} A^m (\sigma^m)^{n^m-1} s_{ij}^m \quad (6.86)$$

The transformation strain rate accounts for the volume change involved during oxidation through

$$\dot{\epsilon}_{ij}^{tr} = \frac{1}{3} \dot{f}^{ox} \ln(PBR_{eq}) \delta_{ij} \quad (6.87)$$

where PBR_{eq} is the Pilling-Bedworth ratio (PBR) of the multiphase aggregate and \dot{f}^{ox} represents the rate at which new oxide is forming.

Finally, the equation that links the stress-strain states in the aggregate and in the phases that compose it is, in rate form:

$$\dot{\sigma}_{ij}^m = \dot{\sigma}_{ij} + 2\mu(1 - \beta_t) (\dot{\epsilon}_{ij}^{cr} - \dot{\epsilon}_{ij}^{m,cr}) \quad (6.88)$$

6.6.3 Integration algorithm

Equations 6.83 - 6.88 form a system that can be referred to as:

$$\dot{\sigma} = \mathcal{F}(\sigma, \dot{\epsilon}, T, \dot{T}, f^m, \dot{f}^{ox}) \quad (6.89)$$

which needs to be solved within the ABAQUS UMAT subroutine in order to provide the stress increments to the FE processor. The terms composing Equation system 6.89 were then numerically integrated, using one integration point, making use of expressions of the type:

$$\dot{\Phi} = \mathfrak{F}[f(t)] \rightarrow \int_{\Phi_0}^{\Phi_0 + \Delta\Phi} d\Phi = \int_{t_0}^{t_0 + \Delta t} \mathfrak{F}[f(t)] dt \quad (6.90)$$

$$\Delta\Phi \approx \mathfrak{F}(f_0 + \varphi \Delta f) \Delta t \quad (6.91)$$

where $f_0 = f(t_0)$, $\Delta f = f(t_0 + \Delta t) - f(t_0)$ and φ is a numerical integration parameter between 0 and 1. After applying the numerical integration explained in

Equations 6.90 and 6.91, Equation system 6.89 can be rewritten in incremental form as

$$\Delta\boldsymbol{\sigma} = \mathcal{G}(\Delta\boldsymbol{\sigma}, \Delta\boldsymbol{\epsilon}, T, \Delta T, f^m, \Delta f^m, \Delta t) \quad (6.92)$$

which is solved using Newton-Raphson's method. The FE processor makes use of two stress Jacobians that can be calculated from Equation 6.92. The first one, $\frac{\partial\Delta\boldsymbol{\sigma}}{\partial\Delta\boldsymbol{\epsilon}}$, is used to estimate the change in the stiffness of the material and the second one, $\frac{\partial\Delta\boldsymbol{\sigma}}{\partial\Delta T}$, is related to the influence of the thermal expansion mismatch in the accumulation of stress.

For a full explanation and derivation of the incremental equations and Jacobians refer to Appendix D.

6.7 Conclusions

This chapter contains a review and full derivation of self-consistent models applied to calculate the elastic, thermal expansion and creep behaviour of multi-phase alloys. The equations that define the constitutive model have been coded in an ABAQUS user defined material subroutine. They allow the inclusion of microstructural data in the stress analysis of TBCs by using the proportions of the phases present in the bond coat and oxide layer.

The subroutine that contains the constitutive model derived in this chapter is used in Chapter 7 to calculate the creep response of several bond coats with different compositions at two temperatures. The predictions from the self-consistent model are then compared with results obtained from unit cells that reproduce the microstructural compositions of the alloys at the different temperatures studied, in order to validate the model.

Finally, the full capabilities of the model are exploited in Chapter 8, where microstructural data obtained from a diffusion analysis that makes use of thermodynamic phase equilibrium calculations are sequentially coupled to a struc-

tural analysis in order to model the degradation and oxidation of the bond coat and the associated stresses that accumulate under those conditions.

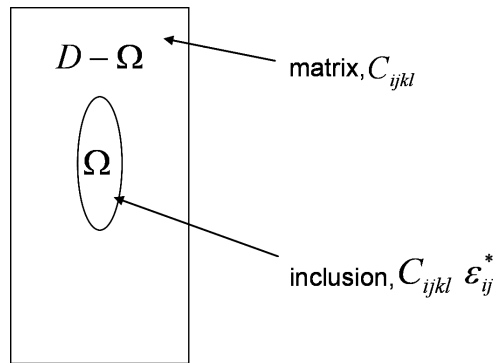


Figure 6.1: Inclusion and surrounding domain.

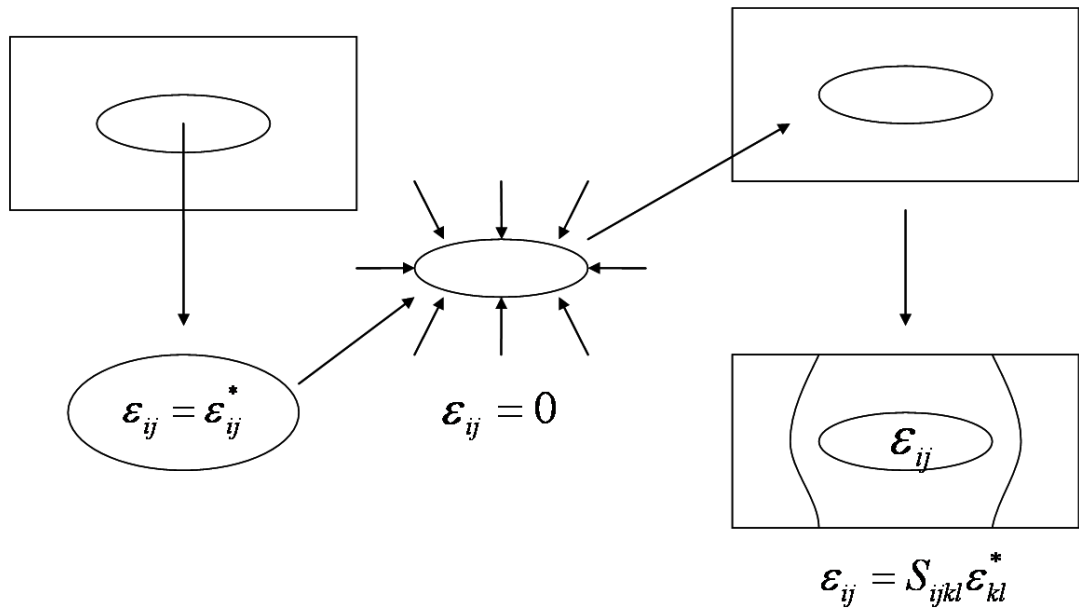


Figure 6.2: Interpretation of Eshelby's equation.

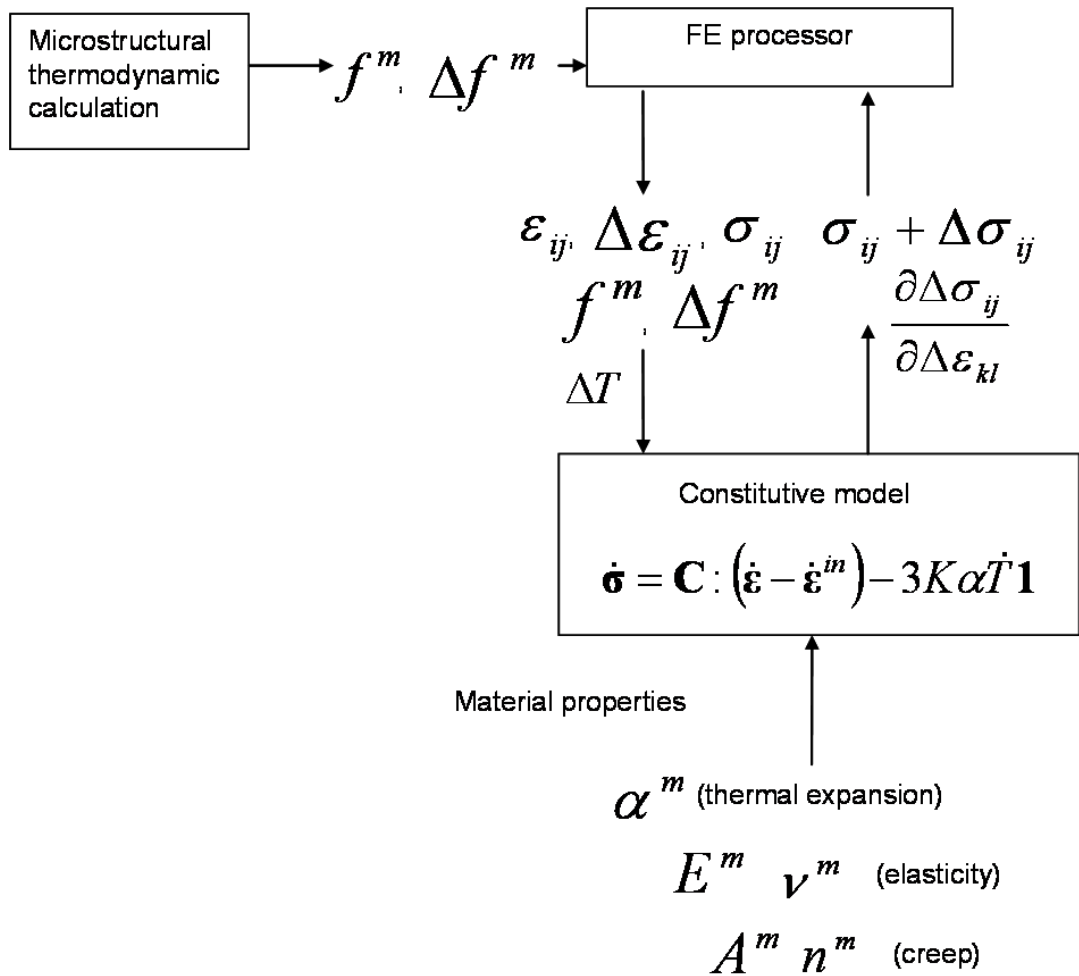


Figure 6.3: Diagram showing the information flow in the coupled microstructural model.

Chapter 7

MCrAlY creep behaviour modelling by means of finite element unit cells and self-consistent constitutive equations

7.1 Introduction

The aim of the work reported in this chapter is to provide a quantitative basis from which the creep properties of MCrAlY bond coats can be predicted as loading and thermal exposure occur at elevated temperature. In particular, it is shown how the creep properties for various MCrAlY compositions can be predicted without the need to carry out extensive experimental testing. While the creep properties for a number of MCrAlYs with various compositions have been published [70–72], and these have been used within the current work, three issues arise in service which make reliance upon test data impractical. These

are:

- Temperature affects the creep behaviour of each of the phases that compose the alloy in accordance with their particular activation energies;
- The microstructure of the alloy and the relative proportions of each of the phases present depend on temperature and exposure time; and
- Diffusion and oxidation effects which occur in service cause the MCrAlY composition to evolve with time and so the resulting variation of microstructure is unlikely to match that of any test specimen.

Therefore, it is desirable to be able to use a fundamental approach to estimate the creep behaviour of MCrAlY bond coats of arbitrary composition. Since MCrAlYs can be regarded as multiphase alloys, a complete understanding of their high temperature behaviour should take into account not only the temperature dependency of the initial isolated phases, but the microstructural changes which occur with time and temperature variations as well. The present research is based on an existing thermodynamic and phase stability model [78,79] in order to predict the phase proportions of MCrAlYs from their thermal and environmental history. In addition, analytical and numerical homogenisation approaches based on the work of Eshelby [80] and Mori and Tanaka [87], which are explained in detail in Chapter 6, together with a unit cell finite element modelling approach are used to predict the creep behaviour of the resulting multiphase material under any specified conditions. In previous studies [89–92] no account was taken of the temperature dependency of the material microstructure; this feature is included in the present investigation through the use of thermodynamic equilibrium-based calculations to obtain the phase proportions at any desired temperature.

Unit cell modelling has been used previously by Weissenbek *et al.* [89] in order to study the elasto-plastic deformation of graded metal-ceramic compos-

ites. The material considered was a layered Ni-Al₂O₃ composite with various geometric configurations such as hexagonal packing, square packing as well as a set of random packing configurations. Results from these unit cell calculations were compared with predictions obtained using mean-field models such as that described by Mori and Tanaka [87], which is based upon Eshelby's inclusion technique [80]. Al₂O₃ was assumed to be linear elastic with temperature dependent properties and Ni was assumed to have temperature dependent elasto-plastic material properties. Finite element calculations reproduced the essential experimental trends exhibited by the layered composite; the mean-field model was also able to reproduce a number of experimentally observed phenomena.

Rangaraj and Kokini [90] studied the thermal conductivity, elastic modulus, coefficient of thermal expansion (CTE) and creep properties of zirconia-NiCoCrAlY particulate composites. Mean-field models based on the Mori-Tanaka approach [87] were used to determine the thermal conductivity, elastic modulus and CTE of the composite which were compared with corresponding experimental results; these showed good agreement. The creep properties of the composite were modelled using the *self-consistent* approach, which provided good correlations with the results obtained from a 2D FE model of a continuum matrix containing a random dispersion of particles.

In a later investigation, Rangaraj and Kokini [91] studied the effects of the inclusion shape and aspect ratio on the creep properties of zirconia-NiCoCrAlY particulate composites using the finite element method (FEM). Cylindrical and spherical particle shapes were considered in 2D axisymmetric unit cell configurations. Results obtained using spherical particles showed good agreement with the predictions obtained from the self-consistent inclusion model used in the previous analysis [90].

Shen *et al.* [92] studied the plastic behaviour of an Al - 3.5 wt% Cu reinforced with 20 vol% SiC whiskers and particles of various shapes; the reinforcements

were considered to be linearly elastic. They used two alternative particle packing patterns when creating the 2D plane strain FE meshes. The stress fields and stress concentrations around the reinforcements were examined but these results were not compared with values obtained through any other means.

In the work described in this chapter, full 3D FE analyses are used in order to represent the alloys in a more realistic manner compared to previous 2D studies [89–92]. Results obtained from the FE models are compared with predictions from the constitutive model developed in Chapter 6, which is based upon Eshelby’s inclusion technique [80]. Unlike the self-consistent model used in Refs. [90, 91], the constitutive model explained in Chapter 6 considers the instantaneous stress tensor present at each phase and averages the strain rate tensor, as suggested by Mori and Tanaka [87].

7.2 Finite element unit cell

The bond coat alloy is assumed to be composed of a spatially uniform three dimensional dispersion of spherical particles within a continuum matrix. The phase with the highest relative volume proportion is assumed to be the matrix and the remaining phases present at the material are modelled as inclusions within the continuum. A unit cell represents the smallest repeatable pattern, with respect to geometry, loading and “boundary conditions”, within the multiphase aggregate material. Two alternative spatial distributions of precipitates within a matrix were used in the present work; these are described as hexagonal close packing and simple cubic packing.

7.2.1 Hexagonal close packing (HCP)

Figure 7.1 shows the uniform spatial distribution of spherical particles that allows for maximum packing of precipitates. Under this configuration, the pre-

precipitates are distributed according to a regular tetrahedral pattern, in which the precipitates within a unit cell are all equi-spaced from each other; this corresponds to hexagonal close packing (HCP) since the precipitates form a hexagonal pattern on appropriate planes through the assembly. The unit cell extracted from that pattern, as shown in Figure 7.1, contains spherical precipitates in four of the eight corners of the unit cell, with each of the precipitates occupying a volume corresponding to $\frac{1}{8}$ of its volume within the unit cell. Moreover, each bounding plane of the unit cell is seen to be a plane of symmetry of the infinitely-repeating system.

If x denotes the dimension of the unit cell and r the radius of the particles (Figure 7.1), the volume proportion of the particles is

$$f = \frac{4 \frac{4}{3} \pi r^3}{x^3} = \frac{2\pi}{3} \left(\frac{r}{x}\right)^3 \quad (7.1)$$

A totally packed configuration, in which the spheres would be in contact, corresponds to

$$2r = \sqrt{2x^2} \quad (7.2)$$

which gives a maximum inclusion volume fraction of

$$f = \frac{2\pi}{3} \left(\frac{\sqrt{2}x}{2x}\right)^3 = \frac{4\sqrt{2}\pi}{24} = 0.74 \quad (7.3)$$

Using Equation 7.1, the geometric parameter $\frac{r}{x}$ of the unit cell for different microstructural compositions of the various MCrAlYs studied in this work can be obtained.

7.2.2 Simple cubic packing(SCP)

An alternative geometry, which can be used to model a dispersion of particles within a continuum medium, has spherical particles distributed at each corner

of a cube-shaped unit cell, as shown in Figure 7.2. In this case, the volume proportion of the precipitates is

$$f = \frac{8 \frac{1}{8} \frac{4}{3} \pi r^3}{x^3} = \frac{4\pi}{3} \left(\frac{r}{x}\right)^3 \quad (7.4)$$

A totally packed configuration, in which the spheres would be in contact, corresponds to

$$2r = x \quad (7.5)$$

which provides the maximum volume fraction of precipitates:

$$f = \frac{4\pi}{3} \left(\frac{1}{2}\right)^3 = 0.52 \quad (7.6)$$

7.3 Boundary conditions and finite element meshes

The cubic unit cells are subjected to unidirectional loads, to account for the bulk aggregate uniaxial loading conditions. Appropriate boundary conditions must be imposed to avoid distortion of the bounding planes. The resulting stress fields induced in each of the phases are multiaxial in nature, due to the heterogeneity of the unit cell.

The displacements of the nodes on three perpendicular planes are constrained to be zero in the direction perpendicular to the plane on which they exist throughout the analysis (Figure 7.3). Equations link the normal displacements of the nodes on the remaining three surfaces in order to ensure that parallel planes remain parallel.

Eight node, three dimensional reduced integration solid elements (C3D8R in ABAQUS [75]) were used to create the unit cell meshes, as shown in Figure 7.4. These consist on cubes where the volume corresponding to the precipitates was intersected from the matrix in order to assign different material properties to them. The nodes on the interfaces between the different phases were not dupli-

cated in order to ensure that they simulated a continuum with no separations, as occurs in real multiphase alloys without any microstructural damage.

7.4 Self-consistent constitutive model

A self-consistent constitutive model that takes into account the microstructure of the material has been implemented, as a user defined material, in ABAQUS, by means of a material user subroutine, UMAT [75], in the Fortran programming language [93], as explained in Chapter 6. The model is based on Eshelby's inclusion technique [80] and considers the redistribution of stresses among the phases that comprise a multiphase material, according to their relative creep strengths. A full derivation and theoretical background of the constitutive model is contained in Chapter 6. A simplified version of that model, which does not take into account thermal stresses, is used in this chapter, as its main objective is the evaluation of the applicability of the self-consistent constitutive models to reproduce the creep behaviour of multiphase alloys.

The aggregate stress rate according to Hooke's law, assuming small material rotation, when inelastic strains are included, is

$$\dot{\boldsymbol{\sigma}} = \mathbf{C} : (\dot{\boldsymbol{\epsilon}} - \dot{\boldsymbol{\epsilon}}^{in}) \quad (7.7)$$

where $\dot{\boldsymbol{\sigma}}$ is the aggregate stress rate tensor, \mathbf{C} is the elastic tensor, defined in terms of Lamé's elastic constants as $C_{ijkl} = \lambda\delta_{ij}\delta_{kl} + \mu\delta_{ik}\delta_{jl} + \mu\delta_{il}\delta_{jk}$, $\dot{\boldsymbol{\epsilon}}$ is the total strain rate tensor, $\dot{\boldsymbol{\epsilon}}^{in}$ is the inelastic strain rate tensor and δ_{ij} is the Kronecker delta. Equation 7.7 relates the aggregate stress rate tensor to the aggregate elastic strain rate tensor, represented by $\dot{\boldsymbol{\epsilon}} - \dot{\boldsymbol{\epsilon}}^{in}$. In this chapter the inelastic strain rate tensor is the creep strain rate tensor. However, the constitutive model can be modified to include additional strain components such as those due to phase changes, as explained in Chapter 6. The aggregate creep strain rate

tensor is calculated, from the contributions of the creep of the phases, through Equation 7.8, as suggested by Mori and Tanaka [87]:

$$\dot{\epsilon}^m = \dot{\epsilon}^{cr} = \sum_g f^g \dot{\epsilon}^{g,cr} \quad (7.8)$$

where $\dot{\epsilon}^{cr}$ is the aggregate creep strain rate tensor, f^g is the volume phase proportion of the g th phase and $\dot{\epsilon}^{g,cr}$ is its corresponding creep strain rate tensor. This creep strain rate is obtained using the stress within that particular phase in the Norton equation, i.e.,

$$\dot{\epsilon}^{m,cr} = \frac{3}{2} A^m (\sigma^m)^{n^m-1} \mathbf{s}^m \quad (7.9)$$

where A^m and n^m are the creep constant and stress exponent, respectively, of the m phase, σ^m is its equivalent stress and \mathbf{s}^m is the deviatoric stress tensor of the m phase.

Using Eshelby's inclusion technique [80], and assuming spherical particles within a continuum matrix, the stress level within each individual phase is obtained from

$$\dot{\sigma}^m = \dot{\sigma} + 2\mu(1 - \beta_t)(\dot{\epsilon}^{cr} - \dot{\epsilon}^{m,cr}) \quad (7.10)$$

which is the same equation as that obtained by Weng [84] for the distribution of stress between the phases in a multiphase material. Chapter 6 contains the complete derivation of Equation 7.10. $\dot{\sigma}_{ij}^m$ is the stress rate tensor in each phase and β_t is the result of the use of Eshelby's fourth order tensor appropriate to the situation in which spherical inclusions are assumed, which reduces to a single scalar value under those conditions. Two components can be identified in the right hand side of Equation 7.10; $\dot{\sigma}$ causes a stress increase in the phases due to an increase in the aggregate stress, the remaining term on the right-hand side of the equation accounts for the redistribution of stress between the different phases, according to their relative creep resistance. More specifically, the fastest creeping phase will carry a lower load than the slowest creeping phase; a steady

state is reached when the creep strain rates are equal for all the composing phases.

The constitutive model assumes that the stress within every particle is uniform. This assumption is likely to result in a stiffer response when compared to FE predictions, since the FE predictions allow for the existence of steep stress gradients within the inclusions and matrix.

The use of Norton's equation to represent creep of the individual phases implies that dislocation glide and diffusional creep can occur within each phase, but no allowance is made regarding the movement of dislocations or sliding across boundaries. The underlying assumption is that the particles and the matrix are perfectly bonded.

Additionally, no assumption is made with respect to the crystal structure of either the matrix or any of the precipitates, which implies that they are behaving as isotropic materials. In any case, the constitutive model is not intended to give perfectly exact predictions of the creep properties of the aggregate from the behaviour of the phases that compose the alloy, unless these have been fitted to reproduce the creep response of a specific alloy. The main application of the self-consistent approach is that it allows to scale the experimental results and extrapolate creep properties obtained from experimental tests to other temperatures, taking into account the thermal effects in the microstructure of the alloy. Moreover, it provides a framework where the influence of the thermal exposure time can be assessed and included into the creep behaviour estimation.

An explicit-implicit integration scheme, explained in Appendix D, for Equations 7.7 - 7.10 has been implemented in an ABAQUS user subroutine [75]. The incremental form of the differential rate equations has been coded and is solved using numerical methods within the subroutine in order to calculate the correspondent aggregate stress increments, and the stress Jacobians required by ABAQUS, following the method detailed in Appendix D.

The approach explained in this section is very convenient for including the complex material behaviour which occurs within bond coats during service. Hence, in the remainder of this chapter the results of predictions based on this constitutive model are compared with unit cell model predictions and experimental data. In order to use the unit cell model, the properties of the individual phases are required; Section 7.5 contains information on these material properties.

7.5 Material properties

Since the MCrAlYs considered in this work are relatively rich in nickel, the phases present within them will be similar to the phases found in Ni-base superalloys, i.e. γ -Ni, γ' -Ni₃Al and β -NiAl, containing several levels of cobalt and chromium. Precipitates rich in chromium may form under certain conditions as its content in MCrAlY alloys is relatively high.

7.5.1 Creep properties of isolated phases

7.5.1.1 β -NiAl

Data extracted from Refs. [94–99] for secondary creep strain rates are plotted in Figure 7.5. The average value of the creep activation energy for NiAl is 315 kJ · mol⁻¹ [94], which is in the range of the expected activation energy for diffusion (305 to 365 kJ · mol⁻¹ [100]). Most of the data points in Figure 7.5 are in reasonable agreement with the others, except for the data obtained by Vandervoort *et al.* [98]. It would be expected that, because of the greater grain size of the material used by Vandervoort *et al.* [98], this would lead to creep strain rates slower than the other published values. However, the strain rates measured by Vandervoort *et al.* [98] are faster than the other published data.

Table 7.1 contains the creep parameters, as determined by various authors.

The data shown in Figure 7.5 (excluding those by Vandervoort *et al.*) were used for a least squares fitting process, in order to obtain the creep parameters at 1175 K. The fitted line is shown in Figure 7.6, where the equation plotted in the graph is $\dot{\epsilon}^{cr} = 2.168 \times 10^{-15} \sigma^{5.417}$.

Hence, A and n values of 2.168×10^{-15} and 5.417 were obtained for a temperature of 1175 K. These values, along with other calculated constants are given in Table 7.2, for a temperature-dependent Norton-type creep equation of the form:

$$\dot{\epsilon}^{cr} = A_0 e^{-\frac{Q}{RT}} \sigma^n \quad (7.11)$$

where $\dot{\epsilon}^{cr}$ is the equivalent creep strain rate, A_0 is the creep constant used in an Arrhenius-type equation, Q is the creep activation energy, R is the universal gas constant, T is the absolute temperature, σ is the von Mises equivalent stress and n is the creep stress exponent.

The relatively Al-rich phase in bond coat alloys is referred to as β , which has a composition of $(\text{Ni, Co})_{0.5-0.7}\text{Al}_{0.5-0.3}$. In this work, it is modelled as NiAl.

7.5.1.2 γ -Ni

Frost and Ashby [101] published creep data for pure nickel. Creep strain rates have been calculated, using these data, for temperatures ranging from 850°C to 1050°C and stresses ranging from 10 to 100 MPa. The creep strain rate values obtained (Figure 7.7) were represented by a Norton-type equation, in order to use it in both the unit cell calculation and as an input for the self-consistent constitutive model; the constants are given in Table 7.2.

The γ phase present in bond coat alloys is a Ni(Co) rich phase with up to 30 wt% chromium. For simplicity its creep behaviour will be assumed to be the same as pure Ni.

7.5.1.3 σ -Cr

By following the same method as that used for γ -Ni, the creep strain rates obtained for σ -Cr, using the data from Frost and Ashby [101], are shown in Figure 7.8 and the constants derived from them are given in Table 7.2.

Under certain thermal conditions, some MCrAlY alloys contain a Cr-rich phase, referred to as σ , which can contain up to 30 mol% (Ni, Co). In this work, it is assumed to behave as pure Cr.

7.5.1.4 γ' - Ni₃Al

Wolfenstine *et al.* [102] published experimental creep data for Ni₃Al single crystals in the 1083 - 1388 K temperature range. The creep tests were performed with the load applied in directions which deviate from the [001] direction in the ($\bar{1}01$) plane by 26°. Two temperatures were used to obtain the constants for a Norton-type equation, i.e. 860°C and 1050°C, with stresses in the range 10 to 100 MPa. The creep strain rates calculated from the fitted equation, using the constants from Table 7.2, and the strain rates presented in Ref. [102], obtained using the elastic constants provided in Ref. [103], are shown in Figure 7.9.

Although the calculated activation energy value of 26.8 kJ · mol⁻¹ might not be very realistic as the temperature dependency of the creep behaviour is being partially masked by the consideration of a linear change of n with temperature, this value of activation energy will be used together with the linear interpolation of the exponent in order to ensure the best possible fit to published experimental data. At 1123 K and 350 MPa applied stress, the calculated creep strain rate, using the parameters from Table 7.2, is 4.52×10^{-7} s⁻¹, which is within the values provided in Ref. [104] for single crystal Ni₃Al, between 2×10^{-7} s⁻¹ for creep along the [111] direction and 1×10^{-6} s⁻¹ along [001].

7.5.2 Creep properties of MCrAlYs

In order to provide experimental comparison between the creep rates predicted from unit cell calculations and from the self-consistent approaches, creep data for three different MCrAlY bond coats, with nominal compositions given in Table 7.3, have been located in published research [70–72].

Wereszczak *et al.* [70] studied the creep behaviour of specimens made from hot isostatic pressed (HIP) Praxair CO211 powder. The grain size of specimens manufactured using that technique was reported to be three or four times larger than for low pressure plasma-sprayed (LPPS) alloys. The creep parameters provided in Ref. [70] for this material are given in Table 7.4.

Hebsur and Miner [71] used the LPPS manufacturing method to produce plates of the PWA 276 alloy. The plates were then heat treated in air for 4h at 1352 K and then for 32h at 1144 K. Creep specimens were manufactured from the LPPS plates and tested at 934, 1123 and 1323 K. Since the creep data presented in the analysis for 1323 K were obtained for stress values lower than 6 MPa, the creep parameters for 1123 K were fitted and extrapolated to 1323 K using the recommended activation energy value of $120 \text{ kJ} \cdot \text{mol}^{-1}$ for the 1123 - 1323 K and 3.9 - 15 MPa region.

Majerus [72] obtained the creep parameters of a vacuum plasma-sprayed (VPS) MCrAlY using a double shear creep testing assembly. Parameters that define the primary and secondary creep in the 750°C - 1050°C interval are provided for an as-deposited coating and for a coating that was annealed for 300 h at 1050°C . The provided creep parameters lead to the constants given in Table 7.4.

7.6 Phase equilibrium calculation of MCrAlYs

Thermodynamics equilibrium-based phase calculation techniques have been used [79] in order to obtain the microstructure of each of the proposed MCrAlYs at 850°C and 1050°C. The results are presented in Table 7.5.

The phase equilibrium calculations give weight proportions as results. In order to create the FE meshes used in the analyses presented in this chapter and to use the self-consistent constitutive model, those weight proportions need to be converted into volume proportions. First of all, the presence of all forms of carbides and TCP phases other than σ was neglected, i.e. the bond coats were assumed to be composed entirely of γ , β and σ . The density values used to convert the results of the phase equilibrium calculations are given in Table 7.6. The obtained volume fractions are listed in Table 7.7. The specific creep parameters used for each composing phase at 850°C and 1050°C, obtained by substituting the temperature value and using the constants in Table 7.2, are given in Table 7.8.

7.7 Results

7.7.1 Praxair CO211

Figures 7.10 and 7.11 show that experimental data obtained from HIP Praxair CO211 powder [70] do not lie within the theoretical boundaries limited by the composing phases. This fact is believed to be a consequence of the manufacturing process of the test specimens. HIP specimens have a lower amount of dislocations and defects than cast materials, which implies that the microstructure of the γ and β phases present in the Praxair CO211 specimens is more regular and uniform than the ones extracted from Ref. [101], where fitting constants have been generated averaging properties from materials manufactured

by various processes and presenting different levels of impurities.

In this case, where the volume proportions of the phases are of the same order of magnitude (50 vol% and 50 vol% for 850°C and 60.9 vol% and 39.1 vol% for 1050°C), the unit cell predictions show a greater disparity when compared to the self-consistent constitutive model, as pointed out in Refs. [89,90]. In particular a better numerical agreement is achieved when SCP is used. As an example, for 850°C and 50 MPa, HCP predicts $6.97 \times 10^{-5} \text{ s}^{-1}$, SCP $1.46 \times 10^{-5} \text{ s}^{-1}$ and the self-consistent constitutive model $9.00 \times 10^{-6} \text{ s}^{-1}$.

7.7.2 PWA 276

Figures 7.12 and 7.13 show the comparison between the creep strain rates of the composing phases of PWA 276 at both 850 and 1050°C and the predicted values using unit cell calculations and the self-consistent model subroutine.

The experimental data lie within the boundaries limited by Ni and NiAl at 850°C for relatively high stress values. The curve extrapolated from experimental values at 1050°C is located between the boundaries delimited by the composing phases for the plotted stress range, demonstrating that the creep data extracted from Ref. [101] are more consistent with the phases present at LPPS specimens than at HIP materials.

LPPS specimens have smaller grain size than HIP specimens, which reflects in faster creep rates. Additionally, the precipitates composing the alloy have a tendency to contain a higher density of dislocations, making the aggregate material less creep resistant.

The phase equilibrium calculation run to obtain the composition of the alloy at 850°C shows that it is composed of three phases. Only HCP has been considered for this calculation, as it allows to alternate distributions of γ and σ within a β matrix. However, since one of the phases is dominant in both

temperatures, the numerical agreement between unit cell calculations and the constitutive model is very good.

7.7.3 VPS NiCoCrAlY

Figures 7.14 and 7.15 show the creep strain rate for an as-deposited and an annealed VPS NiCoCrAlY. These creep strain rates are compared to the creep strain rates predicted by unit cell models with the same phase proportion as the studied VPS NiCoCrAlY at 850°C and 1050°C. The results for the as deposited VPS NiCoCrAlY lie in between the limiting phases γ and β . The creep rates of the annealed material, however, are very close the β strain rate, which represents the lower boundary. The unit cell predictions (using both HCP and SCP) lie close to the experimental data for the annealed material properties. Regarding the unit cell and self-consistent model correlation, the values obtained using the subroutine are in very good agreement with the predictions from the unit cells regardless the precipitate packing pattern used.

VPS produces microstructures with creep properties consistent with the material properties provided by Frost and Ashby [101], as shown by the comparison of the unit cell and self-consistent model predictions with the experimental data corresponding to the annealed VPS NiCoCrAlY. A similar conclusion can be drawn from the results for PWA 276, as expected since both VPS and LPPS, which was the manufacturing method of the PWA 276 alloy studied in this chapter, constitute similar processes.

7.8 Discussion and conclusions

The influence of temperature in the creep properties of MCrAlY alloys is due to two factors: the influence in the creep properties of the isolated phases that compose them, and the microstructural changes that arise upon changes in

temperature and exposure time. This situation is enhanced when the MCrAlY is used as a bond coat on a TBC system. This will provoke the interdiffusion of elements with the underlying substrate, usually a Ni-base superalloy, and will cause microstructural and compositional changes that are very difficult to capture using a standard creep law. In order to overcome this problem, which is studied in detail in Chapter 8, an alternative technique that takes into account the material microstructure has to be considered.

Unit cell models give an idea of the creep properties of multiphase materials, but do not account for microstructural changes, i.e. they are only valid for materials with microstructures which remain stable with both time and temperature; they are also unsuitable for use within a macroscopic finite element analysis of the kind of that used in Chapter 8 due to their computational requirements. A more flexible and computationally efficient approach is provided by the use of a constitutive model based upon Eshelby's inclusion technique [80] that incorporates microstructural data, linked together with thermodynamic phase calculations in order to consider the most realistic microstructure for each temperature.

The objective of this work was to evaluate the compatibility of the unit cell modelling and theoretical constitutive models based on Eshelby's inclusion technique [80] to obtain the creep behaviour of multiphase materials and thus validate the material model that will be used in a subsequent microstructural-mechanical coupled analysis of coatings, explained in Chapter 8. It has been shown that, in general, the predictions obtained from both approaches are in very good numerical agreement. However, the experimental creep properties of MCrAlYs manufactured using different techniques show that in order to fit this model (or the unit cell calculations) to reproduce those results, the properties of the phases should be scaled to match those present at the MCrAlY under consideration. In any case, the work presented in this chapter aims towards

providing a comprehensive framework that allows to include microstructural degradation criteria to be included in the creep behaviour modelling of alloys, and not towards obtaining an exact reproduction of the experimental creep behaviour of multiphase aggregates. The methods explained in this chapter allow to extrapolate the creep behaviour of alloys exposed at different temperatures and exposure times, once the properties of their constituents have been properly scaled for the composition and manufacturing method under consideration.

Creep data of the composing phases have been obtained from published research and compared to the creep properties of the aggregate materials, i.e. MCrAlY alloys. 3D unit cell analyses, considering two alternative particle packing patterns, have been carried out to model the microstructure of various MCrAlYs and the creep properties of each composing phase. The same calculations have been performed using a self-consistent constitutive model, leading to the following conclusions:

- For MCrAlYs manufactured via processes similar to the methods used in practice, i.e. LPPS or VPS, the creep properties lay within the limits established by the creep properties of the composing phases given in Ref. [101], which are assumed to be work-hardened or annealed Ni (γ) and polycrystalline NiAl (β).
- HIP specimens with coarser grain size show a significant creep resistance increase when compared to the creep behaviour of its composing phases after work-hardening or annealing.
- Two alternative unit cell geometries have been used in order to study the effect of two different particle packing patterns within a continuum matrix. Results showed that when one of the phases is dominant, i.e. can be considered as a matrix with dilute precipitates, both geometries predict very

similar creep strain rates. Differences between unit cell predictions arise when the composing phases are present at comparable volume fractions.

- Unit cell predictions and self-consistent constitutive model predictions lie very close to each other, provided that there is a dominant phase that can be considered the matrix of the aggregate.
- The self-consistent constitutive model uses Eshelby's inclusion technique to account for the stress at each individual phase. It assumes that the stress is constant throughout the inclusion. Alternatively, unit cells can represent steep stress and strain gradients within the inclusions and the matrix that translate in a less stiff (in terms of creep) behaviour. The self-consistent constitutive model predicts slower creep rates than the equivalent unit cells.

Although there is some disagreement between the absolute values of the creep behaviour predicted from the individual phases and that measured on actual samples of MCrAlY, there is scope for using the trends predicted from the self-consistent approach to scale or extrapolate from experimentally-measured creep data in order to obtain estimates of creep behaviour where no experimental data are available.

Al. content, at. %	Grain size, μm	T , K	n	Q , $\text{kJ} \cdot \text{mol}^{-1}$	Reference
44 to 50.6	15 to 20	1100 to 1400	5.75	314	[96]
50	450	1073 to 1318	10.2 to 4.6	283	[97]
50	500	1173	4.7	-	[99]
50.4	1000	1075 to 1750	7.0 to 3.3	230 to 290	[98]
50	SX [123]	1023 to 1223	7.7 to 5.4	-	[95]

Table 7.1: Creep parameters for NiAl [94].

	A_0 $\text{MPa}^{-n} \text{s}^{-1}$	Q , $\text{kJ} \cdot \text{mol}^{-1}$	n at 850°C	n at 1050°C
NiAl (β) [94-99]	2.18×10^{-1}	315.0	5.42	5.42
Ni (γ) [101]	2.79×10^5	381.0	5.42	4.90
Cr (σ) [101]	1.24×10^4	384.0	4.94	4.48
Ni_3Al (γ') [102]	8.19×10^{-14}	26.8	3.14	4.30

Table 7.2: Creep parameters fitted for individual phases.

Element wt%	Praxair CO211, [70]	PWA 276 [71]	VPS NiCoCrAlY [72]
Co	38.5	20.3	21.1
Ni	32	48.29	48.3
Cr	21	17.3	17.1
Al	8	13.6	12.6
Y	0.5	0.5	0.61
C	-	0.01	0.4

Table 7.3: Nominal compositions of MCrAlYs considered in the present investigation.

	A_0 MPa $^{-n}$ s $^{-1}$	Q , kJ \cdot mol $^{-1}$	n at 850°C	n at 1050°C
HIP Praxair CO211 [70]	6.31×10^{-6}	165.0	2.20	2.20
LPPS PWA 276 [71]	1.10×10^{-4}	120.0	3.47	3.47
VPS NiCoCrAlY, as deposited [72]	4.89×10^{10}	470.7	3.77	3.22
VPS NiCoCrAlY, annealed [72]	2.01×10^{-3}	234.0	4.33	4.73

Table 7.4: Creep parameters of various MCrAlYs.

	850°C, wt%				1050°C, wt%		
	γ	β	M ₂₃ C ₆	σ	γ	β	M ₂₃ C ₆
Praxair CO211	60.2	39.8	0	0	70.2	29.8	0
PWA 276	4.7	80.7	0.2	14.4	29.5	70.3	0.2
VPS NiCoCrAlY	20.4	72.5	7.1	0	25.5	67.4	7.1

Table 7.5: Microstructure of MCrAlYs at different temperatures produced from thermodynamic phase equilibrium calculations [78, 79], wt% of phases.

Phase	ρ ($\text{g} \cdot \text{cm}^{-3}$)
NiAl (β), [94, 105]	5.9
Ni (γ), [106]	8.91
Cr (σ), [106]	7.14
Ni ₃ Al (γ')	7.23

Table 7.6: Densities of various phases. γ' density was experimentally measured in the laboratory, the obtained value being in agreement with density values of 7.25-7.5 $\text{g} \cdot \text{cm}^{-3}$ from Ref. [107].

	850°C, vol%			1050°C, vol%	
	γ	β	σ	γ	β
Praxair CO211	50.0	50.0	0.0	60.9	39.1
PWA 276	3.3	84.3	12.4	21.7	78.3
VPS NiCoCrAlY	15.7	84.3	0.0	20.0	80.0

Table 7.7: Microstructures of MCrAlYs at different temperatures, vol% of phases.

	850°C		1050°C	
	$A \text{ MPa}^{-n} \text{ s}^{-1}$	n	$A \text{ MPa}^{-n} \text{ s}^{-1}$	n
NiAl (β)	4.86×10^{-16}	5.42	7.98×10^{-14}	5.42
Ni (γ)	5.30×10^{-13}	5.42	2.53×10^{-10}	4.90
Cr (σ)	1.71×10^{-14}	4.94	8.56×10^{-12}	4.48
Ni ₃ Al (γ')	4.64×10^{-15}	3.14	7.16×10^{-15}	4.30

Table 7.8: Creep parameters used in the unit cells and microstructural constitutive model for 850 and 1050°C, calculated using the constants in Table 7.2.

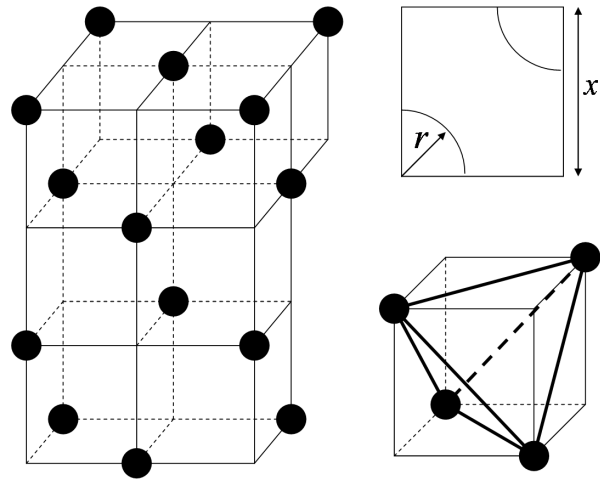


Figure 7.1: Unit cell geometry for possible densest packing configuration (hexagonal close packing).

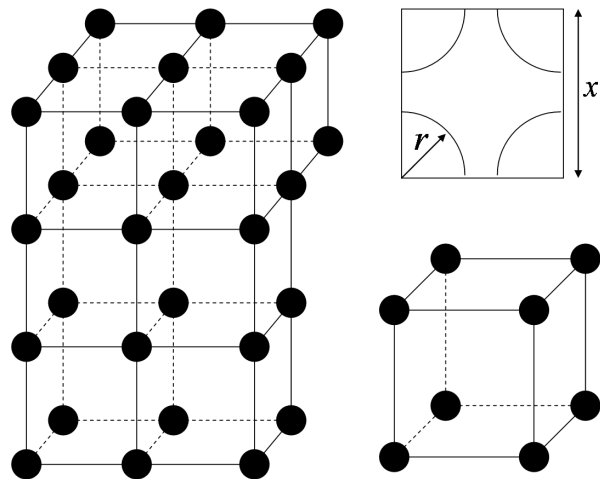


Figure 7.2: Alternative unit cell geometry (simple cubic packing).

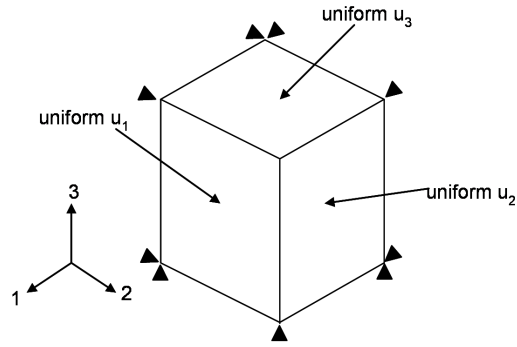


Figure 7.3: Boundary conditions applied to the unit cell.

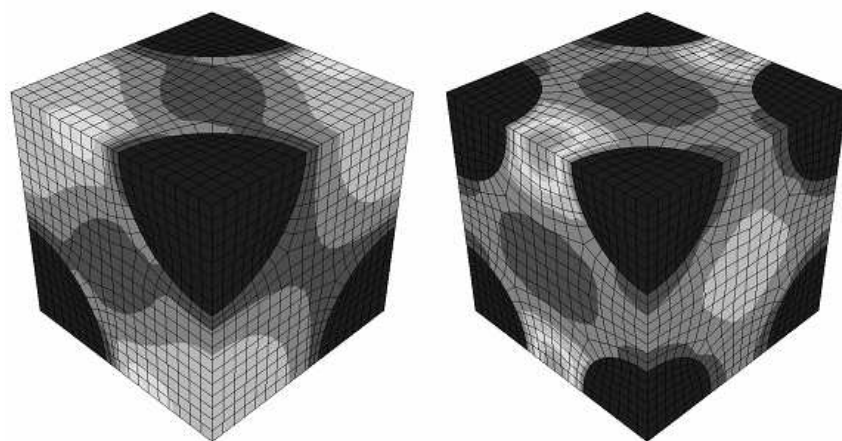


Figure 7.4: FE mesh for HCP (left) and SCP (right) unit cells. The contours represent typical stress distributions under unidirectional loading.

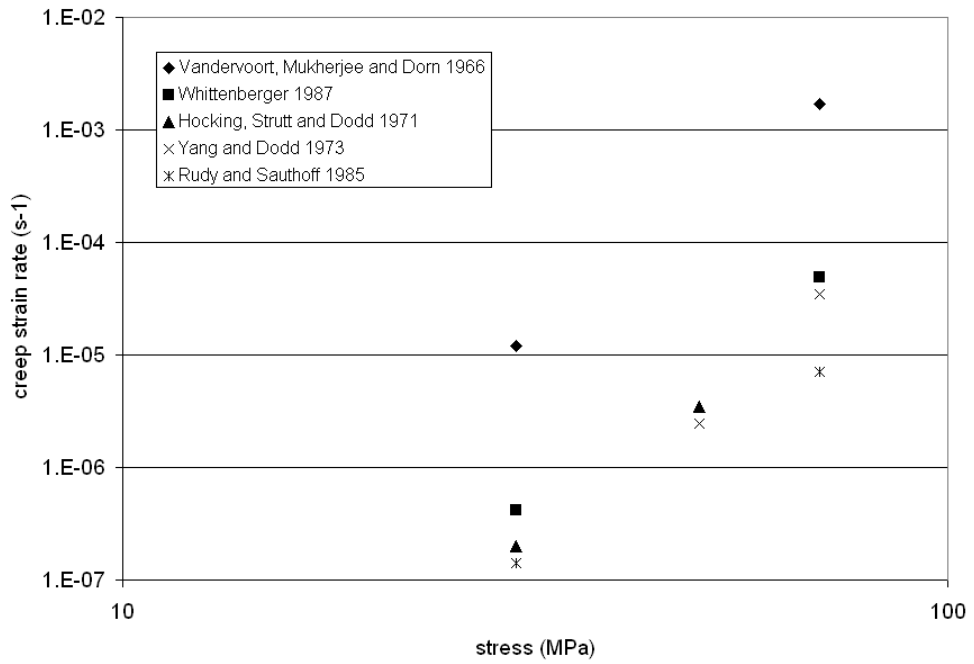


Figure 7.5: Creep strain rate data of NiAl at 1175 K [94].

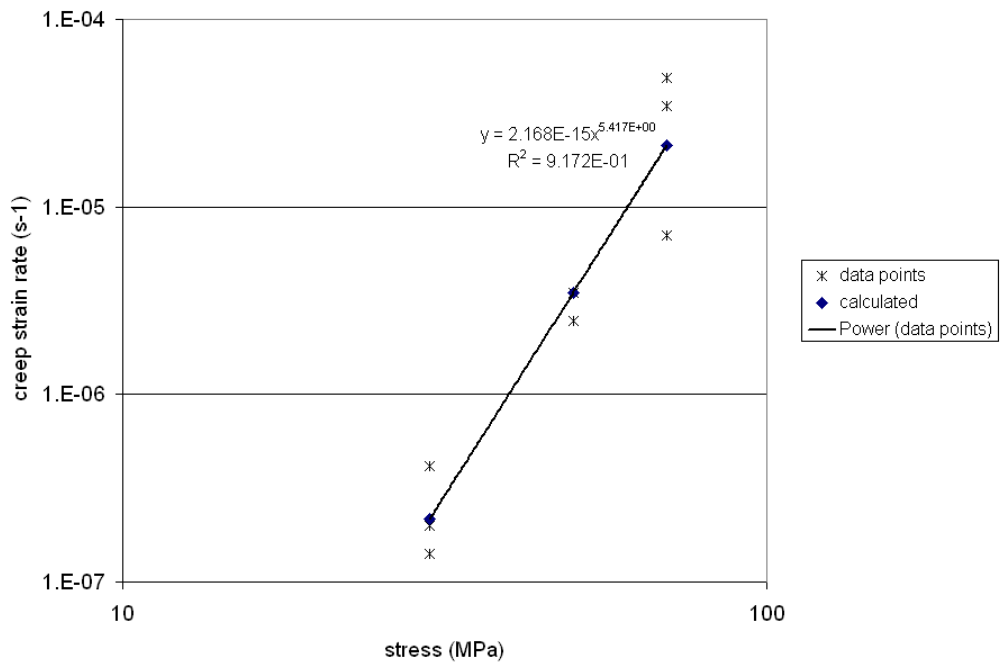


Figure 7.6: Least squares fit to experimental data points of NiAl creep. The data points correspond to those given in Refs. [94–97,99].

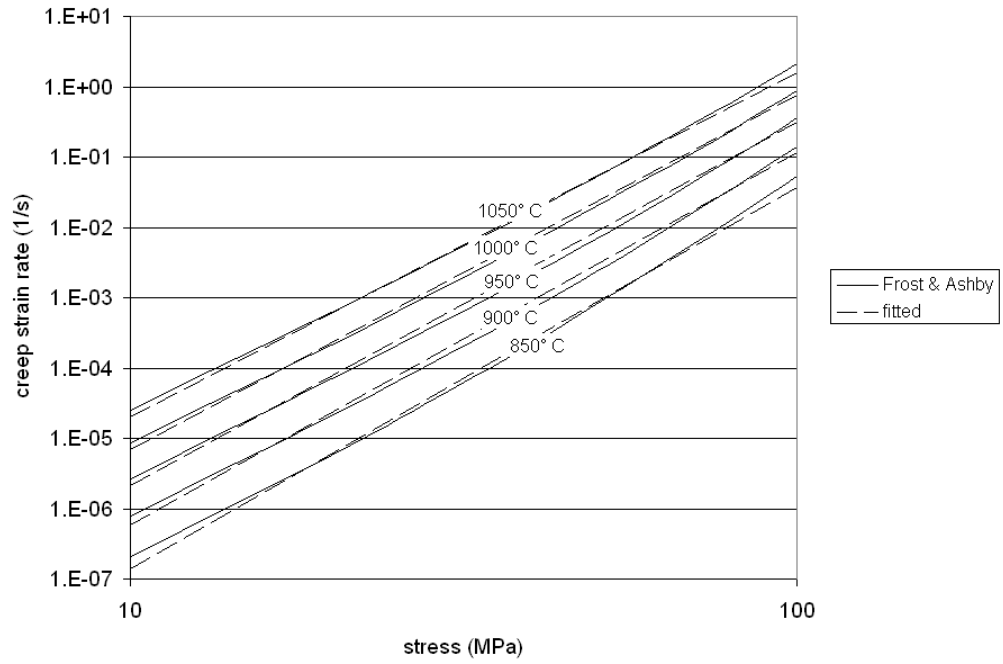


Figure 7.7: Creep strain rates of pure Ni [101].

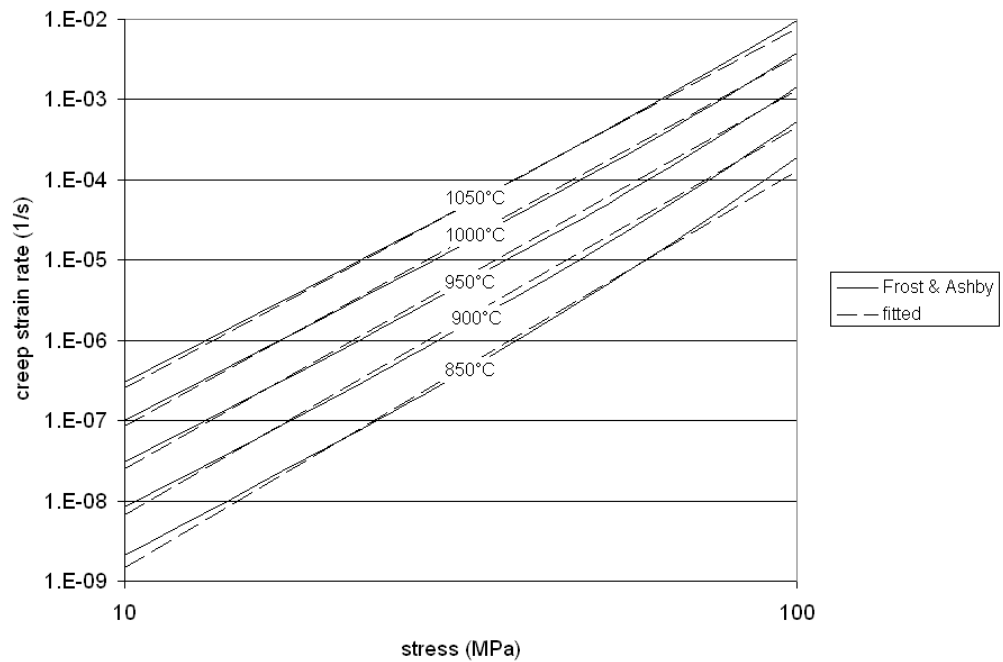


Figure 7.8: Creep strain rates of pure Cr [101].

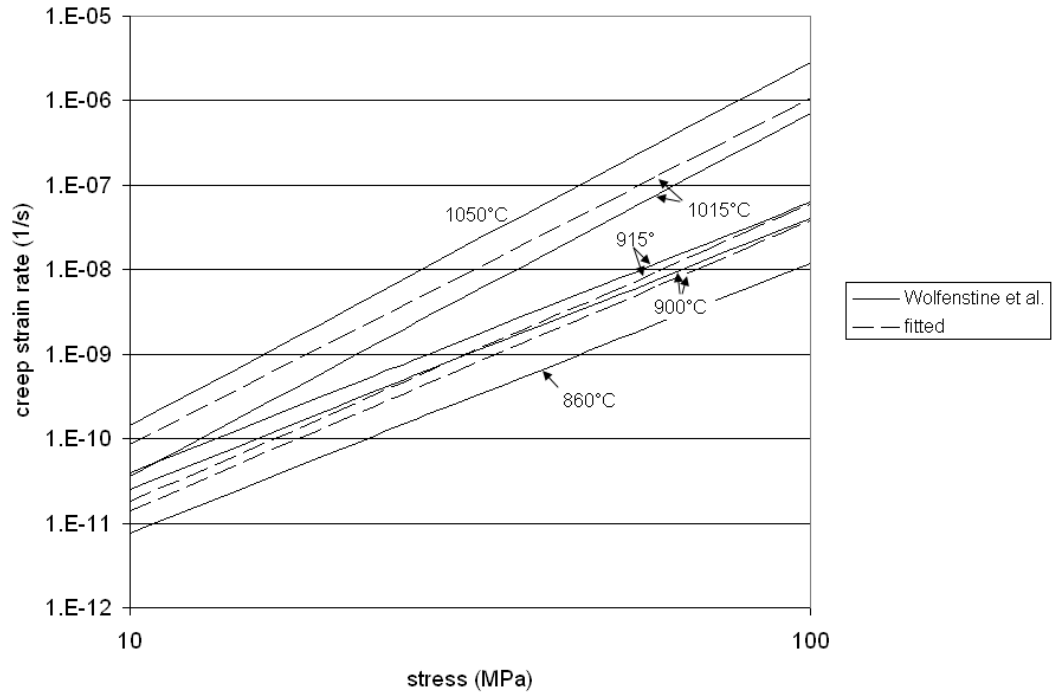


Figure 7.9: Creep strain rates of Ni₃Al creep [102].

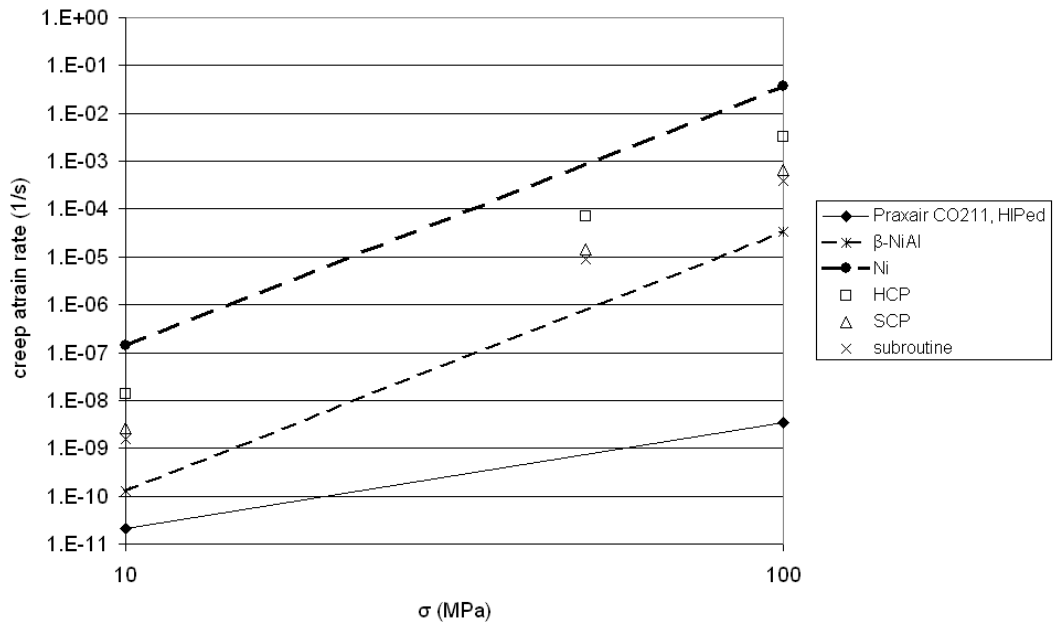


Figure 7.10: HIP Praxair CO211 powder creep strain rate comparison at 850°C.

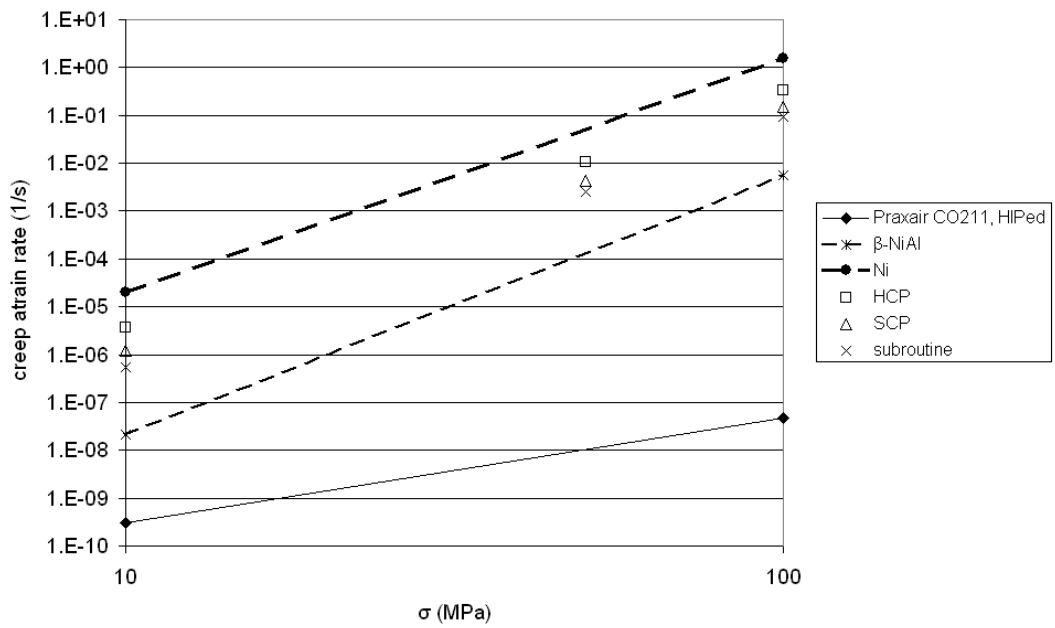


Figure 7.11: HIP Praxair CO211 powder creep strain rate comparison at 1050°C.

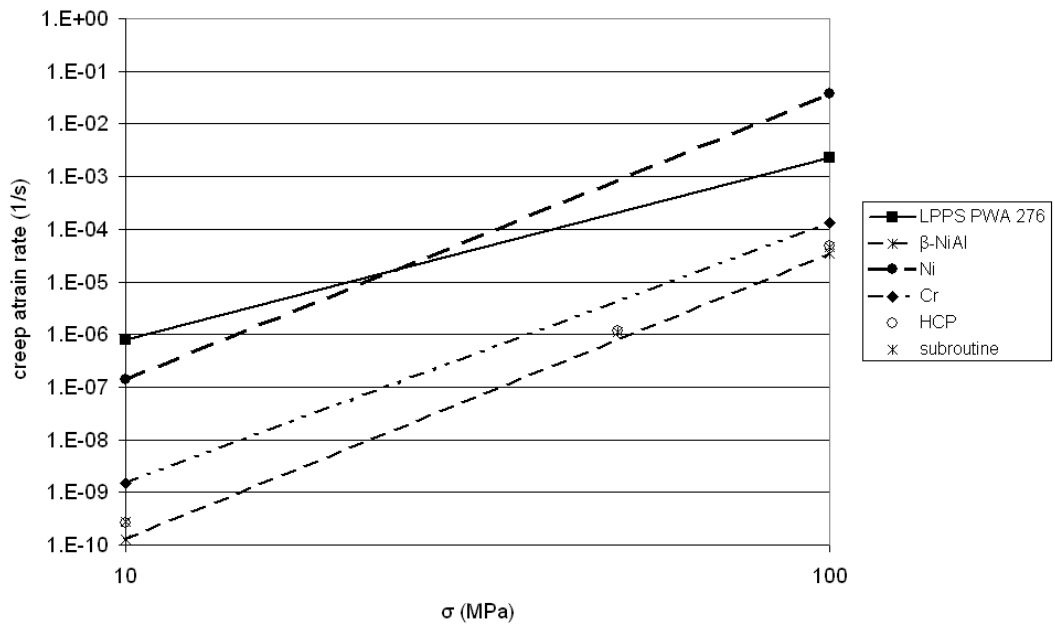


Figure 7.12: PWA 276 creep strain rate comparison at 850°C.

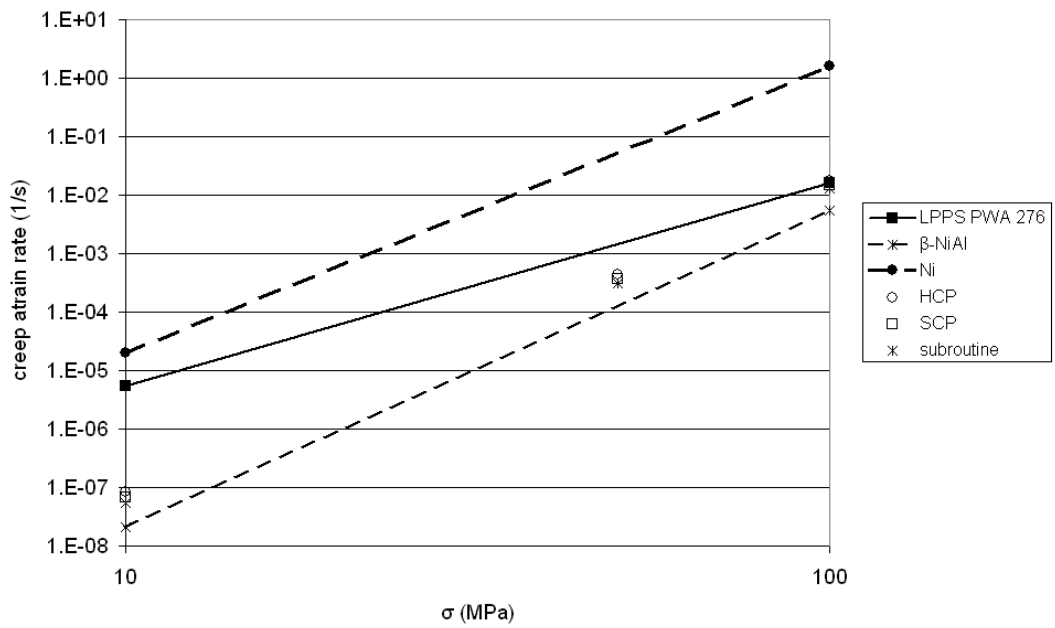


Figure 7.13: PWA 276 creep strain rate comparison at 1050°C.

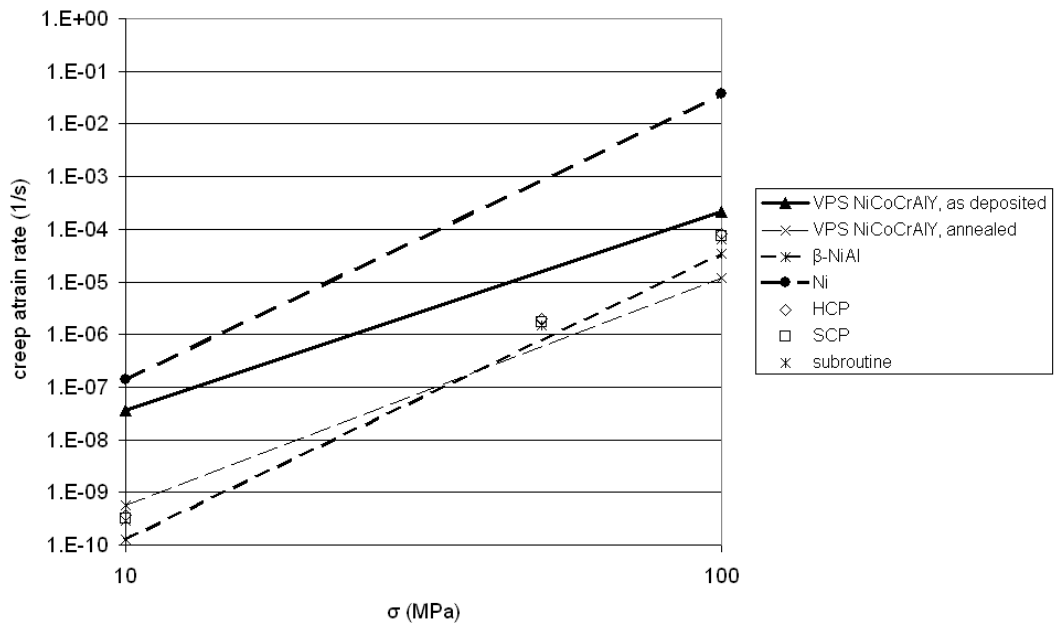


Figure 7.14: VPS NiCoCrAlY creep strain rate comparison at 850°C.

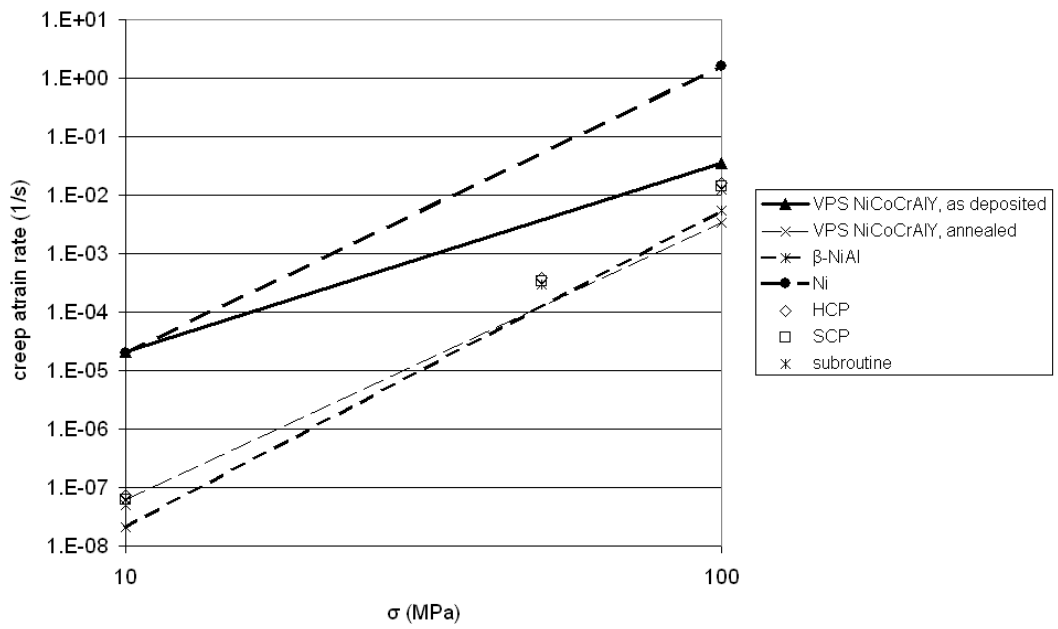


Figure 7.15: VPS NiCoCrAlY creep strain rate comparison at 1050°C.

Chapter 8

Modelling of the high temperature behaviour of TBCs using sequentially coupled microstructural-mechanical FE analyses

8.1 Introduction

The analysis presented in this chapter makes use of the self-consistent model explained in Chapter 6 coupled to a microstructural thermodynamic phase stability model [78,79], which takes into account the degradation that BCs undergo at high temperature. Additionally, the oxidation of the BC to create the TGO is simulated by the change in the phase proportions that originally compose the BC to pure alumina. This change is accompanied by a volume expansion that stresses the TGO and the surrounding layers.

The microstructural data that define the phase changes and oxidation of the

bond coat were obtained by means of an existing thermodynamic and phase stability model [78,79] that couples a calculation of phase equilibrium with a finite difference model of diffusion of elements in metallic alloys. These calculations simulate the diffusion of elements between the substrate material and the bond coat in TBCs. The results of the calculations consist of the microstructural evolution at different temperatures, specifically the phase proportions at each spatial position as a function of time. The TGO growth is simulated within the model and coupled with the diffusion of the oxide-forming elements, notably aluminium. In addition, analytical homogenisation approaches [27, 84] based on the work of Eshelby [80] and Mori and Tanaka [87], which take the form of the self-consistent model detailed in Chapter 6, were used to predict the creep behaviour of the resulting multiphase material under any specified conditions.

In practice, the alloying elements diffuse within and between the layers composing the TBC, provoking microstructural changes in them which are reflected in alterations in their mechanical properties. The self-consistent constitutive model used in this chapter, coupled to microstructural calculations, accounts for the degradation in the material properties arising from the microstructural evolution.

Coupled microstructural-mechanical models have been previously used by Busso *et al.* [25, 26, 51] in order to model the formation of oxide. However, the TGO layer was assumed to be composed of a mixture of alumina and an oxidation resistant phase, i.e. γ -Ni, even in the fully oxidised state. The oxidation process was simulated by means of the evolution of a function that progressed gradually from an initial value of 0 to a final value of 1, which represented the fully oxidised state, driven by the concentration of oxygen calculated from a diffusion analysis run prior to the structural analysis. The implementation of this model resulted in a gradual oxidation of the bond coat, which implied that the oxidising alloy was composed of the phases initially contained in it and of

oxide at the same time throughout the analysis, in contrast with the clear interface between the two layers (bond coat alloy and oxide) that experimental observation shows.

Due to the ranges of stress and temperatures to which TBCs are exposed, the main material properties to take into account are the elastic, coefficient of thermal expansion and creep properties of the composing layers and individual phases. Research carried out using Eshelby's [80] inclusion technique to obtain self-consistent relations applicable for both the calculation of elastic constants [82] and for the modelling of inelastic behaviours [27] such as creep will be presented along this chapter, with a complete explanation of the underlying theory being given in Chapter 6. A self-consistent model used to calculate the thermal expansion of a multiphase aggregate based on some of the results obtained by Wakashima *et al.* [81], again derived in Chapter 6, will also be presented.

The calculation described in this chapter is used to study the accumulation of stresses at high temperature caused primarily by oxidation. TBCs typically fail upon cooling from high temperature, but a certain amount of high temperature exposure is required for spallation to occur, implying that the oxidation and degradation of coated specimens create the critical conditions that are responsible for failure upon cooling, i.e. failure of TBCs is not driven by thermal shock alone, and high temperature processes play a critical role in the origin of the debonding of the layers.

8.2 Constitutive model

The constitutive model, developed in Chapter 6 and used in the present chapter to simulate the behaviour of the bond coat and TGO, incorporates the effect of the microstructural degradation and oxidation at high temperature and accounts

for non-isothermal and inelastic behaviour.

The aggregate stress, in rate form and assuming small material rotation, is expressed as

$$\dot{\boldsymbol{\sigma}} = \mathbf{C} : (\dot{\boldsymbol{\epsilon}} - \dot{\boldsymbol{\epsilon}}^{in}) - 3K\alpha\dot{T}\mathbf{1} \quad (8.1)$$

where $\dot{\boldsymbol{\sigma}}$ is the aggregate stress rate tensor, \mathbf{C} the elastic tensor, $\dot{\boldsymbol{\epsilon}}$ the aggregate total strain rate tensor, $\dot{\boldsymbol{\epsilon}}^{in}$ the aggregate inelastic strain rate tensor, K the aggregate bulk modulus, α the aggregate coefficient of thermal expansion and \dot{T} the rate of temperature change. The aggregate inelastic strain rate tensor, $\dot{\boldsymbol{\epsilon}}^{in}$, is composed of two parts, the strain rate tensor corresponding to creep, $\dot{\boldsymbol{\epsilon}}^{cr}$, and the transformation strain rate tensor, $\dot{\boldsymbol{\epsilon}}^{tr}$, originated from the volume expansion that the precipitation of new oxide causes. The aggregate inelastic strain tensor is then formulated as

$$\dot{\boldsymbol{\epsilon}}^{in} = \dot{\boldsymbol{\epsilon}}^{cr} + \dot{\boldsymbol{\epsilon}}^{tr} \quad (8.2)$$

with the aggregate creep strain tensor obtained as:

$$\dot{\boldsymbol{\epsilon}}^{cr} = \sum_g f^g \dot{\boldsymbol{\epsilon}}^{g,cr} \quad (8.3)$$

where f^g is the volume proportion at which phase g is present and $\dot{\boldsymbol{\epsilon}}^{g,cr}$ is its corresponding creep strain rate tensor. The transformation strain rate is:

$$\dot{\boldsymbol{\epsilon}}^{tr} = \frac{1}{3} \dot{f}^{ox} \ln(PBR_{eq}) \mathbf{1} \quad (8.4)$$

which imposes an isotropic volume expansion to the newly deposited oxide, as explained in Section 6.6.2. \dot{f}^{ox} is the rate at which oxide is being formed and PBR_{eq} the bond coat equivalent Pilling-Bedworth ratio, calculated following Equation 8.9.

Finally, the equation that links the stress-strain states in the aggregate, $\dot{\boldsymbol{\sigma}}$, and in the phases that compose it, $\dot{\boldsymbol{\sigma}}^m$, is, expressed in rate form [27]:

$$\dot{\boldsymbol{\sigma}}^m = \dot{\boldsymbol{\sigma}} + 2\mu(1 - \beta_t)(\dot{\boldsymbol{\epsilon}}^{cr} - \dot{\boldsymbol{\epsilon}}^{m,cr}) \quad (8.5)$$

where β_t is the result of the application of Eshelby's fourth order tensor, \mathbf{S} , to the case of a dispersion of spherical inclusions. Equations 8.1 - 8.5 are solved using an explicit-implicit numerical algorithm within the FE code ABAQUS by means of the UMAT user material subroutine [75]. Appendix D contains a complete reference and derivation of the numerical scheme implemented in the subroutine.

8.2.1 Additional considerations

The elastic tensor, \mathbf{C} , used in Equation 8.1 is fully defined by two elastic constants for isotropic materials. In this work, the elastic constants of the aggregate have been calculated using the expressions originally derived by Budiansky [82], and rederived in Chapter 6, using Eshelby's inclusion technique, as

$$\sum_{i=1}^N \frac{f^i}{1 + \beta_t \left(\frac{G^i}{G} - 1 \right)} = 1 \quad (8.6)$$

$$\sum_{i=1}^N \frac{f^i}{1 + \beta_n \left(\frac{K^i}{K} - 1 \right)} = 1 \quad (8.7)$$

where $\beta_t = \frac{2(4 - 5\nu)}{15(1 - \nu)}$, $\beta_n = \frac{1 + \nu}{3(1 - \nu)}$, $\nu = \frac{3K - 2G}{6K + 2G}$ and the i superscript refers to each of the composing phase.

The coefficient of thermal expansion, α , is calculated using an expression derived in Chapter 6 based upon the same hypotheses used by Wakashima *et al.* [81], but making use of the self-consistency approach instead of the mean-field criterion, which was generalised to take into account the presence of several phases, yielding

$$\alpha = \frac{\sum_g f^g \frac{K^g}{K^g + \frac{2 - 4\nu}{1 + \nu} K} \alpha^g}{\sum_g f^g \frac{K^g}{K^g + \frac{2 - 4\nu}{1 + \nu} K}} \quad (8.8)$$

where α^g are the CTEs of the phases present in the aggregate.

The Pilling-Bedworth ratio assumed in this work was calculated as an equivalent value for a multiphase alloy according to

$$PBR_{eq} = \sum_g f^g PBR^g \quad (8.9)$$

where PBR^g is the Pilling-Bedworth ratio of the phase g , defined as the ratio of the volume of formed oxide to the volume of consumed metal during oxidation.

8.3 Material properties

Calculations have been run assuming a typical configuration of a coated component, i.e. an IN-738LC base material with an MCrAlY bond coat and a plasma-sprayed PSZ top coat. Two alternative compositions were taken into account for the bond coat, namely LCO22 and PWA276, in order to assess any possible influence of their composition in the developed stress levels. The implementation of the different bond coat compositions is carried out by varying the phase proportions present in them.

The properties of the IN-738LC alloy have been extracted from Ref. [62] and are listed in detail in Chapters 4 and 5. Its nominal composition is given in Table 8.1. Temperature dependent elastic constants (see Table 8.2) and coefficient of thermal expansion, shown in Table 8.3, were used [62]. Secondary creep data provided in Ref. [62] were fitted using the least squares method to a Norton-type equation [69] as shown in Equation 8.10,

$$\dot{\epsilon}^{m,cr} = \frac{3}{2} A_0^m e^{-\frac{Q^m}{RT}} \sigma^{n^m-1} \mathbf{s}^m \quad (8.10)$$

where the creep exponent, n^m , was linearly interpolated between the two temperatures for which it is given in Table 8.4 in order to use the numerical values that provide the best approximation to the available experimental data, as explained in Chapter 4.

The material properties of the PSZ are the same as in Chapter 5, which are listed in Tables 8.3 and 8.4. The method of obtaining the creep constants that define the behaviour of the phases present in bond coats is explained in Chapter 7 and the elastic constants and CTEs are listed in Tables 8.2 and 8.3 respectively.

Xu and Wei [108] provide data of the Pilling-Bedworth ratios of γ' and β ; 1.795 and 1.71 were used in this analysis, respectively. No oxidation expansion was assumed for γ and σ , which effectively implies that the volume expansion upon oxidation is proportional to the fraction of aluminium-containing phases, i.e. β and γ' , as shown in Equation 8.9.

8.4 Finite element model

The FE meshes used in the analyses presented in this chapter are the same as in Chapter 5. Details on the model geometries and boundary conditions are explained in Section 5.2. Analyses have been run using 48 μm wavelength and 6 μm amplitude, 48 μm wavelength and 12 μm amplitude and 24 μm wavelength and 8 μm amplitude. An initial oxide thickness of 1 μm was assumed, except for the 48 μm wavelength and 6 μm amplitude model, for which analyses with 1, 3 and 5 μm were run.

8.4.1 Integration of FE and microstructural data

Fig. 8.1 contains a diagram that shows the information flow and coupling of the microstructural and mechanical analyses. The 1D microstructural calculations introduced in Section 8.1 [79] provide a series of ASCII files containing the phase proportions at each depth into the coating and substrate as a function of time, temperature and coating and substrate composition.

Since the microstructural results were generated using unidimensional meshes

and the structural analyses are run on 2D axisymmetric models, the results had to be interpolated from one mesh to the other one. The process to carry out that task involved finding the depth of the nodes in the 2D mesh from the surface of the TGO into the substrate, as the diagram in Fig. 8.2 shows, and using that coordinate to interpolate linearly in the 1D model that represents the TGO, bond coat and substrate arrangement. The interpolated phase proportions were then assigned to the node being considered. Post-processing programs, which use libraries that make it possible to manipulate ABAQUS binary `*.fil` files, have been coded in Fortran [93] and compiled using the `abaqus make` execution procedure [75] for that purpose. The compiled executable files use the geometric parameters a , L and h_0 in order to interpolate between the two different meshes as explained previously. They read the FE mesh data from a `*.fil` file and the microstructural results from the ASCII files. Finally, they generate new `*.fil` files that contain the volume proportion evolution of each individual phase mapped to the 2D models used in the present analyses.

The `*.fil` files obtained at the previous step are then passed onto ABAQUS by means of the “field variable” interface, i.e. each field variable represents the volume proportion of each phase present at the bond coat, the TGO being composed of a single phase corresponding to alumina.

Finally, calculations are run using the ABAQUS solver, where the constitutive model described in Section 8.2, implemented in a user material subroutine, UMAT, defines the behaviour of the bond coat and the oxide layer.

8.5 Results and discussion

Analyses for two different bond coats have been run, LCO22 and PWA276. The coatings were assumed to be stress-free at room temperature [12] and then isothermally heated up over a 30 min period and oxidised for 1000 h. The evo-

lution of the radial stress, which is perpendicular to the TGO-top coat interface and believed to be responsible for crack nucleation and propagation, with time is shown for several TBC systems at the top coat peak and valley and TGO centre locations detailed in Fig. 8.3.

8.5.1 Effect of imperfection size and initial oxide thickness

Fig. 8.4 shows the radial stress evolution in the top coat peak location with time when an LCO22 bond coat is assumed. In the results obtained for low $\frac{a}{L}$ ratios, the growth of the TGO does not reflect in the accumulation of tensile stress values, as opposed to the case for higher $\frac{a}{L}$ ratios, which implies that creep relaxation occurs when $\frac{a}{L}$ is low and stress accumulation for high $\frac{a}{L}$ ratios. A similar phenomenon has been reported in Refs. [13,49], in which it is suggested that there exists a critical imperfection aspect ratio, $\frac{a_c}{L}$, under which stresses responsible of crack opening do not accumulate.

If a PWA276 bond coat is assumed, the corresponding stress histories are shown in Fig. 8.5, which result in higher stress levels and stress rates, compared to those obtained with LCO22 bond coats, due to the increased Pilling-Bedworth ratio that this alloy exhibits. The stress “jumps” in Fig. 8.5 are due to the severe volume expansion imposed upon the elements undergoing oxidation, which is modelled as an instantaneous change from the phases that compose the unoxidised bond coat to pure α -alumina, accompanied by the corresponding expansion as explained in Section 8.2. In this case, the same phenomenon occurs as was found for TBCs with LCO22 bond coats, i.e. higher tensile stress levels and stress rates occur for higher $\frac{a}{L}$ ratios.

Similar observations regarding TC valley stresses can be made, as shown in Figs. 8.6 and 8.7. In this case the stresses are compressive and the oxidation

process imposes a compressive stress rate except for the low $\frac{a}{L}$ with LCO22 bond coat. When a certain value of $\frac{a}{L}$ is exceeded, the oxidation process is reflected in the accumulation of compressive stress in the top coat valley point. This process is more intense when PWA276 bond coats are assumed, as these have a higher aluminium content and thus higher γ' and β proportions resulting in a greater equivalent PBR according to Equation 8.9.

The trends in the growth stresses at the top coat peak point are consistent with other published calculations [26], which show that the oxidation produces tensile stresses at that location with increasing thermal exposure [12]. This phenomenon is more prevalent the higher the $\frac{a}{L}$ ratio is. The trends in the oxidation stresses obtained using the model presented in this chapter contrast with those obtained if the growth of the oxide layer is modelled by means of a swelling strain rate imposed to the oxide layer as in Chapter 5, for which the TC peak experiences compression and the valley tensile stresses [15].

8.5.2 Effect of temperature

The temperature dependency of the top coat peak stresses is shown in Fig. 8.8. Lower temperatures imply slower oxidation rates, which do not produce tensile stresses in the TC peak locations. Fig. 8.8 clearly shows that the PWA276 bond coat produces higher tensile stresses in the top coat peak location than the LCO22 alloy. These stresses are originated by its higher content in oxidation-prone phases such as γ' and β due to its higher content in aluminium.

8.5.3 TGO growth stress

More noteworthy than the evolution of the top coat stresses is the development of stress within the oxide layer. Since oxide formation is accompanied by a volume expansion according to the Pilling-Bedworth ratio of the alloy, the

precipitated oxide is initially subjected to compressive stresses caused by the presence of the surrounding material layers. In order to study the stress evolution of the oxide layer, a study is made of the radial stresses in the element in the central location between the peak and valley points adjacent to the initial oxide layer, i.e. the “TGO centre” location in Fig. 8.3, is considered.

Fig. 8.9 shows the stress evolution at the location previously identified when an LCO22 bond coat is assumed. The effect of different initial oxide thicknesses, h_0 , can be assumed to be minor compared with the imperfection aspect ratio, $\frac{a}{L}$. The first part of the graph shows a steep addition of compressive stress that arises from the restriction to the expansion imposed by the surrounding material. From that point, and as the oxide grows and its interface with the bond coat advances inwards into that layer, the oxide created at the beginning of the analysis begins to accumulate tensile stress, which originates as a reaction to the expansion attempts of the additional oxide being formed. This accumulation of tensile stress at high temperature may be the origin of the cracks within the oxide layer reported in Refs. [25,52] after high temperature exposure.

A similar situation, although with higher stress levels, appears when a PWA276 bond coat is assumed as in Fig. 8.10. In this case, the intensity of the stresses and the rate at which they change is noticeably higher due to the higher content of aluminium and oxidation-prone phases in this alloy, causing the stresses to reach values over 1 GPa.

A comparison of the effect of temperature in both type of TBCs is given in Fig. 8.11, which shows its very significant effect in the development of tensile stress. The steep changes in the stress values is due to the severe volume changes that arise upon the creation of new oxide.

8.6 Conclusions

A coupled microstructural-mechanical model has been implemented using the finite element method. The microstructural results from a one dimensional finite difference diffusion model, which simulated the material degradation and phase transformation upon thermal exposure, were imported in ABAQUS [75] by means of post-processing programs compiled using the `abaqus make` execution procedure. A material user subroutine, based on Eshelby's inclusion technique [80], models the bond coat as a multiphase aggregate taking into account the properties of each individual phase that composes it.

The TGO growth is modelled by changing the microstructure of the bond coat elements adjacent to the oxide layer to that of pure alumina and imposing a volumetric expansion according to the PBR of the oxidation reaction. The PBR used in this chapter was calculated as the equivalent value taking into account the individual ratios of the phases that compose the bond coat alloy and its microstructure. However, in view of the impact of this parameter in the achieved stress levels, further investigations into the estimation of that ratio are needed.

Additionally, the simplifications assumed in the composition and mechanical properties of the phases imply that aluminium is not present in the γ phase, neglecting the contribution to alumina formation of that phase. Another source of stress in the bond coat/TGO vicinity is that reported by Tolpygo and Clarke [11], who suggested that the $\beta \rightarrow \gamma'$ reaction was accompanied by a volume contraction that would influence the stress levels achieved.

Analyses were run for two different temperatures, 800°C and 900°C, for a 1000 h exposure time. All the material layers were assumed to creep at elevated temperature. Stresses at peak and valley points of the top coat and at the centre of the bond coat adjacent to the initial oxide layer, which represents

the first fraction of oxide being formed, were studied, leading to the following conclusions:

- The effect of TGO oxidation and growth on the top coat is the accumulation of tensile stresses in the peak location. However, the results for low $\frac{a}{L}$ ratios do not show any stress accumulation, suggesting the existence of a critical imperfection aspect ratio, $\frac{a_c}{L}$, under which stresses in the top coat do not accumulate.
- Of the two bond coats studied in this work, the PWA276 alloy, which is richer in aluminium, produces higher stress levels than LCO22. The severity of the oxidation model creates abrupt jumps in the stress with time, a phenomenon that is believed to be due to the discrete nature of FE modelling.
- Growth of the TGO produces an inverse effect on the TC valley locations when compared to peak points; the stress normal to the interface, or equivalently the radial stress in the models used in this work, accumulated compressive stress upon oxidation, this process being more intense for higher temperatures, $\frac{a}{L}$ ratios and for higher Al contents in the bond coat.
- Stress values in the vicinity of the initial oxide layer, i.e. the first oxide formed, reveal that they experience a fast compression arising because the Pilling-Bedworth ratio of the bond coat alloy is higher than unity. That process is typically followed by the accumulation of tensile stresses perpendicular to the TGO/TC interface imposed by the oxide that forms subsequently, reaching in some cases levels over 1 GPa.
- Tensile stresses accumulate in the oxide layer; these stresses may be responsible of in-plane cracking of the TGO layer and cause partial debond-

ing and crack initiation at high temperature. This creates the critical conditions for subsequent top coat spalling upon cooling to room temperature.

Element wt%	IN-738LC, [62]	LCO22 [72]	PWA 276 [71]
Ni	61	32	48.29
C	0.11	-	0.01
Co	8.5	38.5	20.3
Cr	16	21	17.3
Mo	1.75	-	-
W	2.6	-	-
Ta	1.75	-	-
Nb	0.9	-	-
Al	3.4	8	13.6
Ti	3.4	-	-
Al+Ti	6.8	-	-
B	0.01	-	-
Zr	0.05	-	-
Fe, Mn, Si, S	low as possible	-	-
Y	-	0.5	0.5

Table 8.1: Nominal compositions of substrate and bond coats.

T (°C)	IN-738LC, [62]	γ -Ni, [101]	γ' -Ni ₃ Al, [103]	β -NiAl, [94]	σ -Cr, [101]	α - Al ₂ O ₃ , [63]
10	-	-	184.536 / 0.32	-	-	-
20	-	-	-	-	-	416 / 0.231
23.9	200.6 / 0.28	-	-	-	-	-
27.0	-	206.718 / 0.31	-	188.0 / 0.313	304.92 / 0.21	-
93.3	195.1 / 0.27	-	-	-	-	-
204.4	190.3 / 0.27	-	-	-	-	-
315.6	184.8 / 0.28	-	-	-	-	-
426.7	179.3 / 0.28	-	-	-	-	-
537.8	175.1 / 0.30	-	-	-	-	-
648.9	167.6 / 0.30	-	-	-	-	-
760	157 / 0.3	-	-	-	-	-
850	-	-	142.2568 / 0.337	-	-	-
871.1	151 / 0.29	-	-	-	-	-
982.2	140 / 0.30	-	-	-	-	-
1000	-	132.1366 / 0.31	-	150.0 / 0.313	236.3377 / 0.21	-
1500	-	-	-	-	-	338 / 0.252

Table 8.2: Elastic properties of materials, E (GPa) / ν .

T (°C)	IN-738LC, [62]	γ -Ni [109]	γ' Ni ₃ Al, [94]	β -NiAl, [94]	σ -Cr [109]	α Al ₂ O ₃ , [63]	APS PSZ, [45]
20	-	13.1	-	13.2	6.2	-	-
23.9	11.23	-	-	-	-	-	-
27.0	-	-	12.5	-	-	-	-
93.3	11.97	-	-	-	-	-	-
100	-	-	-	-	-	-	8.82
200	-	-	-	-	-	-	9.4
204.4	13.23	-	-	-	-	-	-
300	-	-	-	-	-	-	9.75
315.6	14.4	-	-	-	-	-	-
400	-	-	-	-	-	-	10
426.7	15.46	-	-	-	-	-	-
500	-	-	-	-	-	8.3	10.2
537.8	16.2	-	-	-	-	-	-
600	-	-	-	-	-	-	10.4
648.9	16.63	-	-	-	-	-	-
700	-	-	-	-	-	-	10.5
27.0	-	-	16.8	-	-	-	-
760	18.38	-	-	-	-	-	-
800	-	-	-	-	-	-	10.6
871.1	19.42	-	-	-	-	-	-
900	-	-	-	-	-	-	10.7
962.2	20.7	-	-	-	-	-	-
1000	-	-	-	-	-	-	10.8
1100	-	-	-	-	-	-	10.9
1175	-	-	-	-	-	-	11.0
1500	-	-	-	-	-	9.7	-

Table 8.3: CTE $\times 10^6$ of materials ($^{\circ}C^{-1}$).

Material	A_0 ($\text{MPa}^{-n}\text{s}^{-1}$)	Q $\text{kJ} \cdot \text{mol}^{-1}$	n at 850°C	n at 1050°C	s
IN-738LC, [62]	6.68×10^{48}	1721	9.96	6.6	-
$\alpha - \text{Al}_2\text{O}_3$, [63]	415.12	325	1.08	1.08	-
YSZ, [73]	0.026	104.5	0.56	0.56	0.67
NiAl (β) [94–99]	2.18×10^{-1}	315.0	5.42	5.42	-
Ni (γ) [101]	2.79×10^5	381.0	5.42	4.90	-
Cr (σ) [101]	1.24×10^4	384.0	4.94	4.48	-
Ni_3Al (γ') [102]	8.19×10^{-14}	26.8	3.14	4.30	-

Table 8.4: Creep properties of materials.

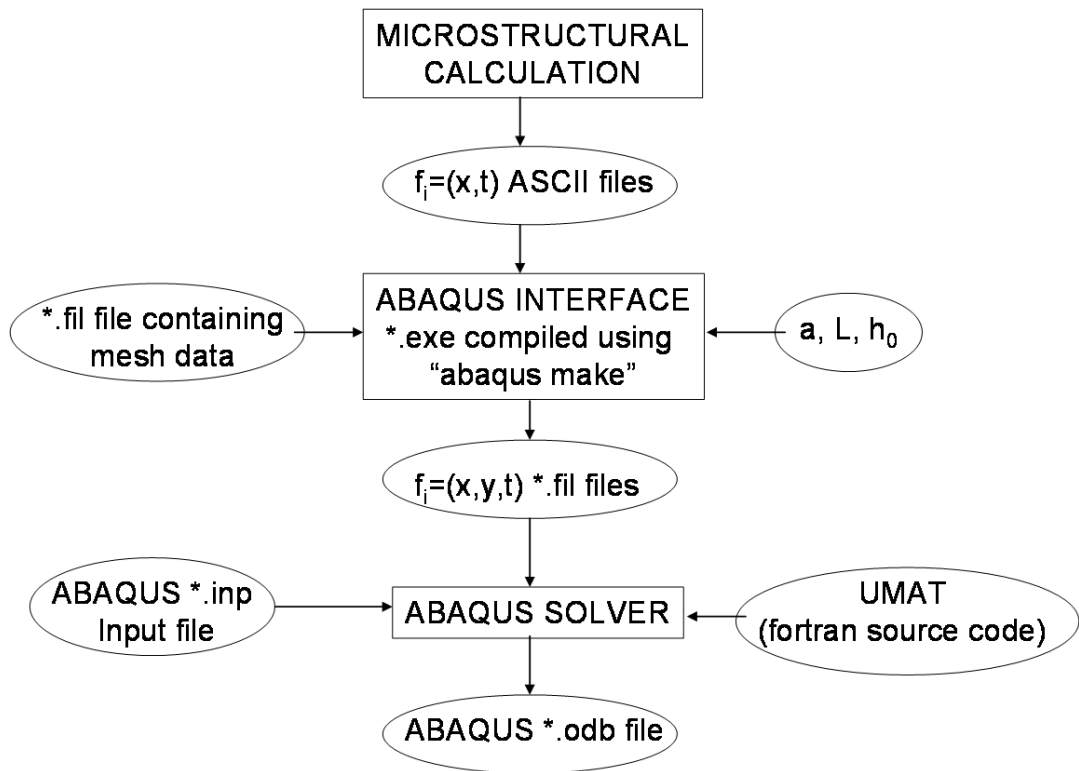


Figure 8.1: Diagram showing the flow of information in the sequentially coupled microstructural-mechanical analysis.

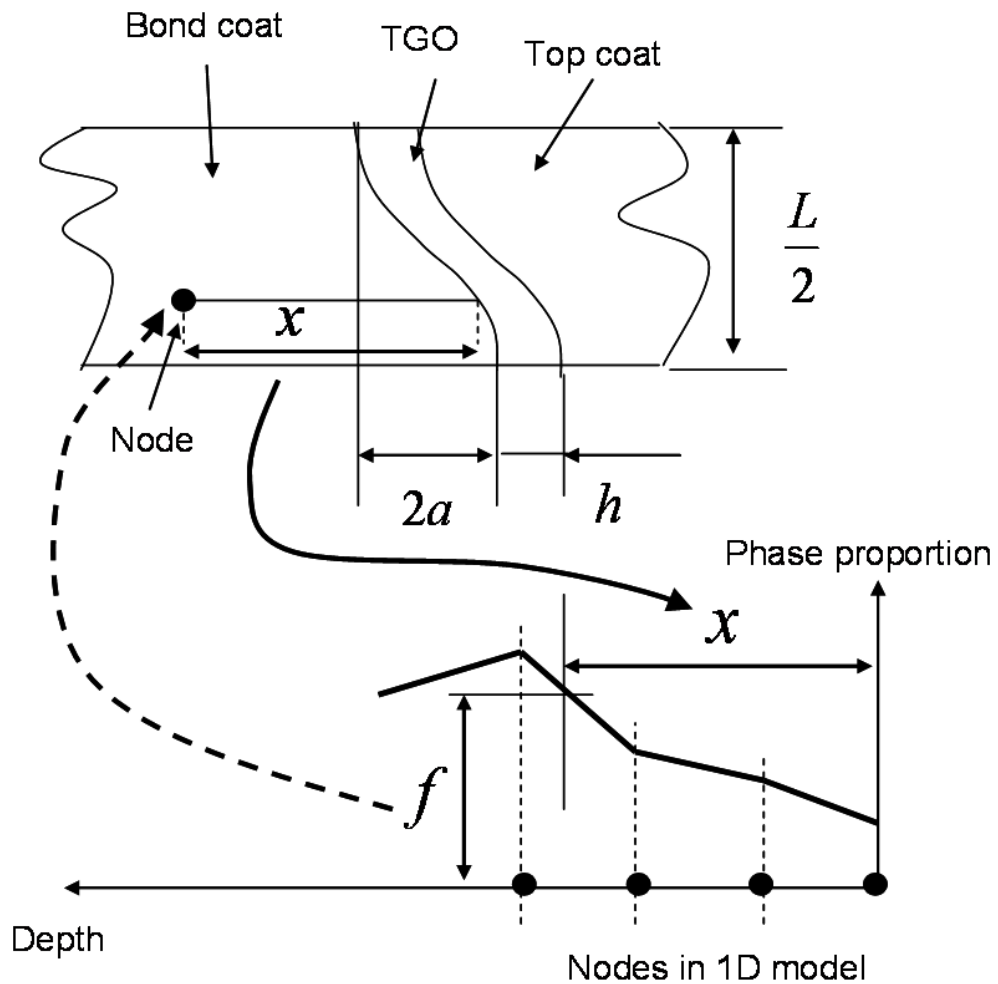


Figure 8.2: Diagram showing the linear interpolation carried out in order to transfer the microstructural data from the 1D finite differences model to the 2D finite element mesh. The continuous arrow represents the use of the depth, x , read from the FE mesh, to interpolate the phase proportions, f , which are then assigned back to the node under consideration, as indicated by the discontinuous line.

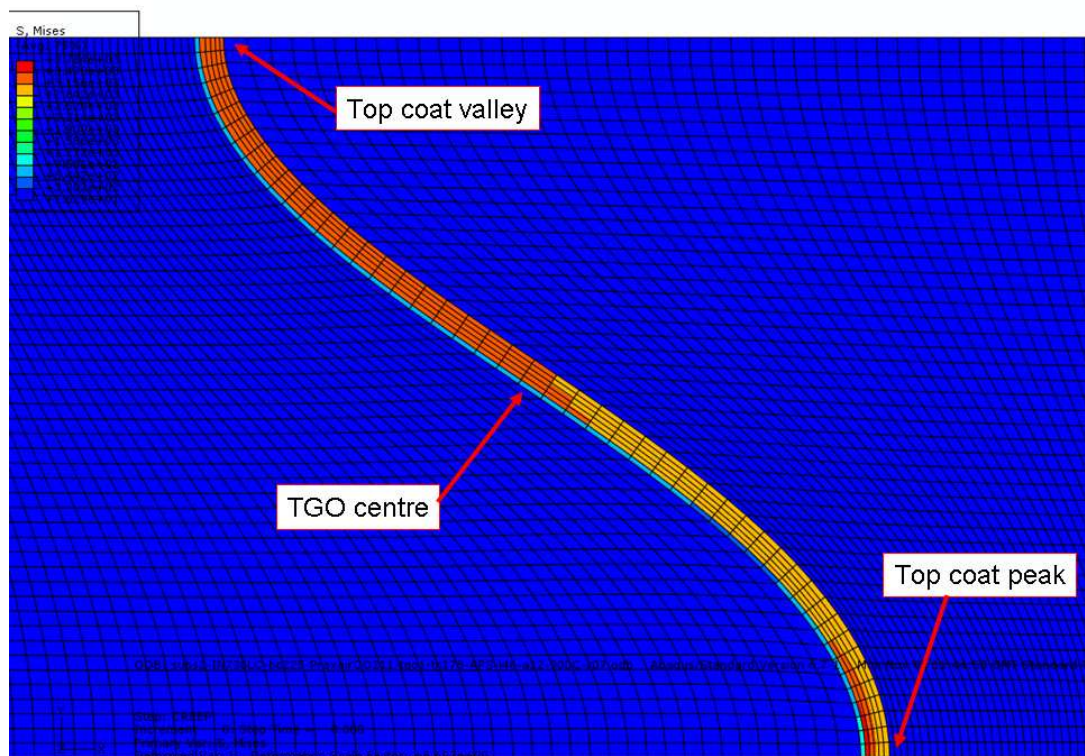


Figure 8.3: Locations where the radial stresses have been studied.

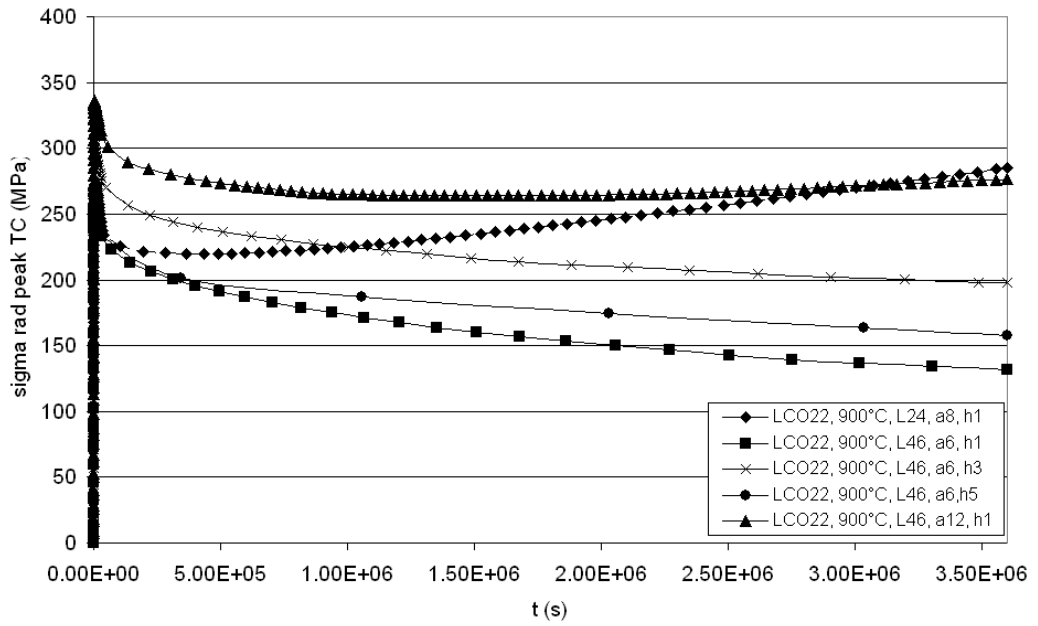


Figure 8.4: TC peak radial stress evolution with time at 900°C using different geometric parameters, assuming an LCO22 bond coat.

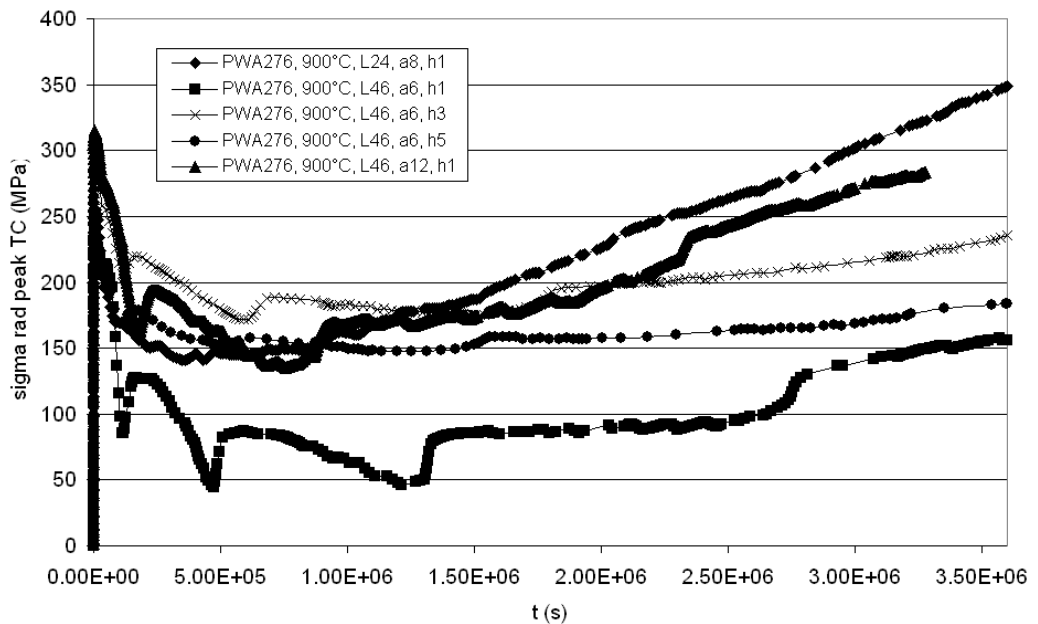


Figure 8.5: TC peak radial stress evolution with time at 900°C using different geometric parameters, assuming a PWA276 bond coat.

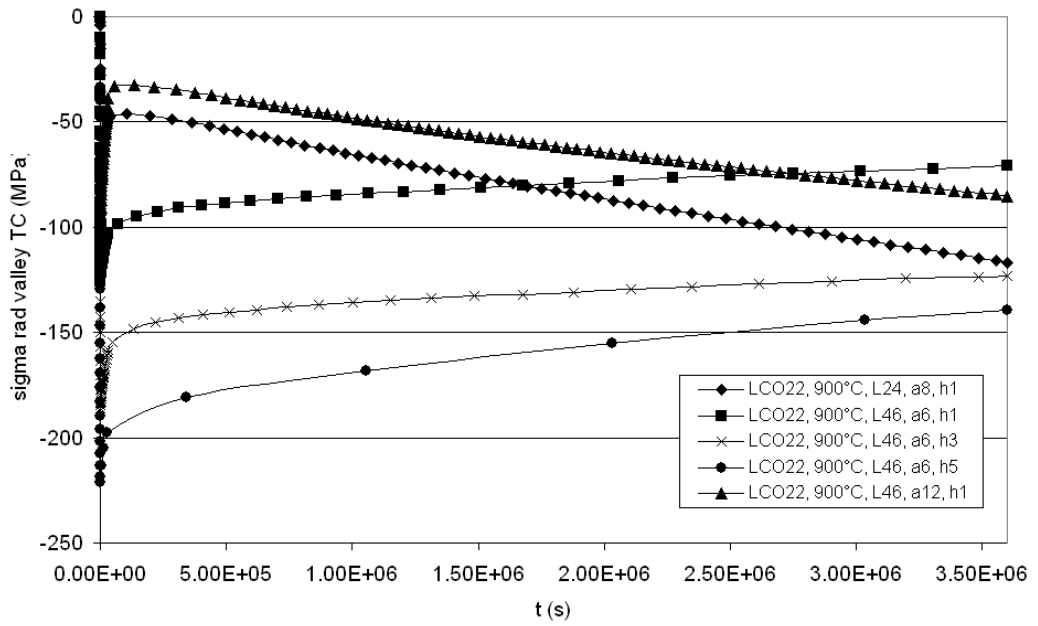


Figure 8.6: TC valley radial stress evolution with time at 900°C using different geometric parameters, assuming a LCO22 bond coat.

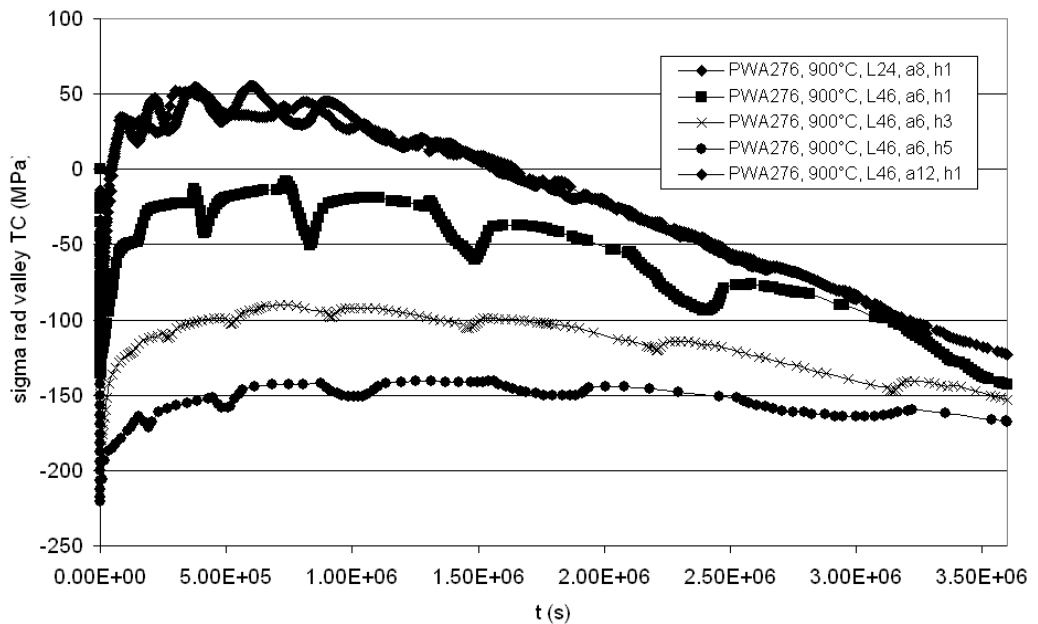


Figure 8.7: TC valley radial stress evolution with time at 900°C using different geometric parameters, assuming a PWA276 bond coat.

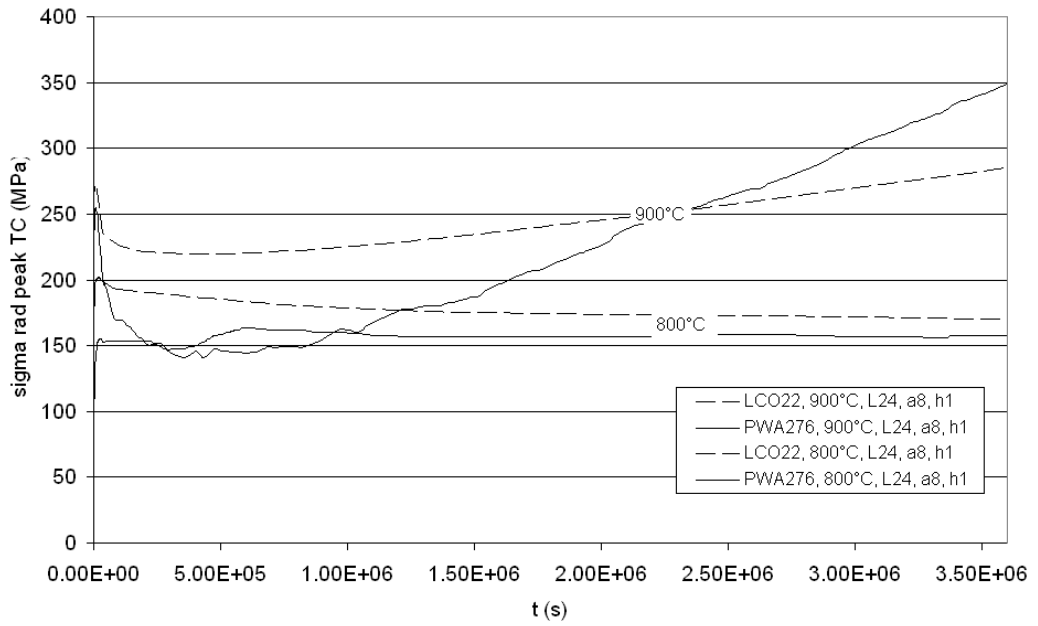


Figure 8.8: Effect of temperature and bond coat composition on the TC peak radial stress evolution with time, with $L=24 \mu\text{m}$, $A=8 \mu\text{m}$ and $h_0=1 \mu\text{m}$.

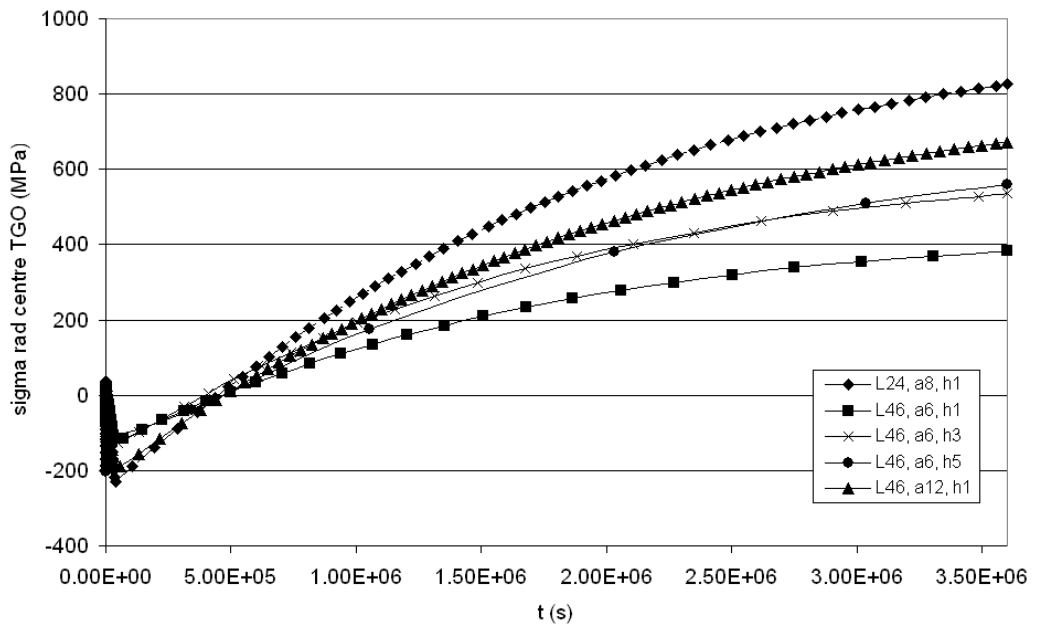


Figure 8.9: TGO centre radial stress evolution with time at 900°C using different geometric parameters, assuming an LCO22 bond coat.

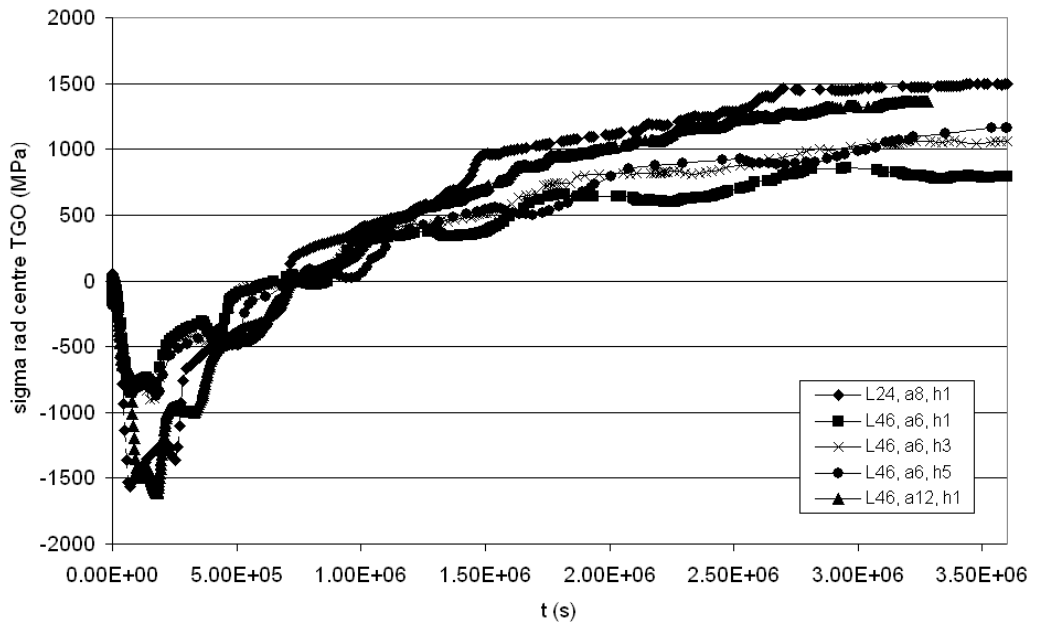


Figure 8.10: TGO centre radial stress evolution with time at 900°C using different geometric parameters, assuming a PWA276 bond coat.

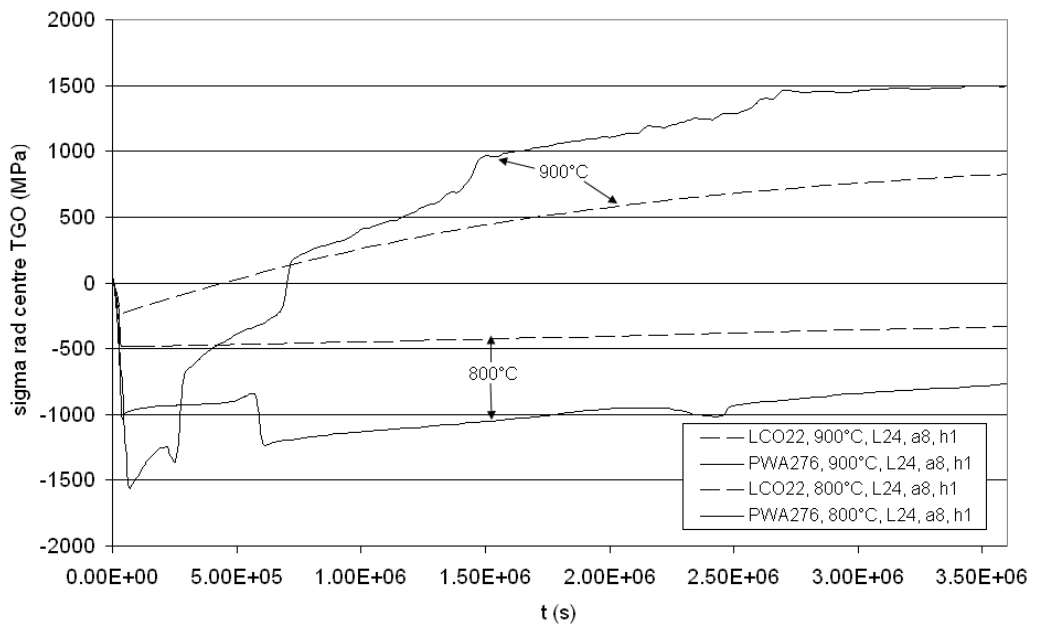


Figure 8.11: Effect of temperature and bond coat composition on the TGO centre radial stress evolution with time, with $L=24 \mu\text{m}$, $A=8 \mu\text{m}$ and $h_0=1 \mu\text{m}$.

Chapter 9

Conclusions

9.1 Thermal analysis of coated tensile specimens

In order to gain an understanding of the temperature distributions involved in high-temperature tensile creep tests on coated specimens, a series of FE analyses was undertaken. Initially, due to the availability of consistent experimental data, EB-PVD top coats were assumed in the calculations, which were finally generalised by assuming a decrease in the PSZ conductivity by one order of magnitude. These last conditions cover the range of thermal properties for both EB-PVD and APS coated specimens.

Transient and steady state thermal conditions were simulated. The thermal gradients obtained across the TBCs, even during the transient stages, were found to be of the order of $\sim 10^{\circ}\text{C}$, much lower than the large temperature differentials across the coating under service conditions. This confirmed that no damage will be initiated by temperature differentials alone during high temperature tests of tensile coated specimens.

Analyses were run assuming both a uniform furnace wall temperature and

a non-uniform temperature distribution similar to that produced by a three zone heater. The axial temperature distribution was found to be dependent on the configuration of the heater, as intuitively presumed. A uniform axial temperature profile in the specimen was obtained when the three zone heater configuration was assumed, which did not depend on the presence of the coating, i.e. uniform temperature distributions were calculated regardless of whether the specimen was coated or uncoated.

The results of the thermal analyses showed that the presence of the coating does not produce a significant temperature drop across them, confirming the feasibility of monitoring the surface temperature during tests and assuming that the underlying substrate is at the same temperature, as occurs with uncoated specimens.

9.2 Creep tests of coated and uncoated specimens

Creep tensile tests at several temperatures were carried out with two Ni-base substrate alloys, IN-738LC and CMSX-4. Extra tests were performed using TBC coated tensile specimens. The experimentally obtained creep response was then compared with theoretical predictions, calculated using models fitted prior to testing from published material data. The experimental and predicted creep showed good numerical agreement.

Regarding the coated specimens, one CMSX-4 EB-PVD coated specimen was tested, which crept at a faster rate than the equivalent uncoated one, suggesting that these kind of coatings do not take any tensile load, in accordance with their “strain tolerant” configuration originated by the columnar grain structure. IN-738LC APS coated specimens, in contrast, showed decreased creep strain rates.

FE modelling was used to study the creep behaviour of these specimens under testing conditions, showing good numerical agreement with the experimental results. The mechanical properties used for the different layers that compose the coating were extracted from published research, which the tests undertaken here served to validate.

9.3 Modelling of oxidation stresses using swelling strain rates

The oxidation and high temperature mechanical behaviour of coatings was studied by means of FE models that incorporated thermal mismatch, creep of the different layers that compose the TBC, and oxidation, based on an experimentally obtained TGO growth equation. The mechanical properties used in this analysis were extracted from published research and validated through comparison with the results of experiments carried out on coated specimens.

The models included the growth of the TGO by imposing swelling strain rates to the elements that compose it, following the practice of existing published research. The TGO swelling strain rates were divided in thickening strain rates, which were perpendicular to the bond coat/TGO/top coat interface, and lengthening strain rates, which accounted for the deposition of new oxide between the grains that compose it.

The main conclusion drawn from these analyses is that the stress level in the top coat is mainly a function of the swelling strain rate imposed on the TGO in order to model its growth. The assumption of different initial oxide thicknesses implies that, in order to achieve the same oxide growth under the same conditions, the swelling strain rate depends on that geometric parameter, as it is calculated as the ratio of the oxide growth rate divided by its thickness.

Results show a very high sensitivity of the stresses believed to be responsible of spallation upon the initial oxide thickness, which does not seem to be a realistic situation. In addition, the calculated stress levels were extremely high when a set of realistic material properties was assumed.

The calculated stresses followed the trends reported by other researchers, but the tensile and compressive stresses were located in different areas of the oxide-top coat interface compared with the stress maps reported using more realistic oxidation models.

9.4 Self-consistent constitutive model development and implementation

A number of papers on the development of constitutive models that deal with the calculation of the elastic, thermal and creep properties of multiphase aggregates were reviewed and the main equations were rederived in order to understand the implications and limitations of the hypotheses under which they were developed. This resulted in the formulation of a constitutive model that makes it possible to calculate the mechanical response of a multiphase aggregate from the behaviour of the isolated phases that compose it. An explicit-implicit integration scheme was developed for the constitutive model and implemented in an ABAQUS user-defined material subroutine, UMAT, in order to overcome the uncertainty that arises from the poor reproducibility of bond coat mechanical properties. The use of this constitutive model allows to evaluate the implications of the high temperature degradation of coatings in the stresses that arise upon oxidation.

Since the microstructure of the aggregate alloy is defined by the volume proportions of the phases present in it, the oxidation of an element of bond coat in an FE mesh can be simulated by a fast change from the phases composing it,

i.e. γ -Ni, γ' - Ni₃Al, σ -Cr and β -NiAl, to α -alumina. The underlying theory is that γ' - Ni₃Al and β -NiAl oxidise to produce α -alumina and γ -Ni and this last element diffuses back into the unoxidised bond coat creating a TGO layer composed purely of alumina. This method of simulating oxidation is more realistic than others available in published research as it produces a clear interface between the unoxidised alloy and the oxide layer, as shown by experimental observation.

9.5 Modelling the creep properties of MCrAlY bond coats using finite element unit cells and self-consistent constitutive models

FE unit cells were used to model the creep behaviour of MCrAlY bond coats. The microstructural data regarding the phases present at each considered temperature for each composition were obtained from thermodynamic phase equilibrium calculations. Creep properties of various MCrAlY alloys manufactured using different methods and of the phases that compose them were gathered from different publicly available sources. The properties of the individual phases were then used to simulate the creep behaviour of the MCrAlYs by means of the aforementioned three-dimensional unit cells and the self-consistent constitutive model coded in an ABAQUS UMAT subroutine.

Results showed that the agreement between the predictions of the unit cells and the self-consistent constitutive model was reasonably good, this last approach showing advantages as the applicability to FE analyses covering a gradual change in the microstructure as that occurred upon β depletion in the outer region of bond coats.

The properties reported for several MCrAlYs showed poor reproducibility

and high dependency on the manufacturing process, which limits the practical applicability of the experimentally obtained data. An additional problem in the modelling of TBCs is that the bond coat undergoes severe microstructural changes caused by oxidation at high temperature and interdiffusion of certain elements, especially aluminium, which depletes from some zones. As a consequence of this depletion, the bond coat alloy is significantly different in the as-deposited condition and after high temperature exposure, which makes the real process that bond coats undergo in service extremely difficult to simulate in experimental tests.

Reasonable agreement was observed between the creep properties predicted using the values reported for the phases that compose the MCrAlY and the alloys manufactured by LPPS or VPS, in contrast with the relatively creep-resistant HIP MCrAlY, which confirms that it is acceptable to use the self-consistent constitutive scheme in the modelling of TBCs.

However, the main applicability of the self-consistent modelling of bond coat alloys is to serve as a reliable method of extrapolating or normalising the trends shown by this alloys from first principles.

9.6 Modelling of the TBC high temperature response using a coupled microstructural-mechanical framework

A sequentially coupled microstructural-mechanical analysis was used in order to study the high temperature behaviour of coatings and the accumulation and concentration of stresses that may cause the critical conditions at elevated temperature responsible for spallation upon cooling. Results were generated from a one dimensional diffusion model, which used thermodynamic phase equilibrium

calculation, assuming different temperature conditions for two different coatings: one being an LCO22 bond coat and the other being a PWA 276 coat. These results were used as the input to FE analyses run using the ABAQUS package. A user material subroutine, UMAT, was coded in order to incorporate the microstructural degradation and oxidation of the bond coat into the FE calculations.

Results showed the accumulation of tensile stresses at the TGO-top coat peak location, which may cause crack nucleation during oxidation. Additionally, high tensile stresses were developed within the oxide layer at the locations where cracks were reported in published research after exposure to high temperatures.

The composition of the bond coat alloy was found to be determinant in the stress levels achieved, due to its influence on the Pilling-Bedworth ratio. The effect of the bond coat/TGO/top coat imperfection aspect ratio was evaluated, identifying the same effect reported using other oxidation models, i.e. higher intensities in the interface flaw result in higher stress concentrations.

However, the most remarkable phenomenon identified in those analyses was the accumulation of tensile stresses perpendicular to the TGO/top coat interface within the oxide layer. The stress levels achieved depend on the composition of the bond coat and are determined by the Pilling-Bedworth ratio of the bond coat alloy next to the TGO, which is a linear function of the aluminium-containing phases, i.e. γ' and β . Steady state stresses over 1 GPa were obtained when a PWA 276 bond coat was assumed, which would imply cracking within the oxide layer after high temperature exposure, as reported in published research.

9.7 General conclusions

The research presented in this thesis explores the high temperature oxidation of TBCs and the stresses developed during that process, which are believed to cause

the initiation of damage and crack nucleation. The coupled microstructural-mechanical calculation predicts the accumulation of high tensile stresses perpendicular to the TGO/top coat interface within the oxide, which may be responsible for crack opening at high temperature, creating the conditions for spallation upon cooling.

In general, high temperature stress levels are conditioned by two opposing phenomena, namely the oxidation stresses due to the volume changes that arise from the precipitation of oxide, and creep, which acts as a stress relieving mechanism. Both processes are enhanced at higher temperatures, but the stress levels achieved are higher for higher temperatures. This implies that oxidation is more powerful in introducing stress than creep in relieving it.

While computed thermal mismatch stresses are large enough to cause cracking in the TGO, reality shows that they cannot explain failure of the TBCs by themselves exclusively; coatings need a certain amount of high temperature exposure before they fail when cooled to room temperature. Published research shows that, even after severe cycling of coated specimens, interfacial cracks appear within the ceramic top coat near to its interface with the oxide layer. This phenomenon is caused primarily by the morphological instability due to ratcheting, or accumulated cyclic inelastic deformation of the bond coat, which results in the “wrinkling” of the TGO. Surprisingly, even under these conditions, TGOs do not show significant cracking, which makes the hypothesis of the implication of the thermal mismatch stresses responsible of TGO cracking unclear.

In particular, two features that define the intensity of the stress concentration, once the temperature and exposure time have been fixed, have been identified. The first feature is the aspect ratio of the imperfections found in the TC/TGO/BC interface. Higher aspect ratios result in greater stress concentrations. From that point of view, a low interface waviness reduces the magnitude of the out-of-plane stresses, improving the durability of coatings, but a certain

level of roughness is required to guarantee mechanical bonding. The second factor to be taken into account is the volume expansion provoked by the precipitation and growth of the TGO. From this point of view, a slow growing oxide layer would improve the lifetime of coatings. The composition of the bond coat plays an important role as ideally the precipitated oxides should produce low volumetric changes in order to reduce the accumulation of growth stress within the oxide and thus avoid crack nucleation during exposure to elevated temperature.

Chapter 10

Future work

10.1 Further research in material properties

Some innovative testing techniques have been developed in published research and applied in order to obtain the mechanical and thermal properties of the materials used in TBCs. However, the effect of long thermal exposure times in the mechanical degradation of bond coats has not been properly addressed. The use of nanoindentation of coated components after service may help in the understanding of the change in material properties an phenomena such as top coat sintering, TGO cracking and bond coat degradation and aluminium depletion.

10.2 Improvements in the material constitutive model

The constitutive model used in the present thesis makes use of Eshelby's inclusion technique to calculate the mechanical response of a multiphase aggregate from the properties of the phases that compose it and the volume proportions at which they are present. However, the constitutive equations were developed

considering that the shape of the precipitates present in the alloy was spherical, which is not a totally realistic assumption. A more detailed modelling of the material behaviour could include the effect of the shape of the precipitates in the response of the aggregate material and account for stress concentrations that induce microcracking of the material. The inclusion of the shape of the precipitates in the constitutive model is carried out by the use of an alternative \mathbf{S} tensor, which is a fourth order tensor that introduces additional complexity to the constitutive equations. A simpler method of including the effect of the precipitate shape is by using alternative β parameters in the constitutive equations. Additionally, damage mechanics can be included in the constitutive model for each of the composing phases. The formulation of a brittle failure damage model for the oxide layer is particularly interesting as it would make it possible to understand the extent of cracking and loss of load bearing cross-section during high temperature exposure.

The TGO growth has been assumed to be isotropic in this work. Other researchers have introduced non-isotropic effects, using preferred growth directions based either on the deviatoric stress tensor or on the through-thickness or transverse growth directions. The directionality of the oxide growth has an impact on the magnitude of the developed stresses, but in order to do realistic estimations of this effect more experimental evidence of this phenomenon is required.

Additional work is required in order to represent the volume changes caused by the precipitation of oxide and microstructural degradation of bond coats in an accurate manner. The approach followed in this thesis considers the expansion of γ' and β upon oxidation in order to obtain the Pilling-Bedworth ratio of a multiphase alloy. However, the composition of each phase present in the bond coat was simplified, neglecting the contribution of some of the phases that contain aluminium, e.g. γ , to the oxide layer growth. Another phenomenon

that has been suggested to take place during high temperature degradation of bond coats is the volume contraction associated with the aluminium depletion in the outer layer of the bond coat, which manifests itself as the $\beta \rightarrow \gamma' \rightarrow \gamma$ reaction.

10.3 Response to thermal and mechanical cycling

This thesis has focused on the high temperature oxidation of TBCs and its associated stress accumulation. However, a broader study of the coatings should include the response to cyclic loading. Thermal cycling has been extensively studied in the literature, being the morphological instability of the TGO the most remarkable consequence of it, according to published research. In any case, the coupled constitutive model used in this work could provide additional insight in the cyclic response.

Cyclic loads, such as those occurring during service start and stop cycles, have not been properly addressed, and they constitute an additional source of damage for coated components.

References

- [1] F. O. Soechting. A design perspective on thermal barrier coatings. *Thermal barrier coating workshop, NASA Conference Publication 3312*, pages 1–15, 1995.
- [2] G. W. Goward. Progress in coatings for gas turbine airfoils. *Surface and Coatings Technology*, 108-109:73–79, 1998.
- [3] J. Stringer. Coatings in the electricity supply industry: past, present and opportunities for the future. *Surface and Coatings Technology*, 108-109:1–9, 1998.
- [4] M. Eskner. *Mechanical behaviour of gas turbine coatings*. PhD thesis, KTH, Royal Institute of Technology, Stockholm, Sweden, 2004.
- [5] H. Herman and C. C. Berndt. Plasma spray processing of TBCs. *Thermal barrier coating workshop, NASA Conference Publication 3312*, pages 127–134, 1995.
- [6] L. B. Chen. Yttria-stabilized zirconia thermal barrier coatings - a review. *Surface Review and Letters*, 13(5):535–544, 2006.
- [7] D. V. Rigney, R. Viguie, and D. J. Wortman. PVD thermal barrier coating applications and process development for aircraft engines. *Thermal barrier coating workshop, NASA Conference Publication 3312*, pages 135–149, 1995.

- [8] C. Leyens, U. Schulz, M. Bartsch, and M. Peters. R&D status and needs for improved EB-PVD thermal barrier coating performance. *Materials Research Society Symposium Proceedings*, 645E:74–85, 2001.
- [9] P. K. Wright and A. G. Evans. Mechanisms governing the performance of thermal barrier coatings. *Current Opinion in Solid State and Materials Science*, 4:255–265, 1999.
- [10] A. G. Evans, D. R. Mumm, J. W. Hutchinson, G. H. Meier, and F. S. Pettit. Mechanisms controlling the durability of thermal barrier coatings. *Progress in Materials Science*, 46:505–553, 2001.
- [11] V. K. Tolpygo and D. R. Clarke. Surface rumpling of a (Ni, Pt)Al bond coat induced by cyclic oxidation. *Acta Materialia*, 48:3283–3293, 2000.
- [12] A. M. Freborg, B. L. Ferguson, W. J. Brindley, and G. J. Petrus. Modeling oxidation induced stresses in thermal barrier coatings. *Materials Science and Engineering A*, 245:182–190, 1998.
- [13] M. Y. He, A. G. Evans, and J. W. Hutchinson. The ratcheting of compressed thermally grown thin films on ductile substrates. *Acta Materialia*, 48:2593–2601, 2000.
- [14] J. Rösler, M. Bäker, and M. Volgmann. Stress state and failure mechanisms of thermal barrier coatings: Role of creep in thermally grown oxide. *Acta Materialia*, 49:3659–3670, 2001.
- [15] J. Rösler, M. Bäker, and K. Aufzug. A parametric study of the stress state of thermal barrier coatings. Part I: Creep relaxation. *Acta Materialia*, 52:4809–4817, 2004.

- [16] A. M. Karlsson and A. G. Evans. A numerical model for the cyclic instability of thermally grown oxides in thermal barrier systems. *Acta Materialia*, 49:1793–1804, 2001.
- [17] M. Y. He, J. W. Hutchinson, and A. G. Evans. Large deformation simulations of cyclic displacement instabilities in thermal barrier systems. *Acta Materialia*, 50:1063–1073, 2002.
- [18] A. M. Karlsson, C. G. Levi, and A. G. Evans. A model study of displacement instabilities during cyclic oxidation. *Acta Materialia*, 50:1263–1273, 2002.
- [19] A. M. Karlsson, J. W. Hutchinson, and A. G. Evans. A fundamental model of cyclic instabilities in thermal barrier systems. *Journal of the Mechanics and Physics of Solids*, 50:1565–1589, 2002.
- [20] A. M. Karlsson, J. W. Hutchinson, and A. G. Evans. The displacement of the thermally grown oxide in thermal barrier systems upon temperature cycling. *Materials Science and Engineering A*, 351:244–257, 2003.
- [21] M. Caliez, J.-L. Chaboche, F. Feyel, and S. Kruch. Numerical simulation of EB-PVD thermal barrier coatings spallation. *Acta Materialia*, 51:1133–1141, 2003.
- [22] H. Yuan and J. Chen. Computational analysis of thin coating layer failure using a cohesive model and gradient plasticity. *Engineering Fracture Mechanics*, 70:1929–1942, 2003.
- [23] M. Jinnestrand and S. Sjöström. Investigation by 3D FE simulations of delamination crack initiation in TBC caused by alumina growth. *Surface and Coatings Technology*, 135:188–195, 2001.

- [24] M. Jinnestrand and H. Brodin. Crack initiation and propagation in air plasma sprayed thermal barrier coatings, testing and mathematical modelling of low cycle fatigue behaviour. *Materials Science and Engineering A*, 379:45–57, 2004.
- [25] E. P. Busso. Oxidation-induced stresses in ceramic-metal interfaces. *Journal de Physique IV*, 9:287–296, 1999.
- [26] E. P. Busso, J. Lin, S. Sakurai, and M. Nakayama. A mechanistic study of oxidation-induced degradation in a plasma-sprayed thermal barrier coating system. Part I: Model formulation. *Acta Materialia*, 49:1515–1528, 2001.
- [27] B. Budiansky and T. T. Wu. Theoretical prediction of plastic strains in polycrystals. In *Proceedings of the fourth U.S. National Congress of Applied Mechanics*, volume 2, pages 1175–1185, 1962.
- [28] M. Caliez, F. Feyel, S. Kruch, and J.-L. Chaboche. Oxidation induced stress fields in an EB-PVD thermal barrier coating. *Surface and Coatings Technology*, 157:103–110, 2002.
- [29] S. Q. Nusier, G. M. Newaz, and Z. A. Chaudury. Experimental and analytical evaluation of damage processes in thermal barrier coatings. *International Journal of Solids and Structures*, 37:2495–2506, 2000.
- [30] E. P. Busso and Z. Q. Qian. A mechanistic study of microcracking in transversely isotropic ceramic-metal systems. *Acta Materialia*, 54:325–338, 2006.
- [31] B. L. Ferguson, G. J. Petrus, and T. M. Krauss. Modeling of thermal barrier coatings. Contractor Report NAS3-26664, NASA, 1992.

- [32] M. Bäker, J. Rösler, and G. Heinze. A parametric study of the stress state of thermal barrier coatings. Part II: Cooling stresses. *Acta Materialia*, 53:469–476, 2005.
- [33] A. M. Karlsson, T. Xu, and A. G. Evans. The effect of the thermal barrier coating on the displacement instability in thermal barrier systems. *Acta Materialia*, 50:1211–1218, 2002.
- [34] M. Y. Ali, S. Q. Nusier, and G. M. Newaz. Mechanics of damage initiation and growth in a TBC/superalloy system. *International Journal of Solids and Structures*, 38:3329–3340, 2001.
- [35] S. Q. Nusier and G. M. Newaz. Growth of interfacial cracks in a TBC/superalloy system due to oxide volume induced internal pressure and thermal loading. *International Journal of Solids and Structures*, 37:2151–2166, 2000.
- [36] A. G. Evans, M. Y. He, and J. W. Hutchinson. Mechanics-based scaling laws for the durability of thermal barrier coatings. *Progress in Materials Science*, 46:249–271, 2001.
- [37] X. Chen, J. W. Hutchinson, M. Y. He, and A. G. Evans. On the propagation and coalescence of delamination cracks in compressed coatings: with application to thermal barrier systems. *Acta Materialia*, 51:2017–2030, 2003.
- [38] A. G. Evans, M. Y. He, and J. W. Hutchinson. Effect of interface undulations on the thermal fatigue of thin films and scales on metal substrates. *Acta Materialia*, 45(9):3543–3554, 1997.

- [39] M. Y. He, A. G. Evans, and J. W. Hutchinson. Effects of morphology on the decohesion of compressed thin films. *Materials Science and Engineering A*, 245:168–181, 1998.
- [40] J. Cheng, E. H. Jordan, B. Barber, and M. Gell. Thermal/residual stress in an electron beam physical vapor deposited thermal barrier coating system. *Acta Materialia*, 46(16):5839–5850, 1998.
- [41] C.-H. Hsueh and E. R. Fuller Jr. Residual stresses in thermal barrier coatings: Effects of interface asperity curvature/height and oxide thickness. *Materials Science and Engineering A*, 283:46–55, 2000.
- [42] A. M. Karlsson. On the mechanical response in a thermal barrier system due to martensitic phase transformation in the bond coat. *Journal of Engineering Materials and Technology, Transactions of the ASME*, 125:346–352, 2003.
- [43] S. Darzens and A. M. Karlsson. On the microstructural development in platinum-modified nickel-aluminide bond coats. *Surface and Coatings Technology*, 177-178:108–112, 2004.
- [44] J. Shi, S. Darzens, and A. M. Karlsson. Aspects of the morphological evolution in thermal barrier coatings and the intrinsic thermal mismatch therein. *Materials Science and Engineering A*, 392:301–312, 2005.
- [45] J. T. DeMasi, K. D. Sheffler, and M. Ortiz. Thermal barrier coating life prediction model development. Phase I - final report. Technical Report CR-182230, NASA, 1989.
- [46] S. M. Meier, D. M. Nissley, and K. D. Sheffler. Thermal barrier coating life prediction model development. Phase II - final report. Technical Report CR-189111, NASA, 1991.

- [47] A. G. Evans, J. W. Hutchinson, and M. Y. He. Micromechanics model for the detachment of residually compressed brittle films and coatings. *Acta Materialia*, 47(5):1513–1522, 1999.
- [48] M. Y. He, J. W. Hutchinson, and A. G. Evans. Simulation of stresses and delamination in a plasma-sprayed thermal barrier system upon thermal cycling. *Materials Science and Engineering A*, 345:172–178, 2003.
- [49] T. Xu, M. Y. He, and A. G. Evans. A numerical assessment of the durability of thermal barrier systems that fail by ratcheting of the thermally grown oxide. *Acta Materialia*, 51:3807–3820, 2003.
- [50] R. Vaßen, G. Kerkhoff, and D. Stöver. Development of a micromechanical life prediction model for plasma sprayed thermal barrier coatings. *Materials Science and Engineering A*, 303:100–109, 2001.
- [51] E. P. Busso, J. Lin, and S. Sakurai. A mechanistic study of oxidation-induced degradation in a plasma-sprayed thermal barrier coating system. Part II: Life prediction model. *Acta Materialia*, 49:1529–1536, 2001.
- [52] E. P. Busso, L. Wright, H. E. Evans, L. N. McCartney, S. R. J. Saunders, S. Osgerby, and J. Nunn. A physics-based life prediction methodology for thermal barrier coating systems. *Acta Materialia*, 55:1491–1503, 2007.
- [53] U. Hermosilla, T. H. Hyde, and I. A. Jones. Thermal analysis of electron-beam physical vapour deposited thermal barrier coated super-alloy tensile specimens. *Submitted to Proceedings IMechE Part L, Journal of Materials: Applications & Design*, 222, 2007.
- [54] D. Wang, X. Huang, and P. Patnaik. Design and modeling of multiple layered TBC system with high reflectance. *Journal of Materials Science*, 41:6245–6255, 2006.

- [55] H. Hayashi, T. Saitou, N. Naruyama, H. Inaba, K. Kawamura, and M. Mori. Thermal expansion coefficient of yttria stabilized zirconia for various yttria contents. *Solid State Ionics*, 176:613–619, 2005.
- [56] B.-K. Jang and H. Matsubara. Thermophysical properties of EB-PVD coatings and sintered ceramics of 4 % Y_2O_3 -stabilized zirconia. *Journal of Alloys and Compounds*, 419:243–246, 2006.
- [57] R. P. Ingel and D. Lewis III. Lattice parameters and density for Y_2O_3 -stabilized ZrO_2 . *Journal of the American Ceramic Society*, 69(4):325–332, 1986.
- [58] K. An and M. K. Han. An experimental technique to evaluate the effective thermal conductivity of Y_2O_3 stabilized ZrO_2 coatings. *Journal of Materials Science*, 41:2113–2120, 2006.
- [59] J. R. Nicholls, K. J. Lawson, A. Johnstone, and D. S. Rickerby. Methods to reduce the thermal conductivity of EB-PVD TBCs. *Surface and Coatings Technology*, 151-152:383–391, 2002.
- [60] M. F. Modest. *Radiative Heat Transfer*. Elsevier Science, 2003.
- [61] K. C. Mills, Y. M. Youssef, Z. Li, and Y. Su. Calculation of thermophysical properties of Ni-based superalloys. *ISIJ International*, 46(5):623–632, 2006.
- [62] The International Nickel Company Inc. Alloy IN-738 technical data.
- [63] R. G. Munro. Evaluated material properties for a sintered $\alpha - Al_2O_3$. *Journal of the American Ceramic Society*, 80:1919–1928, 1997.
- [64] H.-J. Rätzer-Scheibe, U. Schulz, and T. Krell. The effect of coating thickness on the thermal conductivity of EB-PVD PYSZ thermal barrier coatings. *Surface & Coatings Technology*, 200:5636–5644, 2006.

- [65] Y. Moriya and A. Navrotsky. High-temperature calorimetry of zirconia: Heat capacity and thermodynamics of the monoclinic-tetragonal phase transition. *J. Chem. Thermodynamics*, 38:211–223, 2006.
- [66] N. Matan, D. C. Cox, P. Carter, M. A. Rist, C. M. F. Rae, and R. C. Reed. Creep of CMSX-4 superalloy single crystals: effects of misorientation and temperature. *Acta materialia*, 47(5):1549–1563, 1999.
- [67] D. Stöver and C. Funke. Directions of the development of thermal barrier coatings in energy applications. *Journal of Materials Processing Technology*, 92-93:195–202, 1999.
- [68] R. C. Reed, N. Matan, D. C. Cox, M. A. Rist, and C. M. F. Rae. Creep of CMSX-4 superalloy single crystals: effects of rafting at high temperature. *Acta materialia*, 47(12):3367–3381, 1999.
- [69] R. K. Penny and D. L. Marriott. *Design for creep*. Chapman & Hall, 1995.
- [70] A. A. Wereszczak, J. G. Hemrick, T. P. Kirkland, J. A. Haynes, T. J. Fitzgerald, and J. E. Junkin. Stress relaxation of MCrAlY bond coat alloys as a function of temperature and strain. In *International Gas Turbine & Aeroengine Congress & Exhibition Proceedings*, pages 1–7, Stockholm, Sweden, June 1998.
- [71] M. G. Hebsur and R. V. Miner. High temperature tensile and creep behaviour of low pressure plasma-sprayed Ni-Co-Cr-Al-Y coating alloy. *Materials Science and Engineering*, 83:239–245, 1986.
- [72] P. Majerus. *Neue Verfahren zur Analyse des Verformungs- und Schädigungsverhaltens von MCrAlY-Schichten im Wärmedämmschichtsystem/New method for the analysis of the deformation and deterioration of*

- MCrAlY layers in TBCs*. PhD thesis, Fakultät für Maschinenwesen der Rheinisch-Westfälischen Technischen Hochschule Aachen, 2003.
- [73] D. Zhu and R. A. Miller. Determination of creep behavior of thermal barrier coatings under laser imposed temperature and stress gradients. Technical Memorandum 113169, NASA, 1997.
- [74] M. Karunaratne. Personal communication.
- [75] Hibbitt, Karlsson & Sorensen, Inc., Pawtucket, Rhode Island. *ABAQUS Analysis User's Manual, version 6.5-1*, 2004.
- [76] J. A. Thompson and T. W. Clyne. The effect of heat treatment on the stiffness of zirconia top coats in plasma-sprayed TBCs. *Acta materialia*, 49:1565–1575, 2001.
- [77] N. Birks and G. H. Meier. *Introduction to high temperature oxidation of metals*. Edward Arnold Ltd, 1983.
- [78] R. H. Davies, A. T. Dinsdale, J. A. Gisby, J. A. J. Robinson, and S. M. Martin. MTDATA-thermodynamics and phase equilibrium software from the National Physical Laboratory. *Calphad*, 26(2):229–271, June 2002.
- [79] M. S. A. Karunaratne, S. L. Ogden, S. D. Kenny, and R. C. Thomson. A multicomponent diffusion model for the prediction of microstructural evolution in coated Ni-based superalloy systems. *To be submitted*, 2007.
- [80] J. D. Eshelby. The determination of the elastic field of an ellipsoidal inclusion, and related problems. *Proceedings of the Royal Society A*, 241:376–396, 1957.
- [81] W. Wakashima, M. Otsuka, and S. Umekawa. Thermal expansions of heterogeneous solids containing aligned ellipsoidal inclusions. *Journal of Composite Materials*, 8:391–404, October 1974.

- [82] B. Budiansky. On the elastic moduli of some heterogeneous materials. *Journal of the Mechanics and Physics of Solids*, 13:223–227, 1965.
- [83] E. Kröner. Zur Plastischen Verformung des Vielkristalls. *Acta Metallurgica*, 9:155–161, 1961.
- [84] G. J. Weng. Self-consistent determination of time-dependent behavior of metals. *Journal of applied mechanics*, 48:41–46, March 1981.
- [85] M. Taya and R. J. Arsenault. *Metal matrix composites thermomechanical behavior*. Pergamon Press, 1989.
- [86] T. W. Clyne and P. J. Withers. *An introduction to metal matrix composites*. Cambridge solid state science series, 1993.
- [87] T. Mori and K. Tanaka. Average stress in matrix and average elastic energy of materials with misfitting inclusions. *Acta Metallurgica*, 21:571–574, 1973.
- [88] G. Cailletaud and P. Pilvin. Utilisation de modèles polycristallins pour le calcul par éléments finis/Use of polycrystal models for finite element calculations. *Revue européenne des éléments finis*, 3(4):515–541, 1994.
- [89] E. Weissenbek, H. E. Pettermann, and S. Suresh. Elasto-plastic deformation of compositionally graded metal-ceramic composites. *Acta Materialia*, 45(8):3401–3417, 1997.
- [90] S. Rangaraj and K. Kokini. Time-dependent behavior of ceramic (zirconia)-metal (NiCoCrAlY) particulate composites. *Mechanics of Time-Dependent Materials*, 6:171–191, 2002.
- [91] S. Rangaraj and K. Kokini. Influence of particle shape and aspect ratio on thermally activated viscoplastic (time-dependent) response of ceramic

- (zirconia)-metal (NiCoCrAlY) particulate composites. *Materials Science and Engineering A*, 366:356–366, 2004.
- [92] Y.-L. Shen, M. Finot, A. Needleman, and S. Suresh. Effective plastic response of two-phase composites. *Acta metallurgica et materialia*, 43(4):1701–1722, 1995.
- [93] D. M. Etter. *Structured FORTRAN 77 for Engineers and Scientists*. The Benjamin/Cummings Publishing Company, Inc., 4th edition, 1993.
- [94] N. S. Stoloff and V. K. Sikka. *Physical metallurgy and processing of intermetallic compounds*. Chapman & Hall, 1996.
- [95] L. A. Hocking, P. R. Strutt, and R. A. Dodd. Comparison of steady-state compression creep behaviour in stoichiometric CoAl and NiAl single crystals between 850 and 1050°C (1123 and 1323 K, $0.69 > \frac{T}{T_m} > 0.58$). *Journal of the Institute of Metals*, 99:98–101, 1971.
- [96] J. D. Whittenberger. Effect of composition and grain size on slow plastic flow properties of NiAl between 1200 and 1400 K. *Journal of Materials Science*, 22:394–402, 1987.
- [97] W. J. Yang and R. A. Dodd. Steady-state creep and associated microstructures in stoichiometric and non-stoichiometric polycrystalline NiAl. *Metal Science Journal*, 7:41–47, 1973.
- [98] R. R. Vandervoort, A. K. Mukherjee, and J. E. Dorn. Elevated-temperature deformation mechanisms in β' -NiAl. *Transactions of the ASM*, 59:931–944, 1966.
- [99] M. Rudy and G. Sauthoff. Creep behaviour of the ordered intermetallic (Fe,Ni)Al phase. In *Materials Research Society Symposium Proceedings*, volume 39, pages 327–333. Materials Research Society, 1985.

- [100] R. Nakamura, K. Takasawa, Y. Yamazaki, and Y. Iijima. Single-phase interdiffusion in the B2 type intermetallic compounds NiAl, CoAl and FeAl. *Intermetallics*, 10:195–204, 2002.
- [101] H. J. Frost and M. F. Ashby. *Deformation-mechanism maps, The plasticity and creep of metals and ceramics*. Pergamon Press, 1982.
- [102] J. Wolfenstine, H. K. Kim, and J. C. Earthman. Elevated-temperature deformation mechanisms in Ni₃Al. *Materials Science and Engineering A*, 192/193:811–816, 1994.
- [103] R. W. Dickson and J. B. Wachtman Jr. Elastic constants of single-crystal Ni₃Al from 0° to 850°C. *Journal of Applied Physics*, 40(5):2276–2279, 1969.
- [104] C. Knobloch, V. Saß, D. Siebörger, and U. Glatzel. Anisotropic creep behaviour of a nickel-based superalloy compared with single phase nickel solid solution and γ' phase single crystals. *Materials Science and Engineering A*, 234-236:237–241, 1997.
- [105] K. Matsuura, T. Kitamura, and M. Kudoh. Microstructure and mechanical properties of NiAl intermetallic compound synthesized by reactive sintering under pressure. *Journal of Materials Processing Technology*, 63:298–302, 1997.
- [106] D. R. Lide. *CRC Handbook of Chemistry and Physics*. CRC Press/Taylor and Francis, Boca Raton, FL, USA, 88th edition, internet version 2008. <http://www.hbcnetbase.com/>.
- [107] J. Meng, C. Jia, and Q. He. Fabrication of Ni₃Al by hot pressing from element powders. *Rare Metals*, 26(3):222–225, June 2007.

- [108] C. Xu and W. Gao. Pilling-Bedworth ratio for oxidation of alloys. *Materials Research Innovations*, 3:231–235, 2000.
- [109] R. B. Ross. *Metallic materials specification handbook*. Chapman & Hall, 4th edition, 1992.
- [110] W. H. Press, S. A. Teukolsky, W. T. Vetterling, and B. P. Flannery. *Numerical Recipes in Fortran*. Cambridge University Press, 1992.

Appendix A

Calculation of the instantaneous coefficient of thermal expansion

When CTEs are provided in terms of the overall expansion from a reference temperature, T_0 , they need to be converted into instantaneous values, i.e. derivative of expansion with respect to temperature, in order to be usable within FE calculations. If an initial bar of unit length, $L_0 = 1$, is considered, the overall length increase at any temperature is obtained as:

$$\Delta L(T) = L_0 \alpha^*(T - T_0) \quad (\text{A.1})$$

where α^* is the overall expansion coefficient from the reference temperature, which is a nonlinear function of T . The total linear expansion of the solid can be expressed as:

$$L(T) = L_0 + \Delta L(T) \quad (\text{A.2})$$

From the definition of instantaneous CTE, α , the differential increase in length upon a differential temperature increment is

$$dL = L(T) \alpha(T) dT \quad (\text{A.3})$$

Differentiating Equation A.2,

$$dL = \frac{d\Delta L}{dT} dT \quad (\text{A.4})$$

which can be equated to Equation A.3 in order to obtain the expression of the instantaneous coefficient of thermal expansion:

$$\alpha(T) = \frac{\frac{d\Delta L}{dT}}{L_0 + \Delta L} \quad (\text{A.5})$$

The method explained in Equations A.1 to A.5 was applied for the calculation of the instantaneous coefficient of thermal expansion of α -alumina and APS PSZ. CTE values for α -alumina are given as overall values from 0°C [63]. The equation that best fits its linear expansion is (see Fig. A.1)

$$\Delta L(T) = 2.9639 \times 10^{-6} T^{1.1448} \text{ with } R^2 = 0.99 \quad (\text{A.6})$$

and for plasma sprayed PSZ (see Fig. A.2) [45],

$$\Delta L(T) = 5.2577 \times 10^{-6} T^{1.0931} \text{ with } R^2 = 0.99 \quad (\text{A.7})$$

which can be differentiated and substituted in Equation A.5 in order to obtain the instantaneous CTEs. Results for α -alumina are listed in Table A.1 and for APS PSZ in Table A.2.

T ($^{\circ}\text{C}$)	α^* (K^{-1}) from 0°C , [63]	α (K^{-1}) intantaneous
20	4.6×10^{-6}	5.2×10^{-6}
500	7.1×10^{-6}	8.3×10^{-6}
1000	8.1×10^{-6}	9.1×10^{-6}
1200	8.3×10^{-6}	9.4×10^{-6}
1400	8.5×10^{-6}	9.6×10^{-6}
1500	8.6×10^{-6}	9.7×10^{-6}

Table A.1: CTE values for sintered α -alumina.

T ($^{\circ}\text{C}$)	α^* (K^{-1}) from 25°C , [45]	α (K^{-1}) intantaneous
100	9.68×10^{-6}	8.82×10^{-6}
200	1.00×10^{-6}	9.40×10^{-6}
300	9.82×10^{-6}	9.75×10^{-6}
400	9.70×10^{-6}	10.0×10^{-6}
500	9.64×10^{-6}	10.2×10^{-6}
600	9.78×10^{-6}	10.4×10^{-6}
700	9.88×10^{-6}	10.5×10^{-6}
800	10.0×10^{-6}	10.6×10^{-6}
900	10.2×10^{-6}	10.7×10^{-6}
1000	10.3×10^{-6}	10.8×10^{-6}
1100	10.3×10^{-6}	10.9×10^{-6}
1175	10.1×10^{-6}	11.0×10^{-6}

Table A.2: CTE values for APS PSZ.

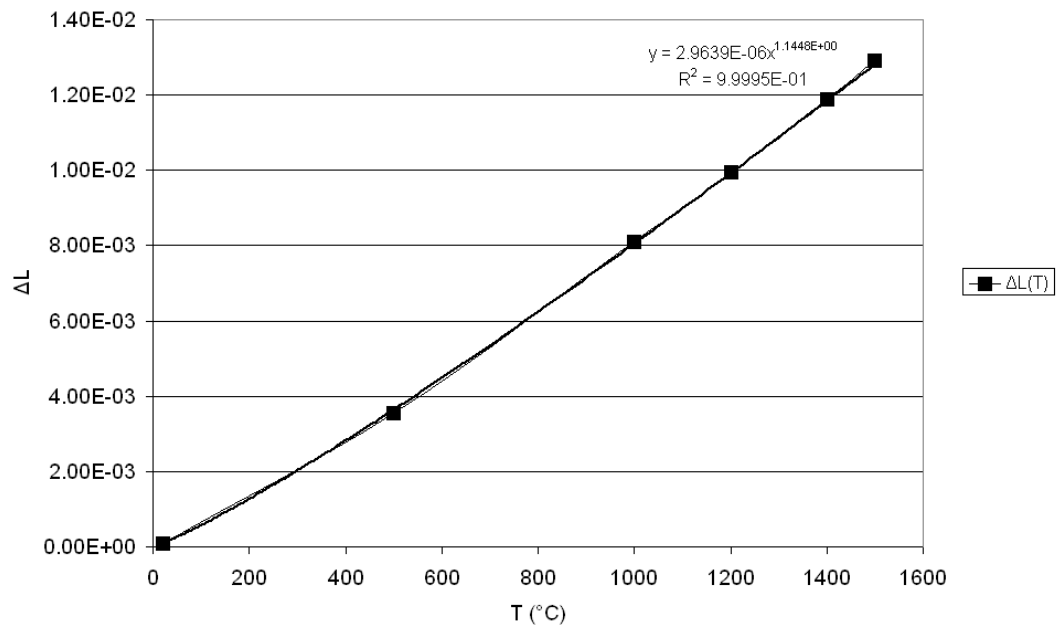


Figure A.1: ΔL vs. T for α -alumina and least squares best fit.

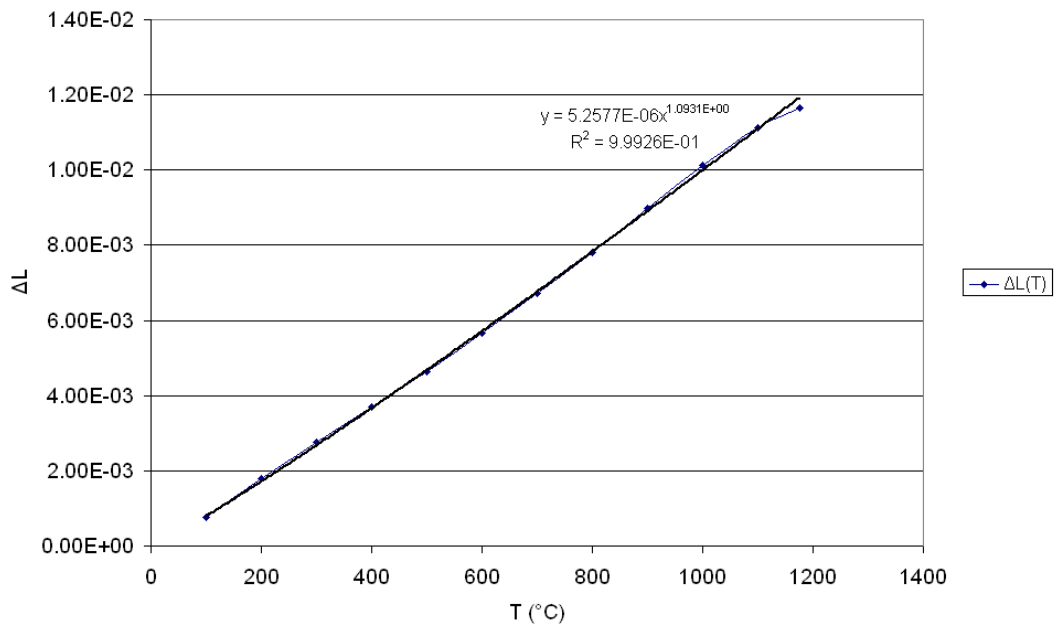


Figure A.2: ΔL vs. T for APS PSZ and least squares best fit.

Appendix B

Calculation of the average shear strain under pure shear stress for a spherical inhomogeneity

A spherical inclusion (being C_{ijkl}^* its elastic tensor) within an infinite matrix (being C_{ijkl} its elastic tensor) is the geometry considered in this appendix. The externally applied stress is $\sigma_{12} = \tau^0$. The shear strain within the inclusion ϵ_{kl}^{inc} is composed of two parts:

$$\epsilon_{kl}^{inc} = \epsilon_{kl}^0 + \epsilon_{kl} \rightarrow \epsilon_{12}^{inc} = \epsilon_{12}^0 + \epsilon_{12} \quad (\text{B.1})$$

ϵ_{kl}^0 is the strain due to the externally applied load and can be obtained from

$$\sigma_{ij}^0 = C_{ijkl}\epsilon_{kl}^0 \rightarrow \sigma_{ij}^0 = C_{ij12}\epsilon_{12}^0 \quad (\text{B.2})$$

ϵ_{kl} is the strain within the equivalent homogeneous inclusion due to an eigenstrain, obtained as

$$\epsilon_{kl} = S_{klmn}\epsilon_{mn}^* \rightarrow \epsilon_{12} = S_{12mn}\epsilon_{mn}^* \quad (\text{B.3})$$

ϵ_{mn}^* is the correspondent eigenstrain and S_{klmn} is Eshelby's tensor [85], which

in the case of spherical inclusions is:

$$S_{ijkl} = S_{jikl} = S_{ijlk} \quad (\text{B.4})$$

$$S_{1111} = S_{2222} = S_{3333} = \frac{7 - 5\nu}{15(1 - \nu)} = \alpha \quad (\text{B.5})$$

$$S_{1122} = S_{2233} = S_{3311} = S_{1133} = S_{2211} = S_{3322} = \frac{5\nu - 1}{15(1 - \nu)} = \delta \quad (\text{B.6})$$

$$S_{1212} = S_{2323} = S_{3131} = \frac{4 - 5\nu}{15(1 - \nu)} = \beta_t \quad (\text{B.7})$$

The use of the equivalent homogeneous inclusion states that its stress must be identical to the stress in the inhomogeneity, which is imposed by Equation B.8; its solution being the eigenstrain necessary to calculate the disturbance stress,

$$C_{ijkl}^* (\epsilon_{kl}^0 + S_{klmn} \epsilon_{mn}^*) = C_{ijkl} (\epsilon_{kl}^0 + S_{klmn} \epsilon_{mn}^* - \epsilon_{kl}^*) \quad (\text{B.8})$$

Since the interest is focused in the study of materials subjected to pure shear stress, only the ϵ_{12} component of the strain is considered from now on,

$$C_{ij12}^* (\epsilon_{12}^0 + S_{12mn} \epsilon_{mn}^*) = C_{ij12} (\epsilon_{12}^0 + S_{12mn} \epsilon_{mn}^* - \epsilon_{12}^*) \quad (\text{B.9})$$

The stiffness matrix for an isotropic material is:

$$C_{ij} = \begin{bmatrix} \lambda + 2\mu & \lambda & \lambda & 0 & 0 & 0 \\ \lambda & \lambda + 2\mu & \lambda & 0 & 0 & 0 \\ \lambda & \lambda & \lambda + 2\mu & 0 & 0 & 0 \\ 0 & 0 & 0 & 2\mu & 0 & 0 \\ 0 & 0 & 0 & 0 & 2\mu & 0 \\ 0 & 0 & 0 & 0 & 0 & 2\mu \end{bmatrix} \quad (\text{B.10})$$

The ϵ_{12}^0 strain component is obtained using Equations B.2 and B.10:

$$\sigma_{12}^0 = \tau^0 = C_{12kl} \epsilon_{kl}^0 = 2\mu \epsilon_{12}^0 \quad (\text{B.11})$$

$$\epsilon_{12}^0 = \frac{\tau^0}{2\mu} \quad (\text{B.12})$$

And the remaining shear strains are zero,

$$\epsilon_{13}^0 = \epsilon_{23}^0 = 0 \quad (\text{B.13})$$

Substituting the values from Equations B.4 - B.7 in Equation B.3, the disturbance component ϵ_{12} is

$$\begin{aligned} \epsilon_{12} &= S_{12mn}\epsilon_{mn}^* = S_{1211}\epsilon_{11}^* + S_{1212}\epsilon_{12}^* + S_{1213}\epsilon_{13}^* + S_{1221}\epsilon_{21}^* \\ &\quad + S_{1222}\epsilon_{22}^* + S_{1223}\epsilon_{23}^* + S_{1231}\epsilon_{31}^* + S_{1232}\epsilon_{32}^* + S_{1233}\epsilon_{33}^* \\ &= \beta_t\epsilon_{12}^* + \beta_t\epsilon_{21}^* = 2\beta_t\epsilon_{12}^* \quad (\text{B.14}) \end{aligned}$$

Substituting back the result from Equation B.14 into Equation B.1, the total shear strain in the inclusion is

$$\epsilon_{12}^{inc} = \frac{\tau^0}{2\mu} + 2S_{1212}\epsilon_{12}^* = \frac{\tau^0}{2\mu} + 2\beta_t\epsilon_{12}^* \quad (\text{B.15})$$

At this stage the only unknown component is ϵ_{12}^* . Equations B.11, B.12 and B.15 are substituted into Equation B.9, taking into account that the only non-zero term corresponds to the σ_{12} stress,

$$2\mu^* \left(\frac{\tau^0}{2\mu} + 2\beta_t\epsilon_{12}^* \right) = 2\mu \left(\frac{\tau^0}{2\mu} + (2\beta_t - 1)\epsilon_{12}^* \right) \quad (\text{B.16})$$

Rearranging Equation B.16, an expression for ϵ_{12}^* is obtained,

$$\epsilon_{12}^* = \frac{\left(1 - \frac{\mu^*}{\mu}\right) \tau^0}{4\beta_t(\mu^* - \mu) + 2\mu} \quad (\text{B.17})$$

Substituting Equation B.17 into Equation B.15, the average shear strain in an inhomogeneous inclusion is

$$\begin{aligned} \epsilon_{12}^{inc} &= \frac{\tau^0}{2\mu} + 2\beta_t\epsilon_{12}^* = \frac{\tau^0}{2\mu} + 2\beta_t \frac{\left(1 - \frac{\mu^*}{\mu}\right) \tau^0}{4\beta_t(\mu^* - \mu) + 2\mu} \\ &= \tau^0 \frac{2\beta_t(\mu^* - \mu) + \mu + 2\beta_t\mu - 2\beta_t\mu^*}{[4\beta_t(\mu^* - \mu) + 2\mu]\mu} = \frac{\tau^0}{4\beta_t(\mu^* - \mu) + 2\mu} \quad (\text{B.18}) \end{aligned}$$

And the strain value that will be used to calculate the stiffness of a multi-phase material is $\bar{\gamma}$, i.e.

$$\bar{\gamma}_i = 2\bar{\epsilon}_i = 2\epsilon_{12}^{inc} = \frac{\tau^0}{\mu + 2\beta_t(\mu^* - \mu)} = \frac{\tau^0}{G + 2\beta_t(G_i - G)} \quad (\text{B.19})$$

with

$$\beta_t = \frac{4 - 5\nu}{15(1 - \nu)} \quad (\text{B.20})$$

Appendix C

Calculation of the average volumetric change under hydrostatic loading for a spherical inhomogeneity

When a solid is applied an external pressure the stress state is purely hydrostatic. The definition of pressure states that

$$p^0 = \frac{1}{3}(\sigma_{11} + \sigma_{22} + \sigma_{33}) \quad (\text{C.1})$$

Note that the usual sign convention is to assume $p^0 = -\frac{1}{3}(\sigma_{11} + \sigma_{22} + \sigma_{33})$. In this case the convention has been changed as the interest is to calculate volumetric contractions. The stress state of the solid is symmetric, which implies

$$\sigma_{11} = \sigma_{22} = \sigma_{33} = p^0 \quad (\text{C.2})$$

The average volumetric change in an inhomogeneity subjected to pressure loading is obtained as

$$\bar{\theta} = \epsilon_{11}^{inc} + \epsilon_{22}^{inc} + \epsilon_{33}^{inc} \quad (\text{C.3})$$

Due to symmetry, all the direct strains are equal, which means that the average volume change $\bar{\theta}$ can be rewritten as

$$\bar{\theta} = 3\epsilon_{11}^{inc} \quad (\text{C.4})$$

The inclusion strain is composed of two terms, one caused by the external load and another originating from the disturbance of the inclusion,

$$\epsilon_{11}^{inc} = \epsilon_{11}^0 + \epsilon_{11} \quad (\text{C.5})$$

where ϵ_{11}^0 is obtained by application of Hooke's law,

$$\begin{Bmatrix} p^0 \\ p^0 \\ p^0 \end{Bmatrix} = \begin{bmatrix} \lambda + 2\mu & \lambda & \lambda \\ \lambda & \lambda + 2\mu & \lambda \\ \lambda & \lambda & \lambda + 2\mu \end{bmatrix} \begin{Bmatrix} \epsilon_{11}^0 \\ \epsilon_{22}^0 \\ \epsilon_{33}^0 \end{Bmatrix}, \text{ with } \epsilon_{11}^0 = \epsilon_{22}^0 = \epsilon_{33}^0 \quad (\text{C.6})$$

The solution to Equation C.6 is

$$\epsilon_{11}^0 = \epsilon_{22}^0 = \epsilon_{33}^0 = \frac{p^0}{3\lambda + 2\mu} = \frac{p^0}{3K} \quad (\text{C.7})$$

where K is the matrix material bulk modulus. The disturbance component is calculated using Eshelby's tensor for spherical inclusions:

$$\begin{aligned} S_{11mn}\epsilon_{mn}^* &= S_{1111}\epsilon_{11}^* + S_{1112}\epsilon_{12}^* + S_{1113}\epsilon_{13}^* + S_{1121}\epsilon_{21}^* \\ &+ S_{1122}\epsilon_{22}^* + S_{1123}\epsilon_{23}^* + S_{1131}\epsilon_{31}^* + S_{1132}\epsilon_{32}^* + S_{1133}\epsilon_{33}^* = \alpha\epsilon_{11}^* + \delta\epsilon_{22}^* + \delta\epsilon_{33}^* \end{aligned} \quad (\text{C.8})$$

Again, due to the symmetry of the problem, $\epsilon_{11}^* = \epsilon_{22}^* = \epsilon_{33}^*$, which implies that Equation C.8 can be simplified to give

$$S_{11mn}\epsilon_{mn}^* = S_{22mn}\epsilon_{mn}^* = S_{33mn}\epsilon_{mn}^* = (\alpha + 2\delta)\epsilon_{11}^* \quad (\text{C.9})$$

Equation B.8, which is a general expression for inhomogeneous inclusions, is expanded assuming that the only non-zero strains are the direct strains. The

equation that corresponds to the σ_{11} stress component is

$$\begin{aligned}
& C_{1111}^*(\epsilon_{11}^0 + S_{11mn}\epsilon_{mn}^*) + C_{1122}^*(\epsilon_{22}^0 + S_{22mn}\epsilon_{mn}^*) + C_{1133}^*(\epsilon_{33}^0 + S_{33mn}\epsilon_{mn}^*) \\
&= C_{1111}(\epsilon_{11}^0 + S_{11mn}\epsilon_{mn}^* - \epsilon_{11}^*) + C_{1122}(\epsilon_{22}^0 + S_{22mn}\epsilon_{mn}^* - \epsilon_{22}^*) \\
&\quad + C_{1133}(\epsilon_{33}^0 + S_{33mn}\epsilon_{mn}^* - \epsilon_{33}^*) \quad (C.10)
\end{aligned}$$

Assuming that stress and strain components are the same in all directions, Equation C.10 is simplified as

$$\begin{aligned}
& C_{1111}^*(\epsilon_{11}^0 + S_{11mn}\epsilon_{mn}^*) + C_{1122}^*(\epsilon_{11}^0 + S_{11mn}\epsilon_{mn}^*) + C_{1133}^*(\epsilon_{11}^0 + S_{11mn}\epsilon_{mn}^*) \\
&= C_{1111}(\epsilon_{11}^0 + S_{11mn}\epsilon_{mn}^* - \epsilon_{11}^*) + C_{1122}(\epsilon_{11}^0 + S_{11mn}\epsilon_{mn}^* - \epsilon_{11}^*) \\
&\quad + C_{1133}(\epsilon_{11}^0 + S_{11mn}\epsilon_{mn}^* - \epsilon_{11}^*) \quad (C.11)
\end{aligned}$$

Substituting for the elastic tensors \mathbf{C} and \mathbf{C}^* in terms of the matrix and inclusion elastic constants respectively:

$$(\lambda^* + 2\mu + \lambda^* + \lambda^*)(\epsilon_{11}^0 + S_{11mn}\epsilon_{mn}^*) = (\lambda + 2\mu + \lambda + \lambda)(\epsilon_{11}^0 + S_{11mn}\epsilon_{mn}^* - \epsilon_{11}^*) \quad (C.12)$$

Equations C.9 and C.7 are used to further simplify Equation C.12,

$$(3\lambda^* + 2\mu^*) \left(\frac{p^0}{3K} + (\alpha + 2\delta)\epsilon_{11}^* \right) = (3\lambda + 2\mu) \left(\frac{p^0}{3K} + (\alpha + 2\delta)\epsilon_{11}^* - \epsilon_{11}^* \right) \quad (C.13)$$

Equation C.13 can be rearranged as shown in Equation C.14, using the bulk moduli of inhomogeneity and matrix, K^* and K , respectively:

$$3K^* \left(\frac{p^0}{3K} + (\alpha + 2\delta)\epsilon_{11}^* \right) = 3K \left(\frac{p^0}{3K} + (\alpha + 2\delta - 1)\epsilon_{11}^* \right) \quad (C.14)$$

The solution for the eigenstrain is obtained from Equation C.14

$$\epsilon_{11}^* = p^0 \frac{1 - \frac{K^*}{K}}{3[(\alpha + 2\delta)(K^* - K) + K]} \quad (C.15)$$

Substituting back the strain disturbance component is obtained:

$$\epsilon_{11} = S_{11mn}\epsilon_{mn}^* = (\alpha + 2\delta)\epsilon_{11}^* = p^0 \frac{(\alpha + 2\delta) \left(1 - \frac{K^*}{K} \right)}{3[(\alpha + 2\delta)(K^* - K) + K]} \quad (C.16)$$

And the direct strain in the inclusion is:

$$\begin{aligned}
\epsilon_{11}^{inc} &= \epsilon_{11}^0 + \epsilon_{11} = \frac{p^0}{3K} + p^0 \frac{(\alpha + 2\delta) \left(1 - \frac{K^*}{K}\right)}{3[(\alpha + 2\delta)(K^* - K) + K]} \\
&= \frac{p^0}{3} \left[\frac{1}{K} + \frac{(\alpha + 2\delta) \left(1 - \frac{K^*}{K}\right)}{(\alpha + 2\delta)(K^* - K) + K} \right] \\
&= \frac{p^0}{3} \frac{(\alpha + 2\delta)(K^* - K) + K + (\alpha + 2\delta)(K^* - K)}{K[(\alpha + 2\delta)(K^* - K) + K]} \\
&= \frac{p^0}{3} \frac{1}{K + (\alpha + 2\delta)(K^* - K)}
\end{aligned} \tag{C.17}$$

The fractional volume change is provided by

$$\bar{\theta} = \epsilon_{11}^{inc} + \epsilon_{22}^{inc} + \epsilon_{33}^{inc} = 3\epsilon_{11}^{inc} = \frac{p^0}{K + (\alpha + 2\delta)(K^* - K)} \tag{C.18}$$

with

$$\alpha + 2\delta = \frac{7 - 5\nu}{15(1 - \nu)} + 2\frac{5\nu - 1}{15(1 - \nu)} = \frac{7 - 5\nu + 10\nu - 2}{15(1 - \nu)} = \frac{1 + \nu}{15(1 - \nu)} = \beta_n \tag{C.19}$$

Appendix D

Complete derivation of the numerical implementation of self-consistent constitutive models

This appendix contains a full explanation and derivation of the numerical method followed to solve the equations that compose the self consistent constitutive model introduced in Chapter 6. That chapter contains the theory underlying the model and some general notes on the numerical algorithm followed in order to achieve the solution of the equations.

D.1 Incremental form of the constitutive equations

Equations 6.83 - 6.88 need to be rewritten in incremental form in order to be implemented in a subroutine and be used in FE calculations. The approach used to achieve that purpose is to transform the equations written in rate form

to equations in terms of total differentials of functions, taking into account that the independent variable of the unknown functions to be solved is time, t . The equations written in terms of total differentials are then integrated between t_0 and $t_0 + \Delta t$, resulting in incremental equations, which can be coded and solved numerically.

Equations 6.83 to 6.88 are re-stated here for convenience:

$$\dot{\sigma}_{ij} = \lambda \dot{\epsilon}_{kk} \delta_{ij} + 2\mu (\dot{\epsilon}_{ij} - \dot{\epsilon}_{ij}^{in}) - 3K\alpha \dot{T} \delta_{ij} \quad (6.83)$$

$$\dot{\epsilon}_{ij}^{in} = \dot{\epsilon}_{ij}^{cr} + \dot{\epsilon}_{ij}^{tr} \quad (6.84)$$

$$\dot{\epsilon}_{ij}^{cr} = \sum_g f^g \dot{\epsilon}_{ij}^{g,cr} \quad (6.85)$$

$$\dot{\epsilon}_{ij}^{m,cr} = \frac{3}{2} A^m (\sigma^m)^{n^m-1} s_{ij}^m \quad (6.86)$$

$$\dot{\epsilon}_{ij}^{tr} = \frac{1}{3} f^{ox} \ln(PBR_{eq}) \delta_{ij} \quad (6.87)$$

$$\dot{\sigma}_{ij}^m = \dot{\sigma}_{ij} + 2\mu(1 - \beta_t) (\dot{\epsilon}_{ij}^{cr} - \dot{\epsilon}_{ij}^{m,cr}) \quad (6.88)$$

Equation 6.83 can be rewritten in rate form using an alternative notation as:

$$\frac{d\sigma_{ij}}{dt} = \lambda \frac{d\epsilon_{kk}}{dt} \delta_{ij} + 2\mu \left(\frac{d\epsilon_{ij}}{dt} - \frac{d\epsilon_{ij}^{in}}{dt} \right) - 3K\alpha \frac{dT}{dt} \delta_{ij} \quad (D.1)$$

As all the derivatives involved in Equation D.1 are total derivatives with respect to time, Equation D.1 can be rewritten substituting those derivatives by total differentials:

$$d\sigma_{ij} = \lambda d\epsilon_{kk} \delta_{ij} + 2\mu (d\epsilon_{ij} - d\epsilon_{ij}^{in}) - 3K\alpha dT \delta_{ij} \quad (D.2)$$

If Equation D.2 is integrated numerically between t_0 and $t_0 + \Delta t$,

$$\int_{\sigma_{ij_0}}^{\sigma_{ij_0} + \Delta\sigma_{ij}} d\sigma_{ij} = \int_{\epsilon_{ij_0}}^{\epsilon_{ij_0} + \Delta\epsilon_{ij}} \lambda \delta_{ij} d\epsilon_{kk} + \int_{\epsilon_{ij_0}}^{\epsilon_{ij_0} + \Delta\epsilon_{ij}} 2\mu (d\epsilon_{ij} - d\epsilon_{ij}^{in}) - \int_{T_0}^{T_0 + \Delta T} 3K\alpha \delta_{ij} dT \quad (D.3)$$

$$\begin{aligned} \Delta\sigma_{ij} \approx & \lambda\delta_{ij}|_{t_0+\varphi\Delta t} \Delta\epsilon_{kk} + 2\mu|_{t_0+\varphi\Delta t} \Delta\epsilon_{ij} \\ & - 2\mu|_{t_0+\varphi\Delta t} \Delta\epsilon_{ij}^{in} - 3K\alpha\delta_{ij}|_{t_0+\varphi\Delta t} \Delta T \end{aligned} \quad (\text{D.4})$$

where the notation $\Phi|_{t_0+\varphi\Delta t}$ indicates that a typical function Φ must be evaluated at $t_0 + \varphi\Delta t$ and φ is typically a number between 0 and 1. $\varphi = 0$ would correspond to a purely *explicit* integration method, $\varphi = 1$ to a purely *implicit* integration method, and values between those limits result in *explicit-implicit* methods. Similarly, Equation 6.85 can be expressed as

$$\frac{d\epsilon_{ij}^{cr}}{dt} = \sum_g f^g \frac{d\epsilon_{ij}^{g,cr}}{dt} \quad (\text{D.5})$$

which, using total differentials takes the form

$$d\epsilon_{ij}^{cr} = \sum_g f^g d\epsilon_{ij}^{g,cr} \quad (\text{D.6})$$

Integrating Equation D.6,

$$\int_{\epsilon_{ij_0}^{cr}}^{\epsilon_{ij_0}^{cr} + \Delta\epsilon_{ij}^{cr}} d\epsilon_{ij}^{cr} = \int_{\epsilon_{ij_0}^{m,cr}}^{\epsilon_{ij_0}^{m,cr} + \Delta\epsilon_{ij}^{m,cr}} f^g d\epsilon_{ij}^{g,cr} \quad (\text{D.7})$$

$$\Delta\epsilon_{ij}^{cr} \approx \sum_g f^g|_{t_0+\varphi\Delta t} \Delta\epsilon_{ij}^{g,cr} \quad (\text{D.8})$$

Following the same process for Equation 6.86,

$$\frac{d\epsilon_{ij}^{m,cr}}{dt} = \frac{3}{2} A^m (\sigma^m)^{n^m-1} s_{ij}^m \quad (\text{D.9})$$

$$\int_{\epsilon_{ij_0}^{m,cr}}^{\epsilon_{ij_0}^{m,cr} + \Delta\epsilon_{ij}^{m,cr}} d\epsilon_{ij}^{m,cr} = \int_{t_0}^{t_0+\Delta t} \frac{3}{2} A^m (\sigma^m)^{n^m-1} s_{ij}^m dt \quad (\text{D.10})$$

$$\Delta\epsilon_{ij}^{m,cr} \approx \frac{3}{2} A^m (\sigma^m)^{n^m-1} s_{ij}^m \Big|_{t_0+\varphi\Delta t} \Delta t \quad (\text{D.11})$$

where no summation is done over m . The m superscript indicates that Equation D.11 is applied to each of the phases present in the aggregate.

Equation 6.87, which represents the strain increments associated to the precipitation of new oxide,

$$\frac{d\epsilon_{ij}^{tr}}{dt} = \frac{1}{3} \ln(PBR_{eq}) \frac{df^{ox}}{dt} \quad (D.12)$$

$$d\epsilon_{ij}^{tr} = \frac{1}{3} \ln(PBR_{eq}) df^{ox} \quad (D.13)$$

$$\int_{\epsilon_{ij0}^{tr}}^{\epsilon_{ij0}^{tr} + \Delta\epsilon_{ij}^{tr}} d\epsilon_{ij}^{tr} = \int_{f_0^{ox}}^{f_0^{ox} + \Delta f^{ox}} \frac{1}{3} \ln(PBR_{eq}) df^{ox} \quad (D.14)$$

$$\Delta\epsilon_{ij}^{tr} \approx \frac{1}{3} \ln(PBR_{eq}) \Big|_{t_0 + \varphi\Delta t} \Delta f^{ox} \quad (D.15)$$

And finally, Equation 6.88, which links the aggregate and individual phase stress-strain states,

$$\frac{d\sigma_{ij}^m}{dt} = \frac{d\sigma_{ij}}{dt} + 2\mu(1 - \beta_t) \left(\frac{d\epsilon_{ij}^{cr}}{dt} - \frac{d\epsilon_{ij}^{m,cr}}{dt} \right) \quad (D.16)$$

$$\begin{aligned} \int_{\sigma_{ij0}^m}^{\sigma_{ij0}^m + \Delta\sigma_{ij}^m} d\sigma_{ij}^m &= \int_{\sigma_{ij0}}^{\sigma_{ij0} + \Delta\sigma_{ij}} d\sigma_{ij} \\ &+ \int_{\epsilon_{ij0}^{cr}}^{\epsilon_{ij0}^{cr} + \Delta\epsilon_{ij}^{cr}} 2\mu(1 - \beta_t) d\epsilon_{ij}^{cr} - \int_{\epsilon_{ij0}^{m,cr}}^{\epsilon_{ij0}^{m,cr} + \Delta\epsilon_{ij}^{m,cr}} 2\mu(1 - \beta_t) d\epsilon_{ij}^{m,cr} \end{aligned} \quad (D.17)$$

$$\Delta\sigma_{ij}^m \approx \Delta\sigma_{ij} + 2\mu(1 - \beta_t)|_{t_0 + \varphi\Delta t} \Delta\epsilon_{ij}^{cr} - 2\mu(1 - \beta_t)|_{t_0 + \varphi\Delta t} \Delta\epsilon_{ij}^{m,cr} \quad (D.18)$$

Equations D.18 and D.4 can be combined to obtain

$$\begin{aligned} \Delta\sigma_{ij}^m - \lambda\delta_{ij}|_{t_0 + \varphi\Delta t} \Delta\epsilon_{kk} - 2\mu|_{t_0 + \varphi\Delta t} \Delta\epsilon_{ij} + 2\mu|_{t_0 + \varphi\Delta t} \Delta\epsilon_{ij}^{tr} \\ + 3K\alpha\delta_{ij}|_{t_0 + \varphi\Delta t} \Delta T + 2\mu\beta_t|_{t_0 + \varphi\Delta t} \Delta\epsilon_{ij}^{cr} + 2\mu(1 - \beta_t)|_{t_0 + \varphi\Delta t} \Delta\epsilon_{ij}^{m,cr} \approx 0 \end{aligned} \quad (D.19)$$

Combining Equations D.19, D.15, D.8 and D.11 gives the system of equations

to solve in order to obtain the stress increments:

$$\left\{ \begin{array}{l} F_{ij}^m = \Delta\sigma_{ij}^m - \lambda\delta_{ij}|_{t_0+\varphi\Delta t} \Delta\epsilon_{kk} - 2\mu|_{t_0+\varphi\Delta t} \Delta\epsilon_{ij} \\ \quad + 2\mu|_{t_0+\varphi\Delta t} \Delta\epsilon_{ij}^{tr} + 3K\alpha\delta_{ij}|_{t_0+\varphi\Delta t} \Delta T \\ \quad + 2\mu\beta_t|_{t_0+\varphi\Delta t} \Delta\epsilon_{ij}^{cr} + 2\mu(1-\beta_t)|_{t_0+\varphi\Delta t} \Delta\epsilon_{ij}^{m,cr} \approx 0 \\ \Delta\epsilon_{ij}^{tr} \approx \frac{1}{3} \ln(PBR_{eq}) \Big|_{t_0+\varphi\Delta t} \Delta f^{ox} \\ \Delta\epsilon_{ij}^{cr} \approx \sum_g f^g|_{t_0+\varphi\Delta t} \Delta\epsilon_{ij}^{g,cr} \\ \Delta\epsilon_{ij}^{m,cr} \approx \frac{3}{2} A^m (\sigma^m)^{n^m-1} s_{ij}^m \Big|_{t_0+\varphi\Delta t} \Delta t, \text{ no sum on } m \end{array} \right. \quad (\text{D.20})$$

Equation system D.20 states a set of equations of the form $F_{ij}^m(\Delta\sigma_{kl}) = 0$. Since ABAQUS passes the aggregate total strain increments to the subroutine, $\Delta\epsilon_{ij}$, the unknown variables of that system of equations are $\Delta\sigma_{ij}^m$, the phase stress increment tensor. Once $\Delta\sigma_{ij}^m$ is calculated, $\Delta\epsilon_{ij}^{m,cr}$ can be obtained using Equation D.11, and $\Delta\epsilon_{ij}^{cr}$ is calculated subsequently through Equation D.8 and $\Delta\epsilon_{ij}^{in}$ from

$$\Delta\epsilon_{ij}^{in} = \Delta\epsilon_{ij}^{cr} + \Delta\epsilon_{ij}^{tr} \quad (\text{D.21})$$

Finally, $\Delta\epsilon_{ij}^{in}$ is substituted back into Equation D.4 to calculate the aggregate stress increment tensor, $\Delta\sigma_{ij}$.

However, the solution of the set of equations defined by $\mathbf{F}^m(\Delta\boldsymbol{\sigma}^m) = \mathbf{0}$ is not straightforward as it is composed of nonlinear equations that cannot be explicitly solved. The modified Newton-Raphson method [110] is used for that purpose. The Jacobian matrix of the system, $\frac{\partial F_{ij}^m}{\partial \Delta\sigma_{kl}^m}$, must be calculated and provided to the numerical algorithm in order to obtain the solution to the system.

D.2 Calculation of $\frac{\partial F_{ij}^m}{\partial \Delta \sigma_{kl}^m}$

From Equation system D.20, the derivative of F_{ij}^m with respect to $\Delta \sigma_{kl}^m$ is:

$$\begin{aligned} \frac{\partial F_{ij}^m}{\partial \Delta \sigma_{kl}^m} &= \frac{\partial \Delta \sigma_{ij}^m}{\partial \Delta \sigma_{kl}^m} + 2\mu|_{t_0+\varphi\Delta t} \frac{\partial \Delta \epsilon_{ij}^{tr}}{\partial \Delta \sigma_{kl}^m} \\ &\quad + 2\mu\beta_t|_{t_0+\varphi\Delta t} \frac{\partial \Delta \epsilon_{ij}^{cr}}{\partial \Delta \sigma_{kl}^m} + 2\mu(1-\beta_t)|_{t_0+\varphi\Delta t} \frac{\partial \Delta \epsilon_{ij}^{m,cr}}{\partial \Delta \sigma_{kl}^m} \end{aligned} \quad (D.22)$$

where the first term on the right hand side can be substituted as

$$\begin{aligned} \frac{\partial F_{ij}^m}{\partial \Delta \sigma_{kl}^m} &= \delta_{ik}^m \delta_{jl}^m + 2\mu|_{t_0+\varphi\Delta t} \frac{\partial \Delta \epsilon_{ij}^{tr}}{\partial \Delta \sigma_{kl}^m} \\ &\quad + 2\mu\beta_t|_{t_0+\varphi\Delta t} \frac{\partial \Delta \epsilon_{ij}^{cr}}{\partial \Delta \sigma_{kl}^m} + 2\mu(1-\beta_t)|_{t_0+\varphi\Delta t} \frac{\partial \Delta \epsilon_{ij}^{m,cr}}{\partial \Delta \sigma_{kl}^m} \end{aligned} \quad (D.23)$$

Equation D.23 can be further simplified taking into account that the transformation strain increments do not depend on the phase stress tensor,

$$\frac{\partial F_{ij}^m}{\partial \Delta \sigma_{kl}^m} = \delta_{ik}^m \delta_{jl}^m + 2\mu\beta_t|_{t_0+\varphi\Delta t} \frac{\partial \Delta \epsilon_{ij}^{cr}}{\partial \Delta \sigma_{kl}^m} + 2\mu(1-\beta_t)|_{t_0+\varphi\Delta t} \frac{\partial \Delta \epsilon_{ij}^{m,cr}}{\partial \Delta \sigma_{kl}^m} \quad (D.24)$$

The next step towards the calculation of the Jacobian is to obtain of the two unknown terms on the right hand side of Equation D.24, i.e. $\frac{\partial \Delta \epsilon_{ij}^{cr}}{\partial \Delta \sigma_{kl}^m}$ and $\frac{\partial \Delta \epsilon_{ij}^{m,cr}}{\partial \Delta \sigma_{kl}^m}$. The first of these two terms is obtained from differentiation of Equation D.8,

$$\frac{\partial \Delta \epsilon_{ij}^{cr}}{\partial \Delta \sigma_{kl}^m} = \sum_g f^g \frac{\partial \Delta \epsilon_{ij}^{g,cr}}{\partial \Delta \sigma_{kl}^m} \quad (D.25)$$

which reduces the problem down to the calculation of the second unknown term in Equation D.24, $\frac{\partial \Delta \epsilon_{ij}^{m,cr}}{\partial \Delta \sigma_{kl}^m}$. From differentiation of Equation D.11, this term can be expressed as

$$\frac{\partial \Delta \epsilon_{ij}^{m,cr}}{\partial \Delta \sigma_{kl}^m} = \frac{3}{2} A^m \left[(n^m - 1) (\sigma^m)^{n^m-2} \frac{\partial \sigma^m}{\partial \Delta \sigma_{kl}^m} s_{ij}^m + (\sigma^m)^{n^m-1} \frac{\partial s_{ij}^m}{\partial \Delta \sigma_{kl}^m} \right] \Big|_{t_0+\varphi\Delta t} \Delta t \quad (D.26)$$

where σ^m is the equivalent stress at each phase, calculated as

$$\sigma^m = \sqrt{\frac{3}{2} s_{rs}^m s_{rs}^m} \quad (D.27)$$

By differentiation of Equation D.27, $\frac{\partial \sigma^m}{\partial \Delta \sigma_{kl}^m}$ is obtained as needed in Equation D.26,

$$\frac{\partial \sigma^m}{\partial \Delta \sigma_{kl}^m} \Big|_{t_0+\varphi \Delta t} = \frac{1}{2} \left(\frac{3}{2} s_{rs}^m s_{rs}^m \right)^{-\frac{1}{2}} \frac{3}{2} s_{pq}^m \frac{\partial s_{pq}^m}{\partial \Delta \sigma_{kl}^m} \Big|_{t_0+\varphi \Delta t} = \frac{3}{2 \sigma^m} s_{pq}^m \frac{\partial s_{pq}^m}{\partial \Delta \sigma_{kl}^m} \Big|_{t_0+\varphi \Delta t} \quad (\text{D.28})$$

Equation D.28 can be rewritten in an alternative way, identifying the two tensors that compose its right hand side term,

$$\frac{\partial \sigma^m}{\partial \Delta \sigma_{kl}^m} \Big|_{t_0+\varphi \Delta t} = \frac{\partial \sigma^m}{\partial s_{pq}^m} \frac{\partial s_{pq}^m}{\partial \Delta \sigma_{kl}^m} \Big|_{t_0+\varphi \Delta t} \rightarrow \frac{\partial \sigma^m}{\partial s_{pq}^m} \Big|_{t_0+\varphi \Delta t} = \frac{3}{2 \sigma^m} s_{pq}^m \Big|_{t_0+\varphi \Delta t} \quad (\text{D.29})$$

Equation D.29 can be substituted back into Equation D.26 giving

$$\frac{\partial \Delta \epsilon_{ij}^{m,cr}}{\partial \Delta \sigma_{kl}^m} = \frac{3}{2} A^m \cdot \left[(n^m - 1) (\sigma^m)^{n^m-2} \frac{\partial \sigma^m}{\partial s_{pq}^m} \frac{\partial s_{pq}^m}{\partial \Delta \sigma_{kl}^m} s_{ij}^m + (\sigma^m)^{n^m-1} \frac{\partial s_{ij}^m}{\partial \Delta \sigma_{kl}^m} \right] \Big|_{t_0+\varphi \Delta t} \Delta t \quad (\text{D.30})$$

which can be expressed, making use of Kronecker's delta, as

$$\frac{\partial \Delta \epsilon_{ij}^{m,cr}}{\partial \Delta \sigma_{kl}^m} = \frac{3}{2} A^m \cdot \left[(n^m - 1) (\sigma^m)^{n^m-2} \frac{\partial \sigma^m}{\partial s_{pq}^m} \frac{\partial s_{pq}^m}{\partial \Delta \sigma_{kl}^m} s_{ij}^m + (\sigma^m)^{n^m-1} \delta_{ip}^m \delta_{jq}^m \frac{\partial s_{pq}^m}{\partial \Delta \sigma_{kl}^m} \right] \Big|_{t_0+\varphi \Delta t} \Delta t \quad (\text{D.31})$$

where the m superscript for δ specifies that it is non-zero only if the Jacobian refers to the derivative of the creep strain increment tensor of a phase m , $\Delta \epsilon^{m,cr}$, with respect of the stress increment tensor of the same phase, $\Delta \sigma^m$.

$\frac{\partial s_{pq}^m}{\partial \Delta \sigma_{kl}^m}$ can be extracted as a common factor to both terms in brackets in Equation D.31, giving as a result

$$\frac{\partial \Delta \epsilon_{ij}^{m,cr}}{\partial \Delta \sigma_{kl}^m} = \frac{3}{2} A^m \cdot \left[(n^m - 1) (\sigma^m)^{n^m-2} \frac{\partial \sigma^m}{\partial s_{pq}^m} s_{ij}^m + (\sigma^m)^{n^m-1} \delta_{ip}^m \delta_{jq}^m \right] \frac{\partial s_{pq}^m}{\partial \Delta \sigma_{kl}^m} \Big|_{t_0+\varphi \Delta t} \Delta t \quad (\text{D.32})$$

or, reordered as

$$\frac{\partial \Delta \epsilon_{ij}^{m,cr}}{\partial \Delta \sigma_{kl}^m} = \frac{3}{2} A^m \Delta t \cdot \left[(n^m - 1) (\sigma^m)^{n^m-2} \frac{\partial \sigma^m}{\partial s_{pq}^m} s_{ij}^m + (\sigma^m)^{n^m-1} \delta_{ip}^m \delta_{jq}^m \right] \frac{\partial s_{pq}^m}{\partial \Delta \sigma_{kl}^m} \Big|_{t_0+\varphi \Delta t} \quad (\text{D.33})$$

Substitutions can now be made in Equation D.33, following the same approach as for Equation D.29, giving the following:

$$\frac{\partial \Delta \epsilon_{ij}^{m,cr}}{\partial \Delta \sigma_{kl}^m} = \frac{\partial \Delta \epsilon_{ij}^{m,cr}}{\partial s_{pq}^m} \frac{\partial s_{pq}^m}{\partial \Delta \sigma_{kl}^m} \Big|_{t_0+\varphi\Delta t} \quad (\text{D.34})$$

The first tensor on the right hand side of Equation D.34, $\frac{\partial \Delta \epsilon_{ij}^{m,cr}}{\partial s_{pq}^m}$, is identified from Equation D.33 to be

$$\frac{\partial \Delta \epsilon_{ij}^{m,cr}}{\partial s_{pq}^m} \Big|_{t_0+\varphi\Delta t} = \frac{3}{2} A^m \Delta t (\sigma^m)^{n^m-2} \left[(n^m - 1) \frac{\partial \sigma^m}{\partial s_{pq}^m} s_{ij}^m + \sigma^m \delta_{ip}^m \delta_{jq}^m \right] \Big|_{t_0+\varphi\Delta t} \quad (\text{D.35})$$

At this point, the calculation of $\frac{\partial \Delta \epsilon_{ij}^{m,cr}}{\partial \Delta \sigma_{kl}^m}$, as needed by Equations D.24 and D.25, has been transformed to the calculation of $\frac{\partial \Delta \epsilon_{ij}^{m,cr}}{\partial s_{pq}^m} \Big|_{t_0+\varphi\Delta t}$ and $\frac{\partial s_{pq}^m}{\partial \Delta \sigma_{kl}^m} \Big|_{t_0+\varphi\Delta t}$, as stated in Equation D.34. $\frac{\partial \Delta \epsilon_{ij}^{m,cr}}{\partial s_{pq}^m} \Big|_{t_0+\varphi\Delta t}$ requires the tensor $\frac{\partial \sigma^m}{\partial s_{pq}^m} \Big|_{t_0+\varphi\Delta t}$ for its calculation, which is obtained using Equation D.29, so the only remaining unknown tensor is $\frac{\partial s_{pq}^m}{\partial \Delta \sigma_{kl}^m} \Big|_{t_0+\varphi\Delta t}$. The deviatoric stress tensor for a given phase, $s_{pq}^m \Big|_{t_0+\varphi\Delta t}$, is calculated as

$$s_{pq}^m \Big|_{t_0+\varphi\Delta t} = (\sigma_{pq}^m \Big|_{t_0} + \varphi \Delta \sigma_{pq}^m) - \frac{1}{3} (\sigma_{uu}^m \Big|_{t_0} + \varphi \Delta \sigma_{uu}^m) \delta_{pq}^m \quad (\text{D.36})$$

Derivating Equation D.36,

$$\frac{\partial s_{pq}^m}{\partial \Delta \sigma_{kl}^m} \Big|_{t_0+\varphi\Delta t} = \varphi \frac{\partial \Delta \sigma_{pq}^m}{\partial \Delta \sigma_{kl}^m} - \frac{1}{3} \varphi \delta_{pq}^m \delta_{kl}^m = \varphi \delta_{pk}^m \delta_{ql}^m - \frac{\varphi}{3} \delta_{pq}^m \delta_{kl}^m \quad (\text{D.37})$$

$\frac{\partial s_{pq}^m}{\partial \Delta \sigma_{kl}^m} \Big|_{t_0+\varphi\Delta t}$ is a tensor that only depends on the numerical integration parameter, φ , and is constant once this value has been fixed in a calculation. All the terms needed for the calculation of $\frac{\partial \Delta \epsilon_{ij}^{m,cr}}{\partial \Delta \sigma_{kl}^m}$ and hence for $\frac{\partial F_{ij}^m}{\partial \Delta \sigma_{kl}^m}$ have been obtained through Equations D.22 - D.37. The equations that allow the calculation of the Jacobian needed by the modified Newton-Raphson method

are listed in Equation system D.38,

$$\left\{ \begin{array}{l}
 \frac{\partial s_{pq}^m}{\partial \Delta \sigma_{kl}^m} \Big|_{t_0+\varphi\Delta t} = \varphi \delta_{pk}^m \delta_{ql}^m - \frac{\varphi}{3} \delta_{pq}^m \delta_{kl}^m \\
 \frac{\partial \sigma^m}{\partial s_{pq}^m} \Big|_{t_0+\varphi\Delta t} = \frac{3}{2\sigma^m} s_{pq}^m \Big|_{t_0+\varphi\Delta t} \\
 \frac{\partial \sigma^m}{\partial \Delta \sigma_{kl}^m} \Big|_{t_0+\varphi\Delta t} = \frac{\partial \sigma^m}{\partial s_{pq}^m} \frac{\partial s_{pq}^m}{\partial \Delta \sigma_{kl}^m} \Big|_{t_0+\varphi\Delta t} \\
 \frac{\partial \Delta \epsilon_{ij}^{m,cr}}{\partial s_{pq}^m} \Big|_{t_0+\varphi\Delta t} = \frac{3}{2} A^m \Delta t \\
 \quad \cdot (\sigma^m)^{n^m-2} \left[(n^m - 1) \frac{\partial \sigma^m}{\partial s_{pq}^m} s_{ij}^m + \sigma^m \delta_{ip}^m \delta_{jq}^m \right] \Big|_{t_0+\varphi\Delta t} \\
 \frac{\partial \Delta \epsilon_{ij}^{m,cr}}{\partial \Delta \sigma_{kl}^m} = \frac{\partial \Delta \epsilon_{ij}^{m,cr}}{\partial s_{pq}^m} \frac{\partial s_{pq}^m}{\partial \Delta \sigma_{kl}^m} \Big|_{t_0+\varphi\Delta t} \\
 \frac{\partial \Delta \epsilon_{ij}^{cr}}{\partial \Delta \sigma_{kl}^m} = \sum_g f^g \frac{\partial \Delta \epsilon_{ij}^{g,cr}}{\partial \Delta \sigma_{kl}^m} \\
 \frac{\partial F_{ij}^m}{\partial \Delta \sigma_{kl}^m} = \delta_{ik}^m \delta_{jl}^m + 2\mu \beta_t \Big|_{t_0+\varphi\Delta t} \frac{\partial \epsilon_{ij}^{cr}}{\partial \Delta \sigma_{kl}^m} + 2\mu(1 - \beta_t) \Big|_{t_0+\varphi\Delta t} \frac{\partial \epsilon_{ij}^{m,cr}}{\partial \Delta \sigma_{kl}^m}
 \end{array} \right. \quad (D.38)$$

D.3 Stress Jacobian calculation

The aggregate stress Jacobian $\frac{\partial \Delta \sigma_{ij}}{\partial \Delta \epsilon_{kl}}$ has to be provided by the subroutine to ABAQUS in order to obtain the stiffness of the material and to form the stiffness matrix needed for the solution of the next increment in the FE calculation. The derivative of Equation D.4 is,

$$\frac{\partial \Delta \sigma_{ij}}{\partial \Delta \epsilon_{kl}} \approx \lambda \delta_{ij} \delta_{kl} \Big|_{t_0+\varphi\Delta t} + 2\mu \Big|_{t_0+\varphi\Delta t} \delta_{ik} \delta_{jl} - 2\mu \Big|_{t_0+\varphi\Delta t} \frac{\partial \Delta \epsilon_{ij}^{in}}{\partial \Delta \epsilon_{kl}} \quad (D.39)$$

with

$$\frac{\partial \Delta \epsilon_{ij}^{in}}{\partial \Delta \epsilon_{kl}} = \frac{\partial \Delta \epsilon_{ij}^{cr}}{\partial \Delta \epsilon_{kl}} + \frac{\partial \Delta \epsilon_{ij}^{tr}}{\partial \Delta \epsilon_{kl}} \quad (D.40)$$

The second term on the right hand side of Equation D.40 is zero as the transformation strain increments do not depend on the total strain increments.

The derivative of Equation D.18 is

$$\frac{\partial \Delta \sigma_{ij}^m}{\partial \Delta \epsilon_{kl}} \approx \frac{\partial \Delta \sigma_{ij}}{\partial \Delta \epsilon_{kl}} + 2\mu(1 - \beta_t)|_{t_0+\varphi\Delta t} \frac{\partial \Delta \epsilon_{ij}^{cr}}{\partial \Delta \epsilon_{kl}} - 2\mu(1 - \beta_t)|_{t_0+\varphi\Delta t} \frac{\partial \Delta \epsilon_{ij}^{m,cr}}{\partial \Delta \epsilon_{kl}} \quad (\text{D.41})$$

Combining Equations D.39 and D.41

$$\begin{aligned} \frac{\partial \Delta \sigma_{ij}^m}{\partial \Delta \epsilon_{kl}} \approx & \lambda \delta_{ij} \delta_{kl}|_{t_0+\varphi\Delta t} + 2\mu|_{t_0+\varphi\Delta t} \delta_{ik} \delta_{jl} - 2\mu|_{t_0+\varphi\Delta t} \frac{\partial \Delta \epsilon_{ij}^{in}}{\partial \Delta \epsilon_{kl}} \\ & + 2\mu(1 - \beta_t)|_{t_0+\varphi\Delta t} \frac{\partial \Delta \epsilon_{ij}^{cr}}{\partial \Delta \epsilon_{kl}} - 2\mu(1 - \beta_t)|_{t_0+\varphi\Delta t} \frac{\partial \Delta \epsilon_{ij}^{m,cr}}{\partial \Delta \epsilon_{kl}} \end{aligned} \quad (\text{D.42})$$

Reordering Equation D.42 and assuming $\frac{\partial \Delta \epsilon_{ij}^{tr}}{\partial \Delta \epsilon_{kl}} = 0$,

$$\begin{aligned} \frac{\partial \Delta \sigma_{ij}^m}{\partial \Delta \epsilon_{kl}} + 2\mu\beta_t|_{t_0+\varphi\Delta t} \frac{\partial \Delta \epsilon_{ij}^{cr}}{\partial \Delta \epsilon_{kl}} + 2\mu(1 - \beta_t)|_{t_0+\varphi\Delta t} \frac{\partial \Delta \epsilon_{ij}^{m,cr}}{\partial \Delta \epsilon_{kl}} \\ \approx \lambda \delta_{ij} \delta_{kl}|_{t_0+\varphi\Delta t} + 2\mu|_{t_0+\varphi\Delta t} \delta_{ik} \delta_{jl} \end{aligned} \quad (\text{D.43})$$

The derivatives in Equation D.43 are with respect to the total strain increments. These derivatives can be expanded to include derivatives with respect to the phase stress tensor, giving as a result

$$\begin{aligned} \frac{\partial \Delta \sigma_{ij}^m}{\partial \Delta \epsilon_{kl}} + 2\mu\beta_t|_{t_0+\varphi\Delta t} \frac{\partial \Delta \epsilon_{ij}^{cr}}{\partial \Delta \sigma_{pq}^m} \frac{\partial \Delta \sigma_{pq}^m}{\partial \Delta \epsilon_{kl}} + 2\mu(1 - \beta_t)|_{t_0+\varphi\Delta t} \frac{\partial \Delta \epsilon_{ij}^{m,cr}}{\partial \Delta \sigma_{pq}^m} \frac{\partial \Delta \sigma_{pq}^m}{\partial \Delta \epsilon_{kl}} \\ \approx \lambda \delta_{ij} \delta_{kl}|_{t_0+\varphi\Delta t} + 2\mu|_{t_0+\varphi\Delta t} \delta_{ik} \delta_{jl} \end{aligned} \quad (\text{D.44})$$

$\frac{\partial \Delta \sigma_{ij}^m}{\partial \Delta \epsilon_{kl}}$ can be extracted as a common factor on the left hand side term of Equation D.44, which is then rewritten as

$$\begin{aligned} \left[\delta_{ip}^m \delta_{jq}^m + 2\mu\beta_t|_{t_0+\varphi\Delta t} \frac{\partial \Delta \epsilon_{ij}^{cr}}{\partial \Delta \sigma_{pq}^m} + 2\mu(1 - \beta_t)|_{t_0+\varphi\Delta t} \frac{\partial \Delta \epsilon_{ij}^{m,cr}}{\partial \Delta \sigma_{pq}^m} \right] \frac{\partial \Delta \sigma_{pq}^m}{\partial \Delta \epsilon_{kl}} \\ \approx \lambda \delta_{ij} \delta_{kl}|_{t_0+\varphi\Delta t} + 2\mu|_{t_0+\varphi\Delta t} \delta_{ik} \delta_{jl} \end{aligned} \quad (\text{D.45})$$

Once Equation system D.20 has been solved using the Jacobian in Equation system D.38 and the phase stress increments $\Delta \sigma^m$ that solve the problem $\mathbf{F}^m(\Delta \sigma^m) = 0$ have been calculated, the terms in brackets on the left hand side of Equation D.45 are all known. The terms on the right hand side correspond to the elastic constants of the aggregate, so the only unknown term is

$\frac{\partial \Delta \sigma_{pq}^m}{\partial \Delta \epsilon_{kl}}$. Hence, Equation D.45 constitutes a linear system of equations used for the calculation of $\frac{\partial \Delta \sigma_{pq}^m}{\partial \Delta \epsilon_{kl}}$. After solving Equation D.45, the $\frac{\partial \Delta \sigma_{ij}}{\partial \Delta \epsilon_{kl}}$ Jacobian is calculated using a simplified version of Equation D.39 where $\frac{\partial \Delta \epsilon_{ij}^{tr}}{\partial \Delta \epsilon_{kl}} = 0$ was assumed and expanding $\frac{\partial \Delta \epsilon_{ij}^{cr}}{\partial \Delta \epsilon_{kl}}$ to use the phase stress increment tensor as in

$$\begin{cases} \frac{\partial \Delta \sigma_{ij}}{\partial \Delta \epsilon_{kl}} \approx \lambda \delta_{ij} \delta_{kl} |_{t_0 + \varphi \Delta t} + 2\mu |_{t_0 + \varphi \Delta t} \delta_{ik} \delta_{jl} - 2\mu |_{t_0 + \varphi \Delta t} \frac{\partial \Delta \epsilon_{ij}^{cr}}{\partial \Delta \epsilon_{kl}} \\ \frac{\partial \Delta \epsilon_{ij}^{cr}}{\partial \Delta \epsilon_{kl}} = \frac{\partial \Delta \epsilon_{ij}^{cr}}{\partial \Delta \sigma_{pq}^m} \frac{\partial \Delta \sigma_{pq}^m}{\partial \Delta \epsilon_{kl}} \end{cases} \quad (\text{D.46})$$

The equations needed to calculate $\frac{\partial \Delta \epsilon_{ij}^{cr}}{\partial \Delta \sigma_{pq}^m}$ are listed in Equation system D.38.

D.4 Stress Jacobian with respect to temperature

In order to improve the convergence rate of calculations when temperature changes are considered, the $\frac{\partial \Delta \sigma_{ij}}{\partial \Delta T}$ Jacobian must be calculated and provided to ABAQUS by the subroutine. From differentiation of Equation D.4,

$$\frac{\partial \Delta \sigma_{ij}}{\partial \Delta T} \approx -3K\alpha |_{t_0 + \varphi \Delta t} \delta_{ij} \quad (\text{D.47})$$